Study of Scalar Non-Standard Neutrino Interactions and Development of a Pre-supernova Alert System at Super-Kamiokande

Zhuojun Hu

Thesis Supervisors:
Prof. Roger Wendell

Kyoto University
Graduate School of Science
Department of Physics
Physics and Astrophysics

September 2025

献给我亲爱的家人
以及我的妻子麦雯静女士

Abstract

The neutrinos produced from core-collapse supernovae (CCSNs) are of crucial importance in terms of exploring the explosion mechanism, the structure of the neutron star, and the formation of black holes. So far, the only observation of supernova burst neutrinos was made from SN1987A, a supernova in the Large Magellanic Cloud 50 kpc away from us. Although the observation was low in statistics, it provided confirmation of the basic theoretical framework of the explosion mechanism. Next generation detectors with state-of-the-art detection techniques are expected to observe CCSN via neutrinos with higher statistics and better energy resolution. Due to the rarity of the CCSNs, it is essential to ensure the observations.

In the final stages preceding a CCSN, various processes produce an increasing amount of neutrinos of all flavors characterized by mounting energies from the interior of massive stars. Of them, electron antineutrinos are potentially detectable by terrestrial neutrino experiments such as KamLAND and SK via inverse beta decay interactions. Once these pre-supernova neutrinos are observed, an early warning of the upcoming core-collapse supernova can be provided. In light of this, KamLAND and SK have been monitoring pre-supernova neutrinos since 2015 and 2021, respectively. We developed and put into operation a pre-supernova alert system combining the KamLAND detector and the SK detector. Fully leveraging the complementary properties of these two detectors, the combined alert is expected to resolve a pre-supernova neutrino signal from a $15\,M_{\odot}$ star within 510 pc of the Earth, at a significance level corresponding to a false alarm rate of no more than 1 per century. For a Betelgeuse-like model with optimistic parameters, the combined alert can provide early warnings up to 12 hours before CCSN to the astrophysics community, allowing for preparation time for supernova burst neutrino and gravitational wave observations.

Beyond supernova neutrino observation, this thesis also explores new physics effects in neutrino oscillations through the study of scalar non-standard interactions. The scalar non-standard neutrino interactions (scalar-NSI) are a type of new physics in which neutrinos couple to a scalar field, inducing matter-dependent corrections to their masses. Such interactions can affect the interpretation of neutrino oscillation data, altering the measurements of the neutrino oscillation parameters. This thesis presents the first study on the scalar-NSI in the Super-Kamiokande (SK), with 1489 days of atmospheric neutrino data from the SK I phase, reconstructed with a precision reconstruction algorithm, fiTQun. The PMT response model for the simulations in the SK I phase is refined using Michel electrons from cosmic-ray muon decays as a calibration source. The updated model is used to produce predictions for this analysis.

We studied both the diagonal and off-diagonal scalar-NSI parameters one at a time, for normal and inverted mass orderings. Throughout the analysis, the lightest

neutrino mass is fixed to zero, and the results are presented at a matter density of 2.6,g/cm^3. No significant signal of the scalar-NSI is found. For the diagonal scalar-NSI parameters, inverted ordering results are consistent with the standard neutrino oscillations at 68% C.L., with $\eta_{\mu\mu}$ and $\eta_{\tau\tau}$ determined to be $-0.04^{+0.08}_{-0.08}$ and $-0.04^{+0.04}_{-0.03}$. The normal ordering results are consistent with the standard neutrino oscillations at 90% C.L. The best-fit values are $\eta_{\mu\mu} = -0.38^{+0.04}_{-0.03}$ and $\eta_{\tau\tau} = -0.36^{+0.06}_{-0.04}$, with large $|\Delta m^2_{32}|$ values of $4.15^{+0.04}_{-0.82} \times 10^{-3}\,\mathrm{eV}^2$ and $3.85^{+0.86}_{-0.65} \times 10^{-3}\,\mathrm{eV}^2$ respectively, suggesting a degeneracy. The off-diagonal analysis indicates a weak preference for $|\eta_{\mu\tau}| \sim 0.3$ with a phase of $\phi_{\mu\tau} \sim \pi$ in the normal ordering and $\phi_{\mu\tau} \sim 0$ in the inverted ordering, also with a large value of $|\Delta m^2_{32}|$, but still consistent with the standard neutrino oscillations. The other off-diagonal scalar-NSI parameters in good agreement with the standard neutrino oscillations.

The results are converted to fundamental parameters $\zeta_{\alpha\beta} = y_q y_{\alpha\beta}/m^2_\phi$ consisting of Yukawa couplings and mass of the scalar mediator, for comparison among different experiments. The 90% allowed intervals for $\zeta_{\mu\mu}$ is $[-640, 152]$ in normal ordering and $[-280, 185]$ in inverted ordering, in units of $10^{-15}\mathrm{eV}^{-2}$. For $\zeta_{\tau\tau}$, the 90% allowed intervals are $[-1188, -1002] \oplus [-637, 83.4]$ in normal ordering and $[-582, -351] \oplus [-314, 185]$ in inverted ordering in units of $10^{-15}\mathrm{eV}^{-2}$. The sign $\oplus$ denotes that there are two allowed intervals for $\zeta_{\tau\tau}$ in both normal and inverted orderings. The constraints on $\zeta_{\mu\mu}$ and $\zeta_{\tau\tau}$ are one or two orders of magnitude weaker compared to the result of a phenomenological study of solar neutrino data [1]. That being said, this is the first experimental study of the scalar-NSI and will be the basis for future studies.

This study uses only a subset of the SK atmospheric neutrino data. For a projected livetime of 9400 days, approximately the total SK exposure, the 68% confidence intervals for the diagonal scalar-NSI parameters are expected to shrink to about one-third of those from SK-I, while the off-diagonal parameters $\eta_{\alpha\beta}$ are expected to be constrained below 0.1 which roughly corresponds to $|\zeta_{\alpha\beta}| = 1.49 \times 10^{-13}\mathrm{eV}^{-2}$.

Acknowledgments

I would like to express my deepest gratitude to my supervisor, Prof. Roger Wendell, for his invaluable guidance, continuous support, and insightful advice throughout my three years and four months of doctoral study. His profound understanding of physics and his perspectives on life have been a constant source of inspiration and have greatly shaped my academic and personal growth.

I am sincerely thankful to Motoyasu Ikeda, Koji Ishidoshiro, Koichi Ichimura, Lucas Nascimento Machado, Lluis Marti Magro, and Keita Saito, with whom I had the great pleasure of collaborating on the study of pre-supernova neutrinos. Their expertise, constructive discussions, and encouragement were instrumental in advancing this research.

I would also like to extend my appreciation to Benjamin Quilain, Christine Quach, Yiyang Wu, and Myung gi Jo for their valuable contributions and cooperation in the preparation of neutrino data for analyses with fiTQun. Their technical proficiency and dedication made the work both productive and rewarding.

I am deeply grateful to all members of the Super Kamiokande Collaboration, past and present, for their collective efforts in maintaining and advancing this remarkable experiment. In particular, I would like to thank Hiroyuki Sekiya and Masayuki Nakahata for their leadership and guidance. I am also indebted to the members of the ATMPD group, Yoshinari Hayato, Edward Kearns, Makoto Miura, Takuya Tashiro, Seisho Abe, and Jun Kameda, for their inspiring suggestions and their help in preparing the neutrino data set. I wish to thank members of the EGADS group and LowE group, especially Mark Vagins, Yusuke Koshio, and Michael Smy, for their valuable comments on my pre-supernova study. My special thanks go to the members of the local energy scale group, Shunichi Mine, Joanna Zalipska, and Rory Ramsden, for their assistance in the estimation of the energy scale uncertainty.

I am also grateful to all present and former members of the High Energy Physics Laboratory at Kyoto University, where I spent three years as a Doctor of Philosophy candidate. I to thank especially members in Room 304: Yutarou Kasai, Jiahui Feng, Licheng Feng, Hironobu Nakata, Hiroku, Takeuchi for providing a stimulating and supportive research environment. It was a truly wonderful experience working with you all. My heartfelt thanks go to Ms. Okazaki, Ms. Ishikura, Mrs. Sekiguchi, and Ms. Ashida for their kind assistance with administrative matters.

I am deeply appreciative of the Japanese Government (MEXT) Scholarship, which generously supported my study and stay in Japan. I would also like to acknowledge all colleagues and friends who have supported me, directly or indirectly, during my doctoral studies. I have received so much help and encouragement that it would be

impossible to name everyone individually.

Finally, I would like to express my gratitude to my family for always supporting me, and especially to my wife for her company and encouragement.

静静好萌好可爱谁敢反对打爆谁的狗头！

Contents

List of Figures

List of Tables

Part 0

Introduction

Chapter 1

Thesis Overview

This thesis contains two works focusing on neutrino physics at the Super-Kamiokande experiment. The first work is the development of a combined pre-supernova early warning system integrating the Super-Kamiokande experiment and the KamLAND experiment. The second work is an experimental search of non-standard neutrino interactions mediated by a scalar particle with the atmospheric neutrino oscillation data at the Super-Kamiokande experiment. The neutrino and the Super-Kamiokande experiment are introduced in Chapter 2 and 3. The two studies are detailed in Part 1 and Part 2.

The pre-supernova early warning system with the KamLAND experiment and the Super-Kamiokande experiment is referred to as the "combined pre-supernova alert system". The first and only direct observation of supernova neutrinos is from SN 1987A [2, 3, 4]. Although it provided a probe for the interior of a supernova, the low statistics from it have limited further development of supernova explosion mechanisms. A galactic core-collapse supernova (CCSN) would provide an opportunity to further develop supernova models. However, galactic CCSNs are estimated to occur only at a rate of $3.2^{+7.3}_{-2.6}$ per century [5]. Therefore, there is a strong motivation to establish an early warning of CCSN to allow multiple observatories time to fully observe the event. The combined pre-supernova neutrino alert system searches for pre-supernova neutrinos, which feature a mounting flux before the CCSN, as a signal of an imminent CCSN. It monitors the neutrino flux from the nearby CCSN candidates and provides the astrophysical community with a real-time result of the search. Details of this work are presented in Chapter 4, 5, 6, and 7.

The second part of the thesis presents a test of new physics beyond the Standard Model of particle physics. The scalar mediated non-standard neutrino interactions (scalar-NSI) assumes couplings of neutrinos to a hypothetical scalar field [6]. The presence of the scalar-NSI has been used to explain the Borexino data [6] as well as the

slight tension in the NOvA and T2K data [7]. Moreover, phenomenology studies show that the effects of the scalar-NSI cannot be ignored in the next generation precision neutrino experiments, e.g. the impact of the scalar-NSI on the CPV measurement can be significant [8, 9, 10]. Motivated by these studies, this work aims to test the pure neutrino oscillations in the atmospheric neutrino data at the Super-Kamiokande experiment against the possible presence of the scalar-NSI. This work presents the first experimental search of the scalar-NSI, which is described in the Chapters 8, 9, 10, 11, and 12. Chapter 8 is an introduction to the scalar-NSI. Chapters 9, 10, and 11 describe the simulation, event selection, and reconstruction of atmospheric neutrinos which work as the probe in this work. The analysis method, systematic uncertainties, and results of the analysis are presented in Chapter 12.

Chapter 2

The neutrino

The neutrino is one of the most fundamental particles in the universe. Over the last century, discoveries surrounding the neutrino have not only confirmed key aspects of the Standard Model of particle physics but also revealed profound mysteries that remain unresolved. Open questions include whether neutrinos are their own antiparticles, which type is heavier, and whether there is charge-parity violation (CPV) in their oscillations. Neutrinos are fascinating not only because of their mysteries, but also because of their ability to convey information inaccessible through other messengers. As they travel almost unimpeded through matter and are not affected by electric or magnetic fields, neutrinos can probe environments such as stellar cores or the Earth's interior.

This Chapter begins with a short history of the neutrino in Section 2.1. The properties of neutrinos are first explained in Section 2.2, followed by discussions of neutrino oscillations in Section 2.3. Experimental status of neutrinos is discussed in Section 2.4.

2.1 Short History of the Neutrino

The neutrino was once a desperate hypothesis to save the law of energy conservation. In the early 20^{th} century, observations of beta decay showed that the emitted electrons had a continuous energy spectrum, contradicting the expectation of discrete energy levels and appearing to violate the law of energy conservation:

$$n \rightarrow p + e^{-} + \text{missing energy}. \tag{2.1}$$

In 1930, Wolfgang Pauli proposed "neutron", a neutral, nearly massless particle, that escaped detection and carried away the missing energy [11, 12]. Later in 1934, this

particle was renamed "neutrino" by Enrico Fermi, who evolved the theory of beta decay and incorporated the neutrino into his theory [13, 14]. The beta decay is written as

$$n \to p + e^- + \nu, \tag{2.2}$$

where ν denotes the neutrino.

For over two decades, the neutrino remained purely hypothetical. The situation changed in 1956 when Clyde Cowan and Frederick Reines succeeded in detecting the electron anti-neutrino ($\bar{\nu}_e$) emitted from a nuclear reactor at the Savannah River Site, South Carolina [15, 16]. Their experiment used a detector consisting of two tanks of water surrounded by liquid scintillator. The water tanks serve as targets for inverse beta decay, where an incoming $\bar{\nu}_e$ converts a proton into a neutron and a positron:

$$\bar{\nu}_e + p \to n + e^+. \tag{2.3}$$

The positron immediately annihilates with an electron and produces two gamma rays, which are detected by the liquid scintillator. The water is doped with $CdCl_2$ to capture neutrons. The coincident detection of the positron and neutron confirmed the existence of the neutrino.

A second type of neutrino, the muon neutrino (ν_μ) was discovered in 1962 by Leon Lederman, Melvin Schwartz, and Jack Steinberger [17]. They conducted an experiment at Brookhaven National Laboratory, using a proton beam to create high-velocity pions which then decayed into neutrinos and muons. By allowing only neutrinos to enter their detector, muons were observed instead electrons. This result confirmed the existence of a second neutrino, ν_μ, different from ν_e. It also demonstrated that a given type of charged lepton (electron or muon) and a corresponding neutrino (ν_e or ν_μ) form a pair. Such grouping in pairs was later recognized fundamental in particle physics (see Section 2.2).

When the tau lepton was discovered in the 1970s, a third neutrino ν_τ was immediately implied. However, it was not directely observed until 2000, when the DONUT (Direct Observation of NU Tau) experiment at Fermilab identified interactions consistent with ν_τ events [18]. DONUT used high-resolution nuclear emulsions to observe short-lived tau leptons, and confirmed the existence of ν_τ.

Apart from the direct observation, measurements of the Z boson decay width at the Large Electron–Positron Collider (LEP) at CERN demonstrated that Z decayed invisibly into neutrinos at a rate consistent with only three neutrino species: ν_e, ν_μ, and ν_τ [19, 20, 21]. This result strongly constrained the number of active neutrinos with mass less than $m_Z/2$ to $N_\nu = 2.984 \pm 0.008$ [22].

In 1998, the Super-Kamiokande (SK) experiment reported a deficit of muon neutrinos coming from atmospheric cosmic-rays, depending on the zenith angle [23]. This provided compelling evidence that muon neutrinos were transitioning into tau neutrinos as they traveled through the Earth. In 2001, the Sudbury Neutrino Observatory (SNO) in Canada resolved the long-standing solar neutrino problem by showing that the total flux of neutrinos from the Sun agreed with theoretical predictions where only about one-third of the solar neutrinos arrived on Earth as electron neutrinos, while the rest had oscillated into muon and tau flavors [24]. These were direct observations of neutrino oscillations and implied that neutrinos have non-zero masses and their flavor states are mixtures of mass states (see Section 2.3.1).

2.2 Neutrinos in the Standard Model

The Standard Model of particle physics is a theoretical framework that describes the fundamental particles of nature and the interactions among them, except for gravity. It was developed in the 1970s by Sheldon Glashow, Steven Weinberg, Abdus Salam, François Englert, Peter Higgs, and others, following decades of both theoretical advances and experimental discoveries. It is highly precise in its predictions and has successfully explained a vast array of experimental results and accurately predicted phenomena like the existence and properties of the W and Z bosons, the top quark, and the Higgs boson.

The Standard Model classifies particles by their spin. Particles with spin-1/2 are called fermions and are fundamental components of matter. The interactions between fermions are mediated by the spin-1 particles called bosons. A special particle, Higgs boson which has 0 spin, gives mass to all massive elementary particles of the Standard Model. As listed in Table 2.1, the Standard Model includes twelve fermions (six quarks and six leptons, organized in three generations), four force-carrying bosons (photon (γ), gluons (g), and W and Z bosons), and the Higgs boson. The six quarks are u, c and t, with +2/3 charge, and d, s and b, with -1/3 charge. Quarks interact via the strong, weak, and electromagnetic forces. The electron (e), muon (μ) and tau (τ) are charged leptons, each has -1 charge and interacts through the weak and electromagnetic interactions. Neutrinos are neutral leptons without charge and have only weak interactions. There are three lepton flavors of neutrinos: the electron neutrino (ν_e), the muon neutrino (ν_μ) and the tau neutrino (ν_τ). Photons mediate the electromagnetic interactions, responsible for charged particles, and gluons mediate the strong interactions between quarks. The W and Z bosons mediate the weak interactions between all fermions.

The Standard Model uses gauge symmetries $\mathrm{SU(3)_c \times SU(2)_L \times U(1)_Y}$ to describe the above interactions. For weak interactions, the intrinsic chirality of a particle is

Table 2.1: Fundamental particles in the Standard Model of particle physics. For each particle, the mass is listed below its symbol, and its charge is shown in the next row. The electron neutrino mass upper limit is measured to $0.45 \text{eV}/c^2$ at 90% confidence level (C.L.) by KATRIN in 2024 [25]. Although the muon and tau neutrino masses are also bounded by direct measurements, recent cosmological data fits have determined the upper limit of the sum of all three neutrino masses to be $\sim 0.072\,\text{eV}/c^2$ at 95% C.L. [26].

Fermions Spin = 1/2			**Vector Bosons** Spin = 1	**Scalar Bosons** Spin = 0
1st generation	2nd generation	3rd generation		
u $2.2\,\text{MeV}/c^2$	**c** $1.28\,\text{GeV}/c^2$	**t** $173\,\text{GeV}/c^2$	**g** $0\,\text{eV}/c^2$	$\mathbf{H}^0$ $125\,\text{GeV}/c^2$
Q = +2/3			Q = 0	Q = 0
d $4.7\,\text{MeV}/c^2$	**s** $96\,\text{MeV}/c^2$	**b** $4.18\,\text{GeV}/c^2$	$\boldsymbol{\gamma}$ $0\,\text{eV}/c^2$	
Q = -1/3			Q = 0	
$\boldsymbol{e}$ $0.51\,\text{MeV}/c^2$	$\boldsymbol{\mu}$ $106\,\text{MeV}/c^2$	$\boldsymbol{\tau}$ $1.78\,\text{GeV}/c^2$	**W** $80\,\text{GeV}/c^2$	
Q = -1			Q = ±1	
$\boldsymbol{\nu_e}$ $< 0.45\,\text{eV}/c^2$	$\boldsymbol{\nu_\mu}$ $< 1\,\text{eV}/c^2$	$\boldsymbol{\nu_\tau}$ $< 1\,\text{eV}/c^2$	$\mathbf{Z}^0$ $91\,\text{GeV}/c^2$	
Q = 0			Q = 0	

crucial. Only particles with left-handed chirality or anti-particles with right-handed chirality can interact via the weak interactions. Quarks and charged leptons have both left-handed and right-handed components, while neutrinos are all left-handed because they only interact weakly. Therefore, parity symmetry is violated in the weak interactions, but charge conjugation parity (CP) symmetry still preserves.

Neutrinos form $\text{SU(2)}_\text{L} \times \text{U(1)}_\text{Y}$ doublets with their correspondingly named left-handed charged leptons:

$$\begin{pmatrix} \nu_e \\ e \end{pmatrix}_L, \begin{pmatrix} \nu_\mu \\ \mu \end{pmatrix}_L, \begin{pmatrix} \nu_\tau \\ \tau \end{pmatrix}_L. \tag{2.4}$$

Neutrino interactions are mediated by the W and Z bosons. Of these, W bosons mediate the weak "charged current" interactions. It is named charged current (CC) because a transfer of charge is involved. In addition, a change in particle type within the same generation also occurs, e.g. from a neutrino into its counterpart charged lepton. Note that a change in particle type across generations is forbidden in the Standard Model. Interactions that exchange a Z boson are known as neutral current (NC) interactions because no transfer of charge is involved. Change in particle type does not happen in an NC interaction. Example Feynman diagrams for CC and NC interactions are in Figure 2.1. Anti-particle interactions are analogous to particle

interactions but with opposite charges. The CC and NC interactions are described by the following Lagrangian:

$$-\mathcal{L}_{\mathrm{CC}} = \frac{g}{\sqrt{2}} \sum_{l} \bar{\nu}_{Ll} \gamma^{\mu} l_{L}^{-} W_{\mu}^{+} + \mathrm{h.c.}, \tag{2.5}$$

$$-\mathcal{L}_{\mathrm{NC}} = \frac{g}{2\cos\theta_{W}} \sum_{l} \bar{\nu}_{Ll} \gamma^{\mu} \nu_{Ll} Z_{\mu}^{0}, \tag{2.6}$$

where g is the coupling constant associated with SU(2) and θ_W is the Weinberg angle. Of these, Eq. 2.6 determines the decay width of Z boson into left-handed neutrinos. Therefore, the number of left-handed neutrino states can be inferred from the measurement of invisible decay width of Z boson as introduced in Section 2.1.

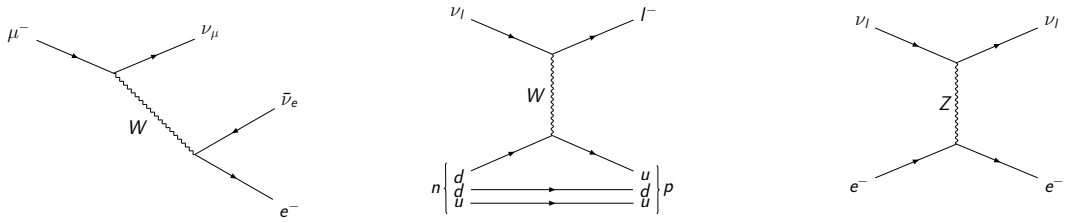

(a) CC (b) CC (c) NC

Figure 2.1: Example Feynman diagrams for charged current (CC) and neutral current (NC) interactions. In (a), a muon decays into a muon neutrino, an electron neutrino and an electron. In (b), a neutrino exchanges a W boson and produces a corresponding charged lepton, with a d quark changes into a u quark. In (c), a neutrino scatters with an electron by exchanging a Z boson. l denotes one of the lepton flavors.

In the Standard Model, neutrinos are precisely massless. The masses of massive fermions are generated via interactions of their left-handed and right-handed components with the scalar Higgs field. Since the model does not contain right-handed neutrinos, such interactions do not occur for neutrinos, leaving them as massless particles. The discovery of neutrino oscillations have confirmed that neutrinos have mass, indicating new physics beyond the Standard Model.

2.3 Neutrino Oscillations

The phenomenon of neutrino oscillations is that as a neutrino propagates through the space, its flavor varies. This phenomenon arises from the mixing between the neutrino mass eigenstates and the neutrino flavor eigenstates. The three neutrino flavor eigenstates $(\nu_e, \nu_\mu, \nu_\tau)$ are each a different mixture of the three neutrino mass states (ν_1, ν_2, ν_3). For each flavor states, the mixture of the mass states can be written

as

$$|\nu_\alpha\rangle = \sum_{i=1,2,3} U^*_{\alpha i}|\nu_i\rangle, \tag{2.7}$$

where α can be e, μ, or τ. U is the Pontecorvo-Maki-Nakagawa-Sakata (PMNS) matrix [27, 28], which is a unitary matrix. The matrix can be parameterized as a product of three rotation matrices, each mixing two out of the three mass states via an euler angle (θ_{12}, θ_{13} and θ_{23}), and three CP-violating phases (δ_{CP}, ρ and σ). Let $c_{ij} = \cos\theta_{ij}$ and $s_{ij} = \sin\theta_{ij}$, U can be written as:

$$U = \begin{pmatrix} 1 & 0 & 0 \\ 0 & c_{23} & s_{23} \\ 0 & -s_{23} & c_{23} \end{pmatrix} \begin{pmatrix} c_{13} & 0 & s_{13}e^{-i\delta_{CP}} \\ 0 & 1 & 0 \\ -s_{13}e^{i\delta_{CP}} & 0 & c_{13} \end{pmatrix} \begin{pmatrix} c_{12} & s_{12} & 0 \\ -s_{12} & c_{12} & 0 \\ 0 & 0 & 1 \end{pmatrix} \begin{pmatrix} e^{i\rho} & 0 & 0 \\ 0 & e^{i\sigma} & 0 \\ 0 & 0 & 1 \end{pmatrix}. \tag{2.8}$$

θ_{ij} are known as neutrino mixing angles. Since the Majorana phases, ρ and σ, are not observable in neutrino oscillations, U is simplified as:

$$U = \begin{pmatrix} c_{12}c_{13} & s_{12}c_{13} & s_{13}e^{-i\delta_{CP}} \\ -s_{12}c_{23} - c_{12}s_{13}s_{23}e^{i\delta_{CP}} & c_{12}c_{23} - s_{12}s_{13}s_{23}e^{i\delta_{CP}} & c_{13}s_{23} \\ s_{12}s_{23} - c_{12}s_{13}c_{23}e^{i\delta_{CP}} & -c_{12}s_{23} - s_{12}s_{13}c_{23}e^{i\delta_{CP}} & c_{13}c_{23} \end{pmatrix}. \tag{2.9}$$

Inverting Eq. 2.7, the mixture of the flavor states for any of the mass states is given by:

$$|\nu_i\rangle = \sum_{\alpha=e,\mu,\tau} U_{\alpha i}|\nu_\alpha\rangle, \tag{2.10}$$

where i can be 1, 2, or 3.

2.3.1 Neutrino Oscillation in Vacuum

Neutrinos propagate as coherent superpositions of their mass states. The neutrino mass state $|\nu_i\rangle$ with momentum $\boldsymbol{p}_i$ is an eigenstate of the vacuum Hamiltonian $\mathcal{H}_{\text{vac}}$:

$$\mathcal{H}_{\text{vac}}|\nu_i\rangle = E_i|\nu_i\rangle, \tag{2.11}$$

where E_i is energy eigenvalues, and

$$E_i = \sqrt{\boldsymbol{p}_i^2 + m_i^2}. \tag{2.12}$$

For a neutrino in vacuum, the Schrödinger equation is written as

$$i\frac{\mathrm{d}}{\mathrm{d}t}|\nu_i(t)\rangle = E_i|\nu_i(t)\rangle, \tag{2.13}$$

The solution to the Schrödinger equation is the time evolution equation of a neutrino mass state:

$$|\nu_i(t)\rangle = e^{-iE_i t}|\nu_i\rangle. \tag{2.14}$$

From Eq. 2.7 and Eq. 2.14, the time evolution of a neutrino flavor state $|\nu_\alpha(t)\rangle$ is given by

$$|\nu_\alpha(t)\rangle = \sum_{i=1,2,3} U^*_{\alpha i} e^{-iE_i t}|\nu_i\rangle. \tag{2.15}$$

This equation implies that the mixture of the neutrino mass states change as the neutrino travels. A different mixture of mass states corresponds to a different mixture of flavor states. That is, a neutrino created with a flavor α can be observed as a different flavor β after some time. Combining Eq. 2.10 and Eq. 2.15, the transition amplitude of $\nu_\alpha \to \nu_\beta$ is written as

$$\begin{aligned} A_{\nu_\alpha\to\nu_\beta}(t) =& \langle\nu_\beta|\nu_\alpha(t)\rangle \\ =& \sum_{i=1,2,3} U^*_{\alpha i} U_{\beta i} e^{-iE_i t}. \end{aligned} \tag{2.16}$$

The corresponding transition probability is given by

$$\begin{aligned} P_{\nu_\alpha\to\nu_\beta}(t) =& |A_{\nu_\alpha\to\nu_\beta}(t)|^2 \\ =& \sum_{i,j} U^*_{\alpha i} U_{\beta i} U_{\alpha j} U^*_{\beta j} e^{-i(E_i - E_j)t}. \end{aligned} \tag{2.17}$$

For ultrarelativistic neutrinos, the energy eigenvalues can be approximated by

$$E_i \simeq \boldsymbol{p}_i + \frac{m_i^2}{2\boldsymbol{p}_i} \approx E + \frac{m_i^2}{2E}, \tag{2.18}$$

where E is the total energy of the neutrino. Let $\Delta m^2_{ij} \equiv m_i^2 - m_j^2$ and replace the time t by the distance L, the transition probability can be rewritten as

$$\begin{aligned} P_{\nu_\alpha\to\nu_\beta}(L,E) =& \sum_{i,j} U^*_{\alpha i} U_{\beta i} U_{\alpha j} U^*_{\beta j} \exp(-i\frac{\Delta m^2_{ij} L}{2E}) \\ =& \delta_{\alpha\beta} - 4\sum_{i>j} \Re\left[U^*_{\alpha i} U_{\beta j} U_{\alpha j} U^*_{\beta j}\right] \sin^2\left(\frac{\Delta m^2_{ij} L}{4E}\right) \\ &+ 2\sum_{i>j} \Im\left[U^*_{\alpha i} U_{\beta i} U_{\alpha j} U^*_{\beta j}\right] \sin\left(\frac{\Delta m^2_{ij} L}{2E}\right). \end{aligned} \tag{2.19}$$

This is the probability of observing a neutrino created with a flavor α as another flavor β at a distance L. The Δm^2_{ij} are called neutrino mass splitting or neutrino mass squared differences. For anti-neutrinos, U is replaced by U^* and the sign of the last term in Eq. 2.19 flips. From Eq. 2.9, if $\delta_{CP} = 0$ then $U = U^*$, which means

anti-neutrinos oscillate exactly the same way as neutrinos do, otherwise CP-symmetry is violated. Therefore, δ is known as the CP-violating phase or CP phase. In this context, the last term in Eq. 2.19, if non-zero, is the CP violating term.

Eq. 2.19 implies two necessary conditions for neutrino oscillations to happen: at least one neutrino mass state is non-zero, and there is mixing between neutrino flavor states and their mass states. If neutrinos are massless, then $\Delta m^2_{ij} = 0$ and a neutrino flavor state would not change as it travels. If there is no mixing, then for $\alpha \neq \beta$, $U^*_{\alpha i} U_{\beta i} = 0$, so that $P_{\nu_\alpha \to \nu_\beta}(t) = \delta_{\alpha\beta}$. The parameters that can be measured by observations of neutrino oscillations are θ_{ij}, $\Delta m^2_{ij} \equiv m^2_i - m^2_j$, and δ. The absolute masses of neutrinos cannot be measured via neutrino oscillations. It is also difficult to determine the sign of Δm^2_{ij} by measuring neutrino oscillations in vacuum. If the CP violating term is zero, then Δm^2_{ij} only appears in the sine squared term in Eq. 2.19, which means $P_{\nu_\alpha \to \nu_\beta}(\Delta m^2_{ij}) = P_{\nu_\alpha \to \nu_\beta}(-\Delta m^2_{ij})$. To determine the sign of Δm^2_{ij}, this symmetry must be broken, either by matter effects (see Section 2.3.2) or by CP violation. The sign of Δm^2_{21} has been determined by solar neutrino oscillation experiments [29, 30, 31, 32, 33]. However, the sign of Δm^2_{31} remains an open question, known as the neutrino mass ordering problem. The possible neutrino mass ordering patterns are illustrated in Figure 2.2.

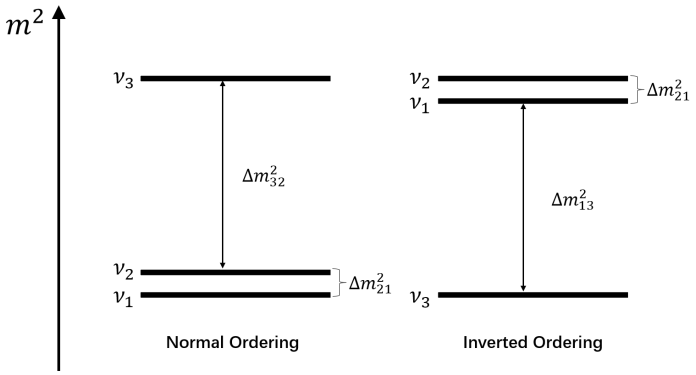

Figure 2.2: Illustration of neutrino mass spectra for normal mass ordering and inverted mass ordering.

To understand how each parameter affects the oscillation probability, two neutrino mixing is introduced next as an approximation in which only two massive neutrinos out of three are considered. In this case, the two neutrino flavor states ν_α and ν_β are linear superpositions of the two neutrino mass states ν_1 and ν_2 with coefficients given by the mixing matrix which contains only one mixing angle

$$U = \begin{pmatrix} \cos\theta & \sin\theta \\ -\sin\theta & \cos\theta \end{pmatrix}. \tag{2.20}$$

There is only one mass squared difference $\Delta m^2 \equiv m^2_2 - m^2_1$. It is straightforward to

derive the oscillation probability for two neutrino mixing from Eq. 2.19

$$P_{\nu_\alpha \to \nu_\alpha}(L, E) = 1 - \sin^2 2\theta \sin^2 \left(\frac{\Delta m^2 L}{4E} \right), \tag{2.21}$$

$$P_{\nu_\alpha \to \nu_\beta}(L, E) = \sin^2 2\theta \sin^2 \left(\frac{\Delta m^2 L}{4E} \right) \quad (\alpha \neq \beta). \tag{2.22}$$

$P_{\nu_\alpha \to \nu_\alpha}(L, E)$ is the probability that a neutrino created as ν_α with energy E to be detected as ν_α at a distance of L. $P_{\nu_\alpha \to \nu_\beta}(L, E)$ is the probability to detect a ν_α transitioning to ν_β. For neutrino oscillation experiments using artificial neutrino sources, it is convenient to write the oscillation probabilities as

$$P_{\alpha\alpha}(L, E) = 1 - \sin^2 2\theta \sin^2 \left(1.27 \frac{\Delta m^2 L}{E} \right), \tag{2.23}$$

$$P_{\nu_\alpha \to \nu_\beta}(L, E) = \sin^2 2\theta \sin^2 \left(1.27 \frac{\Delta m^2 L}{E} \right) \quad (\alpha \neq \beta), \tag{2.24}$$

where L/E is in units of [m/MeV] or [km/GeV], and Δm^2 is in units of [$\mathrm{eV}^2/\mathrm{c}^4$]. The constant 1.27 is the conversion factor calculated using powers of $\hbar$ and c. The way the parameters affect the oscillation probability is now obvious. The mixing angle serves as an amplitude of the oscillation in the form of $\sin^2 2\theta$, while Δm^2 controls the frequency of the oscillation. The mixing angle dependence of the oscillation probability is symmetric under the exchange $\theta \to \pi/2 - \theta$. Therefore, the oscillation probability is degenerate for θ and $\pi/2 - \theta$. This results in an ambiguity of the value of θ_{23} which is measured to be close to $\pi/2$, known as the θ_{23} octant problem. The θ_{23} octant problem can be disentangled by measuring neutrino oscillations in matter.

The standard three neutrino mixing framework has three combinations of m_i and m_j, thus three Δm^2_{ij}s. The two neutrino mixing approximation is valid only if one of Δm^2_{ij} is sufficiently different than the other two. Experimental results are $\Delta m^2_{21} = 7.53 \times 10^{-5}\,\mathrm{eV}^2$, $\Delta m^2_{32} = 2.455 \times 10^{-3}\,\mathrm{eV}^2$ for normal mass ordering, and $\Delta m^2_{32} = -2.529 \times 10^{-3}\,\mathrm{eV}^2$ for inverted mass ordering [22]. Therefore, $|\Delta m^2_{31}| \approx |\Delta m^2_{32}| \gg \Delta m^2_{21}$. From Eq. 2.23 and Eq. 2.24, the oscillation effects are significant when $1.27\Delta m^2 L/E = \pi/2$. Neutrino oscillation experiments using artificial neutrino sources have chosen $L/E \approx 1.24/\Delta m^2$ that maximizes the oscillation effects, as will be discussed in Section 2.4.2 and 2.4.3.

2.3.2 Neutrino Oscillation in Matter

When neutrinos travel through matter, they experience a potential due to the coherent forward elastic scattering with electrons and nucleons in the matter [34]. This potential modifies the mixing of neutrinos and thus the oscillation probabilities. The

coherent interactions include elastic CC and NC scatterings, as illustrated in Figure 2.3. The CC potential ($V_{\rm CC}$) and NC potential ($V_{\rm NC}$) act on the flavor states as

$$\mathcal{H}_{\rm mat}|\nu_\alpha\rangle = (\delta_{\alpha e}V_{\rm CC} + V_{\rm NC})|\nu_\alpha\rangle. \tag{2.25}$$

The V_{cc} only acts on the electron flavor because muons and taus do not exist stably in matter. The total Hamiltonian in matter is

$$\mathcal{H} = \mathcal{H}_{\rm vac} + \mathcal{H}_{\rm mat} \tag{2.26}$$

For a neutrino in matter, the Schrödinger equation in the flavor representation is given by

$$i\frac{\rm d}{{\rm d}t}|\nu_\alpha(t)\rangle = \mathcal{H}|\nu_\alpha(t)\rangle. \tag{2.27}$$

Consider the amplitude of $\nu_\alpha \to \nu_\beta$ transitions ($\psi_{\alpha\beta}(t) = \langle\nu_\beta|\nu_\alpha(t)\rangle$), its time evolution equation is given by

$$i\frac{\rm d}{{\rm d}t}\psi_{\alpha\beta}(t) = \sum_{\rho=e,\mu,\tau}\left(\sum_{i=1,2,3} U_{\beta i}E_i U^*_{\rho i} + \delta_{\beta e}\delta_{\rho e}V_{\rm CC} + \delta_{\beta\rho}V_{\rm NC}\right)\psi_{\alpha\rho}(t). \tag{2.28}$$

Using the ultrarelativistic approximation (Eq. 2.18) and replacing the time t with the distance L, Eq. 2.28 becomes

$$\begin{aligned} i\frac{\rm d}{{\rm d}L}\psi_{\alpha\beta}(L) = &\sum_{\rho=e,\mu,\tau}\left(\sum_{i=1,2,3} U_{\beta i}\frac{\Delta m^2_{i1}}{2E}U^*_{\rho i} + \delta_{\beta e}\delta_{\rho e}V_{\rm CC}\right)\psi_{\alpha\rho}(L) \\ &+ \left(E + \frac{m_1^2}{2E} + V_{\rm NC}\right)\psi_{\alpha\beta}(L), \end{aligned} \tag{2.29}$$

where the last term can be removed by rephasing $\psi_{\alpha\beta}(t)$. Therefore, the NC potential is irrelevant to neutrino oscillations in the standard three neutrino mixing framework. Eq.2.29 can be rewritten in matrix form as

$$i\frac{\rm d}{{\rm d}L}\Psi_\alpha = \frac{1}{2E}(U\mathbb{M}^2U^\dagger + \mathbb{A})\Psi_\alpha, \tag{2.30}$$

where

$$\Psi_\alpha = \begin{pmatrix}\psi_e\\ \psi_\mu\\ \psi_\tau\end{pmatrix}, \tag{2.31}$$

$$\mathbb{M}^2 = \begin{pmatrix}0 & 0 & 0\\ 0 & \Delta m^2_{21} & 0\\ 0 & 0 & \Delta m^2_{31}\end{pmatrix}, \tag{2.32}$$

and

$$\mathbb{A} = \begin{pmatrix} 2EV_{\mathrm{CC}} & 0 & 0 \\ 0 & 0 & 0 \\ 0 & 0 & 0 \end{pmatrix}. \tag{2.33}$$

The effective Hamiltonian in the flavor basis is then given by

$$\mathcal{H}_{\mathrm{F}} = \frac{1}{2E}(U\mathbb{M}^2U^{\dagger} + \mathbb{A}). \tag{2.34}$$

The matter potential V_{CC} depends on the electron number density in the matter N_e, and the Fermi coupling constant G_F

$$V_{\mathrm{CC}} = \pm\sqrt{2}G_F N_e, \tag{2.35}$$

where the sign of V_{CC} is positive for neutrinos and negative for anti-neutrinos.

(a) CC (b) NC

Figure 2.3: Feynman diagrams of the CC (a) and NC (b) coherent forward scattering processes. l denotes one of the lepton flavors.

To understand the effects of the matter potential on neutrino oscillations, the two neutrino mixing framework introduced in Section 2.3.1 is used here. Two neutrino flavor states ν_e and ν_μ and two neutrino mass states ν_1 and ν_2 are considered, and their mixture is defined as Eq. 2.20. From Eq. 2.34, the effective Hamiltonian in the flavor basis in matter for two neutrino mixing is given by

$$\begin{aligned} \mathcal{H}_{\mathrm{F}} =& \frac{1}{2E}\begin{pmatrix} \Delta m^2_{21}\sin^2\theta + A_{\mathrm{CC}} & \Delta m^2_{21}\sin\theta\cos\theta \\ \Delta m^2_{21}\sin\theta\cos\theta & \Delta m^2_{21}\cos^2\theta \end{pmatrix} \\ =& \frac{1}{4E}\begin{pmatrix} -\Delta m^2_{21}\cos 2\theta + A_{\mathrm{CC}} & \Delta m^2_{21}\sin 2\theta \\ \Delta m^2_{21}\sin 2\theta & \Delta m^2_{21}\cos 2\theta - A_{\mathrm{CC}} \end{pmatrix}. \end{aligned} \tag{2.36}$$

Since Eq. 2.36 is a symmetric matrix, it can be diagonalized by orthogonal matrices $\tilde{U}$

$$\tilde{U}^T\mathcal{H}_{\mathrm{F}}\tilde{U} = \mathcal{H}_{\mathrm{M}}. \tag{2.37}$$

Now the diagonal matrix $\mathcal{H}_{\mathrm{M}}$ can be interpreted as the effective Hamiltonian in the mass basis in matter and can be written as

$$\mathcal{H}_{\mathrm{M}} = \frac{1}{2E}\begin{pmatrix} 0 & 0 \\ 0 & \Delta\tilde{m}^2_{21} \end{pmatrix}, \tag{2.38}$$

where $\Delta\tilde{m}^2_{21}$ is the effective neutrino mass splitting in matter and is given by

$$\Delta\tilde{m}^2_{21} = \sqrt{(\Delta m^2_{21}\cos 2\theta - A_{\mathrm{CC}})^2 + (\Delta m^2_{21}\sin 2\theta)^2}. \tag{2.39}$$

$\tilde{U}$ is then the effective mixing matrix in matter and can be written as

$$\tilde{U} = \begin{pmatrix} \cos\tilde{\theta} & \sin\tilde{\theta} \\ -\sin\tilde{\theta} & \cos\tilde{\theta} \end{pmatrix}, \tag{2.40}$$

where $\tilde{\theta}$ is the effective mixing and is given by

$$\tan 2\tilde{\theta} = \frac{\tan 2\theta}{1 - \frac{A_{\mathrm{CC}}}{\Delta m^2_{21}\cos 2\theta}}. \tag{2.41}$$

When $A_{\mathrm{CC}} = \Delta m^2_{21}\cos 2\theta$, the effective mixing angle $\tilde{\theta} = \pi/4$ and the mixing is maximal. This is known as the MSW effect [34, 35, 36], which is important for solar neutrino measurements where the electron number density of the Sun is extremely high. The effective mixing angle $\tilde{\theta}$ presents a dependence on the signed mass squared difference Δm^2, which can break the symmetry of $P_{\nu_\alpha\to\nu_\beta}(\Delta m^2_{ij}) = P_{\nu_\alpha\to\nu_\beta}(-\Delta m^2_{ij})$ as discussed in Section 2.3.1. The solar neutrino oscillation experiments [29, 30, 31, 32, 33] have determined the sign of Δm^2_{21} in the standard three neutrino mixing framework utilizing the MSW effect. It is also used to address the neutrino mass ordering problem with atmospheric neutrinos that travel through the Earth [37]. Moreover, the oscillation probability is no longer symmetric under the exchange $\theta \to \pi/2 - \theta$. It is straightforward to extend the above calculation to the standard three neutrino mixing framework.

Note that the above solution is but an approximate analytical solution which is valid only when the change in the electron number density is sufficiently slow [36]. This approximation is called adiabatic approximation. Under this approximation, the oscillation probability is given by simply replacing U with $\tilde{U}$ and Δm^2_{ij} with $\Delta\tilde{m}^2_{ij}$ in

Eq. 2.19

$$\begin{aligned} P_{\nu_\alpha \to \nu_\beta}(L,E) =& \delta_{\alpha\beta} - 4\sum_{i>j} \Re\left[\tilde{U}^*_{\alpha i}\tilde{U}_{\beta j}\tilde{U}_{\alpha j}\tilde{U}^*_{\beta j}\right] \sin^2\left(\frac{\Delta\tilde{m}^2_{ij}L}{4E}\right) \\ &+ 2\sum_{i>j} \Im\left[\tilde{U}^*_{\alpha i}\tilde{U}_{\beta i}\tilde{U}_{\alpha j}\tilde{U}^*_{\beta j}\right] \sin\left(\frac{\Delta\tilde{m}^2_{ij}L}{2E}\right). \end{aligned} \tag{2.42}$$

A so-called adiabaticity parameter can be used to determine whether or not the adiabatic approximation is valid

$$\gamma = \frac{(\Delta\tilde{m}^2)^2}{2E\sin^2\tilde{\theta}|\mathrm{d}A_{\mathrm{CC}}/\mathrm{d}L|}. \tag{2.43}$$

When $\gamma \gg 1$ everywhere along the neutrino's path, the approximation is valid. This approximation can be applied to solar neutrinos which have relatively low energies and experience slowly varying matter density. For atmospheric neutrinos which pass through the Earth, their energies are too high for a fully adiabatic approximation. Instead, the oscillation probability of atmospheric neutrino is computed in the following way [38].

The entire baseline is first divided into several segments such that the adiabatic approximation holds within each single segment. The oscillation amplitude for each segment is computed and multiplied to obtain the oscillation probability along the entire baseline. For each segment, the matrix X assembling the propagated mass eigenvectors is given by

$$X = \sum_k \left[\prod_{j\neq k} \frac{2E\mathcal{H}_{\mathrm{M}} - \tilde{m}^2_j\mathbf{I}}{\tilde{m}^2_k - \tilde{m}^2_j}\right] \exp\left(-i\frac{\tilde{m}^2_k L}{2E}\right), \tag{2.44}$$

where $\mathcal{H}_{\mathrm{M}}$ is from Eq. 2.38 extended to include three neutrinos

$$\mathcal{H}_{\mathrm{M}} = \frac{1}{2E}\begin{pmatrix} \tilde{m}^2_1 & 0 & 0 \\ 0 & \tilde{m}^2_2 & 0 \\ 0 & 0 & \tilde{m}^2_3 \end{pmatrix}. \tag{2.45}$$

The matrix element X_{ij} is the transition amplitude from mass eigenstate $|\nu_i\rangle$ to $|\nu_j\rangle$. The oscillation probability along the entire baseline is given by

$$P_{\nu_\alpha \to \nu_\beta}(L,E) = \left|\left(U\prod_m X(E,\rho_m,L_m)U^\dagger\right)_{\alpha\beta}\right|^2, \tag{2.46}$$

where U is the PMNS matrix in vacuum, and L_m and ρ_m are the baseline and density of the m^{th} segment, respectively.

2.4 Experimental Status

Neutrinos are ubiquitous, produced by various natural and artificial sources, including nuclear reactors, accelerators, the Sun, cosmic-ray interactions in the Earth's atmosphere, and supernovae. Each source of neutrinos has their characteristic energy spectrum, flavor, and experience different matter density, allowing the study of various physics phenomena. This section provides a review of the experimental status on the reactor, accelerator, solar, and atmospheric neutrinos, as well as the supernova and pre-supernova neutrinos. The former four types of neutrino sources are commonly used to explore the oscillation mechanism. To probe oscillations, experiments select propagation distances L and neutrino energies E that maximize sensitivity to oscillation patterns driven by the corresponding Δm^2_{ij}. Measurements are carried out in two complementary ways: the appearance channel, in which a ν_β is observed in a beam originally composed of ν_α, and the disappearance channel, in which a deficit of ν_α is observed in the same beam.

2.4.1 Solar Neutrinos

The Sun is a powerful and steady source of electron neutrinos, produced in nuclear fusion reactions that convert hydrogen into helium in its core. The dominant processes responsible for neutrino production are reactions in the proton-proton (pp) chain. Among the produced neutrinos, the so-called pp neutrinos, ^{7}Be neutrinos, and ^{8}B neutrinos take a dominant fraction of the flux. They are produced via the following reactions:

$$p^+ + p^+ \rightarrow {}^2\mathrm{H}^+ + e^+ + \nu_e \quad \text{(pp neutrinos)}, \tag{2.47}$$

$$^7\mathrm{Be} + e^- \rightarrow {}^7\mathrm{Li} + \nu_e \quad (^7\text{Be neutrinos}), \tag{2.48}$$

$$^8\mathrm{B} \rightarrow 2(^4\mathrm{He}) + e^+ + \nu_e \quad (^8\text{B neutrinos}). \tag{2.49}$$

The pp neutrinos and ^{8}B neutrinos have continuous spectra, with maximum energies of 0.42 MeV and 14.06 MeV, respectively. For ^{7}Be neutrinos, their energies can be 0.383 MeV or 0.861 MeV. Figure 2.4 shows the solar neutrino spectra predicted by the Standard Solar Model (SSM) [39, 40, 41].

The study of solar neutrinos has played a central role in the development of neutrino oscillation physics. The first solar neutrino experiment, the Homestake experiment [29], used a radiochemical technique with a large tank of perchloroethylene to detect ν_e via the reaction,

$$\nu_e + {}^{37}\mathrm{Cl} \rightarrow e^- + {}^{37}\mathrm{Ar}, \tag{2.50}$$

which has a threshold energy of 0.814 MeV. Throughout the 25 years of data taking

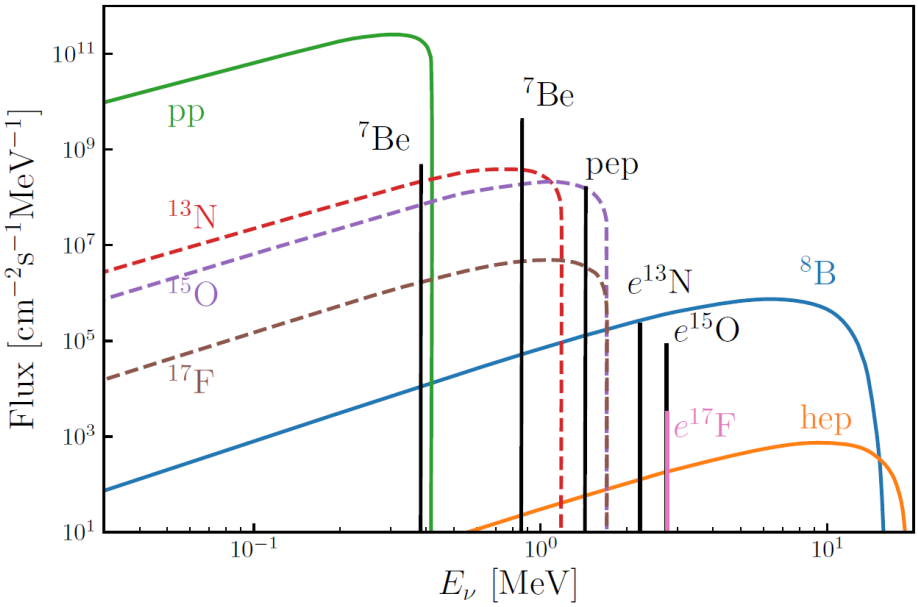

Figure 2.4: The solar neutrino spectra given by the Standard Solar Model [39, 40, 41]. Taken from [42].

started in 1970, it has observed a neutrino flux of only $\sim 1/3$ of the prediction of the SSM, a discrepancy later known as the "solar neutrino problem". Subsequent radiochemical experiments, such as GALLEX/GNO [43] and SAGE [30], employed gallium targets to access lower-energy pp neutrinos through the reaction,

$$\nu_e + {}^{71}\mathrm{Ga} \rightarrow e^- + {}^{71}\mathrm{Ge}. \tag{2.51}$$

These experiments confirmed the flux deficit across a broader energy range.

The solar neutrino problem was addressed by the Sudbury Neutrino Observatory (SNO) [44]. SNO used heavy water to measure solar neutrinos through three types of interactions: CC, sensitive exclusively to ν_e; NC, equally sensitive to all active neutrino flavors; and elastic scattering (ES), primarily sensitive to ν_e but with small sensitivity to ν_μ and ν_τ:

$$\mathrm{CC} : \nu_e + {}^{2}\mathrm{H}^+ \rightarrow p^+ + p^+ + e^- \tag{2.52}$$

$$\mathrm{NC} : \nu_l + {}^{2}\mathrm{H}^+ \rightarrow p^+ + n + \nu_l \quad (l = e, \mu, \tau), \tag{2.53}$$

$$\mathrm{ES} : \nu_l + e^- \rightarrow \nu_l + e^- \quad (l = e, \mu, \tau). \tag{2.54}$$

As presented in Figure 2.5, SNO's observation shows that the NC and ES channels matched SSM predictions, while the CC channel had a deficit. This implied that some of the solar ν_e had transitioned into ν_μ and ν_τ, providing direct evidence for neutrino oscillations.

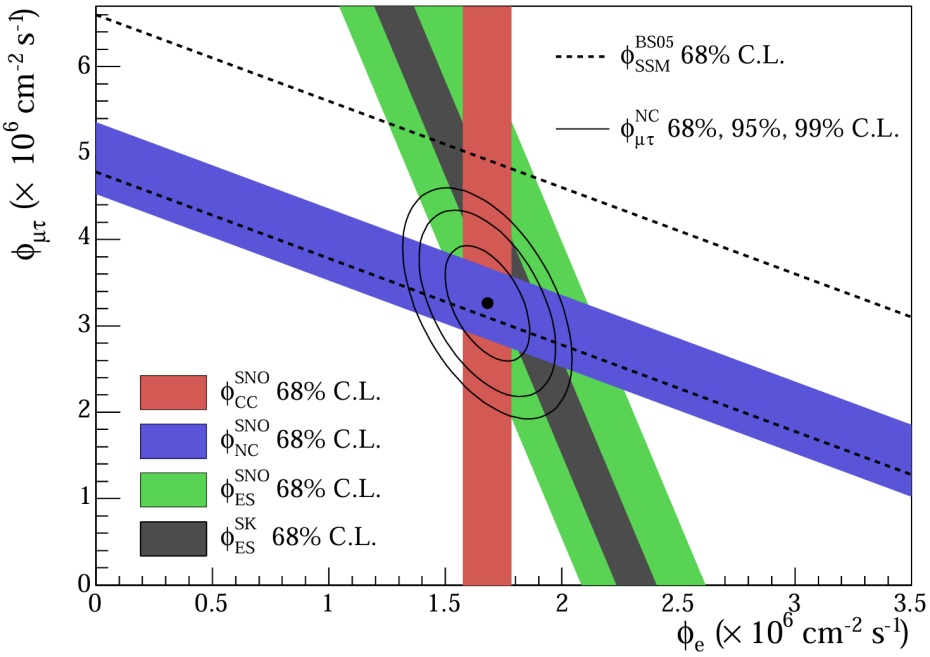

Figure 2.5: Solar neutrino flux measured by the SNO experiment via CC, NC and ES channels [45]. The ES result from SK [46] is also plotted as the gray band. The total ^{8}B solar neutrino flux from SSM is shown as dashed lines. Taken from [45].

Other experiments that contribute to solar neutrino oscillation physics include the Kamiokande experiment and SK, and the Borexino experiment. The Kamiokande experiment and SK use water Cherenkov detectors to observe ^{8}B neutrino via ES interactions. The Borexino [47] detector is an organic liquid scintillator calorimeter with extremely low radioactivity. It has achieved high-precision spectroscopy of low-energy solar neutrinos, including pp, ^{7}Be, pep, and CNO neutrinos.

Solar neutrino oscillations are sensitive to the mixing angle θ_{12} and the signed mass splitting Δm^2_{21} by measuring the ν_e disappearance. Since the energies of solar neutrinos are lower than the threshold of ν_μ and ν_τ CC interactions, the ν_μ appearance and ν_τ appearance cannot be measured. Neutrinos traveling in the Sun experience the MSW effect, as discussed in Section 2.3.2. A resonant enhancement is obtained when A_{CC} approaches $\Delta m^2_{21} \cos 2\theta$, resulting in a high transition probability of $\nu_e \to \nu_x$ ($x = \mu, \tau$). The solar neutrino problem is explained by this effect, and the observed transition probability of $\sim 1/3$ measures θ_{12} and the signed mass splitting Δm^2_{21}.

Current solar neutrino measurements indicate $\sin^2\theta_{12} = 0.307^{+0.013}_{-0.012}$ and $\Delta m^2_{21} = 7.53 \pm 0.18 \times 10^{-5}\,\mathrm{eV}^2$[1] [22]. Ongoing experiments seek to refine the determination of the energy dependence in the solar neutrino oscillation pattern and to detect MSW effects as solar neutrinos traverse the Earth, manifested as a "day–night asymmetry."

[1] Together with measurement from the KamLAND experiment. See Section 2.4.2

2.4.2 Reactor Neutrinos

Nuclear reactors are intense and controllable sources of electron anti-neutrinos ($\bar{\nu}_e$), produced primarily in the beta decays of fission fragments from isotopes such as ^{235}U, ^{239}Pu, ^{238}U, and ^{241}Pu. Reactor neutrino flux can be estimated using the thermal power and the fission fraction of these isotopes. The resulting $\bar{\nu}_e$ spectrum extends up to $\sim$ 10 MeV, with an average energy of a few MeV. Detection is typically achieved through the inverse beta decay (IBD) process,

$$\bar{\nu}_e + p \rightarrow e^+ + n, \tag{2.55}$$

which has a well-understood cross section and produces a characteristic delayed coincidence signature: a prompt signal from the e^+ annihilation followed by a delayed signal from neutron capture. By requiring this characteristic coincidence, low background measurements can be achieved.

The discovery of neutrinos was achieved by Reines and Cowan in 1956 [15, 16], detecting reactor neutrinos from the Savannah River nuclear reactors. Decades later, the KamLAND experiment [48] used a large liquid scintillator detector to measure $\bar{\nu}_e$ from reactors at average baselines of $\sim$ 180 km, so that it is sensitive to the oscillation pattern driven by Δm^2_{21}. KamLAND has provided clear evidence for neutrino oscillations with parameters consistent with those measured by solar neutrino experiments [49].

In the 2010s, a new generation of short-baseline reactor experiments was designed to precisely measure the smallest neutrino mixing angle, θ_{13}, by comparing $\bar{\nu}_e$ rates at near and far detectors to cancel reactor-related uncertainties. The Daya Bay [50], RENO [51], and Double Chooz [52] experiments, located at baselines of 300–2000 m, independently observed a deficit of $\bar{\nu}_e$ consistent with oscillations driven by Δm^2_{31}, establishing a nonzero value of θ_{13}. Daya Bay, in particular, achieved the first precision measurement of $\sin^2 2\theta_{13}$ and provided the most precise determination of $|\Delta m^2_{ee}|$[2] from reactor anti-neutrinos, as shown in Figure 2.6.

Reactor neutrino experiments have also revealed new anomalies, such as the so-called "reactor anti-neutrino anomaly," a $\sim$ 5% deficit in the observed flux compared to updated predictions [54], and the unexpected distortion ("5 MeV bump") in the measured energy spectra [55]. These observations have motivated further short-baseline experiments, such as PROSPECT [56] and STEREO [57], to test the hypothesis of light sterile neutrinos.

Short-baseline reactor neutrino experiments have provided the most precise mea-

[2] $\Delta m^2_{ee} \equiv \cos^2\theta_{12}\sin^2\Delta m^2_{31} + \sin^2\theta_{12}\sin^2\Delta m^2_{32}$, which is independent of the neutrino mass ordering.

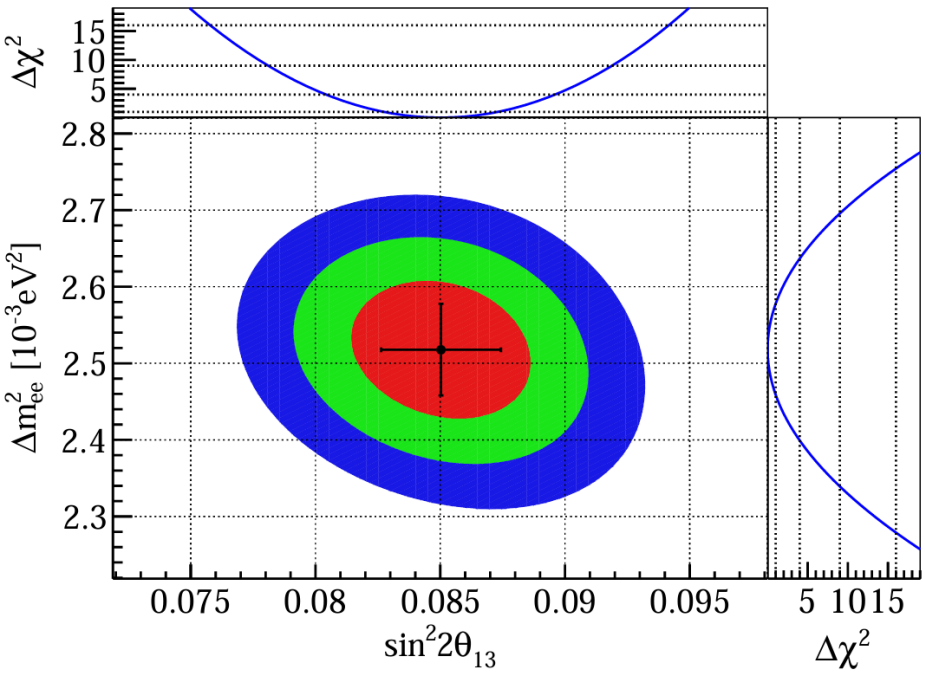

Figure 2.6: The best-fit result of $|\Delta m^2_{ee}|$ and $\sin^2 2\theta_{13}$ from the Daya Bay reactor anti-neutrino experiment. The colored contours indicate 1σ, 2σ, and 3σ deviations. The 1-D profiled $\Delta\chi^2$ for $|\Delta m^2_{ee}|$ and $\sin^2 2\theta_{13}$ are also shown. Taken from [53].

surements of θ_{13} to be 0.0219 ± 0.07 [22]. A next generation reactor neutrino experiment, JUNO [58], is currently under construction. With a target energy resolution of 2.95% at 1 MeV, it aims to address the neutrino mass ordering problem by observing the fine interference pattern in the energy spectrum of reactor anti-neutrinos. It can also measure the oscillation parameters θ_{12}, $|\Delta m^2_{21}|$, and Δm^2_{31} with a high precision of $< 0.6\%$ within 6 years of operation [59].

2.4.3 Atmospheric Neutrinos

Atmospheric neutrinos originate from cosmic-ray interactions in the Earth's atmosphere. Consisting of protons and nuclei, cosmic-rays interact with nuclei in the atmosphere, producing hadron showers of mostly pions and kaons. Atmospheric neutrinos are generated in the pion and kaon decays, as well as the subsequent muon decays. An example decay chain starting from a pion is given by

$$\begin{aligned} \pi^{\pm} &\rightarrow \mu^{\pm} + \nu_{\mu}(\bar{\nu}_{\mu}) \\ &\searrow \\ &\quad e^{\pm} + \bar{\nu}_{\mu}(\nu_{\mu}) + \nu_e(\bar{\nu}_e). \end{aligned}$$

The flux of muon neutrinos relative to electron neutrinos $R \equiv (\nu_\mu + \bar{\nu}_\mu)/(\nu_e + \bar{\nu}_e)$ is roughly 2:1. They expend a wide energy range from tens of MeV to a few TeV, and arrive from all directions, providing a unique opportunity to study neutrino os-

cillations over a wide range of path lengths L and energies E. To study atmospheric neutrino oscillations, it is convenient to use the quantity zenith angle, which is the neutrino direction with respect to the vertical direction above the detector, instead of the baseline. As illustrated in Figure 2.7, the zenith angle θ of atmospheric neutrinos can be converted to the baseline L, and the correspondence is given by

$$L(\cos\theta_z) = -r\cos\theta_z + \sqrt{2rh + h^2 + r^2\cos^2\theta_z}, \tag{2.56}$$

where r is the radius of the Earth, and h is the neutrino production height.

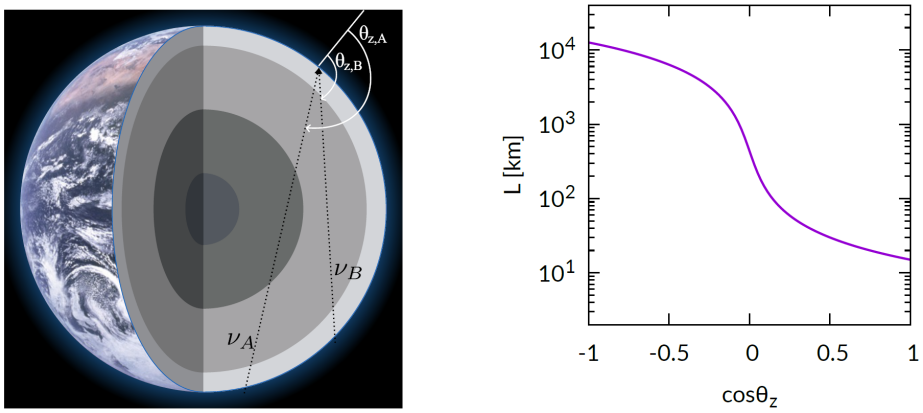

Figure 2.7: Atmospheric neutrino path length correspondence with zenith angle. **Left:** A schematic of two atmospheric neutrinos' paths through the Earth. Neutrinos ν_A and ν_B travels different distances and therefore have different zenith angles, indicated as $\theta_{z,A}$ and $\theta + z, B$. **Right:** Atmospheric neutrino baseline L as a function of the cosine of zenith angle $\cos\theta_z$. $\cos\theta_z = -1$ and $\cos\theta_z = 1$ corresponds to vertically upward and downward neutrino directions. Taken from [60].

The first atmospheric neutrino measurements were performed in the 1960s by the Kolar Gold Field (KGF) experiment in India [61] and the CWI experiment in South Africa [62] which have given evidence for the interaction of high energy atmospheric neutrinos. In the 1980s, the Kamiokande experiment [63] and the IMB experiment [64] observed deficits of muon neutrinos in the atmospheric neutrino flux. The missing ν_μ flux was addressed by SK in 1998 [23]. The deficit was found to appear only in the upward-going muon neutrino flux, while those arriving from above the horizon agree with the predicted atmospheric muon neutrino flux, as shown in Figure 2.8. Moreover, the observed electron neutrino flux was consistent with the prediction. The SK data were analyzed in the two neutrino mixing framework, where the ν_e flavor is assumed un-oscillated. The oscillation probabilities of $\nu_\mu \to \nu_\mu$ and $\nu_\mu \to \nu_\tau$ are given by

$$P_{\nu_\mu\to\nu_\mu} = 1 - \sin^2 2\theta \sin^2\left(\frac{1.27\Delta m^2 L}{E}\right), \tag{2.57}$$

$$P_{\nu_\mu\to\nu_\tau} = \sin^2 2\theta \sin^2\left(\frac{1.27\Delta m^2 L}{E}\right). \tag{2.58}$$

With the SK data, the oscillation parameters were constrained to $\sin^2 2\theta > 0.82$ and $5 \times 10^{-4} < \Delta m^2 < 6 \times 10^{-3}\,\text{eV}^2$ at 90% C.L. [23]. This result provided evidence of neutrino oscillations and the first robust measurement of atmospheric oscillation parameters. Following SK's discovery, other experiments confirmed and refined atmospheric neutrino oscillation measurements. The MACRO [65] and Soudan-2 [66] experiments observed muon neutrino deficits consistent with $\nu_\mu \to \nu_\tau$ oscillations.

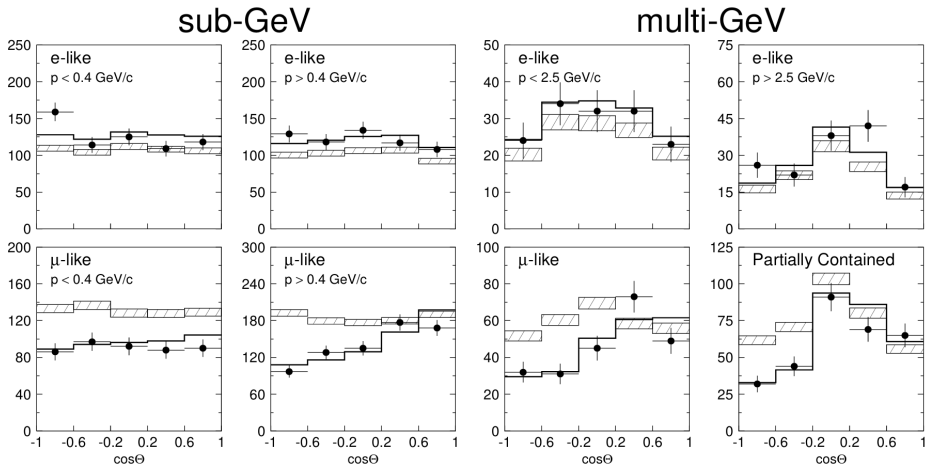

Figure 2.8: Zenith angle distributions of muon-like and electron-like events in the sub-GeV ($E_{vis} < 1330\,\text{MeV}$) and multi-GeV ($E_{vis} > 1330\,\text{MeV}$) energy region. E_{vis} is defined as the energy of an electron that would produce the same amount of Cherenkov light as observed. $E_{vis} = 1330\,\text{MeV}$ corresponds to muon momentum of $1400\,\text{MeV/c}$. The dots are data, and the black lines are best-fit to data assuming two neutrino mixing. The predictions without oscillation with systematic uncertainties are indicated by hatched bands. Taken from [23].

As discussed in Section 2.3.2, for atmospheric neutrinos passing through the Earth, the matter effects they experience help to identify the neutrino mass ordering. The leading term of the $\nu_\mu \to \nu_e$ transition probability in atmospheric neutrinos is given by

$$P_{\nu_\mu \to \nu_e} \approx \sin^2\theta_{23} \sin^2 2\theta_{13} \sin^2\left(\frac{1.27\Delta m^2_{32} L}{E}\right). \tag{2.59}$$

Following Eq. 2.41, the resonant enhancement occurs when

$$A_{\text{CC}} \approx \Delta m^2_{32} \cos 2\theta_{13}, \tag{2.60}$$

leading to $E \approx 3\,\text{GeV}$. Note that this resonance appears only when A_{CC} and Δm^2_{32} have the same signs, thus only for neutrinos with normal ordering, or anti-neutrinos with inverted ordering. Figure 2.9 shows the $\nu_\mu \to \nu_e$ oscillation probabilities for atmospheric neutrinos and anti-neutrinos in the normal and inverted ordering cases. The resonance is observed for $\cos\theta < 0$ and $2 < E < 9\,\text{GeV}$ for neutrinos with normal ordering, and for anti-neutrinos with inverted ordering.

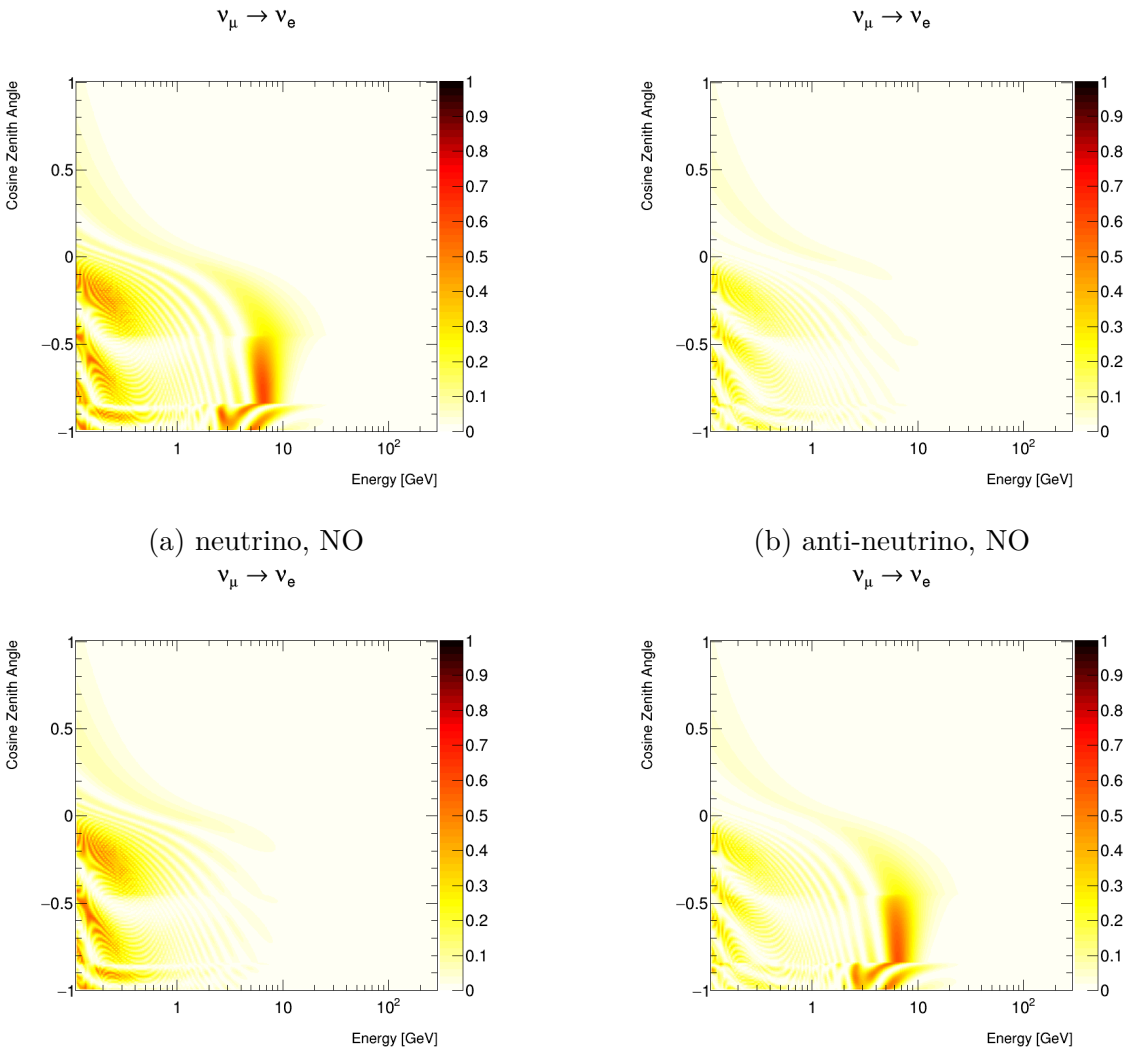

(a) neutrino, NO

(b) anti-neutrino, NO

(c) neutrino, IO

(d) anti-neutrino, IO

Figure 2.9: The transition probabilities for $\nu_\mu \to \nu_e$ for atmospheric neutrinos and anti-neutrinos in the normal and inverted ordering cases. Horizontal axes are neutrino energies. Vertical axes are cosine of zenith angle, where negative values represent upward-going neutrinos. The top and bottom rows are in the normal and inverted ordering cases, respectively. The left column is for neutrino, and the right column is for anti-neutrino. The oscillation parameters are set to $\sin^2\theta_{12} = 0.302$, $\sin^2\theta_{13} = 0.0238$, $\sin^2\theta_{23} = 0.6$, $\Delta m^2_{12} = 7.6 \times 10^{-5}\,\mathrm{eV}^2$, $\Delta m^2_{23} = 2.5 \times 10^{-3}\,\mathrm{eV}^2$, $\delta_{CP} = 0$.

Present-day atmospheric neutrino measurements continue at Super-K [37] and IceCube/DeepCore [67], probing not only oscillation parameters but also matter effects that can reveal the neutrino mass ordering. KM3NeT [68] and PINGU [69] are designed to improve sensitivity to mass ordering using atmospheric neutrinos in the few-GeV energy range. Future experiments such as Hyper-Kamiokande (HK) [70] and INO [71] are expected to address these topics.

2.4.4 Long-baseline Accelerator Neutrinos

Accelerator-based neutrino experiments have contributed to the discovery of ν_μ and ν_τ, as well as precision measurements of neutrino oscillations. They use high-energy proton beams hitting a target to produce charged pions, which subsequently decay into muons and muon neutrinos. Magnetic focusing horns select the charge of secondary mesons, enabling the production of either neutrino or anti-neutrino beams. By tuning the decay pipe length, beamline optics, and detector distance, experiments can be optimized to probe oscillations driven by specific Δm^2_{ij}.

A long-baseline experiment typically uses a near detector to measure the neutrino beam without oscillations, and a far detector located hundreds of kilometers from the source to measure the neutrino beam after oscillations. Exploiting the near-far combination, a relative measurement can be performed such that many flux-related uncertainties and cross-section-related uncertainties can be constrained. The K2K experiment [72] is the first long-baseline experiment, using a beamline from the KEK accelerator to the SK detector, with a baseline of 250 km baseline and an average neutrino energy of 1.3 GeV. It provided the first accelerator confirmation of atmospheric neutrino oscillations, consistent with measurements of θ_{23} and Δm^2_{32} by SK [73]. The MINOS experiment [74], operating over a 735 km baseline from Fermilab to the Soudan mine with a peak neutrino energy of 3 GeV, precisely measured ν_μ disappearance and tested the consistency of oscillations for neutrinos and anti-neutrinos.

More recently, the T2K experiment [75], the successor to K2K, has sent a neutrino beam from J-PARC to the existing SK detector located 295 km away from the source. Its neutrino beam energy spectrum is tuned by setting the beam direction $\sim 2.5°$ off the detector, so that a narrow energy spectrum peaked at 0.6 GeV is achieved. With $L/E \approx 500\,\mathrm{km/GeV}$, it is sensitive to the $\Delta m^2 \approx 2.5 \times 10^{-3}\,\mathrm{eV}^2$. It has achieved the first observation of ν_e appearance in a ν_μ beam [76], suggesting a non-zero value of θ_{13}. The value of θ_{13} was later precisely measured by reactor neutrino experiments (see Section 2.4.2). The NOvA experiment [77] is another state-of-the-art long-baseline neutrino experiment, with a 810 km baseline from Fermilab to northern Minnesota and a peak neutrino energy of 2 GeV, has made complementary measurements of ν_e appearance and ν_μ disappearance. Both T2K and NOvA provide sensitivity to the leptonic CP-violating phase δ_{CP} [78, 79].

Two future accelerator neutrino facilities, the Deep Underground Neutrino Experiment (DUNE) [80] and HK [70], are under construction. DUNE will use liquid argon time projection chambers to measure a neutrino beam from 1300 km away, while HK will use a 260 kton water Cherenkov detector to capture neutrinos from the J-PARC beamline 295 km away. They both aim to deliver unprecedented sensitivity to δ_{CP}, the neutrino mass ordering, and precise measurements of the oscillation parameters.

2.4.5 Status of Oscillation Measurements

As discussed above, the oscillation parameters are measured by different experiments. θ_{13} is mainly constrained by reactor neutrino experiments. Solar neutrino experiments measure θ_{12}, and determine Δm^2_{21} together with long-baseline reactor experiments. θ_{23}, Δm^2_{32} and δ_{CP} are measured by atmospheric and accelerator neutrino experiments. The current global best-fit values of the oscillation parameters are listed in Table 2.2 [22].

Table 2.2: Global best-fit of the oscillation parameters in 2024. Inverted mass ordering is preferred over normal ordering. Taken from [26].

	Global best-fit	
Parameter	Normal Ordering	Inverted Ordering
$\sin^2\theta_{12}$	$0.307^{+0.013}_{-0.012}$	$0.307^{+0.013}_{-0.012}$
Δm^2_{21}	$(7.53 \pm 0.18) \times 10^{-5}\,\mathrm{eV}^2$	$(7.53 \pm 0.18) \times 10^{-5}\,\mathrm{eV}^2$
$\sin^2\theta_{23}$	$0.558^{+0.015}_{-0.021}$	$0.553^{+0.016}_{-0.024}$
Δm^2_{32}	$(2.455 \pm 0.028) \times 10^{-3}\,\mathrm{eV}^2$	$(-2.529 \pm 0.029) \times 10^{-3}\,\mathrm{eV}^2$
$\sin^2\theta_{13}$	$(2.19 \pm 0.07) \times 10^{-2}$	$(2.19 \pm 0.07) \times 10^{-2}$

2.4.6 Supernova Neutrinos

Core-collapse supernovae (CCSNs) mark the catastrophic end stages of massive stars, during which most of the gravitational binding energy, approximately $10^{53}\,\mathrm{erg}$, is released as neutrinos. These neutrinos carry unique information about the physical conditions deep within the collapsing core, where photons cannot escape, and thus provide an indispensable probe into both astrophysical and particle physics phenomena [81, 82].

The first and so far only observation of supernova (SN) burst neutrinos was made from SN1987A, which exploded in the Large Magellanic Cloud at a distance of about 50 kpc [83]. The SN burst neutrinos were detected on February 23, 1987 at 07:35 universal time, three hours earlier than the observation by optical telescopes and lasted for 13 seconds. Three detectors, Kamiokande II in Japan [2], IMB in the US [3], and Baksan in the Soviet Union [4], recorded a total of 24 neutrino events, where Kamiokande II observed 11 events, IMB observed 8 events, and Baksan observed 5 events. Figure 2.10 shows the SN1987A neutrino events observed by the three detectors in 13 seconds. Despite the limited statistics, these detections provided crucial confirmation of the basic theoretical framework of CCSN and the expected burst of neutrino emission accompanying them [84]. The detection of SN burst neutrinos has confirmed the fundamental mechanism of a SN explosion. Furthermore, an upper limit of $20\,\mathrm{eV}/c^2$ is set on the mass of the neutrino.

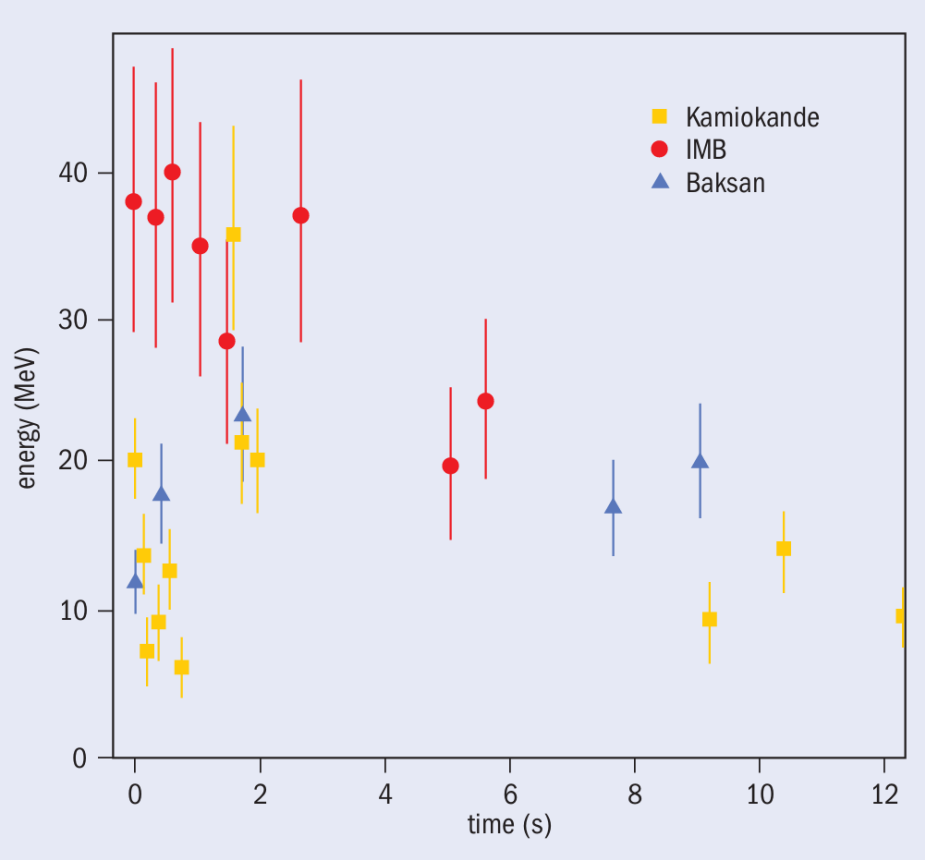

Figure 2.10: Neutrino events observed by Kamiokand II, IMB, and Baksan from SN1987A. Taken from [85].

Since SN1987A, no further galactic supernova has been observed, but the sensitivity and scale of neutrino detectors have improved dramatically. Boosted by this observation, various neutrino experiments, such as Borexino [86], IceCube [87], KamLAND [88], LVD [89], NOvA [90], SNO+ [91], and Super-Kamiokande (SK) [92], equipped with advanced technology and improved capabilities, continued the quest to detect SN neutrino bursts. Some of these experiments are also part of the supernova Early Warning System (SNEWS) [93, 94], which aims to provide prompt alerts to the astronomical community upon the detection of a neutrino burst. Furthermore, a number of next-generation neutrino detectors sensitive to galactic SN neutrinos are under construction, including DUNE [95], Hyper-Kamiokande [70], JUNO [96], and KM3NeT [97].

In parallel, continuous efforts are underway to search for neutrinos from past or distant SNs. The Diffuse Supernova Neutrino Background (DSNB), arising from the integrated emission of all past core collapse events in the universe [98], represents another frontier in experimental neutrino astrophysics. Although not yet observed, recent analyses from SK have placed stringent limits approaching the expected flux predicted by theoretical models [99, 100].

2.4.7 Pre-supernova Neutrinos

Pre-supernova (pre-SN) neutrinos are emitted during the final evolutionary stages of massive stars, prior to SN. In these late burning phases, nuclear fusion of silicon and other heavy elements proceeds rapidly, producing thermal neutrinos through pair annihilation, beta decay, and photo-neutrino processes [101]. These neutrinos gradually dominate the stellar energy loss and can escape freely from the core, carrying direct information about the temperature, density, and composition of the stellar interior. Their detection would therefore provide a unique opportunity to probe stellar evolution immediately before the explosion and could serve as an early warning of an imminent CCSN.

Theoretical studies have predicted observable fluxes of pre SN neutrinos from nearby massive stars [102, 103, 104]. The predicted pre-SN neutrino flux from such stars consist of all flavors of neutrinos. However, given the low energy of pre-SN neutrinos of few MeV, only $\bar{\nu}_e$ neutrinos are considered signals detectable through the inverse beta decay (IBD) channel which has a relatively large cross-section. Although the flux is significantly lower than that from a supernova burst, the emission duration of days to hours before CCSN allows for a time integrated signal that could be distinguished from the background in large, low background detectors. Upon a detection of pre-SN neutrinos, an early warning for the coming CCSN can be issued, allowing for preparation time of follow-up observations by neutrino detectors and gravitational wave observatories.

Efforts to establish such alert systems using pre-SN neutrinos have been carried out in SK and KamLAND. KamLAND developed the first pre-SN neutrino alert system capable of identifying a statistically significant rise in the IBD candidate rate [105]. SK has also developed and implemented a real time pre-SN alert system monitoring pre-SN neutrino flux from nearby stars [106]. These systems rely on continuous monitoring of IBD candidates and real time analysis frameworks optimized for early warning operation. So far, no pre-SN neutrino signal have been found yet. A combined pre-SN alert system integrating KamLAND and SK is my original work, and will be introduced in Part 7.4 of this thesis.

Chapter 3

The Super-Kamiokande Experiment

3.1 Overview

The Super-Kamiokande (SK) experiment is a large-scale underground water Cherenkov detector located in the Kamioka Mine in Gifu Prefecture, Japan [107]. Situated approximately 1,000 meters below Mt. Ikeno, the detector is shielded by an overburden of 2,700 meters water equivalent (m.w.e.), effectively reducing cosmic-ray backgrounds by 5 orders of magnitudes, to a rate of about 3 Hz. A schematic view of the detector is shown in Figure 3.1.

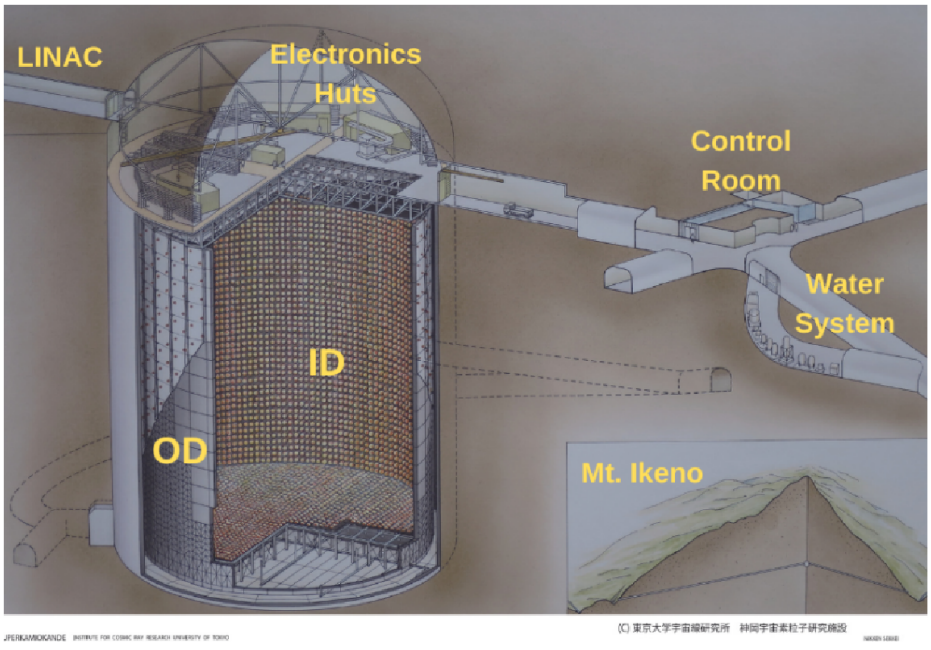

Figure 3.1: A schematic plot of the SK detector, taken from [108].

Constructed in 1996, the detector builds on the legacy of its predecessor, the Kamiokande detector, and represents a significant advancement in sensitivity and detection volume. It was originally a pure water detector, designed to explore fundamental questions in particle physics, including nucleon decay searches, atmospheric and solar neutrino oscillation studies, and investigations into supernova neutrinos, dark matter, and other astrophysical phenomena. Starting in 2020, gadolinium (Gd) was loaded into the detector to enhance its neutron detection efficiency, enabling the detection of pre-supernova neutrinos and supernova relic neutrinos [109, 110]. Moreover, it serves as the far detector of the T2K experiment, measuring neutrino beams from an accelerator located 295 km away [75].

SK has been taking data since 1996. The data-taking periods are divided into several phases, SK I-VIII. Between the SK I phase and the SK II phase, a PMT implosion accident happened during a maintenance work, which destroyed nearly half of the PMTs in the detector. After that, the remaining PMTs were re-distributed across the detector and were covered by acrylic cases to prevent future accidents. New PMTs were installed in 2006, such that the detector resumed a full operation phase (SK III). In 2008, the electronic system of SK was upgraded. This marked the beginning of SK IV phase. In preparation of Gd loading, a series of tank opening work were done in 2018-2019 during which the detector stopped taking data. After that, the last pure-water period (SK V) began.

In 2020, Gd was loaded into the detector, reaching a concentration of 0.01% by mass. This started the SK VI phase. After the second Gd loading, the concentration of Gd increased to 0.03% by mass for the SK VII phase. In October through December 2023, several coils for compensation of geomagnetic fields went off. Upon loss of these coils, the collection efficiencies of photoelectrons (PEs) for some of the PMTs were decreased. This marked a special data-taking phase: SK 7.5. In August 2024, the compensation of geomagnetic fields was recovered by repairing some of the failed coils and installing new coils. For this repair work, roughly 2.5 kilotons of Gd water was drained. After the work, pure water was refilled into the detector, and data-taking resumed, initiating the SK VIII phase. The SK VI-VIII phases are generally called the ”SK-Gd” phase.

This chapter will introduce the detection principle in SK, describe the detector components, and present the calibration methods. The configuration of the SK detector in the SK I and the SK-Gd phases will be introduced: In the scalar-NSI analysis presented in this thesis, the atmospheric neutrino data from the SK I phase are used. As for the combined pre-supernova alarm analysis, the pre-supernova alarm in SK was established in the SK-Gd phase and has been operating since then.

3.2 Detection Principle

The detection mechanism of SK relies on the Cherenkov radiation emitted by charged particles moving faster than the speed of light in water. Although neutrinos themselves are invisible, their interactions with particles in SK can produce visible charged particles. The refractive index of water is $n_{water} = 1.33$ for wavelengths of visible light. Therefore, charged particles traveling at a speed $> 0.75c$ in water emit Cherenkov radiation. As illustrated in Figure 3.2, the angle between the track of charged particle and the Cherenkov radiation is given by

$$\cos\theta_C = \frac{1}{n_{water} \cdot \beta}, \tag{3.1}$$

where β is the speed of the charged particle relative to the speed of light in vacuum. For relativistic particles, this radiation forms a characteristic cone with an opening angle of approximately 42 degrees.

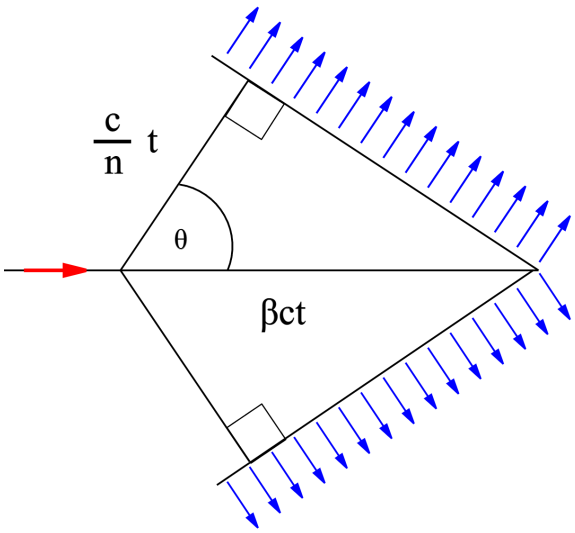

Figure 3.2: An illustration of the geometry of the Cherenkov radiation, taken from [111].

For different charged particles, the momentum thresholds for Cherenkov radiation are different, depending on their masses. Since the speed threshold is $1/n_{water}$, the momentum threshold is given by

$$p_C = \frac{m_0}{\sqrt{n_{water}^2 - 1}}. \tag{3.2}$$

In principle, charged particles with momentum above this threshold are visible in SK, except for those that have short lifetimes or are captured immediately. Photons are also visible in SK as they can cause electromagnetic showers in water. The energy, direction, and type of particle can be reconstructed by analyzing the amount of the Cherenkov radiation, the shape of the Cherenkov ring, and the Cherenkov angle, etc.

Based on these information, the information of the primary particle can be inferred. The details of the event reconstruction are described in Chapter 11.

3.3 Detector Components

The SK detector consists of a cylindrical stainless steel tank measuring 39.3 m in diameter and 41.4 m in height, filled with 50 kilotons of ultra-pure water. The tank is divided into two optically isolated regions: the Inner Detector (ID) and the Outer Detector (OD). A stainless steel structure with 0.55 m in thickness separates the ID and the OD and supports their PMTs.

3.3.1 Inner Detector

The ID, which serves as the primary vessel for neutrino interactions and nucleon decays, contains 32 kilotons of water and is equipped with 11,129 20-inch inward-facing photomultiplier tubes (PMTs). The photo-coverage is approximately 40%. These PMTs are installed in the so-called "supermodule", which is a frame supporting a 3×4 array of PMTs, on the stainless steel structure as shown in Figure 3.3. Each supermodule is 2.1 m in height, 2.8 m in width, and 0.55 m in thickness, connected seamlessly to each other. Therefore, the ID PMTs are mounted on a 0.7 m-spaced grid. The side wall hosts 7650 PMTs, while the top and the bottom of the ID each hosts 1748 PMTs. The surface of the structure is lined with light-proof black polyethylene terephthalate sheets, known as "black sheets", to reduce light reflection.

The ID PMTs are Hamamatsu R3600 20-inch PMTs specially developed for SK [112]. Figure 3.4 shows a schematic view of an ID PMT. The photocathode material is bialkali (Sb-K-Cs). Its quantum efficiency peaks at 360-400 nm with a maximum of $\sim 21\%$, as shown in Figure 3.5. The single-PE pulse height distribution is presented in Figure 3.6. Figure 3.7 shows a typical relative transit time spread of 2.2 ns (1σ) for a single-PE pulse corresponding to 410 nm incident light. After the chain implosion accident in 2001, an acrylic cover was attached to each PMT to prevent future chain reactions of PMT implosions.

3.3.2 Outer Detector

The 0.55 m thick stainless steel structure comprises an insensitive region. The remaining region between the tank walls and the stainless steel structure is the OD. The thickness of the OD region is ~ 2.6 m on top and bottom, and ~ 2.0 m on the barrel wall. Its target mass is 18 kilotons. 1,885 outward-facing 8-inch PMTs are installed on the stainless steel structure, with 302 on top, 308 on bottom and 1275 on the barrel wall.

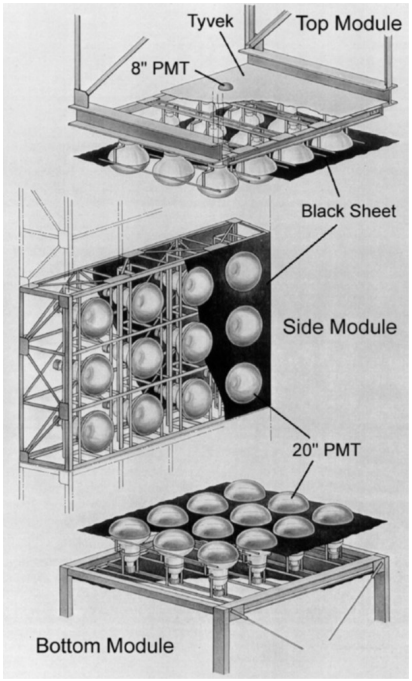

Figure 3.3: Schematic view of PMT support frames for the inner detector. Taken from [107].

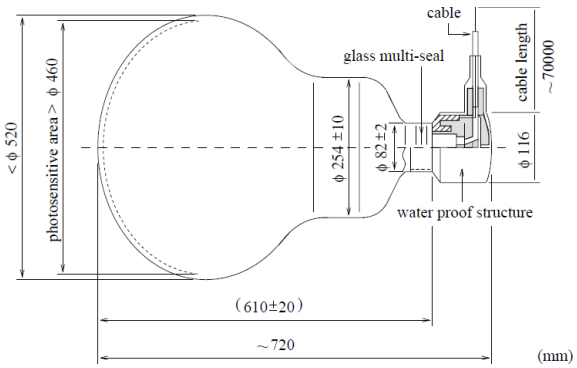

Figure 3.4: Schematic view of a Hamamatsu R3600 20-inch PMT. Taken from [107].

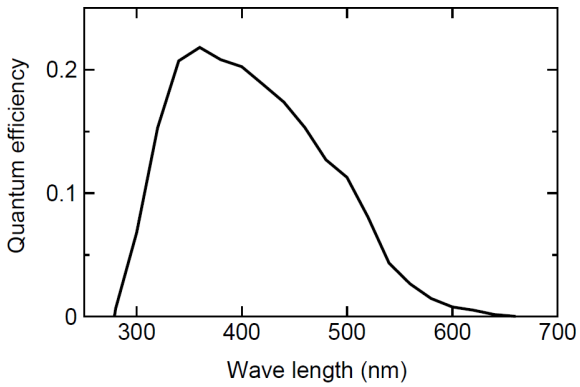

Figure 3.5: Quantum efficiency of the photocathode of a Hamamatsu R3600 20-inch PMT. Taken from [107].

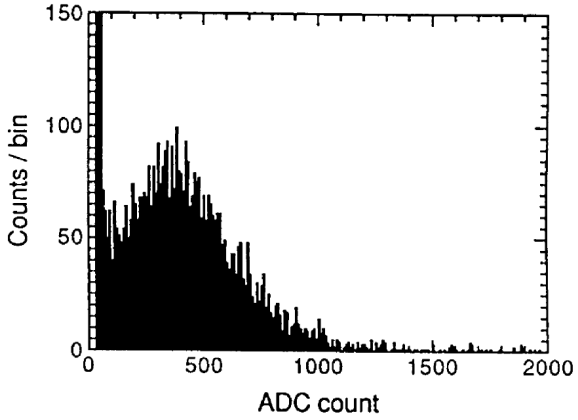

Figure 3.6: Single-photoelectron pulse height distribution of a Hamamatsu R3600 20-inch PMT. Taken from [112].

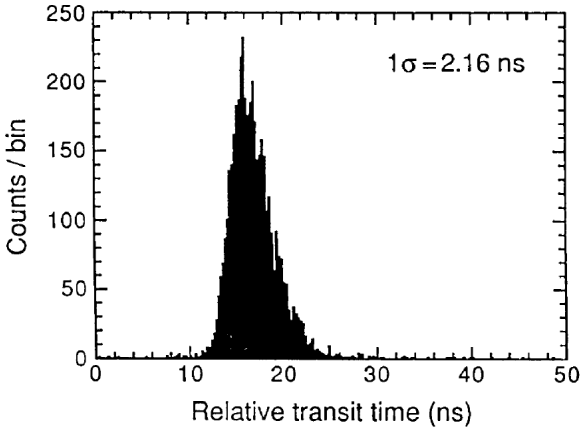

Figure 3.7: Relative transit time spread of a Hamamatsu R3600 20-inch PMT tested with 410 nm wavelength light at the single photoelectron intensity level. Taken from [112].

The OD serves as a cosmic-ray muon veto system and help distinguish neutrino interactions originating within the detector from external background events. If neutrinos interact in the ID, they do not leave visible tracks in the OD. On the other hand, cosmic-ray muons entering the ID deposit light in both the ID and OD. Thus, cosmic-ray muon events can be effectively rejected. The OD also acts as a passive shield, preventing external neutrons and gamma rays from reaching the ID. These background sources originate from surrounding rock and detector components, and their suppression is crucial for low-energy neutrino studies. To improve light collection efficiency, each OD PMT is optically coupled with a 60 $\times$ 60 cm wavelength-shifting (WLS) plate made of acrylic doped with bis-MSB ($C_{24}H_{22}$), which enhances the detection of blue Cherenkov light. Additionally, the OD walls are lined with reflective Tyvek sheets, which maximize the collection of photons and enhance the overall light yield of the detector. The combination of WLS plates and Tyvek reflectors significantly improves the OD's ability to identify external muons.

3.3.3 Water System

The water system is a critical component in ensuring optimal performance of the experiment. Contaminants in the SK detector affect the performance in different ways. Radon from the air produces radioactive decay products, causing low energy background. Dust, particulates, heavy ions and bacteria reduce the transparency of the water and provide possible radiation sources.

The water system is responsible for maintaining the purity and temperature of the water, which are essential for the detection of Cherenkov light and the suppression of backgrounds. In addition to the above responsibilities, the water system replenishes water to the detector when necessary. The water system was upgraded between the SK IV and SK V phases to allow the circulation of water with Gd. Details of the water system in the SK I-IV phases can be found in [107]. The new water system is described in [109].

A schematic view of the SK I-IV water system is shown in Figure 3.8. The 50 kilotons of water in the tank is continuously recirculated at a rate of $\sim$ 60 tons per hour. The water passes through a series of filters and purifiers. Their roles are explained following the sequence of process.

- Nominal 1 μm mesh filters: remove dust and large particulates;
- Heat exchanger (HE): maintain a supply water temperature of $\sim$ 13°C to reduce PMT dark noise and suppress growth of bacteria;
- Cartridge polisher (CP): remove heavy ions;

- Ultra-violet (UV) sterilizer: eliminate bacteria;
- Rn-less-air dissolve tank: dissolve Radon-reduced air into the water for efficient Radon removal;
- Reverse osmosis (RO) system: remove additional particulates;
- Vacuum degasifier (VD): remove dissolved gases in the water to reduce Radon-induced background and suppress growth of bacteria;
- Ultra filter (UF): filter sub-μm particulates;
- Membrane degasifier (MD): remove remaining Radon.

Water rejected by the UF is discarded. After purification, the number of particulates with size $> 0.2\,\mu$m is reduced to 6 particles per cc. Radon concentrations in water after filtration is 0.4 mBqm^{-3}.

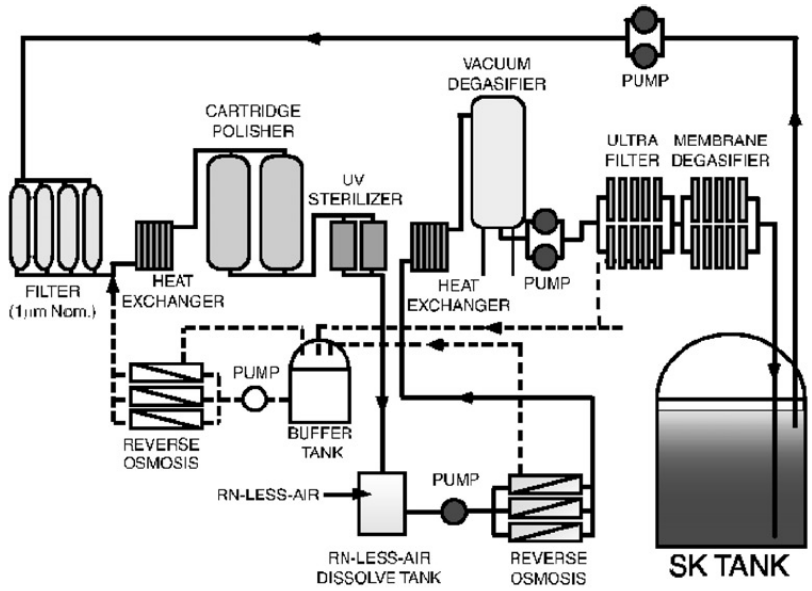

Figure 3.8: A schematic plot of the water system for SK I-IV phases. Taken from [107].

The upgraded water system for the SK-Gd phase was newly designed to allow dissolving $Gd_2(SO_4)_3 \cdot 8H_2O$ into the water and recirculating the Gd-loaded water without removing the Gd. A schematic diagram of the SK-Gd water system is shown in Figure 3.9. The main differences of the SK-Gd water system compared with the SK I-IV water system are the additional Gd-dissolving system and pretreatment system, precision temperature control units, buffer tanks, and resin-based purifiers which removes heavy ions while preserving Gd.

The Gd-dissolving system transports and dissolves $Gd_2(SO_4)_3 \cdot 8H_2O$ in recirculated SK water using a shear blender, ensuring proper mixing before the solution is sent for pretreatment. The pretreatment system for SK-Gd removes impurities from

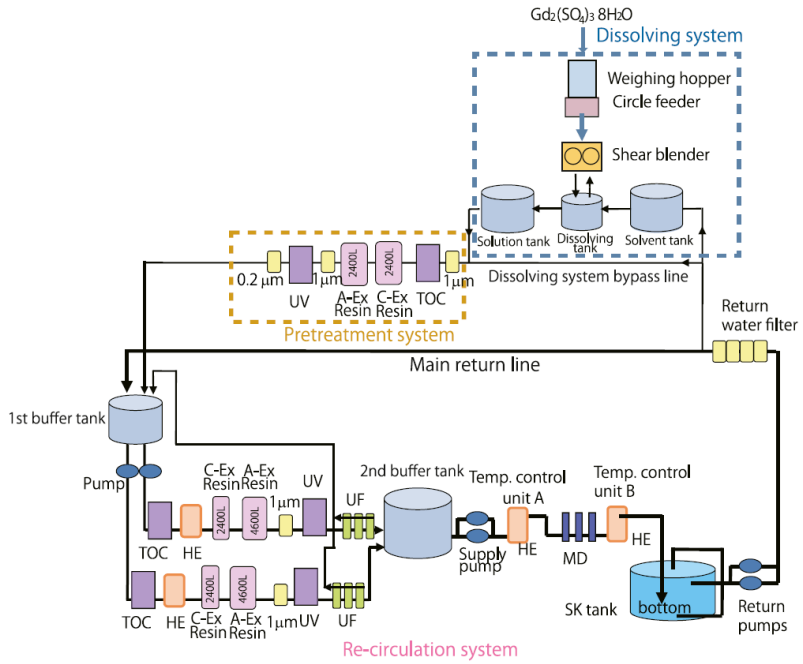

Figure 3.9: A schematic plot of the water system for SK-Gd phase. Taken from [109].

gadolinium-loaded water using UV oxidation, ion-exchange resins tailored to retain Gd and sulfate ions, and filtration, operating only during dissolution before normal recirculation. The water recirculation system basically plays the same role as the SK I-IV water system. A UV total organic carbon reduction lamp (TOC lamp) was used to ionize impurities which will be removed by the down-stream resin-based purifiers. The new HE modules ensure the temperature of the output water is $\sim 13.5°C$. There are two copies of purifiers capable to work in parallel, enabling a maximum processing speed of 120 tons per hour. The Gd water rejected by the UF is not discarded to avoid environmental pollution. Instead, it is returned to the first buffer tank for reprocessing.

The water system is monitored with various sensors and sampling points distributed throughout the detector. Conductivity measurements, optical transparency tests, and chemical composition analyses are performed regularly to verify the stability and effectiveness of the purification system. The Gd concentration is also monitored to prevent loss of Gd sulfate during the purification process.

3.3.4 Electronics and Data Acquisition Systems

The front-end electronics and data acquisition (DAQ) systems in the SK detector are responsible for capturing and recording the charge and time information from the PMTs. The PMTs are connected to the electronics and high voltage supplies via cables. The cables from each quadrant of the detector are routed into one of the four electronics huts at the top of the tank, which houses electronics racks and front-end

DAQ computers for the ID and OD PMTs. For the ID and OD PMTs, high voltage is distributed in different ways. For each OD PMT, a single cable carries both the high voltage and the signal from the PMT. In addition, the high voltage of OD PMTs is distributed across "paddle cards", which supply one high voltage to 12 OD PMTs. In contrast, the high voltage for the ID PMTs is adjustable PMT-by-PMT. For the analysis in this thesis, data were taken using two distinct sets of electronics: one was used in the SK I-III phases, and the other was used in the SK IV and later phases.

SK I-III electronics and data acquisition systems

During the SK I-III phases, the front-end electronics for the ID PMTs were custom built Analog-Timing-Modules (ATMs) [113]. An ATM board has 12 input channels, each is connected to an ID PMT. It functions as a combined Analog-to-Digital Converter (ADC) and Time-to-Digital Converter (TDC), recording the total charge and arrival time of each PMT pulse. A schematic view of the analog input block of the ATM is shown in Figure 3.10. The charge signal is first split into several signals: One is sent to a discriminator with a threshold level of 1/4 pe. One is fed to Charge-to-Analog Converter (QAC). Meanwhile, a Time-to-Analog Converter (TAC) integrates constant current. When the PMT signal is above the threshold level, a wide square wave is sent to the ATM front panel. The analog sum of these 15 mV/channel pulse, known as "HITSUM", is used to generate the global trigger signal. On a global trigger, the information from TAC is converted to the PMT timing offset relative to the trigger. The charge and time information is then sent to an ADC and digitized. The ATM has a dynamic range of ~ 450 pC in charge and ~ 1300 ns in time. A redundant set of TAC/QAC ensures that events can be processed with effectively no deadtime.

The ID DAQ system manages the global trigger and assembles the data as events. Figure 3.11 shows a schematic view of the ID DAQ system. It has 946 ATM boards, 48 Go/No-Go (GONG) modules and 48 Super Memory Partner (SMP) boards. The HITSUM generated by ATM is first sent to the VME TRG (TRiGger) module for global trigger assertion. When the number of hit PMTs is above threshold, a global trigger signal and event number information are distributed to all ATMs via the GONG modules. Then, the data stored in ATM are fed to the SMP modules, and later read out by online computers and assembled as events. The thresholds are set to separate low-energy events and high-energy events for different physics analyses. A summary of SK I-III triggers is found in Table 3.1.

The OD PMTs are connected to a different set of electronics. The signals from the OD PMTs are processed by custom built Charge-to-Time Converters (QTC). The leading edge of the pulse indicated the hit time and its width was proportional to the total charge. Similar to the ID, these signals are sent to the VME TRG module, digitized, and stored in SMP boards for further processing.

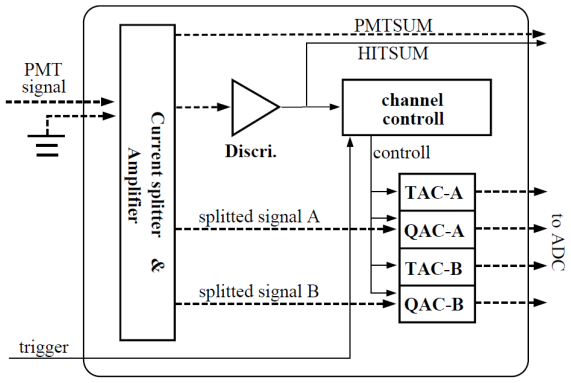

Figure 3.10: A schematic view of the ATM electronics for SK I-III phases. Taken from [107].

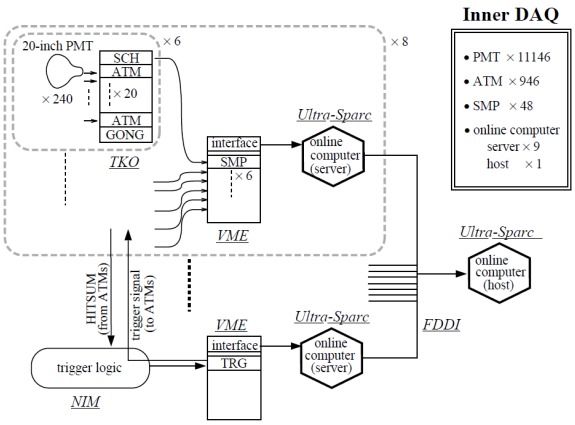

Figure 3.11: The ID DAQ system with ATM boards for SK I-III phases. Taken from [107].

SK IV+ electronics and data acquisition systems

In 2008, the SK front-end electronics were upgraded with QTC-Based Electronics with Ethernet (QBEEs) and a new DAQ system. A schematic view of the input block of the QBEE is shown in Figure 3.12. For a comprehensive review of the QBEE, see [114, 115]. The QBEEs, like SK I-III OD electronics, output a single pulse encoding both total charge and timing of the signal when the signal is above the 1/4 PE threshold. They feature three gain settings in a 1:7:49 ratio, allowing simultaneous processing of multiple gain levels and selection of the best-suited setting. This enhancement provided five times the dynamic range in charge of the previous ATM system. In addition, QBEEs extended the readout duration from 1300 ns to 4000 ns before requiring a reset. Each QBEE manages signals from 20 PMTs, transmitting them to the DAQ system via Ethernet.

A schematic view of the new DAQ system is shown in Figure 3.13. It contains 550 QBEEs, 20 front-end PCs, 10 merger PCs and an organizer PC. Data from the QBEEs are transferred as TCP packets to 20 front-end PCs, each handling data

from $\sim$ 30 boards. These processed data are sent via a 10-Gigabit Ethernet link to 10 Merger PCs, where they are merged, and a software trigger selects events for physics analysis. The selected events are then sent to an Organizer PC via Gigabit Ethernet, merged again, and written to disk for offline analysis. The implementation of software trigger enables variable-length event windows, which facilitate tracking delayed particles such as neutron captures and muon decays. Moreover, a new "after" (AFT) trigger is introduced to store several hundred microseconds of data following isolated ID activity with no OD signals in order to capture possible delayed signals. A summary of the triggers used in the SK IV and later phases is given in Table 3.1.

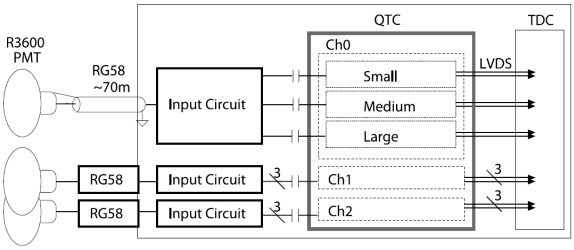

Figure 3.12: A schematic view of the QBEE electronics for SK IV and later phases. Taken from [114].

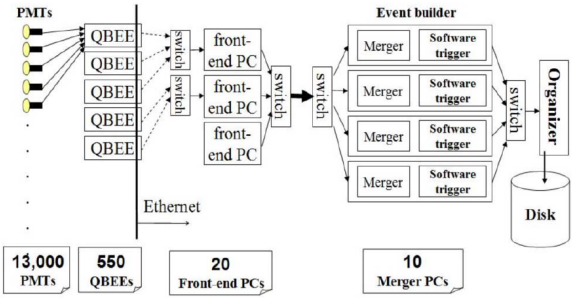

Figure 3.13: The ID DAQ system with QBEE for SK IV and later phases. Taken from [115].

3.4 Calibration

Accurate calibration is crucial for ensuring the reliability and precision of data collected by the SK detector. Calibration procedures are conducted regularly to maintain the performance of photomultiplier tubes (PMTs), monitor water quality, and guarantee the stability of the detector's response to neutrino interactions. This section discusses the calibrations of the ID PMTs and electronics and the light propagation in the detector. A detailed review of the calibrations can be found in [116].

Table 3.1: Trigger thresholds for different SK data-taking phases. The thresholds change over time due to changes in PMT dark rates and failed ID PMTs. SLE refers "super low energy", LE refers to "low energy", HE refers to "high energy", SHE refers to "super high energy", and "AFT" refers to after. AFT triggers were introduced in the SK IV phase to capture possible delayed signals.

	SK I-III		SK IV and later	
Trigger Type	Trigger Logic (hits in 200 ns)	Time window (μs)	Trigger Logic (hits in 200 ns)	Time window (μs)
SLE	20 ID hits	1.3	34→31 ID hits	[-0.5, 1.0]
LE	29 ID hits	1.3	47 ID hits	[-5, 35]
HE	31 ID hits	1.3	50 ID hits	[-5, 35]
SHE	-	-	70→58 ID hits	[-5, 35]
AFT	-	-	after SHE, no OD	[35, 535]
OD	19 OD hits	16	22 OD hits	[-5, 35]

3.4.1 ID PMT Calibration

High-voltage settings

The high-voltage (HV) settings for each ID PMT are adjusted to ensure a uniform response across all tubes, usually done after refurbishment. This process begins with the pre-calibration of 420 reference PMTs using a Xe flash lamp and a scintillator ball inside a μ-metal shielded dark box. The HV for these PMTs is set so that their charge response matches a target value of approximately 30 pe. These reference PMTs are then installed and used as a baseline to calibrate the remaining PMTs, which are grouped based on their geometric relationship to the central light source as shown in Figure 3.14. The HV settings for the remaining PMTs are adjusted to match the average response of the reference PMTs in their respective groups. The scintillator ball/Xe lamp remains at the center of the detector to provide continuous real-time monitoring of PMT gain stability.

Relative gain calibration

The gain of an ID PMT is the conversion factor between the output charge and the input number of PEs. The gain calibration is done in two steps: (1) measure the relative gain differences among the ID PMTs, (2) measure the average gain of all ID PMTs. The relative gain differences are determined by comparing their responses to high- and low-intensity light pulses from a centrally located scintillator ball coupled to a nitrogen laser. High-intensity flashes provide a measurable charge output for each PMT, while low-intensity flashes allow counting of single-PE hits. By taking the ratio of these two measurements, the relative gain of each PMT is obtained, regardless of variations in quantum efficiency and geometric acceptance. These relative gain factors are then used as corrections in the conversion from charge to PE count.

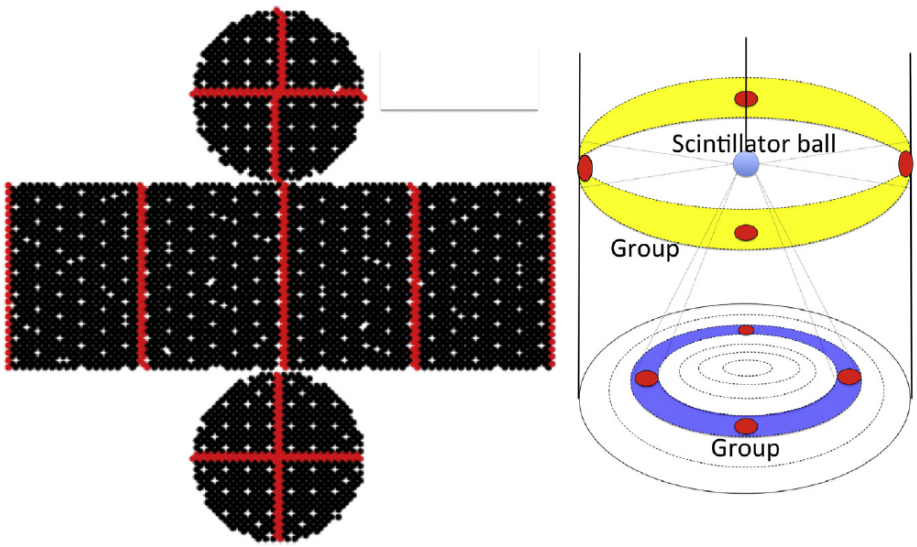

Figure 3.14: A schematic view of the high voltage calibration. Locations of reference PMTs in the ID are shown on the left. Geometrical relationship between the scintillator ball and reference PMTs are shown on the right. Taken from [116].

Absolute gain calibration

The absolute gain conversion factor is determined using a nickel source that isotropically emits gamma rays from neutron captures. The nickel source is installed at the center of the detector, generating lights that produce an average of 0.004 PEs per PMT per event, where 99% of observed signals are single-PE signals. By accumulating charge distributions from all PMTs and applying measured relative gain corrections, a cumulative single-PE spectrum is constructed. This cumulative spectrum largely represents the average single-PE response of the entire ID.

A walk-through of the absolute gain calibration is presented in the following. Figure 3.15 shows the single-PE charge distribution measured at the beginning of the SK III phase. The solid line in the left panel (Q>0.5 pC) shows the data measured using this method. To measure the distribution below the 1/4 PE discriminator threshold, data are taken with half the discriminator threshold and double the PMT gain, shown as the dashed line (0.3<Q<0.5 pC). The dotted line (Q<0.3 pC) is linear extrapolation of the measured distribution. The absolute gain, known as "pC-to-PE" (picocoulomn to photoelectron), is found by averaging the entire pC region. From the distribution shown in Figure 3.15, the pC-to-PE is 2.243 pC per PE. A long-term increase in the absolute PMT gain is observed, requiring adjustments over time. This extracted single-PE distribution is also implemented in Monte Carlo (MC) simulations, ensuring consistency between real and simulated data. However, data-MC discrepancies are found in the SK I phase, initiating a retuning of the single-PE distribution of this phase, detailed in Section 11.3.

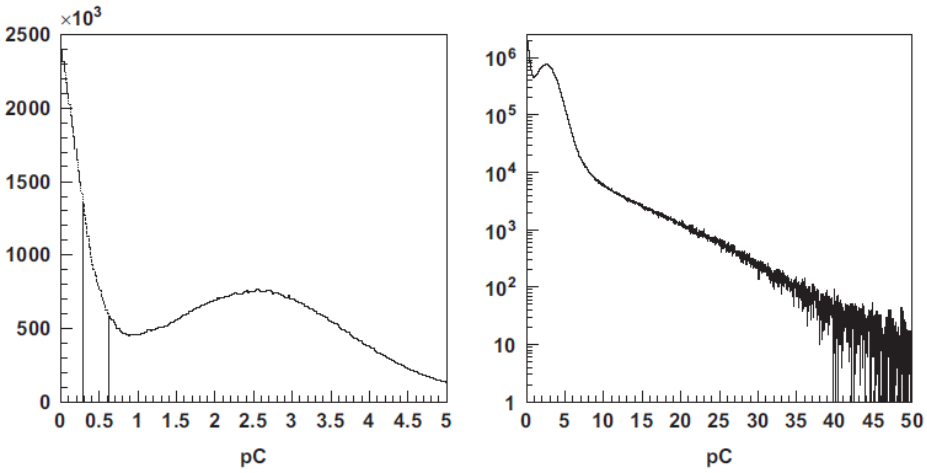

Figure 3.15: The single-PE distributions in pC in SK III data taking phase. Left: linear scale. Right: logarithmic scale. In the left figure, the solid line shows the data with normal PMT gain, while the dashed line shows the data with double gain and half threshold. The left-most dotted line is linear extrapolation of the data. Taken from [116]

Relative quantum efficiency calibration

The PMT-by-PMT differences in quantum efficiencies (QEs) are determined by comparing the observed hit probabilities by the nickel source for each PMT to predictions from MC simulations. The raw hit probabilities are first corrected for geometric factors, such as distance and angular acceptance, and then further refined using simulation-based estimates of photon propagation effects, including scattering and reflections. After corrections, the remaining variations are attributed to differences in QE among PMTs.

Timing calibration

The response time to the same event can vary among different readout channels due to differences in transit time, lengths of PMT cables, processing time of readout electronics, and even the pulse heights of PMTs. Since large pulses register hits earlier than smaller ones, this can cause differences in response time, known as the "time-walk" effect. In order to calibrate the time response of each channel, fast light pulses with varying intensities are injected to PMTs. A schematic view of the timing calibration system is shown on the left panel in Figure 3.16. The light from a nitrogen laser is delivered through an optical fiber to a centrally placed diffuser ball, which emits isotropic flashes with minimal directional bias. Each channel's timing response is measured as a function of pulse height (charge), capturing the "time-walk" effect. The right panel in Figure 3.16 shows the two-dimensional timing versus charge distribution of a readout channel, known as "TQ distribution". These distributions are fitted with polynomial functions to determine the "TQ-map" for each readout

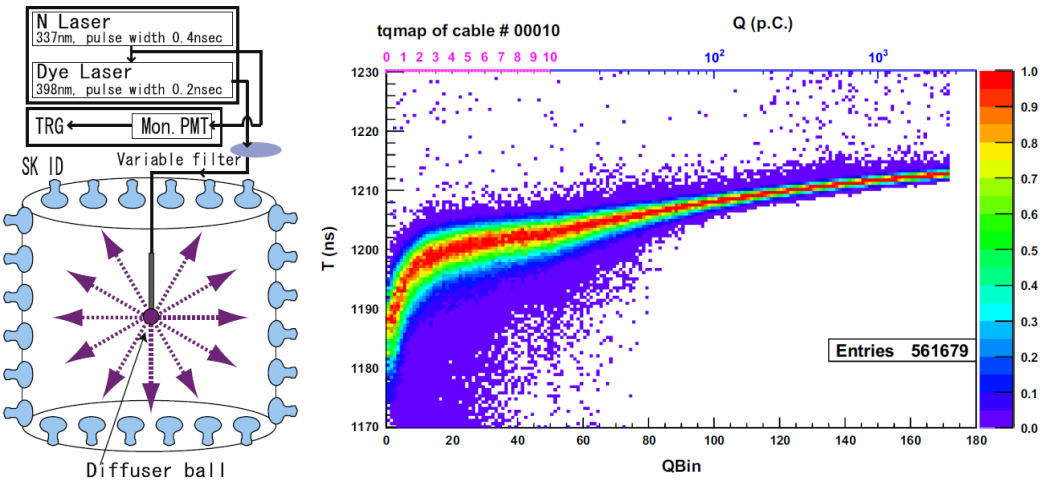

Figure 3.16: An overview of the SK timing calibration. Left: Schematic view of the timing calibration system. Right: typical distribution of hit timing as a function of pulse height. The horizontal axis reflects the observed charge, and the vertical axis is time-of-flight (ToF) corrected hit timing. The horizontal axis is linear scale below 10 pC and logarithmic scale above 10 pC. Taken from [116]

channel, which is used to correct the time response of the readout channel.

3.4.2 Photon Tracking Calibration

Absorption and scattering in water

The optical properties of water in the ID are calibrated using a laser injector installed on the top of the tank. The experimental setup is shown in Figure 3.17. A multi-wavelength laser injector distributes light into the detector with five wavelengths: 337, 375, 405, 445, and 473 nm. PMTs are divided into 6 groups: PMTs at the top and PMTs in B1-B5 regions on the barrel walls. The intensity of light seen by the PMTs can be modeled as

$$I(l,\lambda) = I_0(\lambda)\exp[-l/L(\lambda)], \tag{3.3}$$

where I is the light intensity at distance l from the source, λ is the wavelength, $I(l,\lambda)$ is the source intensity, and $L(\lambda)$ is the total attenuation length incorporating absorption and scattering. The attenuation length is given by

$$L(\lambda) = \frac{1}{\alpha_{abs}(\lambda) + \alpha_{sym}(\lambda) + \alpha_{asy}(\lambda)}, \tag{3.4}$$

where $\alpha_{abs}(\lambda)$, $\alpha_{sym}(\lambda)$, and $\alpha_{asy}(\lambda)$ are absorption amplitude, symmetric scattering, and asymmetric scattering, respectively. A data-MC comparison is shown in Figure 3.18, with the x-axis being the hit time at PMT after ToF correction. The coefficients $\alpha_{abs}(\lambda)$, $\alpha_{sym}(\lambda)$, and $\alpha_{asy}(\lambda)$ are fitted using data from scattered light, i.e. the left region of the distributions. The fitting results are shown in Figure 3.19.

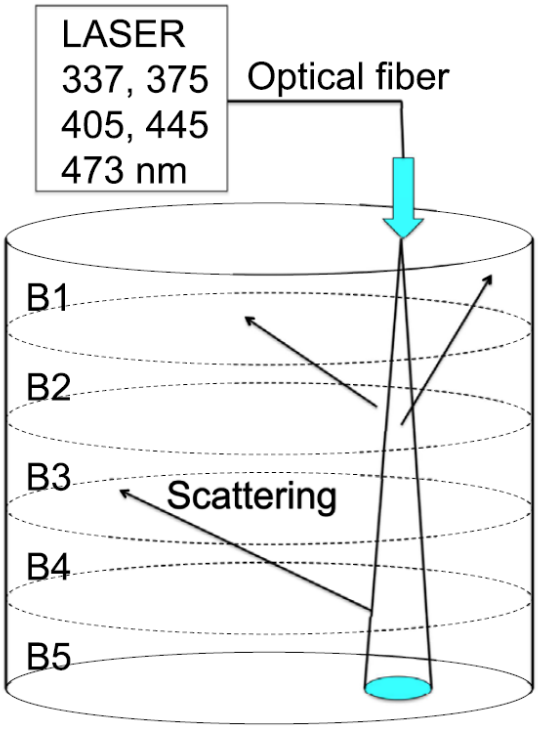

Figure 3.17: A schematic view of the real-time laser system for measurements of absorption and scattering of the Cherenkov light in water and reflectivity at the PMT surface. Laser of different wavelength is injected via optical fiber from the top of the ID. The ID PMTs are divided into six groups: B1-B5 on the barrel region, and the top region. Taken from [116].

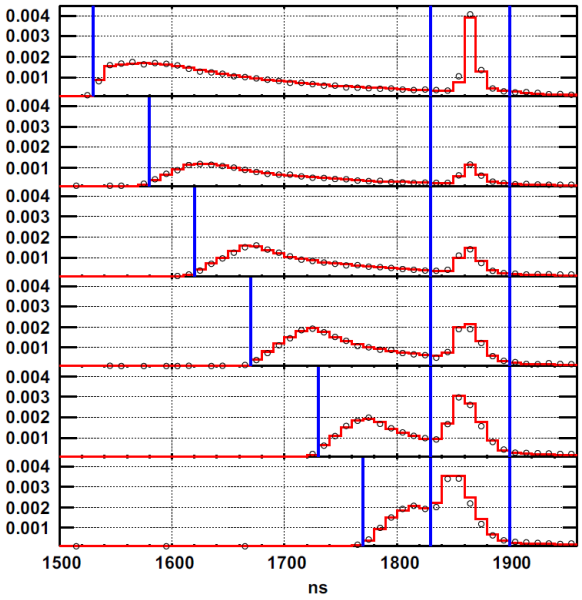

Figure 3.18: Typical ToF corrected timing distribution for the laser data (black circle) and the best-fit MC (red histogram). From top to bottom are the data taken from the top region, and B1-B5 regions. Taken from [116].

Reflection on PMTs and black sheets

The reflectivities of PMTs and black sheets are measured using two distinct approaches. For PMT reflectivity calibration, the same laser data as shown in Fig-

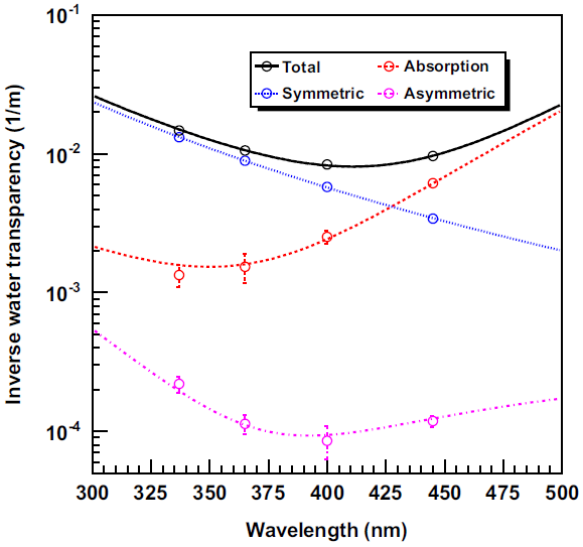

Figure 3.19: Fitting results of the absorption and scattering coefficients obtained from laser calibration data. Taken from [116].

ure 3.18 is used. The right regions of the distributions are from photons reflected on the PMT. In the SK detector simulations, only the PMT surface with bialkali is modeled, which is composed of 4 layers: water in the tank, glass, bialkali, and vacuum inside the PMT, as illustrated in Figure 3.20. The real and imaginary parts of the complex refractive index of the bialkali are fitted. However, the structure in the PMT also contributes to the reflection, resulting in unrealistic refractive indices. Moreover, this model cannot fully address the reflection data, which has been a long-standing issue in SK. An attempt to build a new PMT model that enables simulations of optical processes on the PMT's internal structure is documented in Appendix A.

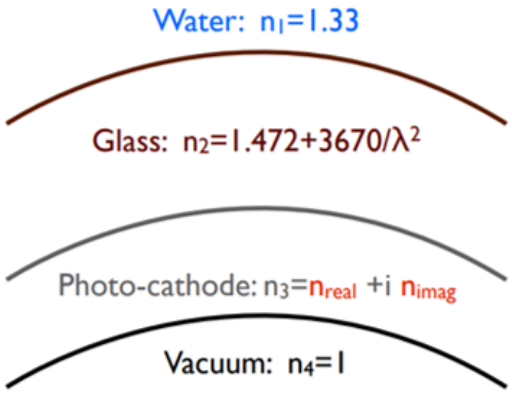

Figure 3.20: A schematic plot of the SK PMT surface.

The reflectivity of the black sheet is measured using a light injector inside the detector, with tests conducted at three wavelengths and incident angles. The reflected charge is compared to direct charge measurements taken without the black sheet, and the reflectivity is determined using their ratio.

SK is a multi-purpose detector for the observations of atmospheric, accelerator, astrophysical, and solar neutrinos, as well as to search for proton decay. Operational since 1996, SK has undergone multiple upgrades and is currently in the SK-Gd phase, featuring Gd-loaded water for enhanced neutron identification. Loading Gd has enabled SK to search for supernova relic neutrinos and pre-supernova neutrinos. The gain and quantum efficiency of each PMT is measured independently and a precision of 1% has been achieved. The time resolution is 2.1 ns for $\sim$1 photoelectron and 0.5 ns for $\sim$100 photoelectrons. As for optical properties, absorption and scattering probability in SK water and reflections on PMT surfaces and the black sheet are determined using light sources. These calibration works are crucial for SK to achieve its goals.

Part 1

Combined Pre-supernova Alert System with KamLAND and Super-Kamiokande

Chapter 4

Introduction

Prior to a core-collapse supernova, various processes produce an increasing amount of neutrinos of all flavors from the interior of massive stars characterized by mounting energies. Among them, the electron antineutrinos are potentially detectable by terrestrial neutrino experiments such as KamLAND and SK via inverse beta decay interactions. While a SN neutrino burst only lasts for a few seconds, which is easy to miss, it is possible to detect pre-supernova (pre-SN) neutrinos several hours before the explosion. Such a detection will provide an early warning of the upcoming CCSN and allow for preparation time for SN neutrino observation. In light of this, KamLAND [105] and SK [106] have been monitoring pre-SN neutrinos since 2015 and 2021, respectively.

This work, we developed a combined pre-SN neutrino alert system [117], which will integrate data from global neutrino detectors to monitor the real-time pre-SN neutrino flux. The motivation is to improve the length of early warning time, extend the horizon, and reduce the dead time of the alert system. The combined alert system[1] has been online and open to registered users since May 2023. As a first step, it hosts two detectors: KamLAND and SK.

In this chapter, we introduce core-collapse supernova and pre-supernova neutrinos. Detection of pre-supernova neutrinos in SK and KamLAND are introduced in Chapter 5 and 6 respectively. Finally, we present the analysis method, the workflow of the system, as well as the detection sensitivity to pre-supernova neutrinos in Chapter 7.

[1] https://www.lowbg.org/presnalarm/

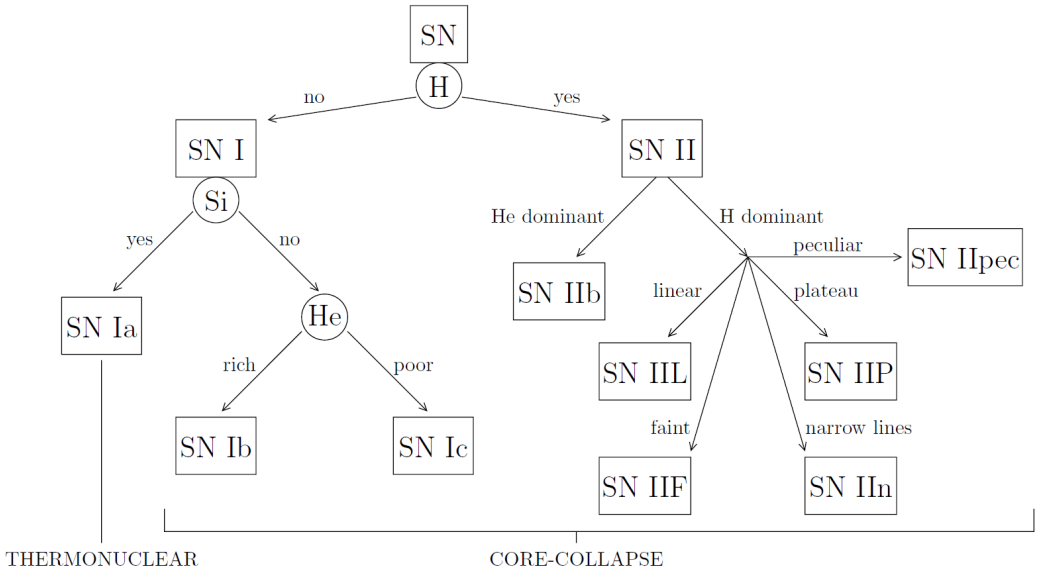

Figure 4.1: Supernovae classification scheme. Taken from [120].

4.1 Supernovae

Supernovae (SNs) represent some of the most energetic phenomena in the universe, marking the terminal evolutionary stages of certain classes of stars. They play a crucial role in the chemical and dynamical evolution of galaxies, enriching the interstellar medium with heavy elements and triggering subsequent generations of star formation. SNs are broadly classified into two categories based on their progenitor systems and explosion mechanisms: thermonuclear supernovae and core-collapse supernovae (CCSNs) [118, 119]. A supernova classification scheme is shown in Figure 4.1.

The classification is made according to the abundance of specific spectral lines and light curve. Type Ia SNs are thermonuclear SNs that arise from the complete disruption of a carbon–oxygen white dwarf in a binary system. When mass accretion or merger drives the white dwarf beyond the Chandrasekhar limit, carbon fusion ignites under degenerate conditions, leading to a runaway thermonuclear explosion that unbinds the star. These events are characterized by the absence of hydrogen lines in their spectra and exhibit remarkable uniformity in their light curves, making them valuable cosmological distance indicators [121]. Type II supernovae, in contrast, have hydrogen lines. The Type II class, together with the hydrogen-poor but core-collapse-origin Type Ib and Type Ic events, are classified as CCSNs.

4.2 Core-collapse Supernovae

CCSNs occur in massive stars with Zero-Age Main-Sequence (ZAMS) masses greater than $8\,M_\odot$. These massive stars undergo a lifecycle dominated by nuclear fusion.

They begin by burning hydrogen into helium in their cores, progressing through successive stages of nuclear fusion to produce heavier and heavier elements such as carbon, oxygen, and silicon. Although the main factors that affect nuclear fusion in the core are considered temperature and density, other factors, such as rotation, or the presence of a massive companion, can significantly alter this process [122]. The change in the chemical composition of a star, forming concentric shells of heavier elements along its volume, is the result of nuclear fusion of heavier elements in the core.

After successive nuclear burning stages produce an iron core, no further exothermic fusion can occur. Once the core mass exceeds the effective Chandrasekhar limit, electron degeneracy pressure fails to support gravity, triggering a catastrophic gravitational collapse. This collapse compresses the core into an extremely dense state, often forming a neutron star. The rebound of this collapse launches a shockwave, expelling the outer layers of the star in a spectacular explosion, a CCSN [123].

The mechanism behind these explosions remains an area of intense research. One key factor is the role of neutrinos produced in large quantities during the core's collapse. Their interactions help re-energize the shockwave, ensuring that the star's outer layers are ejected into space. This explosive nucleosynthesis also creates elements heavier than iron, contributing to the cosmic abundance of gold, uranium, and other heavy elements. The remnants of a CCSN depend on the mass of the progenitor star [124, 125]. Neutron stars are left behind if the mass of the remnant core is below a certain threshold; otherwise, it forms a black hole. The expelled materials enrich the interstellar medium, seeding future generations of stars and planets with the elements necessary for life. CCSNs exemplify the universe's cycle of death and rebirth, transforming dying stars into creators of cosmic chemistry. Their study not only helps us understand stellar evolution but also offers a glimpse into the origins of the elements that make up our world.

While shock revival is considered to be caused by neutrino heating, the details of the heating mechanism are still unknown. Several scenarios have been proposed; hydrodynamical mechanisms such as convection and the standing-accretion-shock instability [126], and magnetic fields [127].

Observation of CCSNs through multiple messengers provides essential constraints on these explosion processes. Electromagnetic observations, spanning from radio to gamma ray wavelengths, trace the ejected material, shock interaction with circumstellar matter, and nucleosynthesis yields. However, observations via electromagnetic signals alone are not sufficient to reveal the mechanism of SNs because of the high matter density at the core.

Neutrinos, which carry away nearly 10^{53} erg of gravitational binding energy,

escape unimpeded from the core and provide a prompt and penetrating probe of the dynamics and thermodynamics of the collapse. The detection of neutrinos from SN 1987A confirmed the basic theoretical picture of core collapse and remains one of the most significant achievements in neutrino astronomy [2, 3, 4]. Boosted by this observation, various neutrino experiments, such as Borexino [86], IceCube [87], KamLAND [88], LVD [89], NOvA [90], SNO+ [91], and Super-Kamiokande (SK) [92], equipped with advanced technology and improved capabilities, continued the quest to detect SN neutrino bursts. Furthermore, a number of next-generation neutrino detectors sensitive to galactic SN neutrinos are under construction, including DUNE [95], Hyper-Kamiokande [70], JUNO [96], and KM3NeT [97]. In terms of SN observation via neutrinos, CCSNs have higher detectability than thermonuclear SNs as CCSNs produce all flavors of neutrinos with higher flux, while the latter only release electron neutrinos.

In addition, gravitational waves (GWs) are expected to be emitted by time dependent asymmetries in the mass distribution and rotation of the collapsing core. While not yet detected from a SN, GWs offer a complementary probe of the innermost region, sensitive to non-spherical motions and rotation that cannot be inferred from neutrinos or photons [128, 129].

The next galactic core-collapse supernova will thus provide a unique multimessenger dataset comprising electromagnetic radiation, neutrinos, and gravitational waves. Combined analysis of these signals will enable stringent tests of explosion models, constrain neutrino properties, and probe the behavior of matter at extreme densities, advancing both astrophysics and fundamental particle physics. The rate of the galactic CCSNs is estimated to be $3.2^{+7.3}_{-2.6}$ per century [5]. Given their rarity, it is imperative to ensure that no such events are missed. Our goal is to develop an early warning system for CCSNs, allowing for preparation time for multi-messenger observations.

4.3 Pre-supernova Neutrino

The ignition of carbon in a massive star means that the star has become a neutrino-cooled star. Starting in this stage, energy loss via neutrino emission becomes the dominant cooling mechanism, taking the place of photon radiation [130]. The duration of this stage is typically a few hundred years. As nuclear burning proceeds, neutrino-cooled stars develop an onion-like shell structure with distinct burning layers of helium, carbon, oxygen, neon, and silicon surrounding an iron core, as illustrated schematically in Figure 4.2.

At core temperatures exceeding $\sim 5 \times 10^8\,\mathrm{K}$, electron–positron annihilation becomes the dominant neutrino production process producing all flavors of neutrino and

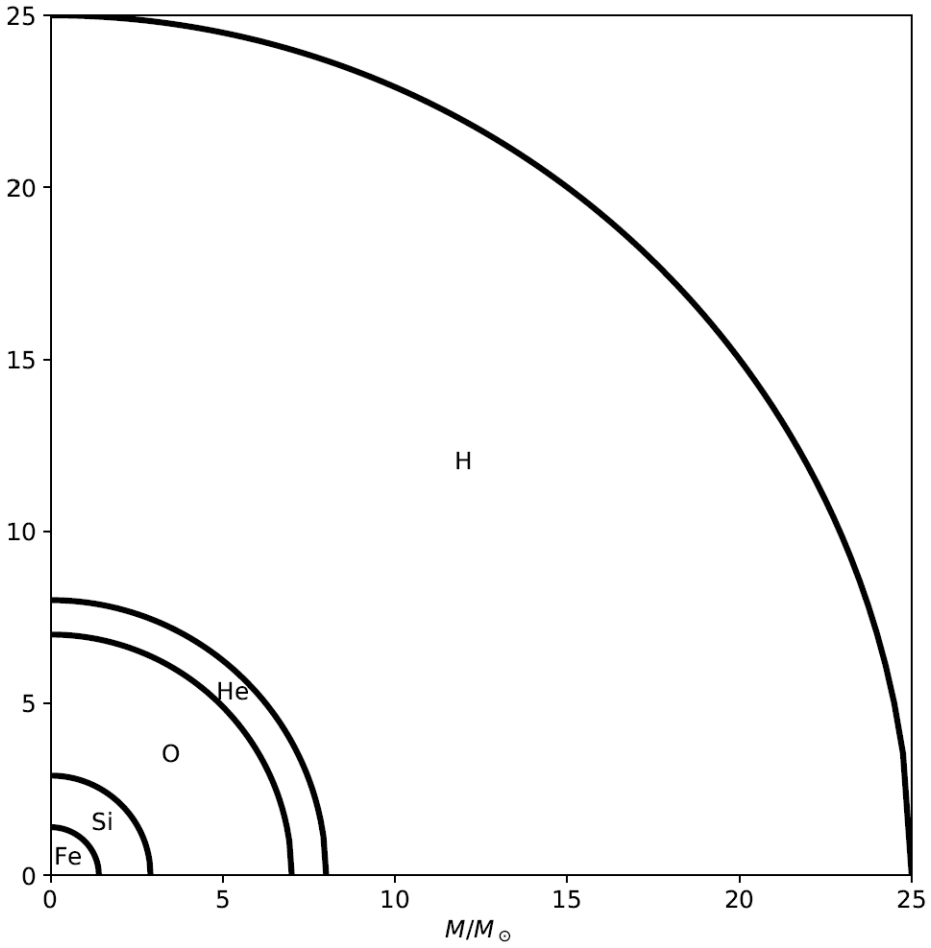

Figure 4.2: Schematic onion-like structure of a massive star prior to core collapse, showing element abundance layers. Taken from [131].

antineutrino pairs [102]:

$$e^+ + e^- \rightarrow \nu_x + \bar{\nu}_x, \tag{4.1}$$

where $x = e, \mu, \tau$. As the star approaches core collapse, the nuclear beta processes (beta decay and electron capture) begins to dominate. The dominant isotopes for beta processes are those with $A = 50 - 60$, such as iron, manganese, cobalt and chromium [103]. As shown in Figure 4.3, beta processes will eventually contribute more to neutrino emission than thermal processes as the star approaches core collapse [103]. Thermal processes include pair annihilation, plasma neutrino process ($\gamma^* \rightarrow \nu + \bar{\nu}$), and photo-neutrino process ($e^\pm + \gamma \rightarrow e^\pm + \nu + \bar{\nu}$), where pair annihilation is dominant. The green lines in this figure are the luminosity of $\nu_\mu(\bar{\nu}_\mu)$ or $\nu_\tau(\bar{\nu}_\tau)$. The other lines are for $\nu_e(\bar{\nu}_e)$. The production of $\bar{\nu}_e$ is strongly suppressed due to the high electron number density in the star. The efficiency of these processes grows rapidly with temperature, accelerating the burning of progressively heavier elements until silicon burning begins. Table 4.1 lists the dominant processes at each stage.

During the final silicon-burning phase, the core temperature reaches approxi-

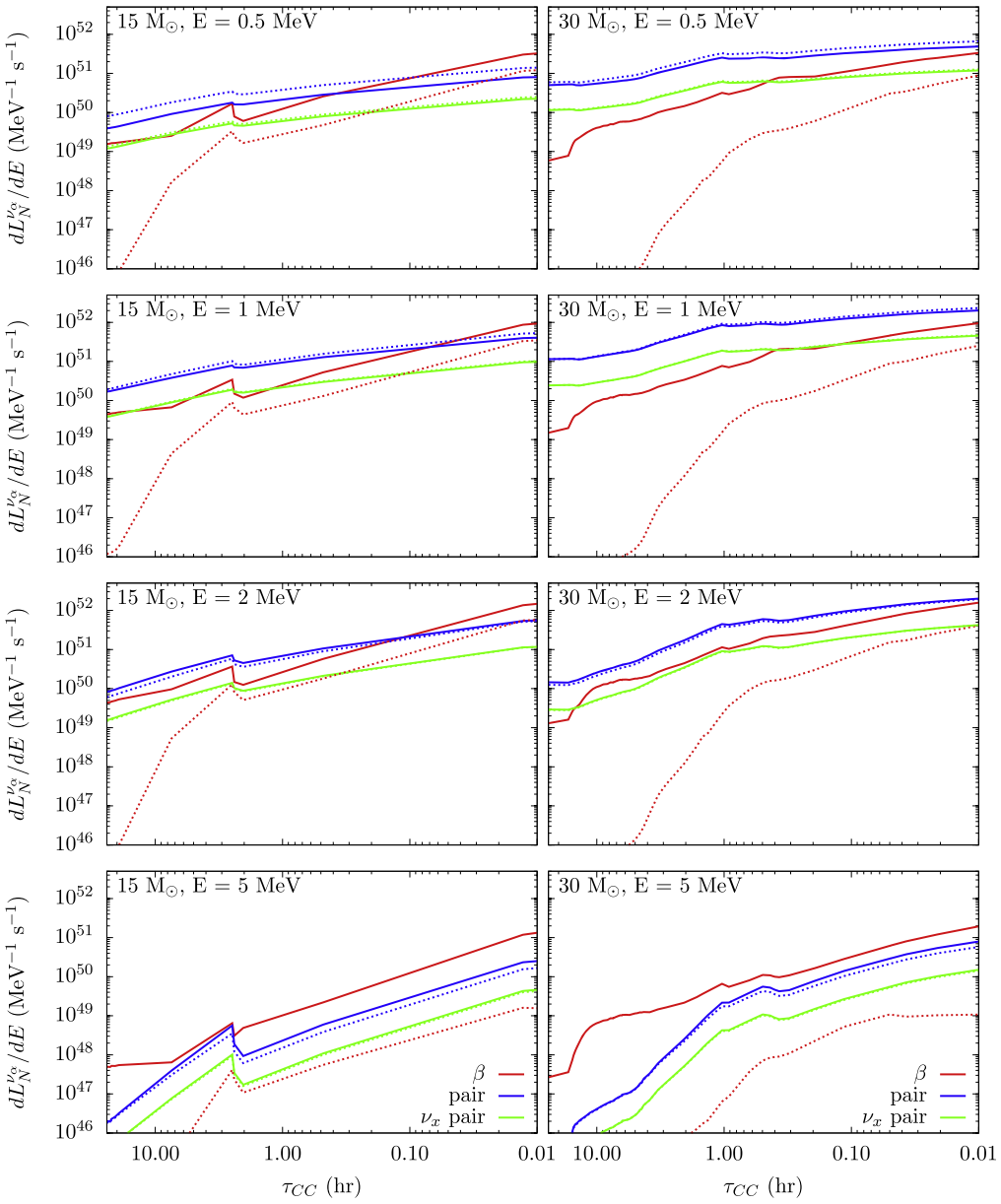

Figure 4.3: The neutrino luminosity of a 15 $M_\odot$ star (left) and a 30 $M_\odot$ (right) as a function of time before core collapse, differential in energy, at selected energies. The solid lines denote neutrinos, while the dashed lines show the anti-neutrino contributions. The contributions from beta process is plotted as red lines. The blue lines represent the contributions from thermal processes of $\nu_e(\bar{\nu}_e)$, while the green lines denote the contributions from thermal processes of ($\nu_\mu(\bar{\nu}_\mu)$ or $\nu_\tau(\bar{\nu}_\tau)$). Taken from [103].

Table 4.1: Neutrino production processes during late burning stages

Stage	**Dominant process**
Carbon burning	Pair annihilation
Oxygen burning	Pair annihilation + photo-neutrino process
Silicon burning	Pair annihilation + beta decay
Final hours pre-collapse	Beta decay + electron capture

mately 3.4×10^9 K, and the star emits intense fluxes of neutrinos and antineutrinos with typical average energies of ~ 1.8 MeV. Stars at this stage are usually referred to as pre-supernova (pre-SN) stars, immediately preceding core collapse. The definition of pre-SN star is not strict. In many literature, neutrino-cooled stars are considered as pre-SN stars, as the time to core collapse is very short compared to the lift of a star. Table 4.2 summarizes the approximate duration and neutrino emission characteristics for a $20\,M_\odot$ progenitor as compiled in [132]. Although pre-SN neutrinos are much lower in luminosity than SN burst neutrinos, their emission lasts a long time scale before the CCSN, allowing for integration of signal with a time window of a few hours or even days. Furthermore, pre-SN neutrinos provide an early warning signal of an imminent CCSN.

Table 4.2: Approximate duration of burning stages for a $20\,M_\odot$ star and the average energy of emitted neutrinos [132].

Burning Stage	**Duration**	ν_e ($\bar{\nu}_e$) **Fraction**	**Average** E_ν **(MeV)**
C	300 yr	42.5%	0.71
Ne	140 d	39.8%	0.99
O	180 d	38.9%	1.13
Si	2 d	36.3%	1.85

4.4 Detection principle of pre-supernova neutrino

Pre-SN neutrinos are potentially detectable by terrestrial detectors if the progenitor is close enough to Earth. They not only signal the imminent SN, but also provide insight into the late stages of stellar evolution of massive stars. A pre-SN neutrino detection can help unravel many uncertainties associated with stellar evolution models: the physical processes that lead to a CCSN, the shell structure formation, the isotopic composition of stars, etc [133, 134, 135]. It can also provide evidence to neutrino mass ordering [136].

The energy of pre-SN neutrinos is at sub-MeV to MeV scale. In this energy range, IBD ($\bar{\nu}_e + p \rightarrow e^+ + n$) is an important detection channel, which has a relatively large cross section for detectors with free protons like Water Cherenkov detectors or Scintillator detectors. The characteristic temporal and spatial correlations of the positron signal and the neutron capture signal can provide a high purity in event selection. The existing pre-SN neutrino detectors, KamLAND and SK, both adopted detection techniques based on IBD. Compared to KamLAND, a liquid scintillator detector, whose energy threshold is typically less than 1 MeV, SK in its pure water phase is less sensitive to low-energy neutrinos. The higher energy threshold (2.5 MeV in electron kinetic energy) limits the detection of neutron capture signals in SK. Starting in 2020, the SK detector was loaded with gadolinium (Gd) to improve the

neutron detection efficiency [109].

Elastic scattering of pre-SN neutrinos on electron could be utilized for pre-SN neutrino detection as well. Although it has a lower cross section than IBD, the pre-SN neutrino flux is much higher than that of anti-neutrino, as shown in Figure 4.3. In addition, the recoil electrons can provide directional information of the SN. This will be extremely valuable to optical telescopes, for they need to rotate in advance to point to the SN.

Chapter 5

Pre-supernova Neutrino Detection in SK

5.1 Overview

The SK experiment has been introduced in Chapter 3. Here we emphasize that the Gd loading after the SK IV phase has improved SK's sensitivity to low-energy $\bar{\nu}_e$, expanding the physics goals of the experiment. It has enabled SK to reveal neutrinos from the Diffuse Supernova Neutrino Background (DSNB) [99, 100] and pre-SN stars, which are yet to be observed.

As mentioned before, SK adopted a detection technique based on IBD featuring a delayed coincidence. For the prompt signal, positrons are detected by the Cherenkov light and annihilation light they produced. For the delayed signal, neutrons are thermalised and captured by Gadolinium or Hydrogen tens of micro-seconds after the prompt signal. The coincidence distance dR, which is the distance between the two signals, and the coincidence time dT, which is the time between the two signals, are characteristic properties that are used to select IBD events.

One of the challenges for pre-SN neutrino detection in SK is that the pre-SN $\bar{\nu}_e$ has very low energy such that a large fraction of the prompt signal may not be identified by SK. The Wide-band Intelligent Trigger (WIT) [137] system handles the trigger of such low-energy events. The WIT system is a computing farm dedicated to real-time data processing. It reconstructs and selects candidate events from the tremendous low-energy background events. The selected events are passed to the pre-SN alert system for subsequent analysis. The pre-SN alert system selects candidate IBD pairs according to the reconstructed information. Two Boosted Decision Tree (BDT) cuts are applied together with rectangular cuts based on dR and dT.

5.2 The WIT System

The implementation of software trigger has enabled greater flexibility in trigger conditions, as mentioned in Section 3.3.4. The WIT system was developed and integrated in the online DAQ system in the SK IV phase. It attempts to handle events from all recorded PMT hits without applying a threshold to the minimum number of hits. The WIT can extract and reconstruct very low energy electron events (2.5 MeV) with an efficiency close to 100%.

The WIT hardware system originally consisted of 8 computers with a total of 256 hyper-threaded CPU cores. It has been continuously improved and now is a computer cluster of 20 computers with 1700 hyper-threaded CPU cores. These grants the WIT with sufficient computational power to process all of the data in the raw stream in real time.

Data are delivered to the WIT system from a dedicated "buffer" machine, referred to as the SN Data Recorder. This machine continuously monitors for a supernova neutrino burst and records all data associated with such an event. The SN Data Recorder transmits continuous data blocks of 23 ms duration, each consisting of 1344 consecutive reads of 17 μs.

Among the 20 computers, 19 of them are responsible for receiving the incoming data blocks, performing trigger decisions, and carrying out event reconstruction. The reconstructed events are subsequently transmitted to the twentieth computer, which sort the events by time because the events may arrive time scrambled. After this time sorting, the events are made available to the pre-SN subsystem. Meanwhile, they are transferred to the offline disk for physics analysis [137]. In addition to the pre-SN alert system, the WIT system also hosts an online SN burst trigger and raw data buffer, which would be preserved in case of a SN event.

5.3 Event Reduction and Reconstruction

The event reduction and reconstruction procedure of the WIT system is designed to efficiently identify low-energy electron events in SK while suppressing background from dark noise and radioactive sources.

5.3.1 Event reduction

Each PMT hit is characterized by its charge and timing information, recorded by Time-to-Digital Converter (TDC) and Analog-to-Digital Converter (ADC) modules every 23 ms within a data block. Given that approximately six Cherenkov photon hits are observed per MeV of deposited energy, an initial Pre-Trigger stage identifies

potential event candidates by searching for coincident hits within a 220 ns time window. A coincidence of at least 11 PMT hits, which corresponds to a visible energy of roughly 2 MeV, is required to exceed the dark noise level. A typical dark noise rate is 12 hits per window. This stage reduces random background activity by approximately 70%.

A second reduction stage, known as STORE (Software Triggered Online Reconstruction of Events), further refines the selection by isolating PMT hits likely originating from a common interaction vertex. For recoil electrons below 20 MeV, the track length in water is only a few centimeters. Therefore, the Cherenkov emission can be treated as a point-like light source. STORE constructs a list of temporally correlated PMT pairs that satisfy the causality condition imposed by the speed of light. From these correlations, all possible four-hit combinations are tested to estimate the vertex position that simultaneously minimizes the timing residuals among the corresponding PMTs. Candidate vertices located within the fiducial volume are then compared against the full list of selected PMT hits. The fiducial volume is defined as 2 m away from the ID wall. Vertices with insufficient spatial or temporal coincidence are rejected. This reduction stage provides an additional 30% background reduction while improving processing efficiency by discarding poorly correlated events early in the reconstruction chain. The overall trigger efficiency of the WIT system is shown in Figure 5.1, which is 100% for electrons above 4 MeV but drops quickly below this energy.. The trigger efficiency is obtained based on simulations with SK IV conditions but still valid in later phases.

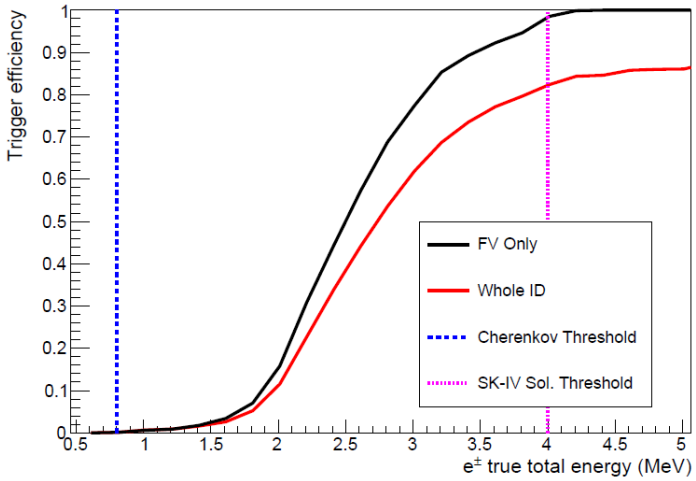

Figure 5.1: WIT efficiency as a function of true total electron energy, obtained from MC simulation. Taken from [138].

5.3.2 Vertex reconstruction

Events that pass STORE selection are subsequently processed by a fast vertex reconstruction algorithm, Clusfit [32], which refines the event topology by excluding

isolated or spurious hits arising from dark noise, scattered light, or reflected light. If the reconstructed vertex from Clusfit lies within the fiducial volume, a more detailed likelihood-based vertex fit, BONSAI (Branch Optimization Navigating Successive Annealing Iterations), is applied to all PMT hits within or near the 220 ns time window. BONSAI maximizes a likelihood function that accounts for both signal and background timing residuals to determine the best-fit event vertex. The timing residual is defined as:

$$T_{residual} = T_{hit} - T_{flight} - T_{vertex}, \tag{5.1}$$

where T_{hit} is the PMT hit time, T_{flight} is the time of flight for light travelling from the testing vertex to the hit PMT, and T_{vertex} is the time of the testing vertex. The hypothesis that maximizes the likelihood is adopted as the reconstructed vertex. The vertex resolution as a function of true total electron energy is shown in Figure 5.2. BONSAI also exports a goodness-of-fit to evaluate the quality of the fit.

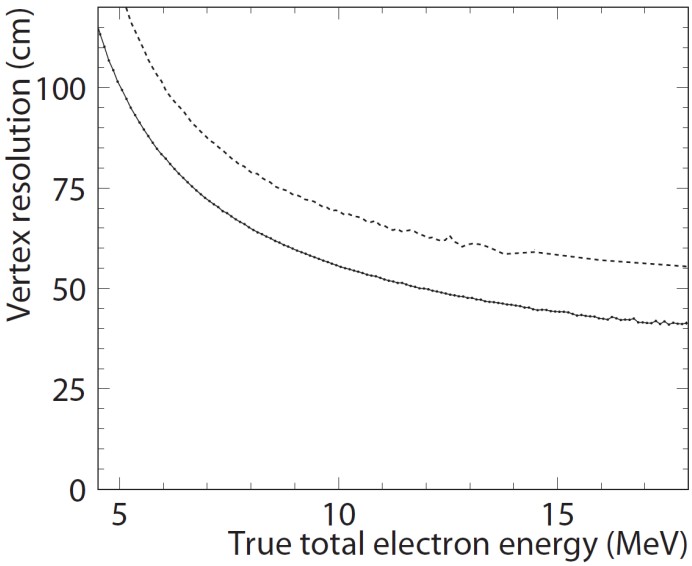

Figure 5.2: Vertex resolution for low-energy events as a function of true total electron energy for SK III (solid) and SK I (dashed). Taken from [139].

5.3.3 Direction reconstruction

A comprehensive description of direction reconstruction for low-energy events in SK is found in [139]. SK uses an energy dependent likelihood to compare the opening angle between data and MC. The opening angle is defined as the angle between the reconstructed direction and the direction from vertex to the hit PMT. Figure 5.3 shows the likelihood as a function of the reconstructed electron energy and the opening angle. The direction of the event that maximizes the likelihood is chosen as the best-fit direction. The performance of direction reconstruction is shown in Figure 5.4.

After that, a circular Kolmogorov-Smirnov test on the azimuthal symmetry of the

Cherenkov cone around the reconstructed direction is applied [140]. The result of this test is referred to as "dirks". A low dirks value indicates a mis-reconstructed vertex. This quantity is used to reject the low-energy background from radioactivity in the PMT material as these background events are too close to the PMTs to produce a good fit.

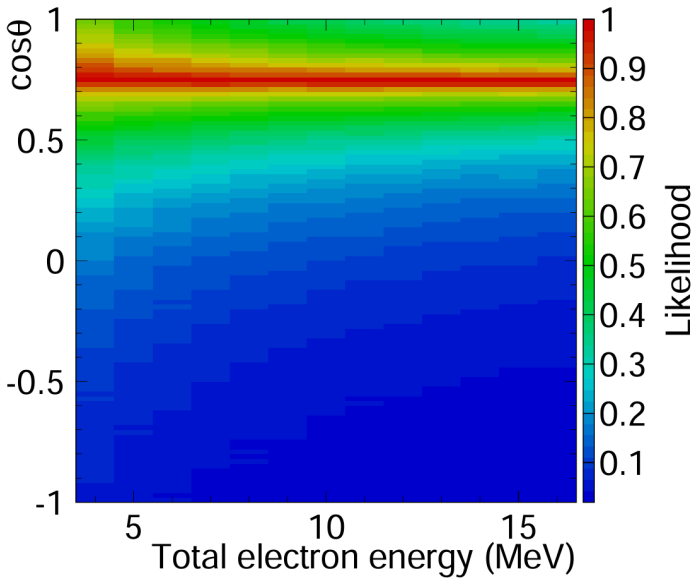

Figure 5.3: Likelihood value for direction reconstruction as a function of total electron energy and opening angle between the reconstructed direction and the direction from vertex to each hit PMT. Taken from [139].

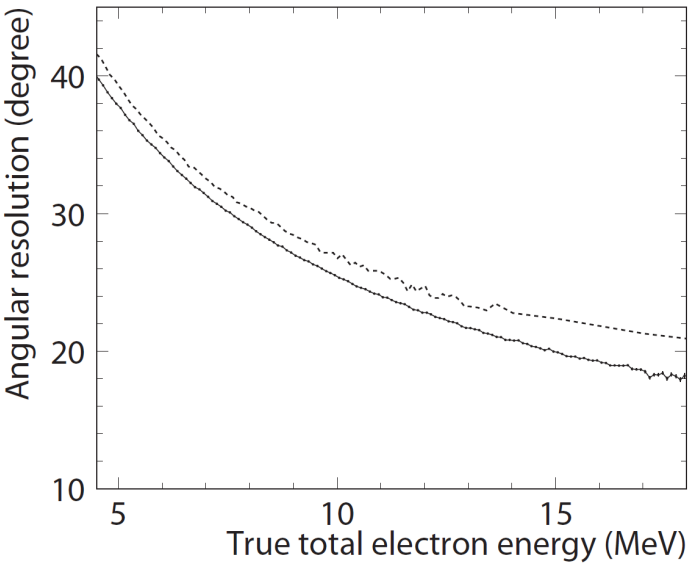

Figure 5.4: Angular resolution for low-energy events as a function of true total electron energy for SK III (solid) and SK I (dashed). Taken from [139].

5.3.4 Energy reconstruction

The energy reconstruction is also well documented in [139]. The energy reconstruction is based on the number of hits within a 50 ns of residual time window, N_{50}. Corrections are applied to N_{50} to obtain a less position-dependent quantity, an effective hit sum N_{eff} which is given by

$$N_{eff} = \sum_{i}^{N_{50}} (X_i + \epsilon_{tail} - \epsilon_{dark}) \frac{N_{all} G_i(t) e^{\frac{r_i}{\lambda(t)}}}{S(\theta_i, \phi_i) N_{alive}}. \tag{5.2}$$

where the correction terms are: PMT occupancy X_i, late hits ϵ_{tail}, dark noise ϵ_{dark}, fraction of good PMTs N_{alive}/N_{all}, direction-dependent photo-cathode coverage $\frac{1}{S(\theta_i,\phi_i)}$, water transparency $e^{\frac{r_i}{\lambda(t)}}$, and relative quantum efficiency of a PMT $G_i(t)$. The total reconstructed energy is calculated from N_{eff} based on calibration data, including the LINAC electron beam, the ^{16}N gamma source, and spallation events. MC simulations are tuned to reproduce these calibration data, ensuring consistency across the detector volume. Figure 5.5 shows the energy resolution as a function of electron energy.

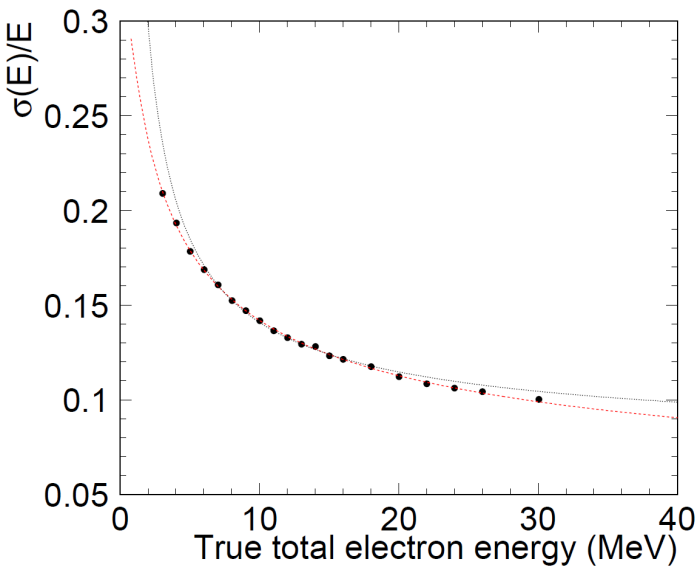

Figure 5.5: Energy resolution from MC simulation (black dots). The data points are fit to a polynomial function to obtain an energy resolution function for SK III (red dashed line). The energy resolution function for SK I (black dotted line) is also shown. Taken from [139].

5.4 Event Simulation in SK

In order to simulate the IBD events, γ-rays vectors are generated externally to the SK simulation software SKDETSIM. Two different γ-ray emission models are considered: the generic liquid scintillator simulator GLG4SIM, developed by the Chooz experiment [141] and a second model created at the Japan Proton Accelerator Research

Complex (J-PARC) after measurements of γ-ray properties with an array of germanium detectors in the Accurate Neutron-Nucleus Reaction Measurement Instrument (ANNRI) at the facility [142]. These two models were included to estimate systematic uncertainties for the pre-SN neutrino sensitivity results in SK. However, we found that the two models are very similar to each other, producing tiny systematic uncertainties. The sensitivity results shown in this thesis are based on GLG4SIM.

To simulate the IBD coincidence events, the simulated γ-ray events from the neutron captured by Gadolinium were combined with simulated positrons in SKDETSIM. These coincidence events were simulated in different positions in the inner detector, with positrons with energies between 0.8 MeV and 7 MeV.

5.5 Background sources in SK

The major backgrounds for the pre-SN neutrino search in SK are:

- Accidental coincidences,

  which are from radioactive decays, dark noise and uncorrelated events that are close in time and distance purely by chance.

- Radioactive Contamination,

  which are from radioactive impurities induced the Gadolinium loading, contributing to backgrounds from (α, n) and spontaneous fission processes.

- Reactor and geoneutrinos,

  which are electron antineutrinos in the same energy region as pre-SN neutrinos.

- Spallation,

  which are induced by cosmic-ray muons.

Radioactive contaminants such as ^{235}U and ^{238}U that came along with the Gd loading can produce background via different processes. ^{235}U chain isotopes can emit α, contributing to the backgrounds from ^{18}O(α,n)^{21}Ne* and ^{17}O(α,n)^{20}Ne* processes. The decay of Neon isotopes produces pairs of neutrons and the signal of one of the neutrons can be mistaken for a positron, becoming a background for coincidence events. Moreover, the spontaneous fission of ^{238}U can emit neutrons that mimic delayed signals or even IBD candidates.

Cosmic-ray muon induced spallation can create unstable daughter nuclei, which can produce β-delayed neutrons (neutrons associated with the beta decay of the fission products). In particular, electron energy from the decay of ^{17}N is in the same energy

region as pre-SN neutrinos. However, they are expected to have a tiny contribution since its resulting background rate is low, and are effectively removed using BDTs.

The dominant background for pre-SN neutrinos is the reactor neutrinos coming from nearby nuclear reactors. They are irreducible background because they are the same particles as pre-SN $\bar{\nu}_e$s, and are in the same energy range. The reactor neutrino background has a strong dependence on the operation situation of the nuclear reactor around the Kamioka mine. Previously, SK estimated the reactor and geoneutrino flux using data from the `geoneutrinos.org` web application [143]. However, for the reasons that some reactors around SK are ready to return to operation, and that we do not have real-time access to the operation situation of the reactors, we choose to measure the total background rate over a 30-day time window and update the measurement frequently to accommodate possible changes in the reactor neutrino flux. This way we also avoid the cumbersome treatment to the correlation between background in SK and KamLAND in the combined pre-SN alert system, as we are measuring the total background rate independently. Details of background treatment will be discussed in Section 7.1.1.

5.6 Event selection in SK

The event selection strategy for pre-SN neutrino detection in SK is summarized below. A more comprehensive description can be found in [106]. Some updates have been made to the selection with the start of the second phase of SK-Gd with 0.03% Gd.

The pre-SN alert system receives reconstructed single events from WIT, for a coincidence trigger is not implemented in WIT. The prompt and delayed parts of the IBD event are reconstructed independently in WIT.

5.6.1 Cut-based selection

The initial search of IBD events utilizes the following reconstructed quantities:

- $n18$: the number of hits within $-6 < T_{residual} < 18\,\text{ns}$,
- bx, by, bz: BONSAI reconstructed vertex position,
- bt: BONSAI reconstructed vertex time,
- $bgoodness$: BONSAI goodness of reconstruction.

First, a fiducial volume cut requiring the reconstructed vertices at least 2 m away from the ID wall is applied. Then, the coincidence search loops over all single events. At this stage, any single event from WIT can be a prompt candidate or a delayed

candidate. For single event with trigger clock C, any other events with trigger clock between $C-1$ and $C+12$ are considered as delayed candidates. This corresponds to a time window of $-17 < dT < 290\,\mu$s.

A delayed candidate must fulfill the following criteria:

- $n18 \geq 26$,
- $effwall \geq 800\,\text{cm}$,

  where $effwall$ is the distance from the reconstructed vertex to the ID wall along the reconstructed direction.

If a delayed candidate is found, then the coincidence distance dR and coincidence time dT for this prompt-delayed pair candidate is calculated. The computation of dT is refined by adding the difference of the trigger clocks times the trigger clock increment ($1.707 \times 10^4\,\text{ns}$) and the reconstructed event time.

Pairs of events with $dR < 3\,\text{m}$ and $0 < dT < 300\,\mu$s are stored, if there is exactly one delayed candidate. In addition, a BDT using reconstructed variables ($n18, bx, by, bz, bt, bgoodness$) available online is implemented to boost the selection process and to improve the detection sensitivity, as will be discussed in Section 5.6.2. The distributions of these reconstructed variables before and after the initial search cuts are shown in Figure 5.6.

In this analysis, the neutrons are assumed to capture at the same vertex as the prompt signal. This is a reasonable assumption because the neutrons travel a much shorter distance ($\mathcal{O}(10)\,\text{cm}$) than the position reconstruction resolution ($\mathcal{O}(100)\,\text{cm}$) at low energies. Therefore, the coincidence distance dR for signal events is dominated by the vertex reconstruction resolution. On the other hand, accidental background events are coincidences of single low-energy events that occurred purely by chance. Their dR mainly depends on the distribution of low-energy events in the ID. The true IBD events and accidental background events have distinct dR distributions, as shown in Figure 5.7.

The IBD events and accidental background events also have very different coincidence time distributions. For accidental background events, the dT distribution is a nearly flat distribution. For true IBD events, the time difference mainly comes from the time for neutrons to thermalise and capture. The simulated dT distributions for true IBD events and accidental background events are shown in Figure 5.8.

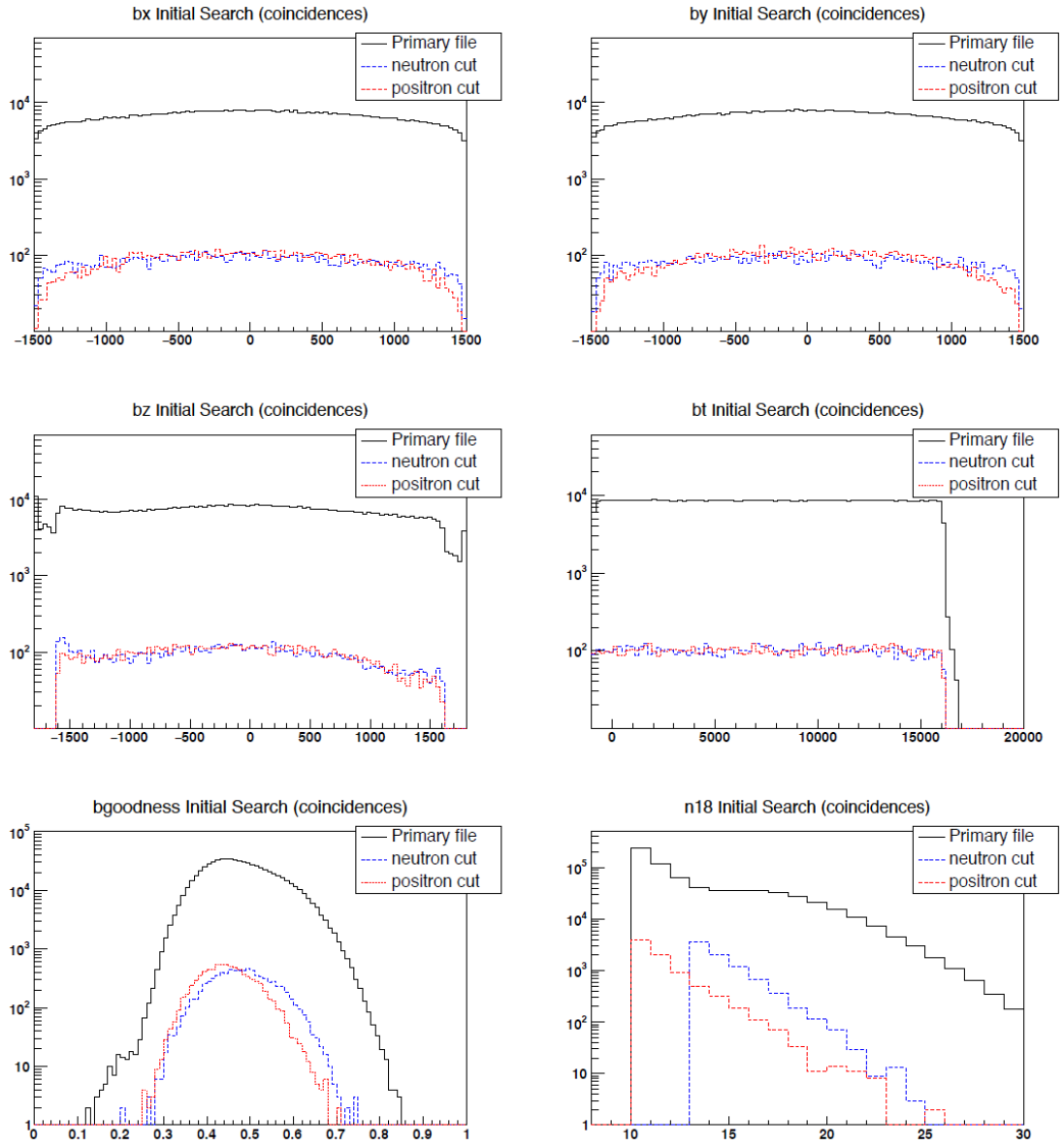

Figure 5.6: Reconstructed variables available through BONSAI online reconstruction ($n18, bx, by, bz, bt, bgoodness$). Black solid lines show the distributions before cut. Red dashed lines and blue dashed lines shows the distributions after the initial search cut for prompt and delayed candidates respectively. Taken from [144].

5.6.2 Multivariate selection

The event selection of pre-SN uses both cut-based method and Boosted Decision Tree (BDT). Although the cut-based selection remains an important process in the event selection, it is not sufficient to remove the backgrounds. This motivates the implementation of a more sophisticated and efficient method using multiple variables. BDT is one of the candidates. Among many multivariate selection methods including Fisher's linear discriminant and artificial neural networks, BDTs show advantages in their robustness to overtraining, straightforward hyperparameter optimization, and interpretability. Therefore, we adopted BDT in for pre-SN neutrino selection in SK.

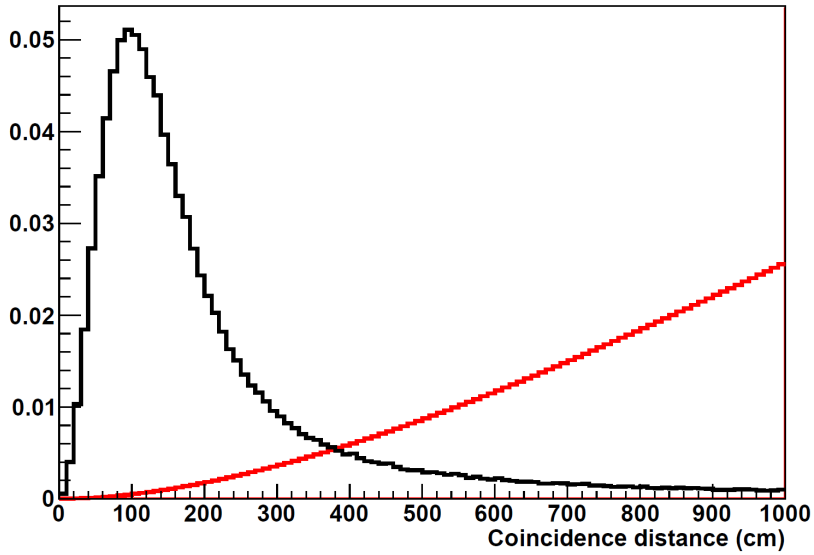

Figure 5.7: Distributions of coincidence distance dR for simulated IBD events (black) and accidental background events (red), normalized by area. Taken from [138].

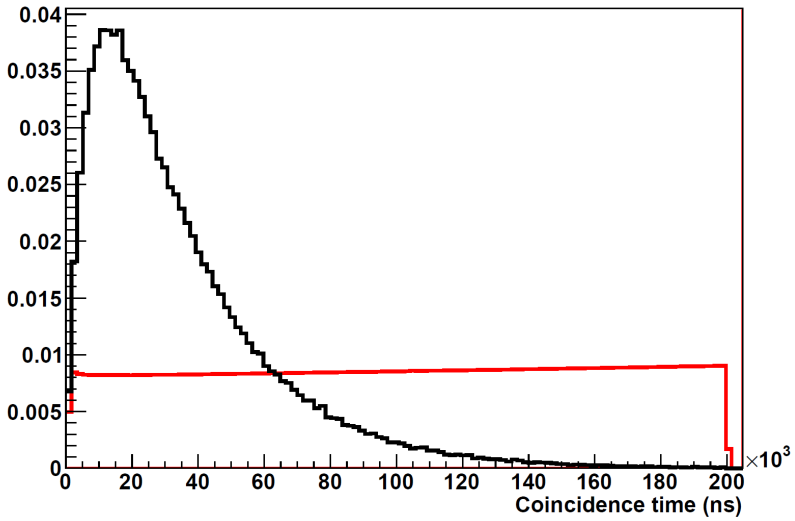

Figure 5.8: Distributions of coincidence time dT for simulated IBD events (black) and accidental background events (red), normalized by area. Taken from [138].

A BDT is a supervised machine learning algorithm widely used in experimental particle physics for classification and regression tasks, such as signal–background discrimination and event reconstruction [145, 146]. The method combines multiple individual decision trees into a strong ensemble model through an iterative training process known as boosting.

In a decision tree, the data are successively split according to optimized threshold values of input variables to maximize a separation criterion, e.g. the Gini coefficient. Each terminal node, or leaf, represents a classification outcome. While a single tree often has limited predictive power and high variance, boosting reduces both bias and variance by sequentially reweighting misclassified events and training subsequent trees

to focus on the difficult cases. The final output of the BDT is a weighted sum of the responses from all trees, providing a continuous discriminant variable that reflects the likelihood of an event being signal-like or background-like. Hyperparameters such as the number of trees, boost rate, and maximum depth control the performance and generalization capability of the model.

In this analysis, we employed the Toolkit for Multivariate Analysis (TMVA) [147] in the ROOT software to train BDTs. Signal MC events are produced using the GLG4SIM model and SKDETSIM as mentioned in Section 5.4. Background samples are taken from the SK-Gd data. The ratio of signal count over background count is roughly 1/2 for the training.

Figure 5.9 presents the performance comparison between BDT, Fisher's linear discriminant, and the cut-based selection. The comparison is performed by evaluating area under the plot of background rejection efficiency against the signal selection efficiency. The boundary of the area is known as the Response Operator Characteristic (ROC) curve. BDT has higher efficiency compared to the other two methods for the pre-SN neutrino selection.

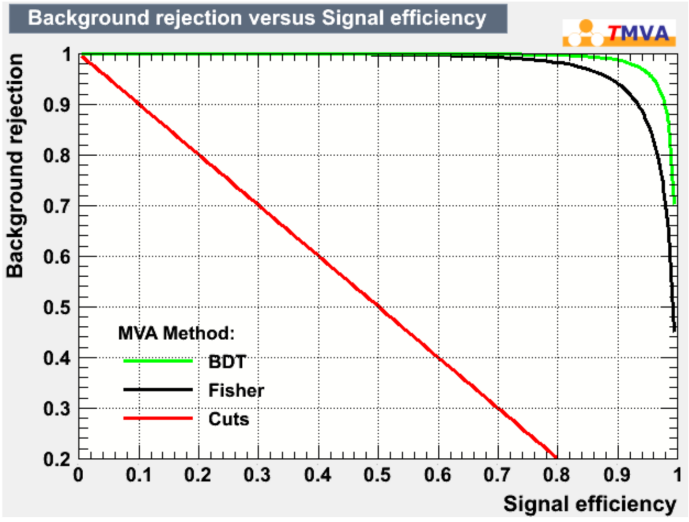

Figure 5.9: Response Operator Characteristic curves for different selection methods on simulated pre-SN neutrinos and background. Taken from [144].

SK adopted two BDTs for pre-SN neutrino selection, taking into account both the processing speed and the selection efficiency. Since we aim to build a pre-SN alert system for early warnings of CCSNs, it is required to process data as fast as possible. For this matter, a BDT_{online} is developed.

The BDT_{online} uses the following reconstructed variables: $n18, bx, by, bz, bt, bgoodness$, all of which are available directly from the WIT system. It is trained using the AdaBoost algorithm [147]. Different values of hyperparameters were tested in the BDT

training to find the best overall performance. In particular, the number of trees and the boosting rate have significant impacts on the performance of the BDT.

While the BDT_{online} is employed to promptly reduce the background events, a more precise, but slower BDT is implemented for the final selection. This BDT uses offline reconstructed variables, thus is referred to as $\mathrm{BDT}_{offline}$. The inputs for $\mathrm{BDT}_{offline}$ include angular distribution of hits, reconstructed energy and quality, and distance from events to the detector wall. The $\mathrm{BDT}_{offline}$ is also trained using the AdaBoost algorithm and optimized by varying the hyperparameters. Details of the training can be found in [138]. Figure 5.10 shows the signal and background separation for both BDTs.

5.6.3 Event selection summary

The system runs the event selection in real time using a cut-based selection method and two BDTs (BDT_{online} and $\mathrm{BDT}_{offline}$) More details can be found in [106]. For the current SK-Gd phase with 0.03% Gd, cuts for the final selection are: $\mathrm{BDT}_{\mathrm{online}} > 0.2$, $dR < 300$ cm, $dT < 80$ μs, and $\mathrm{BDT}_{\mathrm{offline}} > -0.1$. Figure 5.11 shows the efficiency of applying the selection criteria to 10^7 IBD pairs. The irreducible background rate is approximately 0.5 event/hour. Table 5.1 provides the estimated time between DAQ and a decision by the pre-SN alert system.

Table 5.1: Estimated latency time of each step in the pre-SN alert system and update frequency, updated from [106]. Total latency time is the sum of the latency of each step.

Process	**Estimated Time**
Data Fitting (WIT system)	10 seconds
Data organizing (WIT system)	4 minutes
Process Queue ($\sim 2 \times 10^6$ events)	2 minutes
Alert Decision/Export Results	Performed every 5 minutes

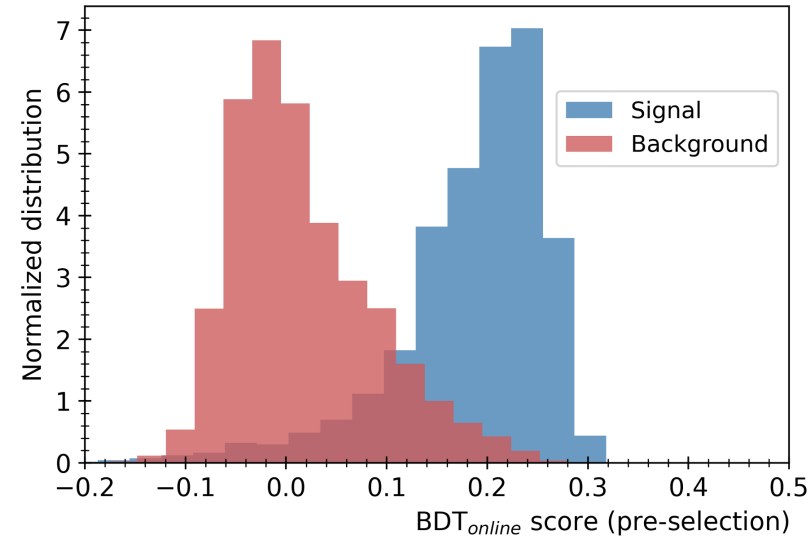

(a)

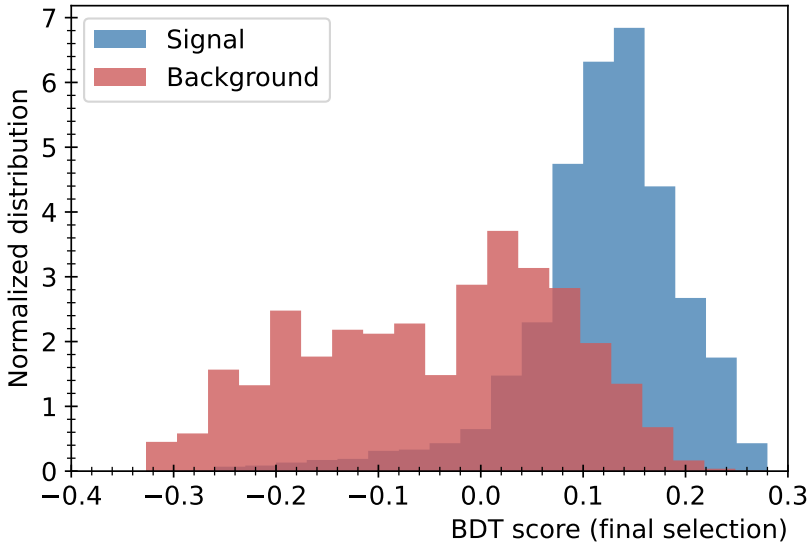

(b)

Figure 5.10: Signal background separation for the two Boosted Decision Tree classifiers used for (a) pre-selection (BDT$_{online}$) and (b) final selection (BDT$_{offline}$).

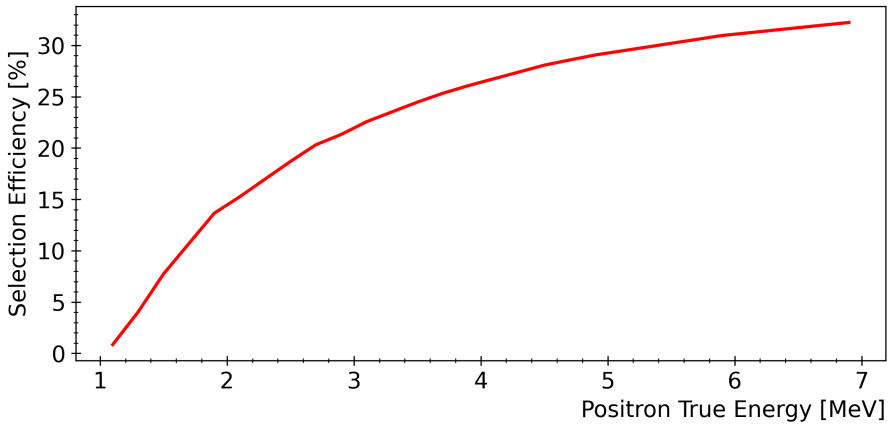

Figure 5.11: Evaluation of the efficiency of selection after the application of cut criteria to 10^7 IBD pairs as a function of positron true total energy for SK.

Chapter 6

Pre-supernova Neutrino Detection in KamLAND

6.1 The KamLAND detector

Kamioka Liquid-scintillator Anti-Neutrino Detector (KamLAND) is a large-scale underground scintillator detector in the Kamioka mine in Gifu prefecture, Japan, roughly the same place as SK. The 1000 m of rock overburden covering the detector sufficiently reduces cosmic-ray muon flux to 10^{-5} of that on the surface, significantly lowering the background rate induced by cosmic-ray muons. Its data taking started in March 2002. Since 2011, KamLAND started a search of neutrinoless double-beta decay and became the KamLAND Zero-Neutrino Double-Beta Decay (KamLAND-Zen) experiment [148]. A schematic view of the KamLAND-Zen experiment is shown in Figure 6.1.

KamLAND was originally designed to study reactor neutrinos, geoneutrinos, and low-energy solar neutrinos. The primary target volume consists of 1 kton of ultrapure LS contained in a 13 m diameter spherical balloon made of 135 μm-thick transparent nylon ethylene vinyl alcohol copolymer (EVOH) composite film. The components of the KamLAND LS are 80% dodecane and 20% pseudocumene (1,2,4-trimethylbenzene) with 1.36 g/L of the fluor PPO (2,5-diphenyloxazole). An array of 1,325 17-inch photomultiplier tubes (PMTs) and 554 20-inch PMTs mounted on the inner surface of an 18 m diameter stainless steel sphere is used to detect the scintillation light from events occurring within the balloon. The 13 m diameter LS containing balloon is positioned at the center of the stainless steel sphere, supported and constrained by a net of Kevlar ropes. Non-scintillating mineral oil fills the space between the balloon and the inner surface of the sphere, balancing gravity and buoyancy of the balloon. Meanwhile, the mineral oil acts as a buffer layer against radioactivity from

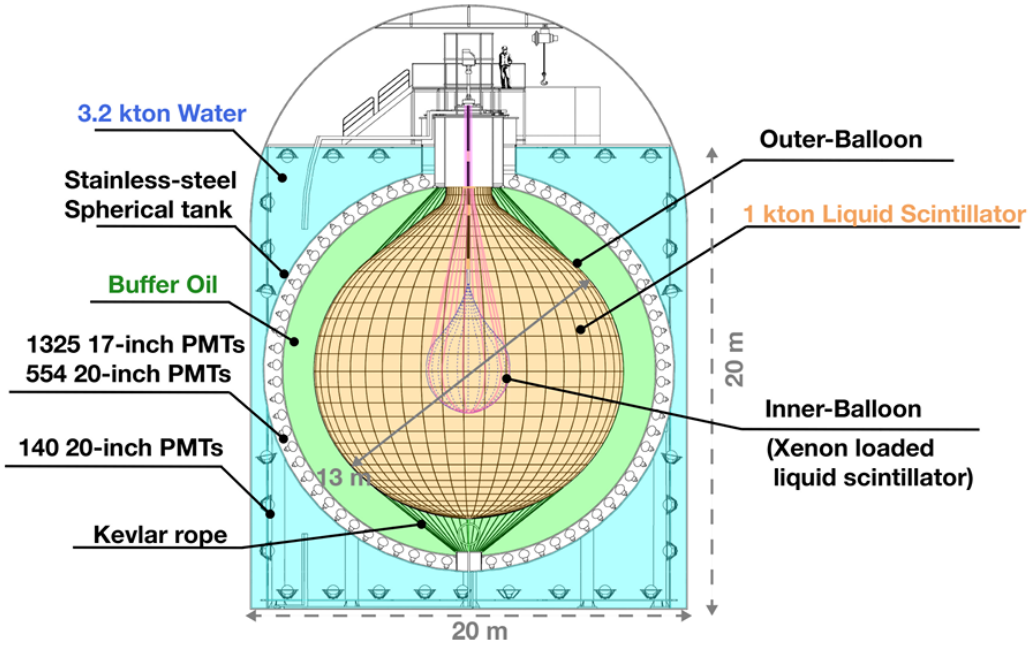

Figure 6.1: A schematic view of the KamLAND detector after installation of the inner balloon. Taken from [149].

the PMTs and the stainless steel sphere. What contained the stainless steel sphere is called the inner detector.

These above structures all surrounded by a 3.2 kton water Cherenkov detector equipped with 140 20-inch PMTs, contained in a resin-coated cylindrical rock cavern. This part is called the outer detector, which plays a role of cosmic-ray muon veto. Cosmic-ray muons passing through the outer detector produce Cherenkov lights and are tagged by the PMTs. Detailed information of the detector is given in [150].

In 2011, an inner balloon of 1.54 m radius containing Xe-loaded liquid scintillator (Xe-LS) was installed in the center of the main balloon as a part of the KamLAND-Zen experiment. The inner balloon was updated to have a 1.92 m radius to house double the amount of Xe-LS in 2018 [151]. The center region is not used for the $\bar{\nu}_e$ analysis because of backgrounds from the inner balloon and its support materials.

Pre-SN $\bar{\nu}_e$ are expected to be detected through IBD processes, which is the main interaction channel for these neutrinos in KamLAND. Positrons produced in the process lose their kinetic energy within the LS medium and annihilate with electrons, emitting two 511-keV γ rays (prompt events). Neutrons, with a mean lifetime of $207.5 \pm 2.8\,\mu$s, are captured by protons, releasing 2.2 MeV γ rays (delayed events). The energy threshold for IBD processes is 1.8 MeV. By using the time and spatial correlation between the prompt and the delayed events, we achieve low-background conditions in the detection of $\bar{\nu}_e$.

6.2 Event Reconstruction in KamLAND

The energy and vertex of an event can be reconstructed using the timing and charge distributions of scintillation photons recorded by the PMTs. The PMT hit data are collected by the data acquisition system as digitized waveform data. Waveform analysis is applied to extract PMT hit time and charge. First, the waveform data are scanned to find the peak position with a 1.49 ns step, which corresponds to the TTS of 17-inch PMTs. Since each PMT channel has a different offset, the first 50 sampling points of a run are used to estimate the pedestal. After pedestal subtraction and removal of high-frequency noise, the first photon arrival time is obtained from a leading-edge fit of the first waveform peak, while the integrated charge provides a measure of total light intensity. PMT charge and timing responses are corrected for gain variations, cable attenuation, and channel-dependent offsets.

6.2.1 Muon track reconstruction

Although rock above the detector has significantly reduced the cosmic-ray muon flux at KamLAND, there are still remainder arriving at a rate of 0.3 Hz. These muons can result in unstable isotopes in the detector, causing background events. Therefore, cosmic-ray muons must be tagged and removed.

Cosmic-ray muon events are identified by their large light yield in the inner detector and characteristic signals in the outer detector. Muon tracks are reconstructed using PMT hit timing information based on a geometrical model that exploits the coincidence of the earliest scintillation photons with the Cherenkov photon trajectory. The track parameters are optimized to reproduce the observed time distribution of hits. The reconstruction effectively separates muons traversing the LS from those crossing only the surrounding mineral oil layer, with a mis-reconstruction fraction of approximately 0.2%. The correlation between reconstructed impact parameters and total charge demonstrates consistency between track geometry and light yield.

6.2.2 Point-like event reconstruction

Low-energy events only travel a short distance in the detector. Therefore, these events are treated as point-like events. Event vertices are reconstructed using the timing information of PMT hits recorded in the inner detector. For an event that occurs at position (x, y, z), the observed hit time T_i^{hit} in a PMT channel i can be expressed as

$$t_i = T_i^{\text{hit}} - T_i^{\text{flight}}(x, y, z), \tag{6.1}$$

where t_i represents the photon emission time and $T_i^{\text{flight}}(x, y, z)$ denotes the photon time-of-flight from the vertex to the PMT. The latter is approximated as

$$T_i^{\text{flight}}(x, y, z) = \frac{\sqrt{(x - x_i)^2 + (y - y_i)^2 + (z - z_i)^2}}{c/n_{\text{eff}}}, \tag{6.2}$$

where c is the speed of light in vacuum and n_{eff} is an effective refractive index representing the average photon propagation velocity in the scintillator, including effects of scattering, absorption, and re-emission.

The vertex position (x, y, z) is determined by minimizing the dispersion of the reconstructed emission times $\{t_i\}$ over all PMT hits. The optimization proceeds by iterating trial vertex positions and selecting the one that minimizes the timing spread. However, the intrinsic temporal characteristics of the liquid scintillator, including delayed photon emission (decay constants of 10–100 ns) and re-emission effects (effective time constants up to 50 ns), cause the emission time distribution to be broadened.

The visible energy of an event, E_{vis}, is reconstructed from the total calibrated PMT charge after applying corrections for detector response and optical effects. The visible energy is defined such that the 2.22 MeV gamma ray from neutron capture on a proton corresponds to a visible energy of 2.22 MeV. The relationship between the observed and expected charge is expressed as

$$E_{\text{vis}} = E_0 \frac{\sum_i \left(Q_i^{\text{obs}} - Q_{\text{dark}}\right)}{\sum_i Q_i^{\text{exp}}}, \tag{6.3}$$

where Q_i^{obs} is the measured charge at PMT i, Q_{dark} accounts for the contribution of dark hits estimated from single-PMT rates, and E_0 is a normalization factor.

The expected charge Q_i^{exp} is calculated from the reconstructed vertex position while considering photon propagation effects,

$$Q_i^{\text{exp}} = \frac{e^{-L_i/\lambda}}{4\pi L_i^2}\, \eta_i\, \xi_i\, \cos\theta_i, \tag{6.4}$$

where L_i is the distance between the vertex and the PMT, λ is the light attenuation length in the LS, η_i represents the geometrical shadowing correction from the detector structure, ξ_i accounts for the discriminator threshold efficiency of each FEE channel, and θ_i is the incident angle of photons on the PMT surface.

The reconstruction algorithms are calibrated with radioactive sources deployed from the top of the detector [152, 153]. Using these calibration sources, the energy resolution is estimated to be $6.4\%/\sqrt{E_{\text{rec}}(\text{MeV})}$ and the vertex resolution is estimated to be $12\,\text{cm}/\sqrt{E_{\text{rec}}(\text{MeV})}$, respectively, where E_{rec} is reconstructed energy.

The detection threshold for $E_{\rm rec}$ in KamLAND is as low as 0.9 MeV. The nonlinear and particle-dependent effects of the conversion between deposited (real) energy and $E_{\rm rec}$ are also calibrated with the Birk's formula [154] and contribution of Cherenkov emission.

6.3 Event selection in KamLAND

KamLAND performs muon veto prior to selecting prompt-delayed pairs (delayed coincidence method) as neutrino events. Cosmic-ray muons produce events with bright scintillation light and multiple spallation products, including neutrons. This makes it challenging to reconstruct the correct vertex and energy of low-energy events and to select prompt-delayed pairs immediately following the muon event. Thus, all events within 2 ms of the arrival time of muons are vetoed. However, the 2-ms veto is not enough for high energy muons which make cascade showers in the detector. Such muons generate a non-negligible amount of long-lived spallation products such as ^{9}Li, which has a lifetime of 257.2 ms. Therefore, KamLAND performs a 2-s whole-volume veto for high energy muons [155]. Alternatively, a cylindrical cut along the trajectory is applied when the reconstruction quality is good. These three muon veto are determined by the total observed charge, the residual charge, which means the difference between the observed charge minus the charge that would be expected if the muon simply penetrated the detector, and the quality of muon event reconstruction.

After applying the muon veto, KamLAND applies the following criteria:

1. reconstructed prompt energy: $0.9 < E_p\,(\mathrm{MeV}) < 4.0$;
2. reconstructed delayed energy: $1.8 < E_d\,(\mathrm{MeV}) < 2.6$ (capture on proton), or $4.4 < E_d\,(\mathrm{MeV}) < 5.6$ (capture on ^{12}C);
3. spatial correlation between the prompt and delayed events: $\Delta R < 200$ cm;
4. time difference between prompt and delayed events: $0.5 < \Delta T\,(\mu\mathrm{s}) < 1000$;
5. fiducial volume (FV) radii: $R_p, R_d < 600$ cm;
6. inner balloon cut: $R_d < 2.5$ m and $\sqrt{x_d^2 + y_d^2} < 2.5$ m for $z_d > 0$ m, where (x_d, y_d, z_d) is the reconstructed delayed vertex.

Note, the reconstructed prompt energy (E_p) is the sum of the positron kinetic energy and annihilation γ energies with the quenching effect.

Although the delayed coincidence method strongly suppresses accidental background events, KamLAND performs an additional likelihood-based selection to differentiate $\bar{\nu}_e$ from accidental backgrounds, which become more likely at lower energies

and as the vertices are reconstructed closer to the balloon edge [156].

The total selection efficiency is calculated using a GEANT4 Monte-Carlo simulation. A total of 10^7 $\bar{\nu}_e$ events are generated uniformly in the 750 cm radius volume for each prompt energy bin, and the delayed-coincidence selection with the likelihood selection are applied. The selection efficiency is calculated as the ratio of the number of surviving events after the selection to the number of events generated within the 600 cm FV, shown in Figure 6.2. The efficiency at low energies mirrors the spectrum of the accidental background because of the likelihood-based selection. At high energies, it remains nearly constant. The efficiency loss is dominated by the inner balloon cut. Without this cut, the efficiency is higher, ∼90% above 4 MeV. The muon veto has an additional effect of reducing the analysis time. The residual analysis time after this reduction is defined as the livetime. The KamLAND data are divided into runs. The average lifetime ratio in any single run is approximately 0.903.

In the following, we estimate the latency of the KamLAND pre-SN alert due to data processing. All PMT waveforms undergo digitization through front-end electronics and are collected by the Data Acquisition (DAQ) software. Event energy and vertex are reconstructed from these waveforms and are collected as a single file, each covering approximately 6 minutes of data. It takes 300–900 s, on average 700 s, from the time of the last event in the file to the end of the reconstruction. The latency is 800–1200 s, on average 1120 s, when we consider the first event in the file. The latency strongly depends on the status of other processes. The pre-SN monitoring process is scheduled to run at 5 minute intervals. Upon the identification of a new file, the process applies the selection criteria described above to detect neutrino events. Additionally, the process counts the number of events that passed the selection criteria within the past 24 hours for pre-SN analysis.

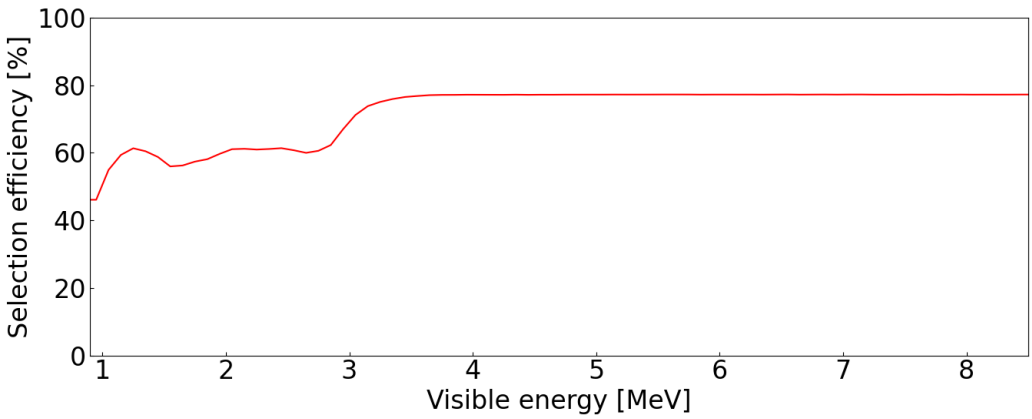

Figure 6.2: The total IBD selection efficiency in KamLAND [157].

6.4 Background sources in KamLAND

The backgrounds for pre-SN neutrinos interacting via IBD can be categorized into two types. One type includes non-neutrino events, such as $^{13}\mathrm{C}(\alpha, n)^{16}\mathrm{O}$ reactions and accidental prompt and delayed coincidences. The other type is neutrino backgrounds, including reactor and geoneutrinos.

Reactor $\bar{\nu}_e$ is the dominant background for pre-SN neutrino search in KamLAND, similar to the situation in SK. The reactor background estimation will be discussed in Section 7.1.1. Geoneutrinos, generated by beta decays of nuclear isotopes such as $^{238}\mathrm{U}$ and $^{232}\mathrm{Th}$ in the Earth, constitute a background as their energies can be up to 3.27 MeV. The expected geoneutrino event rate in KamLAND is 0.030 /day.

In the early stages, KamLAND suffered from fake prompt-delayed pairs, which are $^{13}\mathrm{C}(\alpha, n)^{16}\mathrm{O}$ generated from α-decay of $^{210}\mathrm{Po}$ in the LS [158]. However, this $^{13}\mathrm{C}(\alpha, n)^{16}\mathrm{O}$ reaction was substantially reduced during two distillation campaigns in 2007 and 2008. Currently, the rate of $^{13}\mathrm{C}(\alpha, n)^{16}\mathrm{O}$ events is 0.003 /day. The accidental background is effectively suppressed by the likelihood selection. The accidental event rate is 0.015 /day.

Chapter 7

Combined Pre-supernova Neutrino Alert System

7.1 Combined Pre-supernova Neutrino Alert System

We developed a combined pre-SN alert system to provide a real-time result of an online search of pre-SN neutrino signals. The system integrates global experimental data to search for data excess of pre-SN neutrino candidate events. It now hosts two neutrino detectors, SK and KamLAND. Introductions to the detectors are given in Chapter 5 and Chapter 6. In the following, we introduce how pre-SN neutrino signals are sought for in a pre-SN neutrino sensitive detector and explain the method of the combined search and our treatment to the *Look-elsewhere Effects*.

7.1.1 Background assumptions

The background rates in KamLAND and SK can be largely affected by the nuclear reactors near the Kamioka mine. Reactor $\bar{\nu}_e$ are mainly generated through the beta decays of the fission products of ^{235}U, ^{238}U, ^{239}Pu and ^{241}Pu in nuclear reactors. The Great East Japan Earthquake of 2011 caused numerous reactors in Japan to be shut down, and they have been gradually restarting since 2015. A constant monitoring of the situation in Japan's nuclear power plants is being conducted, and backgrounds are being updated. Nonetheless, it is difficult to predict when and which reactors will start operation in the future. Therefore, we assume for the sensitivity study different reactor background conditions according to three scenarios: low, medium and high reactor activities. The low reactor activity scenario assumes that all reactors in Japan are not in operation. For the medium reactor activity scenario, reactors near the Kamioka mine (Mihama 3 unit, Ohi $3, 4$ units and Takahama $1, 2, 3, 4$ units) are assumed to

be operating with a 100% load factor. We note this is close to the situation as of the winter of 2023-2024. The high reactor activity scenario assumes the amount of reactor neutrinos is doubled compared to the medium reactor activity scenario.

Figure 7.1 shows the expected reactor fluxes at the Kamioka mine considering these three reactor scenarios, as well as the expected geoneutrino fluxes. The fluxes are calculated based on the $\bar{\nu}_e$ spectra per fission from [159, 160, 161], with relative fission yields (^{235}U,^{238}U,^{239}Pu,^{241}Pu) assumed be (0.570,0.078,0.295,0.057) [49]. The values of neutrino oscillation parameters are $\Delta m^2_{21} = 7.53 \times 10^{-5}\,\mathrm{eV}^2$, $\tan^2\theta_{12} = 0.436$, and $\sin^2\theta_{13} = 0.023$. The thermal power of each reactor is estimated from publicly available data on reactor electric power. In the low reactor activity scenario, where all reactors in Japan are assumed to be off, the only contribution we consider comes from reactors in Korea. In addition to the reactor neutrino fluxes, we also plot the geoneutrino flux at the Kamioka mine for comparison. The geoneutrino flux is calculated based on the model in [162]. For $\bar{\nu}_e$ energy below 2.2 MeV, the geoneutrino flux is comparable to the reactor neutrino flux under the high reactor activity assumption. It decreases rapidly at ∼2.2 MeV, and is roughly the same as the reactor neutrino flux assuming low reactor activity between 2.2 MeV and 3 MeV. Above 3 MeV, the geoneutrino flux becomes negligible.

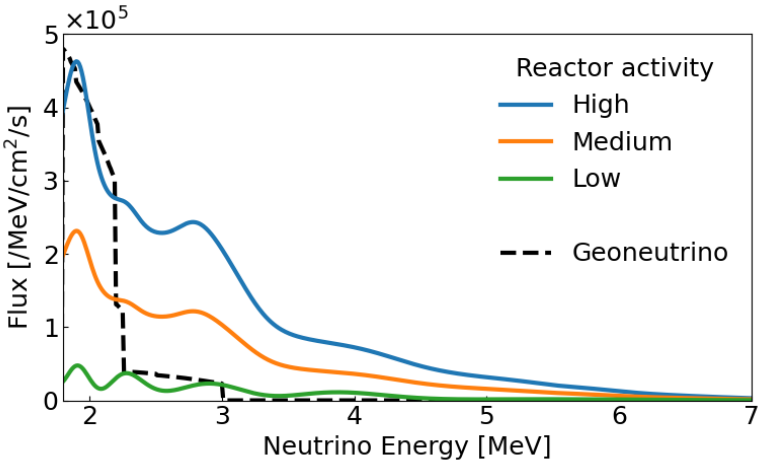

Figure 7.1: Reactor $\bar{\nu}_e$ fluxes at the Kamioka mine assuming low, medium and high reactor activities. The relative fission yields (^{235}U,^{238}U,^{239}Pu,^{241}Pu) are assumed be (0.570,0.078,0.295,0.057) [49]. The $\bar{\nu}_e$ spectra per fission are from [159, 160, 161]. The values of neutrino oscillation parameters are $\Delta m^2_{21} = 7.53\times10^{-5}\,\mathrm{eV}^2$, $\tan^2\theta_{12} = 0.436$, and $\sin^2\theta_{13} = 0.023$. Geoneutrino flux (black) is calculated using the parameters from [162].

7.1.2 Analysis in Single Detectors

In a single detector, the expected signal features a rapid increase in the candidate event rate. Considering a rate-only analysis, without explicit reference to any pre-

SN neutrino models, a Poisson likelihood function is used to measure how well the observed data fit the null hypothesis. Here, the null hypothesis is that the observed event rate is consistent with the expected background rate within the sampling error. The likelihood function can be written as

$$\mathcal{L}_{\mathrm{x}} = \frac{(\lambda_{\mathrm{x}})^{N_{\mathrm{x}}} \exp^{-\lambda_{\mathrm{x}}}}{N_{\mathrm{x}}!}, \tag{7.1}$$

where the subscript x can be any single detector. N_{x} is the observed number of events within the sliding analysis time window. The term λ_{x}, being the expected number of events, is given by

$$\lambda_{\mathrm{x}} = S_{\mathrm{x}} + B_{\mathrm{x}}, \tag{7.2}$$

where S_{x} is the parameter for the number of signal and B_{x} is the expected number of background.

Then, the test statistic based on the likelihood ratio is given by

$$\Lambda_{\mathrm{x}} = -2 \ln \frac{Max\left(\mathcal{L}_{\mathrm{x}}|_{S_{\mathrm{x}}=0}\right)}{Max(\mathcal{L}_{\mathrm{x}})}, \tag{7.3}$$

where the numerator and denominator are the maximum likelihoods with and without imposing a background-only scenario $S_{\mathrm{x}} = 0$ [163]. The more the observation disagrees with the null hypothesis, the larger Λ_{x} is. As the test statistic Λ_{x} asymptotically approaches χ^2 distribution, we consider $\sqrt{\Lambda_{\mathrm{x}}}$ as the detection significance for a single detector.

In the likelihood function from Eq. 7.1, systematic uncertainties are not taken into account. This treatment is reasonable because the search of pre-SN neutrinos is statistic dominant and the systematic uncertainties have small impact on the result. The requirement of a fast processing speed and a robust computation also justifies the omission of the systematic uncertainties.

7.1.3 False Alarm Rate

It is common practice to quantify the false positive rate of a statistical test using the p-value of the test. However, in this search, we find it misleading to report the results using the p-value or the significance of a single test. The online search for pre-SN neutrinos is performed continuously, while the time when the pre-SN neutrino signal appears is not known in advance. An appropriate way to estimate the global p-value is to determine the probability, assuming background-only, of finding a signal at any time that is at least as extreme as the one observed. This global p-value can be substantially higher than the p-value of a single test. This is known as the *Look-elsewhere Effects* [164].

To resolve this issue, we introduce the quantity "false alarm rate" to report the result of the search. The false alarm rate is the expected frequency that a false alarm may happen per century. A false alarm is caused by a significant signal due to background fluctuations. The false alarm rate can be derived from toy Monte-Carlo simulations, assuming a background-only scenario. In practice, we generate a time series of Poisson random events with the expected value being the background rate. The statistical test is performed following Eq. 7.3. Then we evaluate the frequency with which the random events cause a significant signal. Thereby, a false alarm rate is found. Considering the frequency of CCSN in the galaxy is approximately once every few decades [5], we set a false alarm rate ≤ 1 per century as the ultimate pre-SN alert criteria.

7.1.4 Analysis in the Combined Alert System

Data from the different detectors are processed by the combined alert system. It performs a test-of-significance every five minutes based on the observed numbers of candidates and the expected numbers of background events. The following likelihood function is constructed, which is a product of the Poisson likelihood of each detector,

$$\mathcal{L}_{\text{combine}} = \prod \mathcal{L}_{\text{x}}. \tag{7.4}$$

The test statistic based on likelihood ratio Λ_{combine} can be calculated by substituting $\mathcal{L}_{\text{combine}}$ for $\mathcal{L}_{\text{x}}$ in Equation 7.3. The corresponding significance is found by calculating the chi-square quantile for n degrees of freedom, where n is the number of detectors.

It is important to note that the combined alert system assumes that there is no correlation between the detectors. For any pre-SN neutrino model, the neutrino fluxes in both detectors should be the same, and thus there are correlations between numbers of signal events in the different detectors in the combined alert system. However, we note that the test statistic $\mathcal{L}_{\text{combine}}$ merely reflects the level of agreement between the data and the null hypothesis. Whether the data are consistent with a pre-SN neutrino model is not tested. Therefore, the signal parameters are treated as independent parameters.

We note, SK and KamLAND are located roughly in the same location. Therefore, there is correlation between the background in these two detectors. This correlation does not affect the statistical test, because the expected number of background B is estimated from the data taken in the background time window and normalized to the analysis time window, based on the assumption that the background rate is consistent with the background data taken before. However, such an assumption may not hold, as the background can change significantly in a short time. For example,

when nuclear reactors near a detector are turned on or off, reactor $\bar{\nu}_e$ background can change significantly within a week. An unexpected increase in reactor $\bar{\nu}_e$ flux, for example, when several nearby reactors are turned on, may cause an excess of $\bar{\nu}_e$ events in the detectors. For pre-SN neutrino detection via IBD, the reactor neutrino background is irreducible, as its energy range overlaps that of the signal. Concerning this issue, the detectors should perform frequent background measurements to keep the background prediction updated.

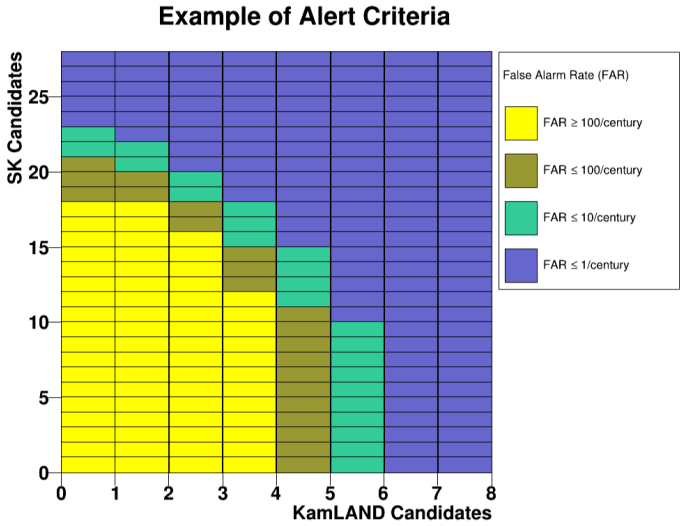

Figure 7.2: Example contour of the false alarm rates extracted from toy Monte-Carlo simulation assuming the background-only hypothesis. The x-axis and y-axis are numbers of candidates observed in KamLAND (in 24 hours) and SK (in 12 hours). The assumed background rates are 12.4 events per day in SK and 0.19 events per day in KamLAND, the same as those in the medium reactor activity scenario.

The combined alert system reports the results of the pre-SN neutrino search with false alarm rate. Figure 7.2 shows an example contour of the false alarm rate resulting from toy Monte-Carlo simulation. The x-axis and y-axis are numbers of candidates observed in KamLAND (in 24 hours) and SK (in 12 hours), respectively. The color of each box indicates the false alarm rate level of the corresponding numbers of observed events. If the observation drops in the yellow regions, which indicates a false alarm rate ≥ 100 per century, there is no hint of a pre-SN neutrino emission. If the observation is in the blue regions, where the false alarm rate ≤ 1 per century, it is considered as a significant excursion of the observed event rate which could be caused by pre-SN $\bar{\nu}_e$.

7.1.5 Workflow of the Combined Pre-supernova Alert System

Currently, the combined alert system is installed on both the SK server and the KamLAND server. It receives continuous data stream from the detectors. The data stream

includes a time stamp, a status code, the number of pre-SN neutrino candidates, and the expected number of background. Processed by the DAQ systems, events in the two detectors are selected by their own selection processes following the descriptions in Section 6.3 and Section 5.6. The individual pre-SN alert software of KamLAND (SK) then counts the number of observed candidates N_{KL} (N_{SK}) within a 24-hour (12-hour) time window. The expected number of background B_{KL} (B_{SK}) is estimated using data from a background time window of ∼90 (∼30) days, as described in Section 7.1. Validity of data is also taken into consideration. Detector status is monitored and marked by the status code. When a detector undergoes calibration work, a test run or shutdown, the status of the detector is marked as "abnormal" and the data from this period will be invalidated. In addition to the above situations, there may also be network connection problems which can delay the data transfer. Therefore, the differences between the current time and the time when data are processed will also be checked. The individual KamLAND and SK pre-SN alert systems gather the above information, and exchange them between the servers of KamLAND and SK, as illustrated in Figure 7.3. The update frequency of the input is once every 5 minutes for each of the experiments. These inputs will be processed by the combined pre-SN alert software, yielding a result of the combined pre-SN search. The result will be exported to users, and the alert decision will be made based on the result.

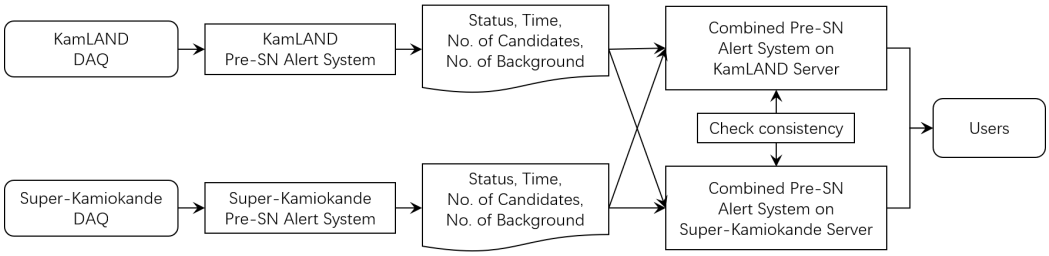

Figure 7.3: Illustration of the input of the combined pre-SN alert system.

On the two servers, identically functioning software for the combined pre-SN alert system are installed. If either of the software pipelines fails, the other one can still output the search result and issue alerts. Figure 7.4 illustrates the workflow of this software. The software runs on a precise repeating schedule once every 5 minutes. Validity of inputs is first checked by examining the status of each detector and the timestamps of the inputs. If a detector has an abnormal status, or if data from it is delayed for over 15 minutes, input from this detector is invalidated. In this case, instead of exporting the combined search result, the system will output a result based only on the valid input. If all of the inputs are invalid, the result is not applicable. Only when both KamLAND and SK are in normal status and the data are up-to-date, the system exports the result of the combined search.

In order to determine the corresponding false alarm rate, the software loads three pre-calculated false alarm rate tables, for KamLAND-only, SK-only, and their combi-

nation. Once the software finds a false alarm rate ≤ 1 per century, an alarm will be sent to the Gamma-ray Coordinates Network (GCN) via an email-based circular. In addition, a text file containing the false alarm rate, along with a timestamp, and a code that denotes whether the result is for KamLAND-only, SK-only or the combined search, is available to users who have registered on the official website of the combined pre-SN alert system.

The above processes, called main processes, are identical in both servers, as pictured in the blue box with solid border in Figure 7.4. An additional process as shown in the orange box with dashed border is uniquely installed on the SK server. In this process, the false alarm rate tables are updated automatically upon any changes $> 5\%$ in the expected numbers of background. This process, typically takes $\sim$40 minutes, and is in parallel with the main processes, in order not to delay the output of the results. Therefore, the pre-calculated false alarm rate tables do not always correspond to the current background values. However, we note that a significant change in the background rates within an hour is unusual, because the background rates are obtained from measurements of a specific time window long enough to mitigate the effects of statistical fluctuations.

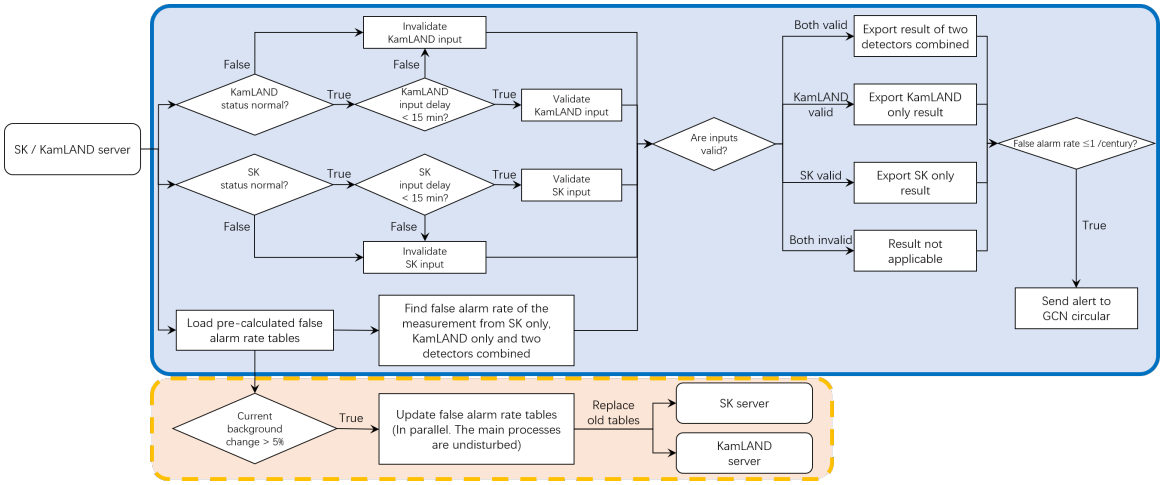

Figure 7.4: Illustration of the workflow of the combined pre-SN alert system. The main processes to produce results of statistical tests as pictured in the blue box with solid border are identical for the systems on both servers. The process to update false alarm rate tables as plotted in the orange box with dashed border is installed exclusively on the SK server.

This alert system, operational since May 2023 and accessible to the public, is designed to promptly notify astronomers and particle physicists to maintain operational readiness at their observatories, ensuring they do not miss any impending SN events. Once registered via the official website[1], users can acquire identical results contained in the above mentioned text file from either of the servers and are encouraged to

[1] https://www.lowbg.org/presnalarm/

check the consistency of the results from the two servers before putting into scientific use. Directional information of pre-SN neutrinos is not available from either SK or KamLAND.

7.2 Sensitivity to Pre-supernova Neutrinos in Individual Detectors

In this section, we present sensitivities studies for KamLAND and SK, respectively. Previous sensitivity studies for detection of pre-SN neutrinos in KamLAND and SK are given in [105, 165, 106]. In [105], the sensitivity for KamLAND's detection of pre-SN neutrinos assuming the model from [101] is presented. [165] presents a preliminary overall sensitivity for SK doped with 0.1% Gd by mass. In [106], an improved sensitivity to pre-SN neutrinos in SK is shown, using data from the first phase of SK-Gd (with 0.01% Gd) to predict realistic backgrounds and new event selection methods.

At this time, both analyses in KamLAND and SK have been updated. KamLAND has now taken the additional pre-SN neutrino model from [103] into consideration and re-optimized the selection parameters, the analysis time window, and the detector status. As for SK, it has entered a new SK-Gd phase with 0.03% Gd loaded, further enhancing the sensitivity to low-energy $\bar{\nu}_e$. The loading of Gd has brought radioactive contaminants into the FV of the detector, affecting the background rate. Moreover, the reactor-neutrino-induced backgrounds in both detectors have changed substantially since the previous studies because many of the nuclear reactors in Japan have been restarted. This section presents a new assessment of the sensitivity to pre-SN neutrinos in KamLAND and SK. Analysis strategies are re-optimized to adapt to the changes.

Although KamLAND and SK are at nearly identical locations, they are in rather different experimental conditions, such as target mass, detection energy threshold, background rates, and duty cycle, etc. These factors affect the choices of background time window and analysis time window. SK chooses a 30-day background time window, while KamLAND's choice is a longer 90-day background time window due to its lower background rate. The analysis time windows are chosen based on the principle of achieving the longest warning time. As a result, KamLAND has chosen an optimal time window of 24 hours. For SK, the time window was optimized to 12 hours, maximizing the warning time for Betelgeuse-like models and reducing the impact that potential interruptions in DAQ and calibration work in the detector may have in the pre-SN alert system.

7.2.1 Pre-supernova neutrino flux models

At this time, two pre-SN neutrino flux models were used: Odrzywolek model [101, 132] and Patton model [103]. Both models provide data sets for the calculation of $\bar{\nu}_e$ emission during the pre-SN stage. Odrzywolek model provides data sets for stars with 15 $M_\odot$ and 25 $M_\odot$ and Patton model for 15 $M_\odot$ and 30 $M_\odot$.

Odrzywolek model assumes that the entire neutrino flux comes from pair annihilation. For the nuclear isotopic composition of the star, the model assumes a nuclear statistical equilibrium (NSE), which is a treatment only dependent on the temperature, density, and electron fraction, making it a simple flux estimated by only post-processing an already existing stellar model. Patton model includes a more complete evaluation of the neutrino flux from the pre-SN star, including contributions not only from pair annihilation, but also from plasmon decay, photo-neutrino process, beta decay, and electron/positron captures. Using the star evolution code MESA (Modules for Experiments in Stellar Astrophysics) [166], this model couples the isotopic evolution to the stellar evolution, giving a more robust estimation of the neutrino fluxes from nuclear weak processes.

Neutrinos undergo flavor conversion, i.e. neutrino oscillations, from the point of production to the point of detection. To calculate the expected signal from the considered models, adiabatic neutrino oscillations in the matter of the star, and neutrino oscillations in vacuum are taken into account. For the former, the ratio of $\bar{\nu}_e$ is changed at high Mikheyev–Smirnov–Wolfenstein resonance, which depends on the mass ordering of neutrinos [167]. Different transition probabilities are assumed for normal and inverted neutrino mass orderings to account for the change in ratio of $\bar{\nu}_e$ due to the dense stellar medium and the effects of neutrino oscillations in vacuum.

We attempt to explore the sensitivities for detecting pre-SN neutrinos from the well-known red supergiant α-Ori (Betelgeuse), which will potentially end up a CCSN. The current estimation of its mass and distance suggests 16.5-19 $M_\odot$ and 168^{+27}_{-15} pc [168]. Limited by the available data sets, we chose 15 $M_\odot$ and 150 pc to simulate a Betelgeuse-like pre-SN star in this work. Although we focus on detecting pre-SN neutrinos from a Betelgeuse-like star, pre-SN neutrinos from other stars could also be observable. A list of candidate pre-SN stars with updated distance and mass estimates can be found in [106]. Figure 7.5 shows the expected number of IBD candidates per kton of water for different pre-SN models as a function of the $\bar{\nu}_e$ energy, assuming a Betelgeuse-like pre-SN star. The event spectra are obtained by integrating the expected candidates over the last 24 hours, 12 hours, 6 hours and 1 hour prior to core collapse. These candidates predominantly cluster around $E_{\bar{\nu}_e} \approx 2.6$ MeV, but can be found at higher energies. The expected event rate increases over time, leading to a large fraction of the total IBD candidates concentrated in the last hour. Although we present the

event spectra only for water, the discussion above is common for both water and LS detectors.

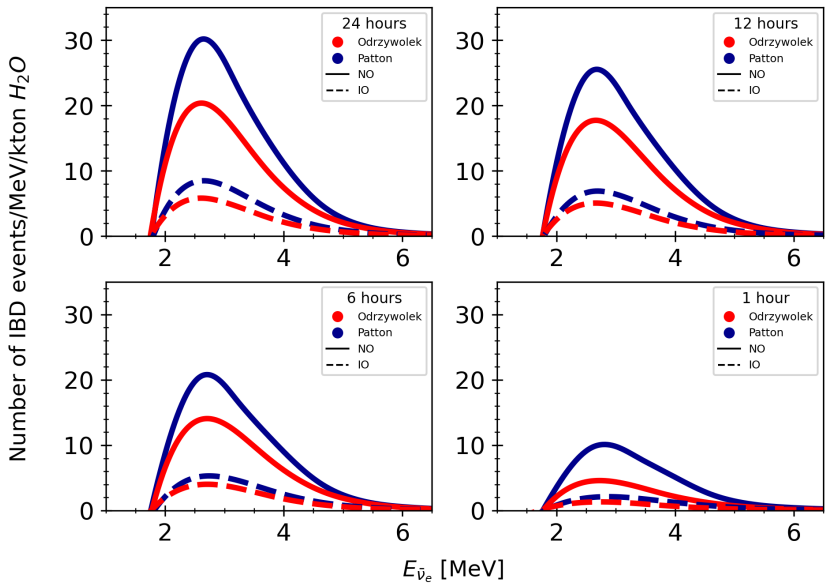

Figure 7.5: Number of pre-SN IBD interactions per kton of water integrated over the last 24 hours, 12 hours, 6 hours, and 1 hour prior to the CCSN as a function of the $\bar{\nu}_e$ energy, $E_{\bar{\nu}_e}$. The Betelgeuse-like models consider stars with initial masses of $15\,M_\odot$ located 150 pc away from Earth, for both normal neutrino mass ordering (NO) and inverted neutrino mass ordering (IO).

7.2.2 Sensitivity to pre-SN neutrinos at KamLAND

We evaluate the expected numbers of signal events in KamLAND for the two pre-SN neutrino models with neutrino oscillation effects, assuming a Betelgeuse-like pre-SN star. Figure 7.6 (a) shows the expected number of signal events, integrated over a sliding 24-hour time window, as a function of time to CCSN. Figure 7.6 (b) shows the integrated number of signals for the last 24 hours before core collapse at different distances. The expected background counts integrated over 24 hours are 0.07, 0.19, and 0.32 events for low, medium, and high reactor activities, respectively. The background rate in KamLAND is sufficiently low, such that a few candidate events can cause a significant signal.

Figure 7.7 presents the time evolution of the expected detection significance assuming medium reactor activity. The significance corresponding to false alarm rates of 1, 10, and 100 per century are also plotted as horizontal dotted-dashed lines. The remaining time to core collapse, when KamLAND observes an excess of pre-SN neutrino candidates as extreme as false alarm rate ≤ 1 per century, is defined as the warning time. Note that the latency due to data processing is not taken into account when

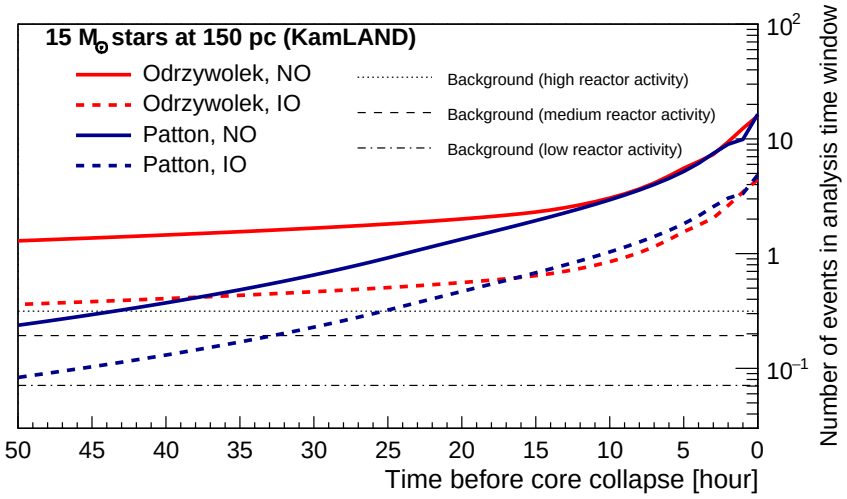

(a)

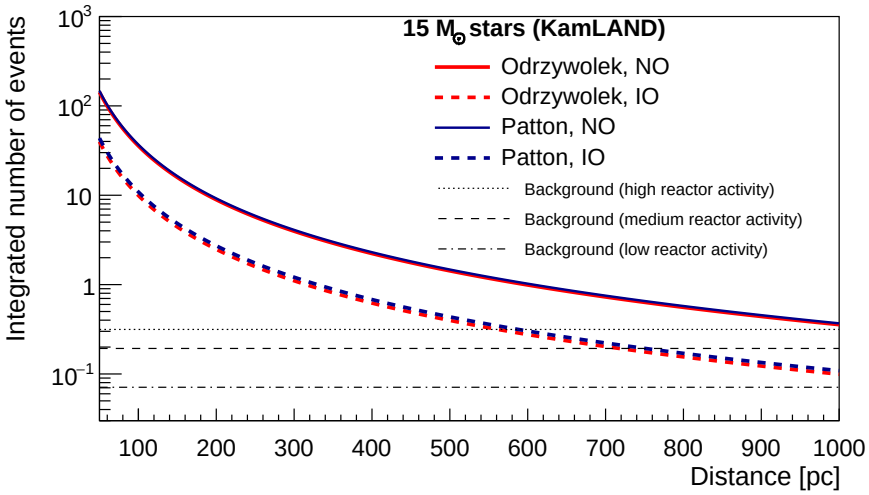

(b)

Figure 7.6: Expected number of signal events in KamLAND as a function of (a) time to core collapse, and (b) distance. Pre-SN $\bar{\nu}_e$ fluxes from a star with $15\,M_\odot$ are considered, following the Odrzywolek model (red) and the Patton model (blue). For (b), the signal rates are integrated over the last 24 hours before the CCSN. Solid curves show normal neutrino mass ordering and dashed curves show inverted neutrino mass ordering.

calculating the warning time. For a Betelgeuse-like pre-SN star, KamLAND is capable of issuing a pre-SN alert 6.5 hours before the CCSN, assuming the Odrzywolek model and normal mass ordering. In the case of inverted mass ordering, the warning time is largely shortened as the pre-SN neutrino fluxes become lower. The worst case is, with the Odrzywolek model and inverted mass ordering, the expected detection significance cannot reach the alert criteria. The discussions above are based on the medium reactor activity scenario. Table 7.1 summarizes the warning time for all three reactor activity assumptions. If the reactor activity assumption shifts from medium to high, for the normal ordering cases, the warning time will be shortened by roughly 1 hour. For the inverted ordering cases, with the high reactor activity assumption, KamLAND is unable to issue an alert with a false alarm rate of 1 per century, noted as "N/A (Not Applicable)" in Table 7.1.

Figure 7.8 pictures the warning time as a function of distance. The lines are estimations assuming medium reactor activity. The upper edges of the bands are for low reactor activity, and the lower edges are for high reactor activity. These results indicate that, for nearby pre-SN candidates, KamLAND can send alerts tens of hours before the explosion. For the medium reactor activity case, KamLAND is sensitive to pre-SN candidates within an optimistic distance of 280 pc away from Earth.

7.2.3 Sensitivity to pre-SN neutrinos at SK

The fluxes of pre-SN neutrinos are taken from the two pre-SN models, with neutrino oscillation effects assuming normal and inverted mass orderings. The expected signal rates are aggregated over a 12-hour sliding time window, resulting in the expected number of signal events as a function of time, as pictured in Figure 7.9 (a). Figure 7.9 (b) presents the number of signals integrated over the last 12 hours for different distances. The expected background counts for low, medium, and high reactor activities in SK are 4.6, 6.2 and 8.1 events. Although the background rate is much higher than that in KamLAND, the large target volume allows SK to collect signal events an order of magnitude larger than KamLAND. Thus the statistical significance in SK can increase rapidly when approaching core collapse.

Based on the estimations of signal and background, we assessed the sensitivity of pre-SN neutrino detection in SK-Gd with 0.03% Gd loading. Figure 7.10 presents the time evolution of the expected detection significance in SK-Gd, assuming medium reactor activity. The results show that SK-Gd is capable of providing an early warning before the CCSN, at most 10.9 hours assuming the Patton model and normal ordering, and at least 2.1 hours for the Odrzywolek model and inverted ordering. The warning time for all simulated scenarios are summarized in Table 7.1. If the reactor neutrino fluxes around the Kamioka mine are doubled, the warning time can be shortened by

0.2-1.1 hours.

We plot the warning time as a function of distance in Figure 7.11. The upper (lower) edges of the bands are for low (high) reactor activity, and the lines in between are for medium reactor activity. Under neutrino flux assumptions of the Patton model and normal ordering, the SK alert can cover 15 $M_\odot$ stars with a distance of 500 pc from Earth, for the medium reactor activity case.

7.2.4 Discussion

The results shown above suggest that the two detectors, KamLAND and SK, have different advantages in pre-SN neutrino detection. For KamLAND, the low background rate is an advantage in terms of resolving a small signal. As shown in Figure 7.6 (a), for a Betelgeuse-like pre-SN candidate, the expected number of signal events exceed the background count even tens of hours prior to the CCSN. As a result, KamLAND can provide a warning for nearby SNs earlier than SK. On the other hand, the number of signal events in KamLAND is limited by the target mass, making it hard to reach stars at far distances. SK is sensitive to CCSN candidates further away from Earth compared to KamLAND. The large target mass of SK can increase the significance rapidly when approaching the CCSN, resulting in a much higher $\bar{\nu}_e$ event rate. But due to its relatively high background rate, SK is less sensitive to small signals. By noting that these two detectors are complementary in pre-SN neutrino searches, a joint search combining measurements from these two detectors should improve the current detection sensitivity. We show in Section 7.3 that the combined alert benefits from the advantages of these two detectors. We expect the complementary properties of the two detectors to create a synergistic bond, enhancing the sensitivity to pre-SN neutrino signals.

7.3 Combined Sensitivity

We perform a joint sensitivity study based on the estimations of S_{KL}, S_{SK}, B_{KL} and B_{SK} presented in Section 7.2.2 and Section 7.2.3. Figure 7.12 shows the time evolution of the combined sensitivity of pre-SN neutrinos from a Betelgeuse-like star of 15 $M_\odot$, assuming medium reactor activity. For the Patton model and normal mass ordering, the warning time is extended to 12.4 hours prior to the CCSN. Similar to the discussions above, we assessed the sensitivities for the two pre-SN models, the three reactor activity cases, and the two neutrino mass orderings. Table 7.1 summarizes the warning time of the combined alert and the individual alerts. These results indicate that the combined alert presents an improved performance, because the warning times are longer compared to either of the individual alerts. It is important to note that, even in the high reactor activity case, the warning time is at least 2.2 hours before

the CCSN.

Table 7.1: Warning time of the KamLAND-only, SK-only, and combined search for each pre-SN neutrino model, neutrino mass ordering and reactor activity, assuming a Betelgeuse-like pre-SN star of 15 $M_\odot$. The latency due to data processing is not taken into account.

Alert system	**Pre-SN model**	**Mass ordering**	**Warning time [hour]**		
			Low	**Medium**	**High**
			reactor activity		
KamLAND	Odrzywolek	NO	8.3	6.5	5.5
		IO	0.9	N/A	N/A
	Patton	NO	8.1	6.1	5.0
		IO	0.8	0.2	N/A
SK	Odrzywolek	NO	6.7	6.3	5.9
		IO	2.4	2.1	1.9
	Patton	NO	12.0	10.9	9.8
		IO	4.7	4.3	3.9
Combined	Odrzywolek	NO	9.8	8.0	7.3
		IO	3.0	2.5	2.2
	Patton	NO	14.2	12.4	11.2
		IO	5.4	4.6	4.2

Figure 7.13 presents the expected warning time and the star distance coverage of the combined alert. Variations due to changes in the reactor neutrino flux are shown as shaded, enveloped by the upper edges resulting from low reactor activity, and the lower edges resulting from high reactor activity. Significant improvements in star distance coverage are observed when comparing to the individual alerts shown in Figure 7.8 and Figure 7.11. Assuming 15 $M_\odot$ stars, the combined alert is able to cover 510 pc for the medium reactor activity case.

These results demonstrate the complementarity of the KamLAND and the SK-Gd detectors. Taking advantage of the low background rate of KamLAND and the large target mass of SK, the combined alert presents improvement in extending the warning time as well as the distance coverage.

7.4 Conclusion and Outlook

In this study, we present updates on the sensitivity to pre-SN neutrinos from a Betelgeuse-like star of the individual alert systems of KamLAND and SK, and introduce a combined pre-SN alert system with the two detectors. Pre-SN neutrino fluxes are calculated based on the models from [101] and [103], with neutrino oscillation effects. Due to their similar energy range, reactor neutrinos originating from Japanese nuclear reactors constitute an important source of background for pre-SN neutrinos. Different reactor activity conditions in Japan are considered in this study,

where reactor fluxes vary from low to high. The following results are estimated assuming that nuclear reactors near the Kamioka mine (Mihama 3 unit, Ohi 3, 4 units and Takahama 1, 2, 3, 4 units) operate with a 100% load factor. The corresponding background rates are 0.19 events per day and 12.4 events per day in KamLAND and SK, respectively.

The best warning times are attained by each detector under different neutrino flux assumptions. In the ideal case, for the Odrzywolek model and normal ordering, KamLAND can provide an early warning 6.5 hours prior to core collapse, and a pre-SN neutrino emission can be observed up to 280 pc from Earth. The SK pre-SN alert has an optimistic warning time of 10.9 hours, and is able to cover a distance of 500 pc, assuming the Patton model and normal ordering.

The combined pre-SN alert system performs a joint statistics test based on the data from the KamLAND and the SK detectors. It has been operational and accessible to the public since May 2023. Integrating the complementary properties of the two detectors, the combined alert shows improved sensitivity to pre-SN neutrinos. An optimistic warning time of 12.4 hours is obtained, for the Patton model and normal ordering, 1.5 hours longer than the SK alert and ∼6.3 hours longer than the KamLAND alert, with the medium reactor activity assumption. At the same background level, its distance coverage for 15 $M_\odot$ progenitors is 510 pc, which exceeds those of the individual alerts. Although doubling the neutrino fluxes from nearby reactors increases the backgrounds significantly and affects the sensitivity of both detectors individually, the combined alert remains sensitive to pre-SN neutrino emission with an expected warning time of no less than 2.2 hours for a Betelgeuse-like pre-SN star, sufficiently long to cover the latency due to data processing. In addition, the combined alert system reduces the dead time for pre-SN neutrino detection, promoting continuous monitoring even if one of the detectors is temporarily offline. All of these demonstrate the benefits of having a combined search for pre-SN neutrinos.

Currently, the combined alert system cannot provide directional information of supernovae, as both KamLAND and SK adopted detection techniques based on IBD. The correlation between the positron direction and the neutrino direction is smeared out. In SK, a study on detecting pre-SN neutrinos via elastic scattering on electrons is being performed. We are looking forward to its results. Another possible upgrade for the combined alert system is the shape analysis taking into account the time evolution of pre-SN neutrino fluxes. The system is already receiving continuous data stream from detectors with time distribution of candidate events. By switching to a shape analysis, it is possible to further extend the capability of early warning.

In the future, we would like to incorporate more pre-SN neutrino sensitive detectors in this combined alert system, such as JUNO, HK, and DUNE. For this purpose,

we need to consider different levels of participation. Although currently both SK and KamLAND are exchanging time distribution of candidate events and expected background rates, other detectors may only provide a significance or an alert. The system must be feasible, in order to incorporate more detectors.

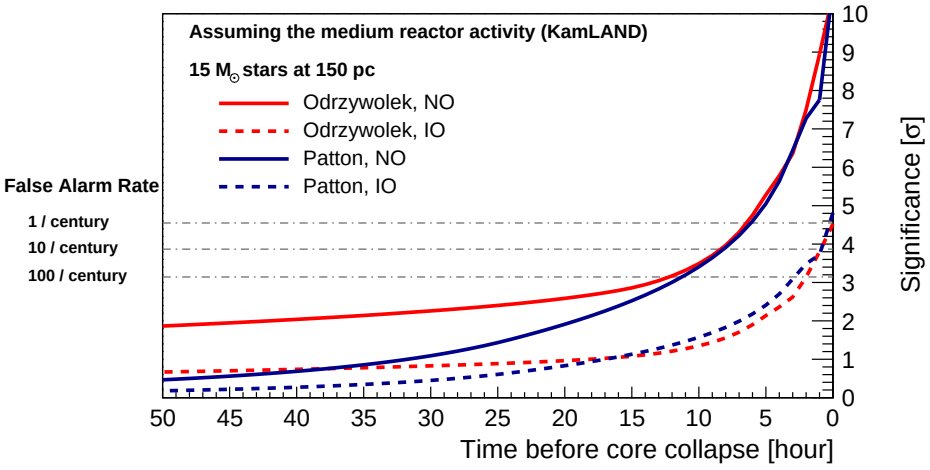

Figure 7.7: Time evolution of the sensitivity to pre-SN neutrinos in KamLAND, assuming medium reactor activity, following the Odrzywolek model (red) and the Patton model (blue). Solid (dashed) lines are for normal (inverted) neutrino mass ordering. Horizontal dotted-dashed lines indicate false alarm rates of 1, 10, and 100 per century.

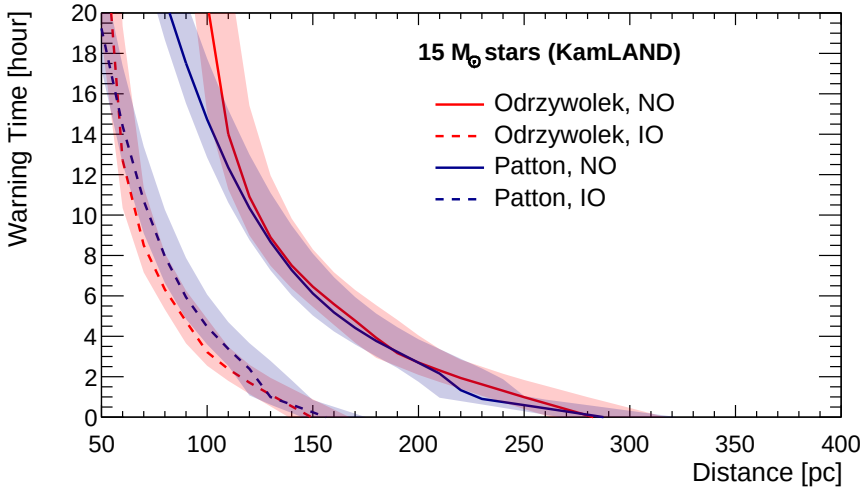

Figure 7.8: Expected warning time in KamLAND as a function of distance. The lines are estimations assuming medium reactor activity. The upper (lower) edges of the bands are for the low (high) reactor activity case.

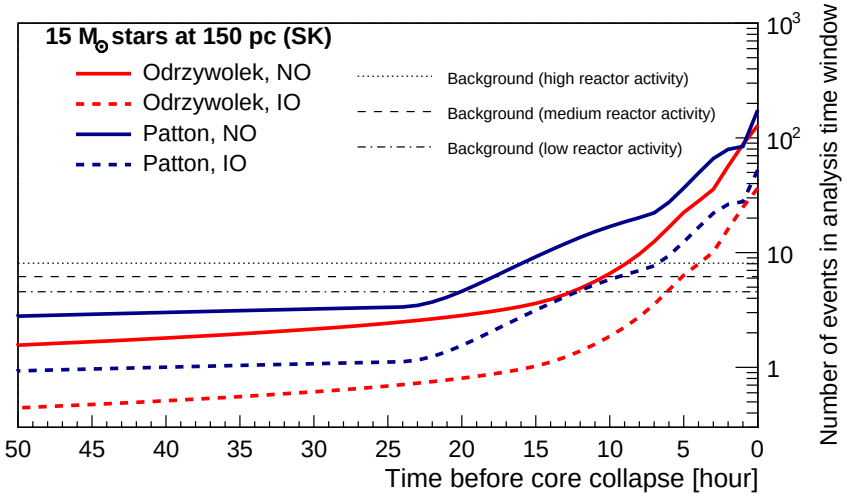

(a)

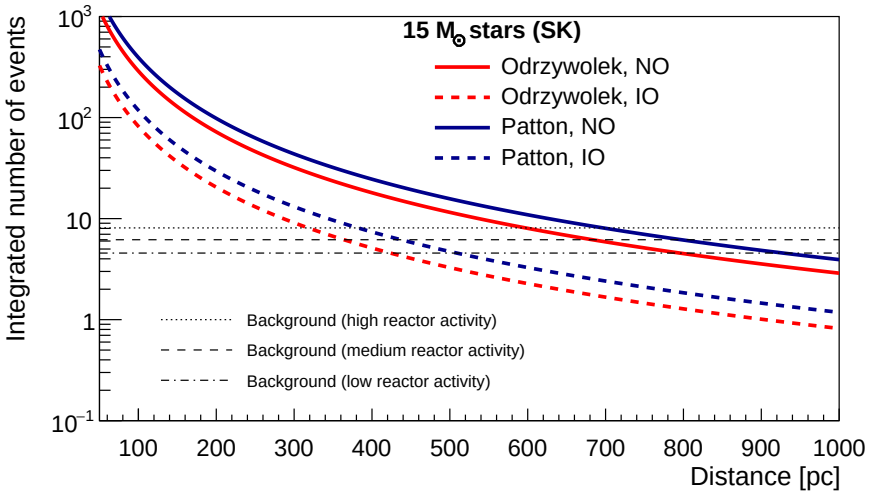

(b)

Figure 7.9: Expected number of signal events in SK with 0.03% Gd concentration as a function of (a) time to core collapse, and (b) distance. Pre-SN $\bar{\nu}_e$ fluxes from a star with $15\,M_\odot$ is considered, following the Odrzywolek model (red) and the Patton model (blue). For (b), the signal rates are integrated over the last 12 hours before the CCSN. Solid curves show normal neutrino mass ordering and dashed curves show inverted neutrino mass ordering.

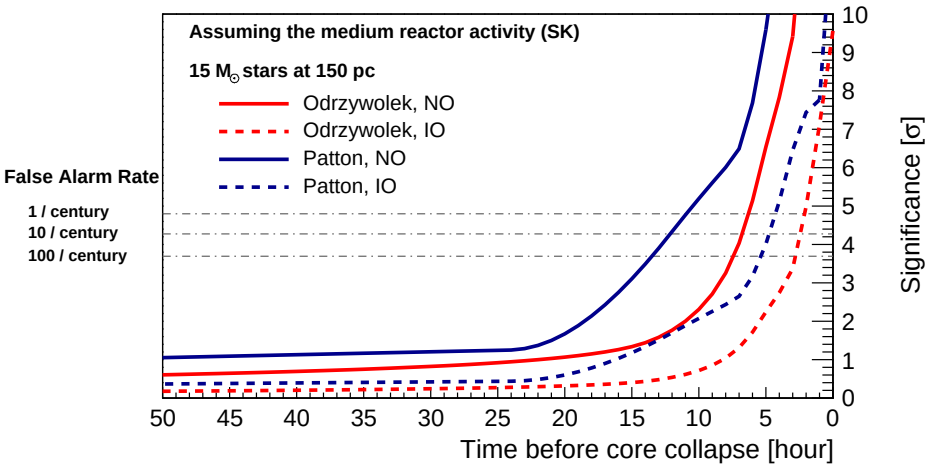

Figure 7.10: Time evolution of the sensitivity to pre-SN neutrinos in SK with 0.03% Gd concentration, assuming medium reactor activity, following the Odrzywolek model (red) and the Patton model (blue). Solid (dashed) lines are for normal (inverted) neutrino mass ordering. Horizontal dotted-dashed lines indicate false alarm rates of 1, 10, and 100 per century.

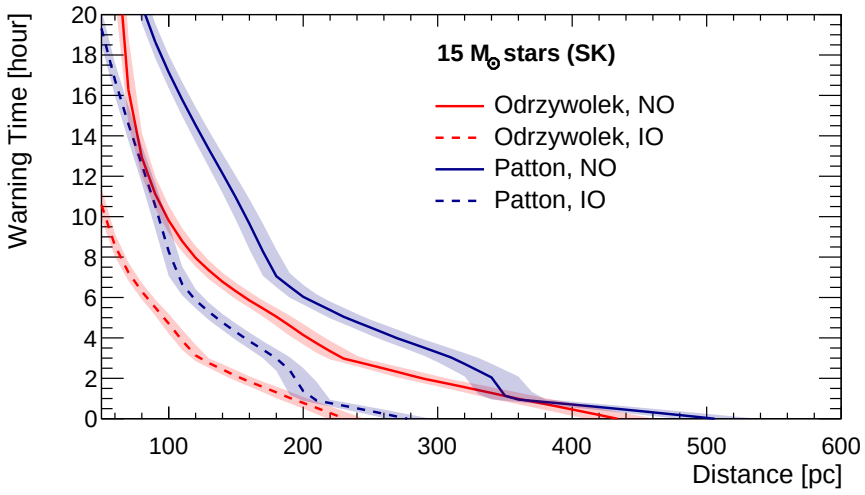

Figure 7.11: Expected warning time in SK as a function of distance. The lines are estimations assuming medium reactor activity. The upper (lower) edges of the bands are for the low (high) reactor activity case.

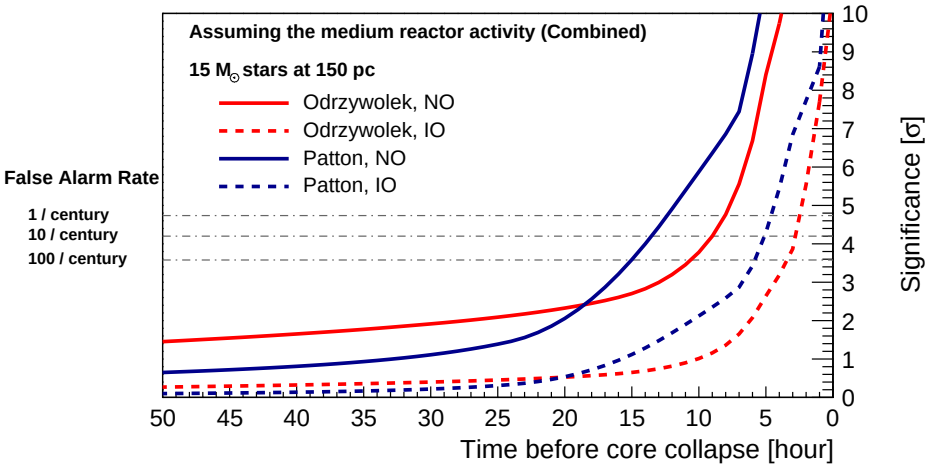

Figure 7.12: Combined sensitivity to pre-SN neutrinos as a function of time based on the detection capability of KamLAND and SK-Gd with 0.03% Gd concentration, assuming medium reactor activity, following the Odrzywolek model (red) and the Patton model (blue). Solid (dashed) lines are for normal (inverted) neutrino mass ordering. Horizontal dotted-dashed lines indicate false alarm rates of 1, 10, and 100 per century.

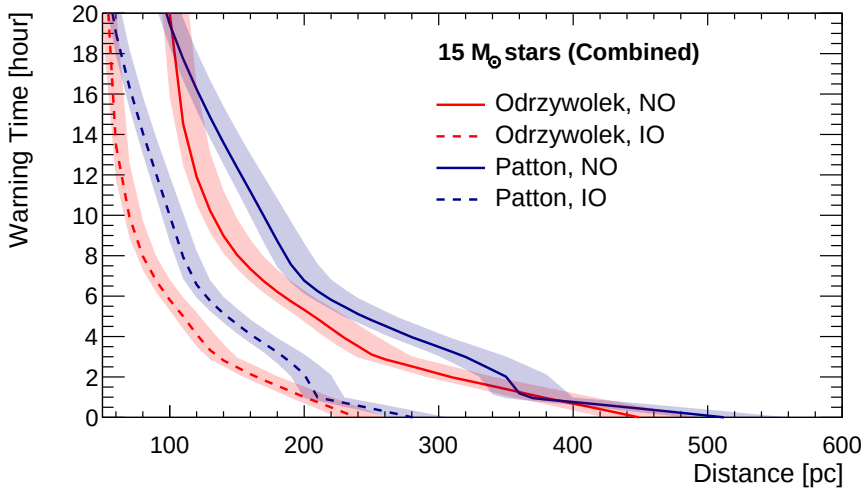

Figure 7.13: Expected warning time of the combined search as a function of distance. The lines are estimations assuming medium reactor activity. The upper (lower) edges of the bands are for the low (high) reactor activity case.

Part 2

Scalar Non-Standard Neutrino Interactions in Atmospheric Neutrinos

Chapter 8

The Scalar-NSI

8.1 Motivation

Neutrino oscillation studies have now reached an era of precision measurement, where increasingly accurate measurements allow us to test not only the standard three-flavor framework but also possible new effects that may appear as small corrections. Although experimental results have confirmed that three flavor neutrino oscillation is the underlying mechanism of the phenomenon of neutrino flavor transitions [23, 24], various new physics beyond the Standard Model, e.g. sterile neutrino oscillation [169], non-standard neutrino interactions (NSI) [34, 6], and Lorentz invariance violation [170], etc., may coexist with neutrino oscillation with subdominant contributions. We focus on the non-standard neutrino interactions (NSIs), which describe unknown couplings of neutrinos beyond the Standard Model.

The idea of NSI was first introduced in Wolfenstein's paper on neutrino matter effects [34]. In general, NSIs are grouped into two categories: the vector-NSI and the scalar-NSI. The vector-NSI describes interactions of neutrinos with a vector field. Its effect is similar to the standard matter effect, but it may appear in a different flavor basis or with a different dependence on the surrounding matter particles. The scalar-NSI, on the other hand, describes couplings of neutrinos with a scalar field. It acts as corrections to the neutrino mass terms. The idea of the scalar-NSI was developed more recently by Ge and Parke in 2018 [6], and has since been studied by many theorists.

The scalar-NSI is a natural mechanism motivated by the origin of neutrino masses. Neutrino oscillation measurements show that at least two of the three light neutrinos have nonzero masses, and one well-motivated mechanism for generating these masses is through interactions with a scalar field that has a nonzero vacuum expectation value. Such a scenario cannot be easily ruled out. Because left-handed neutrinos be-

long to $SU(2)_L$ doublets together with their corresponding charged leptons, a scalar field that couples to neutrinos may also couple to charged leptons, for example via mixing with the neutral Higgs boson field. If such couplings exist, they could produce matter effects on neutrino propagation analogous to the standard matter effect, but mediated by a scalar particle instead of a vector boson. The scalar-NSI are especially interesting because they directly modify the neutrino mass matrix, rather than the matter potential during propagation. This means the scalar-NSI can affect the interpretation of oscillation data and alter the measurements of oscillation parameters, such as the mass splittings, the mixing angles, and the CP-violating phase δ_{CP}. Because of this, it is essential to test the presence of the scalar-NSI with data and to place experimental limits on their size.

Several phenomenological studies have examined how the scalar-NSI could affect current and future oscillation experiments, including KamLAND, JUNO, DUNE, HK, and ESSnuSB. It has been shown that the scalar-NSI can cause large uncertainties in the determination of θ_{12} and Δm^2_{21} at long-baseline reactor experiments like KamLAND and JUNO [171]. At accelerator experiments, the scalar-NSI may significantly reduce the CP sensitivity [9]. Studies for ESSnuSB also show that the scalar-NSI can strongly affect the measurements of Δm^2_{31} and δ_{CP} [172]. These results demonstrate that the scalar-NSI could have wide-ranging impacts on our understanding of neutrino oscillation physics.

An important feature of the scalar-NSI is that their effects are energy independent because they appear in the neutrino Hamiltonian as corrections to the neutrino mass terms. Their effects scale with the matter density encountered by neutrinos, meaning that neutrinos traveling through dense matter are especially sensitive probes, regardless of their energies. Solar neutrinos therefore provide a natural place to study the scalar-NSI. However, atmospheric neutrinos that pass through the Earth also travel across regions of high matter density. In addition, they cover many different baselines and encounter a variety of density profiles, which makes them a powerful tool for testing the scalar-NSI.

In this analysis, we aim to perform the first direct fit of the scalar-NSI using the atmospheric neutrino data in SK. We aim to search for evidence of the scalar-NSI in the data, to place experimental constraints on their strength, and to study their impact on the measurement of standard oscillation parameters, in particular Δm^2_{32} and θ_{23}. In doing so, we hope to provide new insight into the possible existence of the scalar-NSI and their implications for neutrino physics.

8.2 Neutrino Oscillation with Scalar-NSI

The effective Lagrangian for scalar-NSI mediated by a scalar mediator ϕ is given by

$$\mathcal{L}_{\text{eff}}^{\text{scalar}-\text{NSI}} = \frac{y_f y_{\alpha\beta}}{m_\phi^2}(\bar{\nu}_\alpha \nu_\beta)(\bar{f} f), \tag{8.1}$$

where y_f and $y_{\alpha\beta}$ are the Yukawa couplings to the matter fermions and the Dirac neutrinos, and m_ϕ is the mass of the scalar mediator. Although the scalar-NSI is a kind of neutrino interaction with matter fermions, it cannot be considered as a matter potential as in Section 2.3.2, because the Lagrangian cannot be converted to vector currents [173, 174]. Instead, it can be considered as a Yukawa interaction term for Dirac neutrinos and appears as a correction to the neutrino mass. The standard form of Dirac equation for neutrinos is

$$\bar{\nu}_\beta \left[i\partial_\mu \gamma^\mu + M_{\beta\alpha} \right] \nu_\alpha = 0, \tag{8.2}$$

where $M_{\beta\alpha}$ is the Dirac mass matrix of the neutrinos. Taking into account the effect of scalar-NSI, the Dirac equation after spin summation over the matter fermions is given by

$$\bar{\nu}_\beta \left[i\partial_\mu \gamma^\mu + \left(M_{\beta\alpha} + \frac{\sum_f N_f y_f y_{\alpha\beta}}{m_\phi^2} \right) \right] \nu_\alpha = 0, \tag{8.3}$$

where N_f is the number density of the matter fermions. Defining

$$\delta M \equiv \frac{\sum_f N_f y_f y_{\alpha\beta}}{m_\phi^2}, \tag{8.4}$$

the effective Hamiltonian in the flavor basis in Eq. 2.34 is modified as

$$\mathcal{H}_F^{\text{scalar}-\text{NSI}} = \frac{\left(U\mathbb{M}U^\dagger + \delta M\right)\left(U\mathbb{M}U^\dagger + \delta M\right)^\dagger + \mathbb{A}}{2E}, \tag{8.5}$$

where $\mathbb{M} \equiv \text{diag}(m_1, m_2, m_3)$ is the neutrino mass matrix, and δM is the correction term introduced by the scalar-NSI. δM can be parameterized as

$$\delta M = S_m \begin{pmatrix} \eta_{ee} & \eta_{e\mu} & \eta_{e\tau} \\ \eta_{e\mu}^* & \eta_{\mu\mu} & \eta_{\mu\tau} \\ \eta_{e\tau}^* & \eta_{\mu\tau}^* & \eta_{\tau\tau} \end{pmatrix}, \tag{8.6}$$

where $S_m = 0.05\,\text{eV}$ is a constant scaling term with the dimension of mass, and

$$\eta_{\alpha\beta} = \frac{1}{m_\phi^2 S_m} \sum_f N_f y_f y_{\alpha\beta}. \tag{8.7}$$

The size of δM is scaled relative to S_m so that the parameters $\eta_{\alpha\beta}$ are dimensionless. The choice of the scale factor also makes the scalar-NSI effects easy to compare with the genuine neutrino mass splitting $\Delta m^2_{32} \approx 2.5 \times 10^{-3}\,\mathrm{eV}^2$ which experiments are sensitive to. Note that δM is a hermitian matrix. The Hermicity of the Hamiltonian allows the diagonal elements $\eta_{\alpha\alpha}$ to be real and off-diagonal elements $\eta_{\alpha\beta}$ ($\beta \neq \alpha$) to be complex.

Since $\eta_{\alpha\beta}$ has a dependence on the number density of matter fermions N_f, the size of the scalar-NSI effect is proportional to matter density. To better compare results among different experiments with different matter densities, it is convenient to establish a base density for the subsequent calculations. In this analysis, the base density is set to ρ_0 =2.6 g/cm^3, which is the typical matter density for short-baseline terrestrial experiments. The $\eta_{\alpha\beta}$ presented to be at 2.6 g/cm^3 are seen as a benchmark $\hat{\eta}_{\alpha\beta}$. The corresponding values of $\eta_{\alpha\beta}$ to be used in an experiment is rescaled

$$\eta_{\alpha\beta} = \hat{\eta}_{\alpha\beta}\frac{\rho}{\rho_0}, \tag{8.8}$$

where ρ is the matter density of the experiment.

In the presence of scalar-NSI, the effective Hamiltonian has a dependence on neutrino mass, unlike the pure neutrino oscillation Hamiltonian (Eq. 2.34). Therefore, scalar-NSI provides an opportunity to probe the absolute neutrino mass, parameterized as the lightest neutrino mass m_l. In the normal mass ordering case, $m_l = m_1$. In the inverted mass ordering case, $m_l = m_3$. If scalar-NSI coexists with neutrino oscillation, measurable parameters are $\eta_{\alpha\beta}$ and m_l, in addition to those measurable in pure neutrino oscillations.

In the scalar-NSI case, the computation of oscillation probability is analogous to that in the pure neutrino oscillation case. $\mathcal{H}_F^{\mathrm{scalar-NSI}}$ can be diagonalized by the effective mixing matrix $\tilde{U}_{\mathrm{scalar-NSI}}$ to become the effective Hamiltonian in the mass basis $\mathcal{H}_M^{\mathrm{scalar-NSI}}$. Then, the oscillation probability is given by Eq. 2.42.

8.3 Status of Scalar-NSI Data Fits

Since the scalar-NSI was first proposed by Ge and Parke in 2018 [6], there have been growing interest in testing this scenario against pure oscillation. Although most of the analyses are sensitivity studies, some theorists have performed data fits with scalar-NSI [6, 7, 1]. Data fits assuming the presence of the scalar-NSI are reviewed in the following. Since the effect of the scalar-NSI increases with the matter density, the scalar-NSI parameters $\eta_{\alpha\beta}$ reported in different analyses are not directly comparable. Therefore, $\eta_{\alpha\beta}$s are converted to fundamental parameters in this section and in any

subsequent comparison using the approach in [1]. By assuming that the scalar mediator ϕ couples only to up and down quarks in matter with equal strength, the matter density can be directly related to the number density of fermions. From Eq. 8.7, the parameter $\zeta_{\alpha\beta} \equiv y_q y_{\alpha\beta}/m_\phi^2$ is fundamental and is given by

$$\zeta_{\alpha\beta} \equiv \frac{y_q y_{\alpha\beta}}{m_\phi^2} = \frac{S_m}{\sum_q N_q}\eta_{\alpha\beta}, \tag{8.9}$$

where q denotes up quarks and down quarks. The scalar-NSI parameters $\eta_{\alpha\beta}$ reported in an analysis will be converted to $\zeta_{\alpha\beta}$ taking into account the matter density and S_m used in the analysis. It is also important to note that the scalar-NSI parameters are usually reported one at a time by fixing all the other scalar-NSI parameters to zero.

Solar neutrinos are the best oscillation means of exploring the scalar-NSI because they pass through the dense matter of the Sun. An analysis performs data fits to the latest Borexino [175] and SNO [33] data, with extra constraints on θ_{13} and Δm^2_{21} from other experiments measuring oscillations in vacuum [1]. Table 8.1 lists the allowed regions at 90% C.L., with parameters converted to $\zeta_{\alpha\beta} = 6.7 \times 10^{-15}\,\mathrm{eV}^{-2}\eta_{\alpha\beta}$ taking into account the average matter density of $100\,\mathrm{g/cm^3}$ and the $S_m \approx 0.0087\,\mathrm{eV}$. Note that the off-diagonal parameters are presented in the form of real part and imaginary part. Both $\zeta_{\mu\mu}$ and $\zeta_{\tau\tau}$ have two allowed regions.

Table 8.1: The 90% allowed regions on scalar-NSI parameters from the latest Borexino and SNO data, converted to $\zeta_{\alpha\beta} \equiv y_q y_{\alpha\beta}/m_\phi^2 = 6.7 \times 10^{-15}\,\mathrm{eV}^{-2}\eta_{\alpha\beta}$. The values are in units of $10^{-15}\,\mathrm{eV}^{-2}$. Taken from [1].

Parameter	Borexino+SNO+External Constraints ($10^{-15}\,\mathrm{eV}^{-2}$)
ζ_{ee}	[-8.17,1.74]
$\zeta_{\mu\mu}$	[-19.23,-16.75]$\oplus$[-6.77,1.00]
$\zeta_{\tau\tau}$	[-17.22,-15.28]$\oplus$[-4.96,0.40]
$\Re\zeta_{e\mu}$	[-7.17,-0.87]
$\Im\zeta_{e\mu}$	<0.07
$\Re\zeta_{e\tau}$	[2.81,13.73]
$\Im\zeta_{e\tau}$	[-0.13,0.13]
$\Re\zeta_{\mu\tau}$	[0.00, 0.20]
$\Im\zeta_{\mu\tau}$	[-7.37,7.37]

Another analysis attempted to explain the tension in the NOvA [176] and T2K [177] data with the presence of off-diagonal parameters of the scalar-NSI [7]. The best-fit values assuming the lightest neutrino is massless can be found in Table 8.2. The values are properly converted to $\zeta_{\alpha\beta}$, taking into account the matter density of $3\,\mathrm{g/cm^3}$ and the $S_m \approx 0.05\,\mathrm{eV}$. Note that the off-diagonal parameters are presented as an absolute value and a phase angle.

Note that [178] investigated the non-oscillation constraints on scalar-NSI, such

Table 8.2: The best-fit scalar-NSI parameters from the NOvA and T2K data, converted to $\zeta_{\alpha\beta} \equiv y_q y_{\alpha\beta}/m_\phi^2 = 1.29 \times 10^{-12}\,\mathrm{eV}^{-2}\eta_{\alpha\beta}$. The absolute values are in units of $10^{-15}\,\mathrm{eV}^{-2}$. Taken from [7].

		NOvA+T2K	
Mass Ordering	Parameter	Absolute Value ($10^{-15}\,\mathrm{eV}^{-2}$)	Phase (Rad)
NO	$\zeta_{e\mu}$	11.61	1.40
	$\zeta_{e\tau}$	20.64	1.42
	$\zeta_{\mu\tau}$	7.74	1.22
IO	$\zeta_{e\mu}$	20.64	1.82
	$\zeta_{e\tau}$	16.77	0.66
	$\zeta_{\mu\tau}$	73.53	1.60

as early universe constraints and fifth-force probes, under many assumptions mainly about the mediator mass. Although some of them may provide stronger constraints than neutrino oscillation experiments, we focus on the oscillation data and disregard these constraints here. In addition, the early universe has a very different environment than the present environment and may result in a different behavior of the scalar-NSI.

Chapter 9

Atmospheric Neutrino Simulation

Precise prediction of atmospheric neutrino interactions is essential for accurate measurements of neutrino oscillation parameters and investigation of new physics. The SK prediction consists of three components: atmospheric neutrino flux, cross section, and detector response. The complexity of them makes it difficult to build an analytic prediction. Instead, SK adopts MC simulation.

The atmospheric neutrino interactions are simulated via the following procedure. The atmospheric neutrino flux is first calculated based on primary cosmic-ray flux and cross sections. This analysis adopts the atmospheric neutrino flux derived by Honda *et al.* [179]. Then, the NEUT event generator (version 5.6.4) [180] is used to simulate neutrino interactions with nuclei in the SK detector. The final step is to simulate how the detector responds to the outgoing particles from the NEUT interaction. The SKDETSIM software, developed internally by the SK collaboration based on GEANT 3 [181], is used to track secondary particles and simulate detector response.

9.1 Atmospheric Neutrino Flux

The primary cosmic-ray flux consists of protons and nuclei. When they pass through the geomagnetic field and enter the atmosphere, their interactions produce secondary hadrons that can decay to atmospheric neutrinos. The atmospheric neutrinos are produced mainly by the two-body decays of pions and kaons as well as in the subsequent muon decays. Therefore, the atmospheric neutrino flux can be computed based on the primary cosmic-ray flux and hadronic interaction models. However, several effects must be taken into account, such as the geomagnetic effect, length of muon decay path, and time variation of the solar wind. These effects are introduced below, following the discussion of the primary atmospheric neutrino spectrum. A comprehensive review of the atmospheric neutrino flux calculation can be found in [182].

Primary cosmic-ray fluxes are measured by balloon experiments [183, 184, 185] at heights of $\sim 30\,\mathrm{km}$ and a spacecraft-based experiment AMS [186, 187, 188] at heights greater than 100 km. The geomagnetic effect is applied to the measured cosmic-ray flux, filtering out the cosmic-rays with low momentum.

The flux measurements are then convolved with hadronic interaction models [189, 190] to produce the energy spectra of secondary hadrons. These models are based on measurements made by accelerators [191, 192]. However, they do not cover the entire phase space of incident protons and outgoing hadrons relevant for atmospheric neutrino production. Cosmic muon flux data are used as a supplement.

The decay chain that produces neutrinos from pions is

$$\begin{aligned} \pi^{\pm} \rightarrow \mu^{\pm} + & \nu_{\mu}(\bar{\nu}_{\mu}) \\ & \searrow \\ & e^{\pm} + \bar{\nu}_{\mu}(\nu_{\mu}) + \nu_{e}(\bar{\nu}_{e}). \end{aligned}$$

Neutrinos from kaons are produced through the following decay modes,

$$\begin{aligned} K_L^0 &\rightarrow \pi^{\pm} + e^{\mp} + \nu_e \\ K_L^0 &\rightarrow \pi^{\pm} + \mu^{\mp} + \nu_{\mu}. \end{aligned}$$

Since the production rate of pions per interaction is higher than that of kaons, neutrino production is dominated by pion decays at low energies. Therefore, the muon-to-electron neutrino flavor ratio $(\nu_{\mu} + \bar{\nu}_{\mu})/(\nu_e + \bar{\nu}_e)$ is roughly 2 below 1 GeV. At higher energies (above 1 GeV), fewer pions and muons decay into neutrinos because of hadronic interactions and a longer muon travel distance. This results in an increasing fraction of neutrinos from kaons. Thus, $(\nu_{\mu} + \bar{\nu}_{\mu})/(\nu_e + \bar{\nu}_e)$ increases with energy. Figure 9.1 shows the atmospheric neutrino fluxes and flavor ratios calculated for SK.

In addition to the filtering effect, the geomagnetic field also results in an anisotropic atmospheric neutrino flux. As primary cosmic-rays are positively charged, they are deflected by the geomagnetic field, resulting in asymmetric zenith angle dependence and azimuthal angle dependence in the atmospheric neutrino flux. Figure 9.2 shows the zenith angle dependence of the flux, where an up-down asymmetry is observed below 1 GeV. Above 1 GeV, the fluxes are basically up-down symmetric. The distributions peak around $\cos\theta = 0$ where muons can travel a longer path in the atmosphere and are more likely to decay before reaching the ground. The azimuthal angle dependence features an east-west asymmetry known as the east-west effect, where the atmospheric neutrino flux from the west is higher than that from the east. Therefore, the flux needs to be calculated as a function of the zenith angle and the azimuth angle, in addition to the neutrino energy.

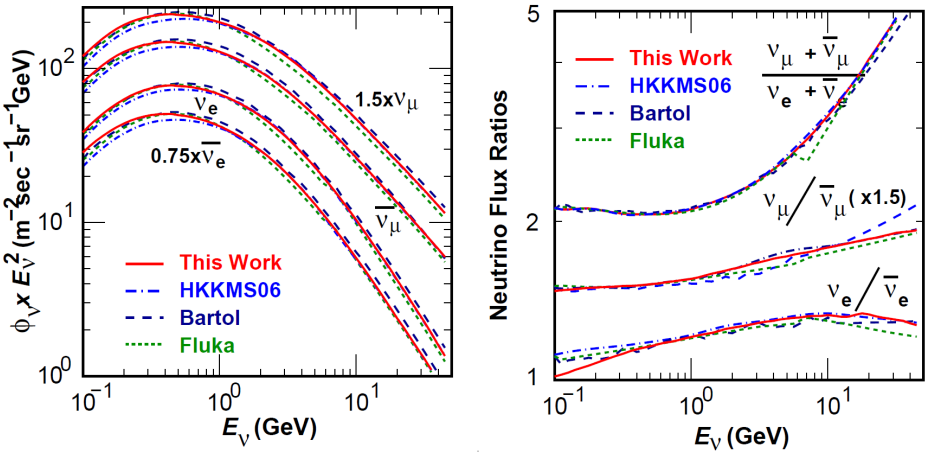

Figure 9.1: Atmospheric neutrino fluxes for different neutrino flavors (left) and flux ratios (right) calculated for SK. Red lines are Honda model used in this analysis. Taken from [179].

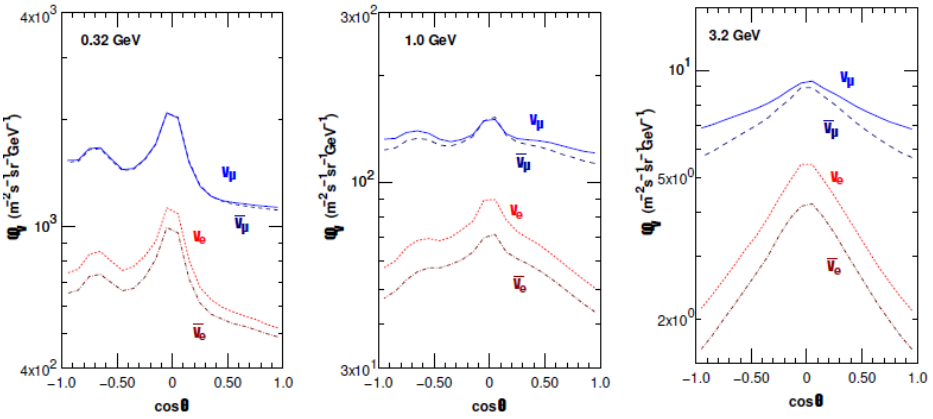

Figure 9.2: Atmospheric neutrino fluxes as a function of the cosine zenith angle $\cos\theta$ at selected energies at SK, averaging over azimuthal angle. $\cos\theta = 1(-1)$ is for vertically downward (upward) going neutrinos. Taken from [179].

Further, the magnetized plasma from the Sun, known as solar wind, can be a barrier to primary cosmic-rays. The strength of the suppression to primary cosmic-ray flux depends on the solar activity, which varies periodically. The Honda flux model provides atmospheric neutrino fluxes with three levels of solar activities: minimum, maximum, and middle. For a specific SK phase, the simulated neutrino events are generated assuming the flux at solar middle, re-weighted by the fraction of data-taking time in solar minimum and solar maximum conditions. The weight is given by

$$w_{\rm sol} = \frac{f_{\rm max}\phi_{\rm max} + f_{\rm min}\phi_{\rm min}}{\phi_{\rm mid}}, \tag{9.1}$$

where $\phi_{\rm min}$, $\phi_{\rm mid}$, and $\phi_{\rm max}$ are the atmospheric neutrino fluxes of solar minimum, middle, and maximum conditions. The fractions of solar minimum $f_{\rm min}$ and solar maximum $f_{\rm max}$ are calculated based on cosmogenic neutron counts from a neutron

monitor [193]. Table 9.1 lists the fractions for each SK phase.

Table 9.1: Fractions of solar minimum and maximum for each SK phase.

Phase	Fraction of solar minimum	Fraction of solar maximum
SK I	70%	30%
SK II	30%	70%
SK III	100%	0%
SK IV	44%	56%
SK V	100%	0%
SK VI	76%	24%

9.2 Neutrino Interactions

The calculated atmospheric neutrino flux is fed into the NEUT event generator [180]. NEUT randomly assign an energy, direction, flavor, and interaction mode to each neutrino, and simulates the interaction and the outgoing particles. For atmospheric neutrinos between 100 MeV and a few TeV, they mostly interacts with nucleons in SK's water target. Example Feynman diagrams of the interactions are shown in Figure 9.3. In NEUT, the interactions with hydrogen nuclei (almost free proton) and with the bound nucleons in the oxygen nucleus are treated separately. In this analysis, the relevant interactions are quasi-elastic scattering, single-pion production, and deep inelastic scattering (DIS). NEUT predicts the cross sections and the kinematics of the products of the interactions.

9.2.1 Quasi-Elastic

For neutrino energies between ∼100 MeV and 1 GeV, quasi-elastic scattering is the dominant interaction. In this analysis, quasi-elastic scatterings that free a single nucleon, leaving a hole in the nuclear target, are considered. They can be either charged current (CC) processes that produce a charged lepton or neutral current (NC) processes that produce a neutrino, e.g.,

$$\begin{aligned} \text{(CC)}: &\quad \nu_l + n \to l^- + p \\ \text{(CC)}: &\quad \bar{\nu}_l + p \to l^+ + n \\ \text{(NC)}: &\quad \nu_l(\bar{\nu}_l) + p, n \to \nu_l(\bar{\nu}_l) + p, n. \end{aligned}$$

This kind of processes is also known as one-particle one-hole (1p1h) processes.

The cross section of quasi-elastic (QE) interactions was formalized by Llewellyn

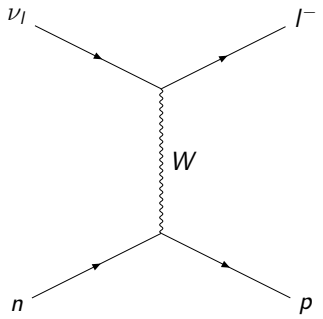

(a) CC 1p1h

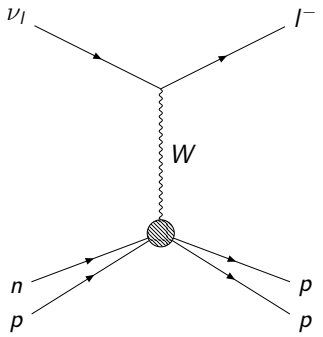

(b) CC 2p2h

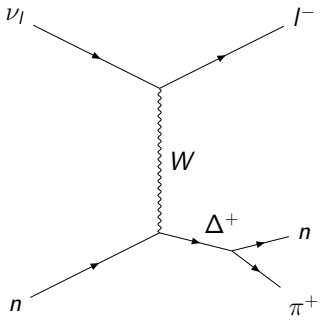

(c) CC 1π

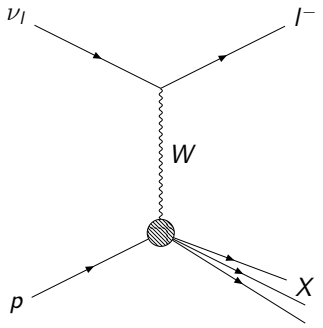

(d) CC DIS

Figure 9.3: Example Feynman diagrams for major interaction modes. Details of the interaction modes are found in the text.

Smith [194]. The differential cross section for QE with free nucleon is given by

$$\frac{d\sigma}{dq^2} = \frac{M^2 G_F^2 \cos^2\theta_C}{8\pi E_\nu^2}[A(q^2) + B(q^2)\frac{s-u}{M^2} + C(q^2)\frac{(s-u)^2}{M^4}], \tag{9.2}$$

where $q \equiv p_\nu - p_l$ is the four-momentum transfer, E_ν is the neutrino energy, M is the nucleon mass, G_F is the Fermi coupling constant, θ_C is the Cabibo angle, and s and u are Mandelstam variables [194]. The coefficients A, B, and C are given by

$$\begin{aligned}
A(q^2) =& \frac{m^2 - q^2}{4M^2}[(4 - \frac{q^2}{M^2})|F_A|^2 - (4 + \frac{q^2}{M^2})|F_V^1|^2 \\
&- \frac{q^2}{M^2}|\xi F_V^2|^2(1 + \frac{q^2}{4M^2}) - \frac{4q^2 F_V^1 \xi F_V^2}{M^2} \\
&- \frac{m}{M}((F_V^1 + \xi F_V^2)^2 + |F_A|^2)], \\
B(q^2) =& \frac{q^2}{M^2}(F_A(F_V^1 + \xi F_V^2)), \\
C(q^2) =& \frac{1}{4}(|F_A|^2 + |F_V^1|^2 - \frac{q^2}{4M^2}|\xi F_V^2|^2),
\end{aligned} \tag{9.3}$$

where m is the mass of the outgoing lepton, ξ is defined as the anomalous magnetic moment $3.71\mu_N$, where $\mu_N \equiv e\hbar/2m_p c$ is the nuclear magneton. Vector form factors

$F_V^1(q^2)$ and $F_V^2(q^2)$ and axial vector form factor $F_A(q^2)$ are given by

$$\begin{aligned} F_V^1(q^2) =& (1 - \frac{q^2}{4M^2})^{-1}[G_E(q^2) - \frac{q^2}{4M^2}G_M(q^2)], \\ \xi F_V^2(q^2) =& (1 - \frac{q^2}{4M^2})^{-1}[G_E(q^2) - G_M(q^2)], \\ F_A(q^2) =& g_A(1 - \frac{q^2}{M_A^2})^{-2}, \end{aligned} \tag{9.4}$$

where G_E and G_M are the electric and magnetic form factors, and $G_E = (1 + \xi)^{-1}G_M(q^2) = (1 - \frac{q^2}{M_V^2})^{-2}$. The coupling constant $g_A \equiv G_A(q^2 = 0)$ is precisely measured to 1.27 by neutron beta decay [195]. The vector mass M_V is set to $0.84\,\mathrm{GeV}/c^2$. The axial mass M_A, known to have a large experimental uncertainty [196, 197, 198], is set to $1.21\,\mathrm{GeV}/c^2$.

In order to simulate neutrino interactions with bound nucleons, three nuclear models are implemented in NEUT. In this analysis, the local Fermi gas (LFG) model by Nieves *et al.* [199] is used for the baseline simulation, while the spectral function (SF) model by Benhar *et al.* [200] is used to estimate systematic uncertainties. The LFG model treats the nucleus as a collection of non-interacting fermions that fill energy levels up to the Fermi energy. In the SF model, the spectral function is calculated by combining the single-particle components, partly supported by experimental data, and the correlated components, evaluated in local-density approximation. Pauli blocking is applied by requiring that the recoiling nucleon momentum be greater than the Fermi momentum ($225\,\mathrm{MeV}/c$).

In addition to the 1p1h processes, there are quasi-elastic processes where neutrino interacts with a strongly-correlated nucleon pair and generate multiple nucleons and leave the same number of holes in the nuclear target. Among them, those processes that free two nucleons and create two holes are referred to as "2p2h". The 2p2h processes are dominated by the meson exchange current (MEC) which are two-body currents that involve the exchange of mesons between nucleons and virtual excitation of nuclear resonances. The 2p2h processes are implemented in NEUT and are considered in this analysis only for CCQE. The Valencia model by Nieves *et al.* [199] is used to describe the 2p2h processes.

9.2.2 Single Pion Production

Neutrino-nucleus interactions that produce a single pion have significant contributions to the cross section for neutrino energies between 1 GeV and 3 GeV. There are two main mechanisms: resonant pion production and coherent pion production. The former accounts for over 90% of the single pion production processes.

Resonant pion productions are processes in which the neutrino interacts with a nucleon, and a single pion is generated from the decays of intermediate resonances. Omitting the excited baryon resonances, the CC processes can be written as

$$\begin{aligned}
&(\mathrm{CC}): && \nu_l(\bar{\nu}_l) + p \to l^{\mp} + p + \pi^{\pm} \\
&(\mathrm{CC}): && \nu_l(\bar{\nu}_l) + n \to l^{\mp} + n + \pi^{\pm} \\
&(\mathrm{CC}): && \nu_l + n \to l^{-} + p + \pi^{0} \\
&(\mathrm{CC}): && \bar{\nu}_l + p \to l^{+} + n + \pi^{0},
\end{aligned}$$

and the NC processes are

$$\begin{aligned}
&(\mathrm{NC}): && \nu_l(\bar{\nu}_l) + p \to \nu_l(\bar{\nu}_l) + n + \pi^{+} \\
&(\mathrm{NC}): && \nu_l(\bar{\nu}_l) + n \to \nu_l(\bar{\nu}_l) + p + \pi^{-} \\
&(\mathrm{NC}): && \nu_l(\bar{\nu}_l) + p \to \nu_l(\bar{\nu}_l) + p + \pi^{0} \\
&(\mathrm{NC}): && \nu_l(\bar{\nu}_l) + n \to \nu_l(\bar{\nu}_l) + n + \pi^{0}.
\end{aligned}$$

NEUT uses the Rein-Sehgal model [201] to simulate resonant pion production. The excited baryon resonance is restricted to have invariant mass less than $2\,\mathrm{GeV}/c^2$, where there are 18 resonances above the pion production threshold. NEUT first calculates the cross section for producing a baryon resonance, considering interference between the possible resonance states. Then, decays of the resonances into pions are computed.

As in the case of CCQE, an axial form factor,

$$C_A^5(q^2) = C_A^5(0)\left(1 - \left(\frac{q}{M_A^{\mathrm{Res}}}\right)^2\right)^{-2}, \tag{9.5}$$

modifies the resonant pion production cross section. The normalization $C_A^5(0)$ and the resonant pion production axial mass M_A^{Res} are considered unconstrained by experiments, and are set to be 1.01 and $0.95\,\mathrm{GeV}/c^2$ respectively. Some of the decays of the resonances do not produce a pion in the final state. This effect is also considered in the simulation by adding the contribution from these isospin-1/2 states incoherently to the channels of resonant states. A free normalization parameter $I_{\frac{1}{2}}$ modifies the size of this contribution, and is set to 1.3 in this analysis.

In coherent pion production, the neutrino interacts with the whole nucleus instead of a nucleon, e.g.,

$$\begin{aligned}
&(\mathrm{CC}): && \nu_l(\bar{\nu}_l) + A \to l^{\mp} + A + \pi^{\pm} \\
&(\mathrm{NC}): && \nu_l(\bar{\nu}_l) + A \to \nu_l(\bar{\nu}_l) + A + \pi^{0}.
\end{aligned}$$

Since the nucleus is much heavier than the neutrino, the nuclear recoil is small and the pion angular distribution is peaked in the forward direction. NEUT uses the Berger-Sehgal model [202] to simulate the processes in this analysis.

9.2.3 Deep Inelastic Scattering

Deep inelastic scattering (DIS) is a kind of process in which a neutrino interacts with a quark, breaking the nucleon target and potentially generating multiple hadrons in the final state. These processes become dominant interaction channels when the neutrino energies reach several GeV. The simulations are performed using two different models depending on the invariant mass of the hadronic system. For invariant mass between $1.3\,\mathrm{GeV}/c^2$ and $2\,\mathrm{GeV}/c^2$, NEUT uses a custom-built multi-pion production model. The double differential cross section is given by

$$\begin{aligned}\frac{d^2\sigma}{dxdy} =& \frac{G_F^2 M_N E_\nu}{\pi}((1-y+y^2+C_1)F_2(x,q^2) \\ & \pm y(1-\frac{y}{2}+C_2)xF_3(x,q^2)), \\ C_1 =& \frac{M_l^2}{4E_\nu^2} - \frac{xyM_N}{2E_\nu} + \frac{M_l^2 y}{4xM_N E_\nu} - \frac{M_l^2}{2xM_N E_\nu}, \\ C_2 =& -\frac{M_l^2}{4xM_N E_\nu},\end{aligned} \tag{9.6}$$

where E_ν is the neutrino energy, q^2 is the squared four-momentum transfer, M_N is the nucleon mass, M_l is the outgoing lepton mass, and F_2 and F_3 are parton distribution functions. The parton distribution functions are based on GRV98 [203] with corrections in the low-q2 region from Bodek and Yang [204]. The variables $x \equiv -q^2/(2M_N(E_\nu - E_l))$ and $y \equiv (E_\nu - E_l)/E_\nu$ are the Bjorken scaling parameters, where E_l is the energy of the outgoing lepton. Above $2\,\mathrm{GeV}/c^2$, PYTHIA 5.7 [205] is used with the same parton distribution functions. To avoid double counting with the single pion production modes, only multi pion production channels are considered in DIS.

9.2.4 Final State Interactions

Hadrons produced via neutrino interactions in the nucleus can undergo interactions with the surrounding nucleons before exiting. This is referred to as final state interactions (FSIs). NEUT uses a custom semiclassical intranuclear cascade (INC) model to simulate FSIs. Since pion is the most important among the hadrons in this analysis, we take the simulation of pion FSI as an example. The simulations of other hadrons' FSI can be found in [180]. Pions are allowed to undergo quasi-elastic scattering, charge exchange, absorption, and pion production within the nucleus. The interaction positions and kinematics of the initial and final states are determined us-

ing a Woods–Saxon nucleon density function [206] and the local Fermi-gas model. The mean free path for pion interactions is modeled by Salcedo *et al.* [207]. Other mesons are treated similarly as high momentum pions. The same interactions with other nuclei in the detector outside the target nucleus are referred to as secondary interactions (SIs). NEUT includes six parameters that scale the probabilities of different FSI processes. For absorption and pion production processes, each of them is assigned a scale parameter. For charge exchange and elastic scattering without additional hadron production, separate scale parameters are defined for pions with momentum above and below 500 MeV/c.

9.2.5 Summary

The $\nu_e(\bar{\nu}_e)$ and $\nu_\mu(\bar{\nu}_\mu)$ cross sections as a function of neutrino energy for a water target are shown in Figure 9.4. The total cross sections are broken down to the contribution from each interaction mode.

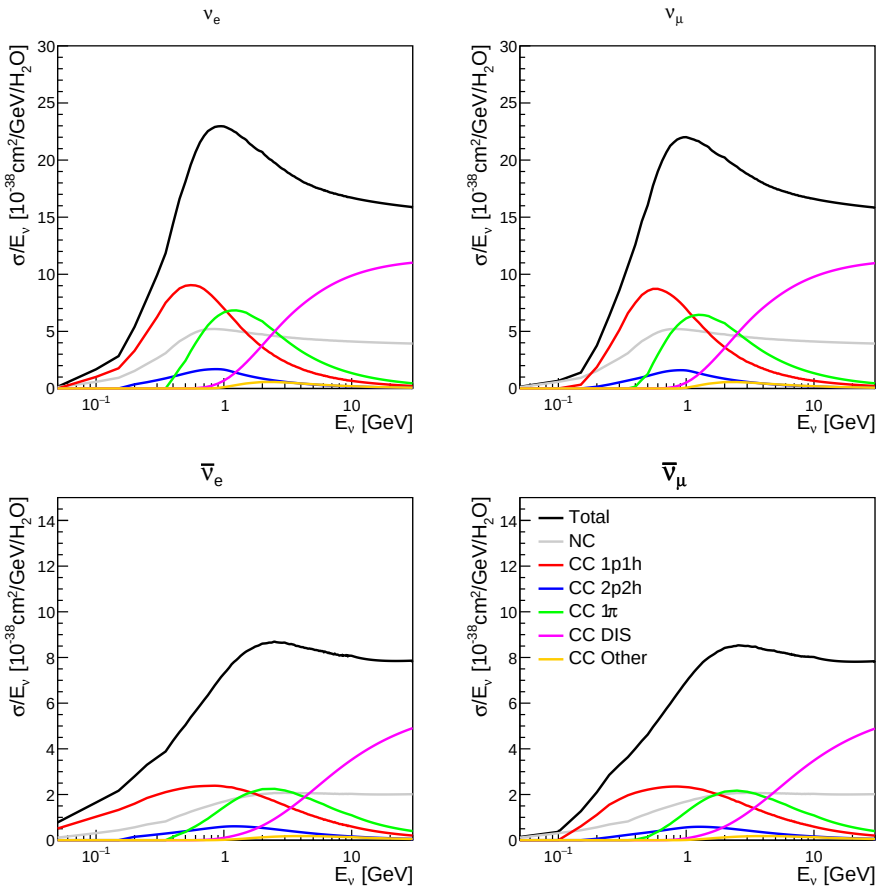

Figure 9.4: Neutrino cross sections as a function of energy for a water target for electron neutrino (top left), muon neutrino (top right), electron anti-neutrino (bottom left), and muon anti-neutrino (bottom right). The different lines show the contribution from each interaction mode. "CC DIS" refers to the sum of deep-inelastic scattering and multi-pion production. "CC Other" refers to single, non-pion hadron production.

9.3 Detector Response

After simulation of neutrino interactions by NEUT, the outgoing particles are input into SKDETSIM. SKDETSIM, developed based on CERN's GEANT [181] package, handles particle tracking, secondary interactions, Cherenkov radiations, detector photoelectric conversion, and detector electronics. It provides a model of the SK detector, calibrated as described in Sec. 3.4.

Within SKDETSIM, SIs are simulated using a combination of hadronic interaction models. For hadrons with momenta lower than 500 MeV/c, the NEUT FSI model (Sec. 9.2.4) is called. Above 500 MeV/c, the GEANT built-in CALOR package [208] is used to simulate hadronic interactions.

Cherenkov radiation emission in water for charged particles is simulated within GEANT. Additional custom features are implemented to model the SK detector precisely. The Rayleigh and Mie scattering of the water transparency model is tuned for SK (see Sec. 3.4.2). Customized Tyvek and PMT models (see Sec. 3.4.2) are also implemented. The PMT model considers the incident angle and wavelength of incident photons and the relative quantum efficiency of each PMT. In addition to relative quantum efficiency, an overall quantum efficiency, COREPMT, measured using downward through-going cosmic-ray muons, is applied to all PMTs.

Optical processes upon the PMT surface are simulated such that photons may produce photoelectron, or may be reflected, absorbed, or transmitted through the photocathode without generating a photoelectron. However, as discussed in Sec. 3.4.2, the internal structure of the PMT is missing in this model, which may be the reason for the discrepancies in the PMT reflectivity calibrations. The development of a new PMT model that enables simulations of optical processes on the PMT's internal structure is outlined in Appendix A. Note that none of the MCs in this analysis used the new PMT model.

The detector electronics are also simulated to predict the PMT signals. The measured single photoelectron distributions (see Sec. 3.4.1) are used to model the conversion between the number of incident photoelectrons and the pulse height. Dark noise and saturation effects are also considered.

For the purpose of this analysis, 500 years of atmospheric neutrino MC events are generated under the SK I phase detector condition. Figure 9.5 shows the neutrino energy distribution for the simulated SK I atmospheric neutrino MC. The distribution is broken down to the contribution from each interaction mode.

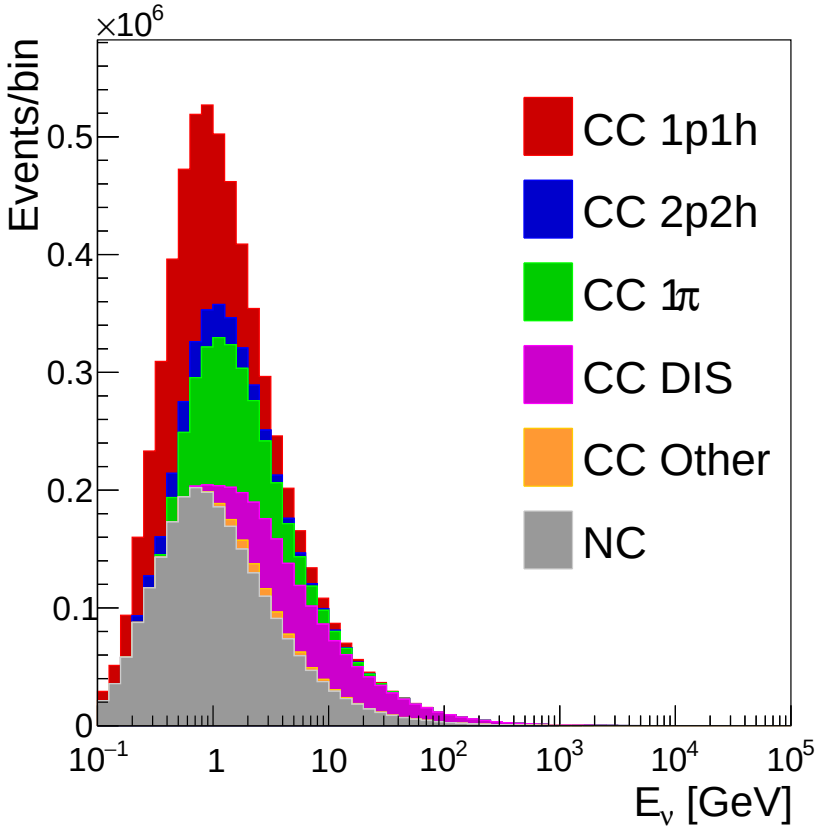

Figure 9.5: Neutrino energy distribution of 500 years of atmospheric neutrino MC. The different stack histograms show the contribution from each interaction mode. "CC DIS" refers to the sum of deep-inelastic scattering and multi-pion production. "CC Other" refers to single, non-pion hadron production.

Chapter 10

Data Reduction

Among the tremendous triggers recorded in the SK detector, only a small fraction of them are true atmospheric neutrino interactions. This requires a selection of the atmospheric neutrino candidate events, called "data reduction". In SK, the following types of background events are known to contaminate the atmospheric neutrino data:

- Cosmic-ray muons
- PMT light emission due to discharge (referred to as "flasher")
- Low-energy events due to radioactivity

Data reduction can remove the above background event efficiently.

Atmospheric neutrino candidates can be classified as fully-contained (FC) events, partially contained (PC) events, and upward-going muon (Up-μ) events. In this analysis, only SK I FC events are used. Therefore, the data reduction for partially contained events and upward-going muon events are not described. A comprehensive review of data reduction for atmospheric neutrino data in SK can be found in [209]. In this chapter, data reduction for fully-contained events is described.

10.1 Data Reduction for Fully-Contained Events

The definition of an FC event is that the neutrino interacts in the fiducial volume of the detector, and the generated particles deposit all energy in the ID. This analysis uses a 2 m fiducial volume cut ($D_{\mathrm{wall}} > 200\,\mathrm{cm}$), i.e. an inner cylindrical volume located 2 m from the ID walls. The FC reduction consists of five sequential reduction steps which are described below. The first and second reductions are rough, simply using PMT-level information, to quickly reduce the number of events to be processed in subsequent reductions. The third, fourth and fifth reductions use output quantities

from fitters to make more precise selections.

10.1.1 First Reduction

In the first reduction, two cuts are applied:

1. $PE_{300} > 200$ p.e. (100 p.e. in SK II),

   where PE_{300} is the number of photoelectrons in the ID within a 300 ns sliding window. The unit "p.e." denotes photoelectron.

2. $NHITAC_{800} \leq 50$ (55 for SK IV and later periods).

   where $NHITAC_{800}$ is the number of OD hits between -500 ns and +300 ns around the trigger time.

Criterion 1 rejects radioactive background. Figure 10.1 shows the PE_{300} distributions for the raw data and the FC data. The threshold roughly corresponds to a momentum of 22 MeV/c assuming an electron. Criterion 2 rejects cosmic-ray muons, which produce a lot of hits in the OD. The $NHITAC_{800}$ distributions for the raw data and the FC data are shown in Figure 10.2. After the first step, the event rate decreases from 10^6 events/day to $\sim$ 3500 events/day, with almost 100% selection efficiency for neutrinos.

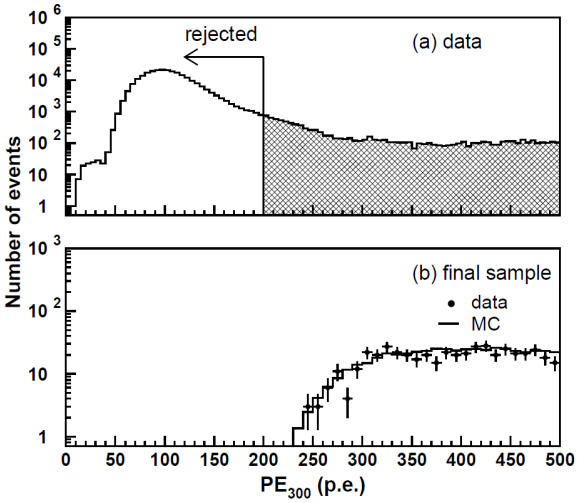

Figure 10.1: The PE_{300} distributions for (a) the data before selection and (b) the final FC sample in comparison with un-oscillated MC for SK I. The number of the MC events is scaled to that of data. Criterion 1 in the first reduction is indicated by the arrow. Taken from [210].

10.1.2 Second Reduction

The second reduction consists of the following selection criteria:

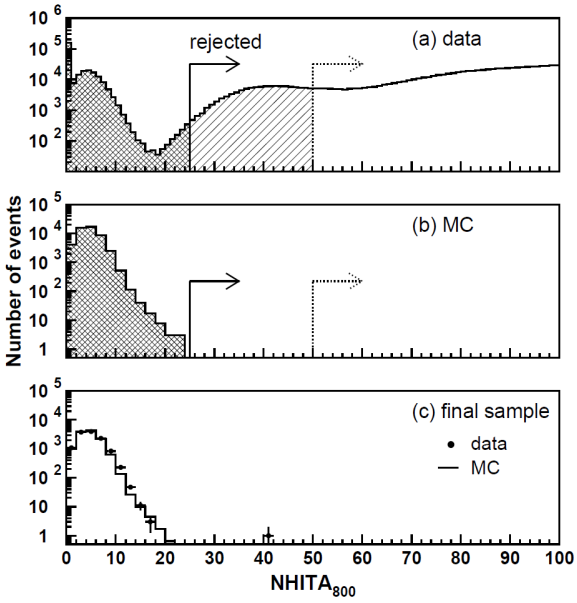

Figure 10.2: The $NHITAC_{800}$ distributions for (a) the data before selection, (b) the FC MC events with a vertex 2 m away from the ID wall, and (c) the final FC sample in comparison with un-oscillated MC for SK I. The number of the MC events in (c) is scaled to that of data. The dotted arrows indicate Criterion 2 in the first reduction, while the solid arrows indicate Criterion 2 in the second reduction. Taken from [210].

1. $PE_{max}/PE_{300} < 0.5$,

   where PE_{max} is the maximum charge observed in a single ID PMT.

2. $NHITAC_{800} \leq 25$ (30 for SK IV and later periods), or $PE_{total} > 100\,000$ p.e. (50 000 p.e. for SK II),

   where PE_{total} is the total number of photoelectrons in the ID.

Criterion 1 rejects low-energy events and flasher events, where a large fraction of the charge may be detected by a single PMT. A flasher event is caused by a PMT undergoes internal discharge and emits light detectable by other PMTs. Figure 10.3 shows the distributions of the ratio PE_{max}/PE_{300} for the data before and after this cut. Criterion 2 is used to reject cosmic-ray muons by a tighter threshold than the first reduction. This criterion is shown in Figure 10.2. The second step reduces the event rate to $\sim$ 200 events/day.

10.1.3 Third Reduction

Cosmic-ray muons that for some reason have a small number of OD hits may pass the first and second reductions. The reason may be that muons lose energy as a result of radiation or pair production, instead of ionization, leaving short bursts of light in the OD. It may also be due to muons entering the detector through the cable holes

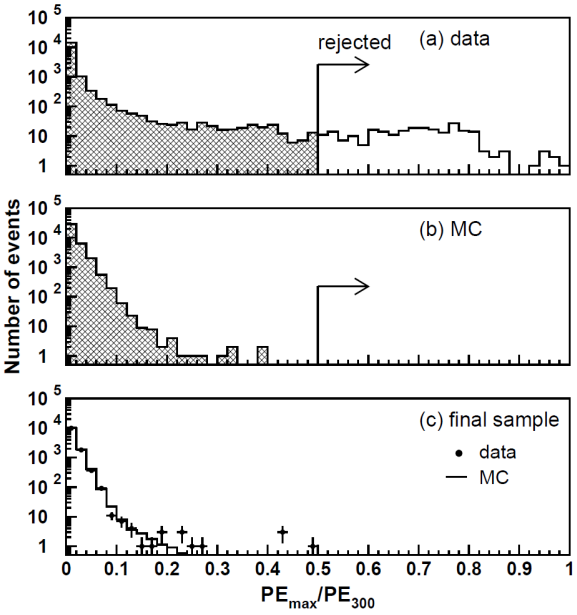

Figure 10.3: The distributions of the ratio PE_{max}/PE_{300} for (a) the data before the second reduction, (b) the FC MC events with a vertex 2 m away from the ID wall, and (c) the final FC sample in comparison with un-oscillated MC for SK I. The number of the MC events in (c) is scaled to that of data. The arrows indicate Criterion 1 in the second reduction. Taken from [210].

where there are no active OD PMTs around. Low-energy events may also pass the previous reductions due to accidental coincidence. In addition, some flasher events remain after the second reduction. The third reduction addresses these background events, as discussed in the following.

Through-going muon cut

Cosmic-ray muons that enter and exit the ID are referred to as through-going muons. These muons are identified using a muon track fitter. For events satisfying the following criterion:

1. There are more than 1000 ID hits, and the maximum charge on a single PMT is greater than 230 photoelectrons.

The entry point for a through-going muon candidate is found by searching for the earliest saturated ID PMT. The exit point is assumed to be at the geometric center taken over all saturated ID PMTs, found by maximizing the *goodness*:

$$goodness = \frac{1}{\sum_i \frac{1}{\sigma_i^2}} \sum_i \frac{1}{\sigma_i^2} \exp -\frac{(t_i - t_0)^2}{2(\sigma_i \times 1.5)^2}, \tag{10.1}$$

where t_i and σ_i are the observed hit time at the i^{th} PMT corrected by the time of flight (TOF) and its resolution, t_0 is the muon entry time chosen to maximize the

goodness at each test exit point. Events are rejected if the following criteria are met.

2. *goodness* > 0.75.

3. There are no less than 10 OD hits within an 8 m radius of the entry or exit point.

The distributions of the number of OD hits near the entry and exit point of muons for data before and after Criterion 3 in SK I are shown in Figure 10.4.

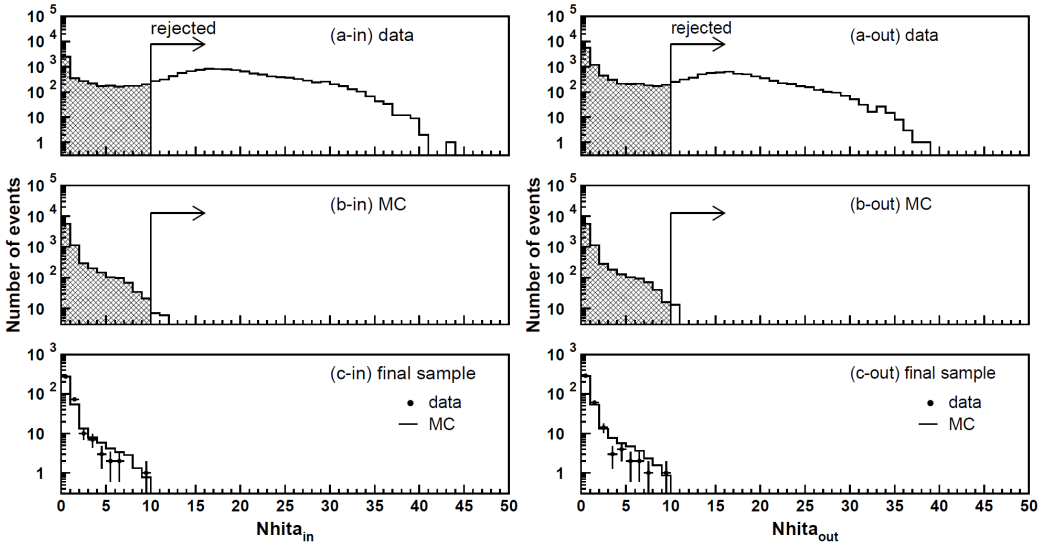

Figure 10.4: Number of OD hits within an 8 m radius of the entry point (left) and the exit point (right) of muons. The distributions for (a) the data before the third reduction, (b) the FC MC events, and (c) the final FC sample in comparison with un-oscillated MC for SK I. The number of the MC events in (c) is scaled to that of data. The arrows indicate Criterion 3 in the through-going muon cut in the third reduction. Taken from [210].

Stopping muon cut

A stopping muon is a cosmic-ray muon that enters the ID and stops, thus there is no exit point. The entry point of a stopping muon candidate is found by maximizing the same *goodness* as used in the through-going muon cut. If a stopping muon candidate meets the following criteria, it will be rejected.

1. There are no less than 5 OD hits within an 8 m radius of the entry point (10 for SK II and later periods).

2. *goodness* ≥ 0.5 (SK I only, Eq. 10.1).

Cable hole muon cut

Cosmic-ray muons passing through the cable holes may not produce enough hits in the OD to be rejected in the previous reductions. These events are defined as cable

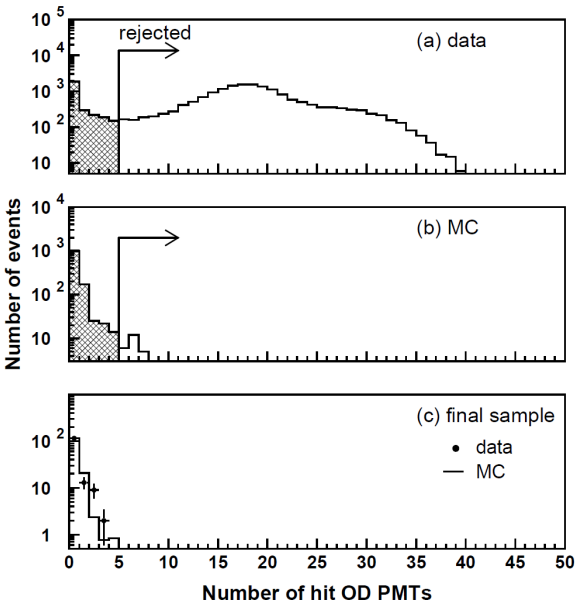

Figure 10.5: Number of OD hits within an 8 m radius of the entry point of muons. The distributions for (a) the data before the third reduction, (b) the FC MC events, and (c) the final FC sample in comparison with un-oscillated MC for SK I. The number of the MC events in (c) is scaled to that of data. The arrows indicate Criterion 2 in the stopping muon cut in the third reduction. Taken from [210].

hole muons. Veto modules are installed above four out of the twelve cable holes, as illustrated in Figure 10.6. Events that fulfill the following criterion are rejected.

1. Any veto module is activated within a 4 m radius of the entry point. which is found using the stopping muon fitter.

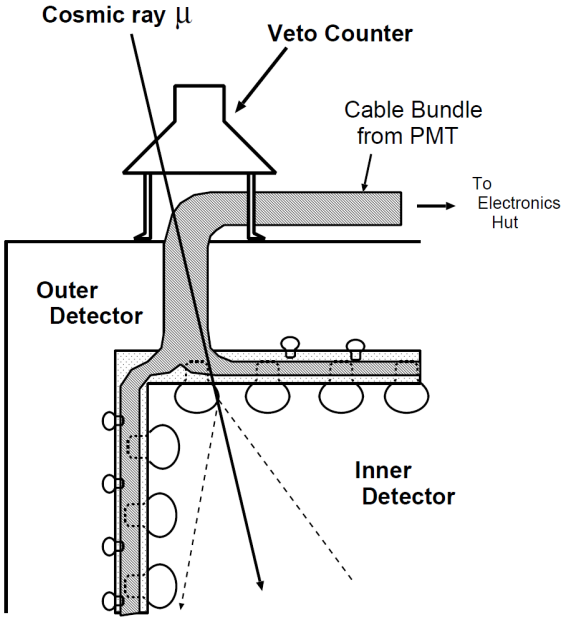

Figure 10.6: A schematic of a veto module for cable hole muons. Taken from [210].

Low-energy event cut

Low-energy events due to multiple accidental coincidences can evade the previous reductions. The key characteristic to separate neutrinos from these background is that a single vertex is expected for a true neutrino, otherwise there is no single best-fit vertex. The vertex is chosen to maximize the *goodness* defined in Eq.(10.1). This vertex is TOF-subtracted to be used in the cuts below. Events that meet the following criteria are rejected.

1. $\mathrm{NHIT}_{\mathrm{total}} < 500$,

   where $\mathrm{NHIT}_{\mathrm{total}}$ is the number of ID hits.

2. $N_{50} < 50$ (25 for SK II),

   where N_{50} is the number of TOF-subtracted ID hits within a sliding 50 ns time window.

Coincidence muon event cut

A cosmic-ray muon arriving after a low-energy event can still pass the above cuts because there is no OD hits around the trigger time. These events are referred to as coincidence muon events. They are identified and rejected if they satisfy the following criteria:

1. $\mathrm{NHITAC}_{\mathrm{late}} \geq 20$,

   where $\mathrm{NHITAC}_{\mathrm{late}}$ is the number of OD hits found between +300 ns and +800 ns.

2. $\mathrm{PE}_{\mathrm{late}} > 5000$ p.e. (2500 p.e. for SK II),

   where $\mathrm{PE}_{\mathrm{late}}$ is the total number of photoelectrons in the ID between +300 ns and +800 ns.

Flasher event cut

Since flasher events feature a long tail in the timing distribution, different from Cherenkov light, the following criteria are used to identify and reject flasher events:

1. (SK I only) $\mathrm{NHIT}_{\mathrm{min100}} \geq 15$ (10 if $\mathrm{NHIT}_{\mathrm{total}} \leq 800$),

   where $\mathrm{NHIT}_{\mathrm{min100}}$ is the minimum number of ID hits within a sliding 100 ns window from +200 ns to +700 ns, and $\mathrm{NHIT}_{\mathrm{total}}$ is the total number of ID hits.

2. (SK II and later periods) $\mathrm{NHIT}_{\mathrm{min100}} \geq 20$.

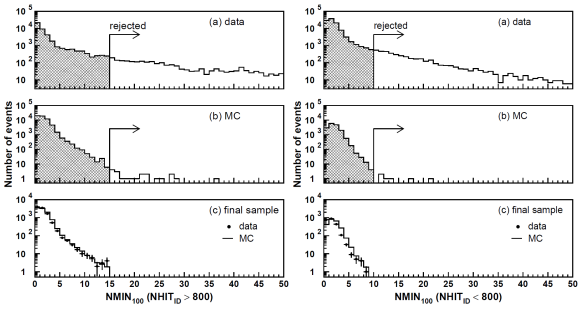

Figure 10.7: The $\mathrm{NHIT}_{\mathrm{min100}}$ distributions in SK I (left) for the events with $\mathrm{NHIT}_{\mathrm{total}} > 800$ and (right) $\mathrm{NHIT}_{\mathrm{total}} \leq 800$. The distributions for (a) the data before the third reduction, (b) the FC MC events, and (c) the final sample are shown. The number of the MC events are normalized to that of the data. The arrows indicate Criterion 1 in the flasher event cut in the third reduction. Taken from [210].

Figure 10.7 shows the $\mathrm{NHIT}_{\mathrm{min100}}$ distributions for the data before and after Criterion 1 in SK I. In addition to the above criteria, flasher events are also found using the low-energy event fitter. Events are rejected if the following criteria are met:

3. $\mathrm{NHIT}_{\mathrm{total}} \leq 250$.

4. *goodness* ≤ 0.4 (Eq. 10.1).

Approximately 50 events/day remain after this reduction step.

10.1.4 Fourth Reduction

The fourth reduction is to further remove flasher events using a pattern match algorithm. Reference flasher events are selected by experts and put into a database. A new event is compared with the reference events found within one year before or after the candidate event. Two variables, the correlation r and the Kolmogorov-Smirnov (KS) test statistic d_{KS}, are used to compare the hit patterns of the reference events and the new events to be processed.

To compute these two variables, ID PMTs are first grouped into 2 m × 2 m patches. Then r is written as:

$$r = \frac{1}{N} \sum_i \frac{(Q_i^A - \langle Q^A \rangle) \times (Q_i^B - \langle Q^B \rangle)}{\sigma_A \times \sigma_B}, \tag{10.2}$$

where N is the number of patches, i is the index of the patch, $Q_i^{A(B)}$ is the total charge of the i^{th} patch for event A and event B, respectively. $\langle Q^{A(B)} \rangle$ and $\sigma_{A(B)}$ are the average charge and its standard deviation. A large value of r indicates a similarity between the two events. d_{KS} is defined as the largest difference of normalized cumulative distribution functions of $Q_i^{A(B)}$. Events with a similar hit pattern produce

a small value of d_{KS}.

The 10 largest values of r and the 10 smallest values of d_{KS} are fed into a likelihood function. Events which produce a likelihood value with exceed a pre-defined threshold are rejected. After this step, the event rate decreases to $\sim$ 18 events/day.

10.1.5 Fifth Reduction

The fifth reduction is to further remove the coincidence muons, flasher events, stopping muons, and cable hole muons. In addition to these background events, the fifth reduction also addresses background caused by "invisible muons".

Invisible muon cut

Low-energy cosmic-ray muons may enter the ID without producing signals in the OD sufficient for veto, thus being invisible. This can also happen for low-energy neutrino interactions where a pion or a muon with a momentum below the Cherenkov threshold is produced. However, decay electrons from these muons can produce background events. Typically, the invisible muon background is accompanied by OD hits several μs before the ID trigger. In light of this, two types of OD activities are sought, i.e., the OD hit cluster within a 200 ns sliding time window from -9000 ns to -200 ns, and the OD hit cluster within a fixed time window between -200 ns and 200 ns. $\mathrm{NHITAC_{early}}$ and $\mathrm{NHITAC_{500}}$ denote the number of OD hits found in the first and second clusters, respectively. Based on these two quantities, the following criteria are introduced to identify and reject the invisible muon background.

1. The total charge in the ID is smaller than 1000 p.e. (500 p.e. for SK II).
2. $\mathrm{NHITAC_{early}} \geq 5$, if the two OD hit clusters are at least 500 cm away from each other.
3. Otherwise, $\mathrm{NHITAC_{early}} + \mathrm{NHITAC_{500}} \geq 10$.

Events that meet the above criteria are rejected as invisible muons. Figure 10.8 illustrates Criterion 2. The distributions of $\mathrm{NHITAC_{early}}$ for the data before and after this criterion and satisfying Criterion 1 are shown.

Coincidence muon event cut

The remaining coincidence muon events that passed the third reduction are addressed here. Events that meet the following criteria are rejected as coincidence muon events:

1. $\mathrm{PE_{500}} < 300$ p.e.,

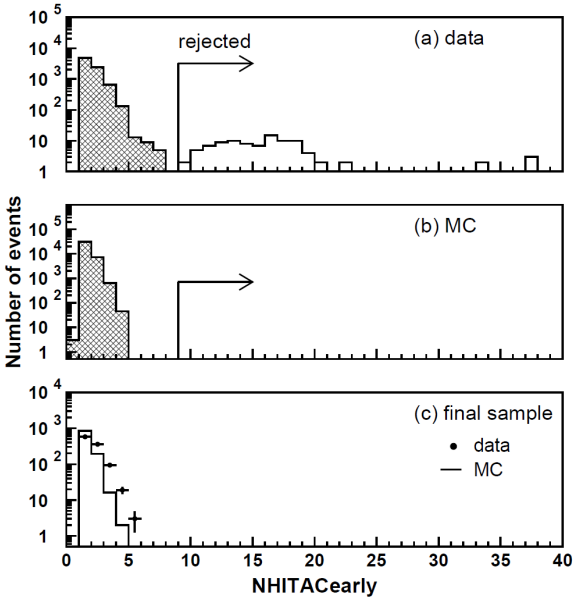

Figure 10.8: The distributions of $\mathrm{NHITAC}_{\mathrm{early}}$ for (a) the data before the fifth reduction, (b) the FC MC events, and (c) the final sample are shown. The samples shown here are with a total charge greater than 1000 p.e. and a distance of at least 500 cm between the two OD hit clusters. The number of the MC events are normalized to that of the data. The arrows indicate Criterion 2 in the invisible muon cut in the fifth reduction. Taken from [210].

where PE_{500} is the number of photoelectrons found in the ID between -200 ns and +300 ns.

2. $\mathrm{NHITAC}_{\mathrm{late}} \geq 20$ (16 for SK IV and later periods),

   where $\mathrm{NHITAC}_{\mathrm{late}}$ is the maximum number of OD hits found in a 200 ns sliding time window from +400 ns to +1600 ns.

Flasher event cut

Stricter cuts than those in the third reduction are applied to reject the remaining flasher events. Events that match any of the following criteria are rejected:

1. $goodness < 0.3$,

   where *goodness* is computed using Eq.(10.1).

2. $goodness < 0.4$ and $\mathrm{NHIT}_{\mathrm{min}} \geq 6$, where $\mathrm{NHIT}_{\mathrm{min}}$ is defined in Sec. 10.1.3.

Stopping muon cut

The remaining stopping muons are further removed based on the reconstructed entry point. Events that satisfy the following criterion are rejected:

1. There are no less than 4 OD hits found in a 200 ns window sliding from -500 ns to +300 ns, within an 8 m radius of the entry point.

Cable hole muon cut

Stricter cuts are introduced to reject the remaining cable hole muons that passed the third reduction. The output quantities of the stopping muon fitter are used.

1. $goodness \geq 0.4$.
2. $\mathrm{PE}_{\mathrm{total}} > 4000$ p.e..
3. $\cos\theta_z > 0.6$,

   where θ_z is the reconstructed zenith angle, and $\cos\theta_z = 1$ means the particle is vertically downward-going.
4. $d_{\mathrm{hole}} < 2.5$ m,

   where d_{hole} is the distance from the muon entry point to the closest cable hole.

10.1.6 FC reduction summary

After the FC reduction, the FC event rate decreases to $\sim$ 16 events/day. To select the final FC sample, the following cuts are applied:

1. NHITAC < 10 (16 for SK II and later periods),

   where NHITAC is the number of OD hits in the most energetic OD cluster.
2. Reconstructed visible energy $E_{vis} > 30$ MeV.

   where E_{vis} is defined as the sum of the reconstructed kinetic energy above the Cherenkov threshold for all rings,
3. $dwall > 200$ cm,

   where $dwall$ is the minimum distance from the reconstructed primary event vertex to the ID wall.

Events that satisfy the above criteria are selected as the final FC sample. Since most of the remaining background are near the ID wall, a fiducial volume cut, as described in criterion 3, is introduced. This defines a fiducial volume of 22.5 kton. After the final cuts, 12259 FC events are selected in the 1489.2-day SK I data-taking period. The event rate for SK I is 8.23 ± 0.07 events/day. The FC neutrino detection efficiency and the total event rate for each reduction step are summarized in Table 10.1.

All selected events are manually inspected to determine the background rate and the corresponding systematic uncertainty in the final analysis sample. The major background sources that remain are cosmic-ray muons and flasher events.

Table 10.1: The event rate per day and the detection efficiency in each reduction step for SK I.

Reduction step	Event rate [day^{-1}]	Efficiency [%]
Pre-reduction	$\sim 1.2 \times 10^6$	-
1st reduction	~ 3000	99.95
2nd reduction	~ 200	99.94
3rd reduction	~ 45	99.85
4th reduction	~ 18	99.17
5th reduction	~ 16	99.15
Final cut	8.23 ± 0.07	97.59

Chapter 11

Event Reconstruction

The properties of the selected particles, including the event vertex, momenta, directions, particle types, and number of visible particles, are inferred from the charge and timing information collected by PMTs. This process is called "event reconstruction". In SK, there is a conventional reconstruction tool "APFit" that has been used for nearly 30 years, and a newer precision reconstruction tool "fiTQun".

FiTQun is more precise than APFit as shown in the previous study for SK IV [211]. In this analysis, fiTQun is applied to the SK I data. However, discrepancies between the data and the MC are observed in the reconstructed quantities. The same discrepancies are not observed when using APFit. Possible reasons are investigated and detector simulation is optimized to resolve this issue. This chapter will provide a short introduction to APFit, followed by a description of fiTQun. The optimization of detector simulation is also presented.

11.1 Conventional reconstruction algorithm APFit

APFit is an algorithm that sequentially reconstructs the event vertex, number of rings, particle types, and momenta. Further information can be found in [212]. The algorithm begins by estimating the interaction vertex using the hit time from PMT. This initial estimate is refined through additional fits that incorporate the TOF of photons and the expected charge distribution. Once the vertex is established, APFit identifies Cherenkov rings using the Hough transformation method, which detects ring patterns by summing virtual circles drawn around PMT hits. Candidate rings are evaluated using a likelihood test to determine whether they represent true Cherenkov rings, with up to five rings reconstructed per event.

Each ring is then classified as either electron-like or muon-like based on the shape of the Cherenkov ring and the measured Cherenkov angle. An electron-like ring has

a fuzzier edge than a muon-like ring, as shown in Fig 11.1. Low-energy muons and pions tend to have smaller Cherenkov angles, while it is usually 42° for electrons.

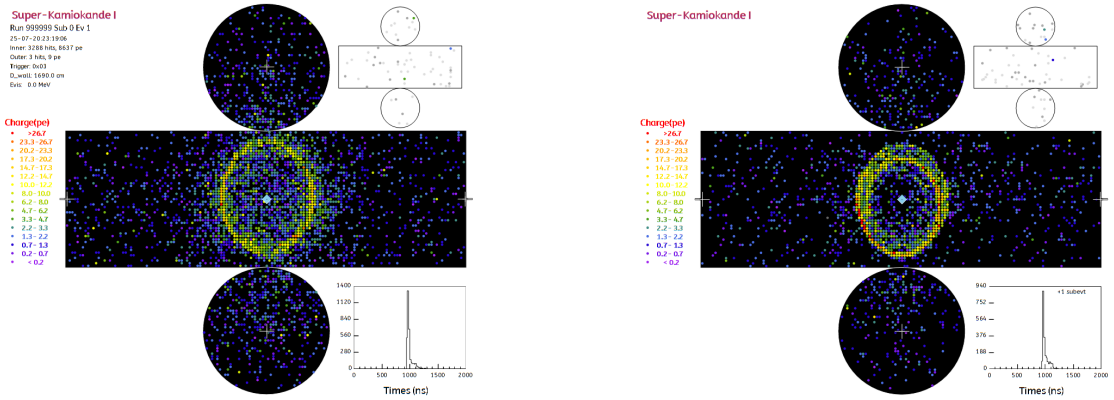

(a) Positron (b) Anti-muon

Figure 11.1: Event display of simulated Cherenkov rings for (a) a 1 GeV positron and (b) a 1 GeV anti-muon.

In single-ring events, the vertex and ring direction are further refined using a likelihood-based approach. For multi-ring events, APFit separates the observed charge among the different rings, enabling an accurate momentum estimation for each ring. The momentum is calculated using corrected charge values, taking into account factors like water attenuation and scattered light. Finally, low-energy rings that are likely to be noise or redundant are merged or discarded based on energy and angular criteria.

In terms of performance, APFit achieves a vertex resolution of about 30 cm for single-ring events and roughly 1 m for multi-ring cases. Directional resolution for charged particles is around one degree for high-energy events and a few degrees at lower energies, whereas momentum resolution is typically within a few percent, with better accuracy for muons.

11.2 Precision reconstruction algorithm fiTQun

FiTQun is an algorithm for reconstructing events at SK, developed based on the algorithm [213] for the MiniBooNE experiment. While APFit only takes into account the hit PMTs around the Cherenkov cone, fiTQun uses more information, including the hit PMTs outside the Cherenkov cone and the PMTs which do not register hits. In addition, fiTQun iterates several times to determine the best kinematics parameters, instead of the sequential single iteration of APFit. These support the precision of fiTQun, but also make the fitting process more time-consuming. FiTQun has been used for the SK IV analyzes [211], the T2K analyzes [78], and the SK-T2K joint analyzes [214], allowing fiducial volume expansion thanks to the improved precision of reconstruction quantities.

11.2.1 The Likelihood Function

The likelihood function is the basis of event reconstruction in fiTQun. The track parameters to be reconstructed for a single particle in the detector are: vertex position $\boldsymbol{x}$, time t, zenith angle θ, azimuth angle ϕ, and momentum p. The most likely values for these parameters are found by maximizing the likelihood function, which is written as below:

$$L(\boldsymbol{x}) = \prod_{j}^{\text{unhit}} P_j(\text{unhit}|\boldsymbol{x}) \prod_{i}^{\text{hit}} (1 - P_i(\text{unhit}|\boldsymbol{x})) f_q(q_i|\boldsymbol{x}) f_t(t_i|\boldsymbol{x}), \tag{11.1}$$

where $\boldsymbol{x}$ denotes a set of track parameters. The index i runs over all PMTs that registered a hit and j runs over the PMTs that didn't register a hit. For the PMTs that do not register a hit, the unhit probability $P_i(\text{unhit}|\boldsymbol{x})$ is multiplied, which is the probability of the i^{th} PMT does not a hit given the track parameters $\boldsymbol{x}$. For the PMTs that register a hit, the hit probability $(1 - P_i(\text{unhit}|\boldsymbol{x}))$, the charge likelihood $f_q(q_i|\boldsymbol{x})$, and the time likelihood $f_t(t_i|\boldsymbol{x})$ are multiplied. The charge likelihood is the probability density function (PDF) of observing charge q_i at the i^{th} PMT, given $\boldsymbol{x}$. The time likelihood is the PDF for the i^{th} PMT to register a hit at time t_i, given $\boldsymbol{x}$.

Since the Cherenkov photon emission process is independent of the properties of the PMTs and the electronics, the track parameters $\boldsymbol{x}$ in the charge likelihood can be replaced with the expected charge $\mu_i(\boldsymbol{x})$ liberated on the i^{th} PMT, given $\boldsymbol{x}$. Thereby, the Cherenkov photon emission process is addressed by the calculation of $\mu_i(\boldsymbol{x})$. The unhit probability and the charge likelihood reflect only the detector's PMT response and electronics.

The expected charge μ_i consists of the expected charge from direct light and that from indirect light. The term direct light refers to the Cherenkov photons that directly hit the PMT. Indirect light is the photons that are scattered or reflected before generating photoelectrons. The expected charge from direct light is calculated by modeling how many Cherenkov photons, emitted by a particle as it moves through water, reach a PMT and produce a signal. This depends on the path and energy of the particle, the direction of emitted light, how much light is lost in water, and how efficiently the PMT detects it. All of these factors are combined to estimate the expected charge from direct light at each PMT.

The expected charge from indirect light is estimated by averaging the light emission over all directions along the path of the particle and applying a pre-computed "scattering table" that accounts for how indirect light spreads through the detector. This table is built from simulations and depends on the positions and orientations of the particle and the PMT. For multiple tracks, the expected charge of each track

is calculated and summed to form a total expected charge at the PMT. The unhit probability and the charge likelihood are computed assuming that the number of photoelectrons obey a Poisson distribution with mean being the expected charge μ.

The time likelihood is computed by comparing the observed PMT hit time to the expected arrival time of Cherenkov photons. Since the time likelihood has a complex dependency on $\boldsymbol{x}$ and the PMT position *etc*, approximations are necessary to realize the computation. Instead of the raw hit time t_i, the residual time t_i^{res} is used, which is defined as:

$$t_i^{\mathrm{res}} \equiv t_i - t - s_{\mathrm{mid}}/c - |\boldsymbol{R}_{\mathrm{PMT}}^i - \boldsymbol{x} - s_{\mathrm{mid}}\boldsymbol{d}|/c_n, \tag{11.2}$$

where $\boldsymbol{x}$ and t are the position and time of the vertex, $\boldsymbol{d}$ is the direction of the particle, $\boldsymbol{R}_{\mathrm{PMT}}^i$ is the position of the i^{th} PMT, s_{mid} is half the track length, and c and c_n are the speed of optical photons in vacuum and water, respectively. This formula assumes that the particle is relativistic and that the Cherenkov photons are emitted at the midpoint of the track. The time likelihood is then approximated to depend only on t_i^{res}, the expected charge from direct light and that from indirect light, and the momentum of the particle. Separate time models are used for direct and indirect light as they have distinct t_i^{res} distributions. The t_i^{res} PDF of direct light is assumed to be Gaussian, with parameters depend on the momentum of the particle and the expected charge from direct light. The indirect light model captures delayed signals from scattered or reflected photons and assumes a broad, asymmetric distribution featuring a long tail. The contributions from direct light and indirect light are then weighted based on the predicted charges: the more direct light is expected at a PMT, the more likely it is that the observed hit comes from direct light. This combined PDF is the time likelihood contribution that will be multiplied into Eq. 11.1.

11.2.2 Fitting Procedure

The fiTQun reconstruction procedure consists of four steps. The first step is vertex pre-fitting, where the primary vertex of the event is roughly estimated using only the PMT hit time. Then, fiTQun searches for subevents, which are PMT hits clustered in time. This is referred to as hit clustering. The third and fourth steps are single-ring fitting and multi-ring fitting, where the events are fitted literally assuming a single visible particle and multiple visible particles. MINUIT [215] package is used to minimize the negative log likelihood ($-\ln L$).

Vertex pre-fitting

FiTQun uses a fast algorithm to obtain a rough vertex position $\boldsymbol{x}$ and time t, which is used as a seed in subsequent fittings. This is called the vertex pre-fitter and is run at

the beginning of processing every event. The most likely values of $\boldsymbol{x}$ and t are found by maximizing the goodness which is written as

$$G(\boldsymbol{x}, t) \equiv \sum_{i}^{\text{hit}} \exp(-(T^i_{\text{res}}/\sigma)^2/2), \tag{11.3}$$

where

$$T^i_{\text{res}} \equiv t_i - t - |\boldsymbol{R}^i_{\text{PMT}} - \boldsymbol{x}|/c_n. \tag{11.4}$$

T^i_{res} is analogous to t^{res}_i Eq. 11.2, however, assumes a point-like light source located at the vertex instead of a the midpoint of the track. The vertex pre-fitter first performs a coarse grid search in the ($\boldsymbol{x}$, t) parameter space. The grid search will iterate several times while shrinking the allowed parameter space. After that, $-G(\boldsymbol{x}, t)$ is minimized using MINIUIT with $\sigma = 4\,\text{ns}$.

Hit clustering

Multiple subevents which are clusters of ID PMT hits in time can be contained in one event, e.g. a muon decaying into an electron can produce a delayed hit cluster in addition to the primary event trigger by the muon itself. FiTQun uses several algorithms to identify and separate these subevents.

The first step is the Peak Finder, which identifies the subevent activities around the event trigger time. By fixing the vertex position $\boldsymbol{x}$ at the pre-fit vertex and varying the time t, the Peak Finder scans the goodness as given by Eq. 11.4. The parameter σ is set to 6.3 ns and the scan starts at 300 ns before the event trigger time, with an 8 ns step. Figure 11.2 is an example of the goodness distribution for a muon decay event. Two dominant peaks are hits caused by the muon and the decay electron. There are also fake peaks after the two dominant peaks, which can be produced by scattered light or reflected light. To identify peaks, a threshold function is constructed as

$$F(t) \equiv 0.25 \max_{i \in M}(G(\boldsymbol{x}, t) f(t - t_i)) + \eta, \tag{11.5}$$

where

$$f(t - t_i) \equiv \frac{1}{1 + (t - t_i)^2/\gamma^2}, \gamma = \begin{cases} 25\,\text{ns} & (t - t_i < 0) \\ 70\,\text{ns} & (t - t_i \geq 0). \end{cases}$$

M represents all local maxima of the goodness $G(\boldsymbol{x}, t)$, and the offset η is set to 9. During the scan, the first peak is found at the first local maximum where the goodness exceeds $F(t)$, shown as the blue line. In order to suppress fake peaks, another threshold is employed. A subsequent peak is found when the local maximum is greater than $F(t)$ and there is at least one scan point after the previous peak falls below $0.6 \times F(t)$, shown as the green line.

While the Peak Finder assumes the vertices of the subevents are can near the pre-fit vertex, this assumption can be broken if the primary particle travels a long distance before producing secondary particles. The peak in the goodness distribution can be smeared, resulting in a missing subevent. This usually happens to a muon decaying into an electron. To resolve this issue, the vertex pre-fitting is rerun after masking the hits in the first subevent, such that the best-fit vertex position is close to the secondary particle. Then, the Peak Finder is run again to search for subevents with updated vertex position. More information is documented in [216]. The number and the time of the peaks that are found by the Peak Finder are regarded as the number and the time of the subevents associated with the event.

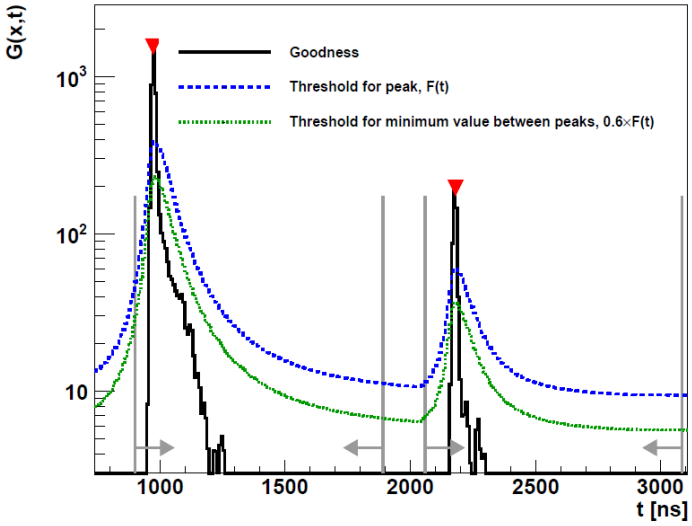

Figure 11.2: An example of the scanned goodness $G(\boldsymbol{x}, t)$ distribution for a muon decay event, as a function of time t. The black line is the scanned goodness. Two thresholds $F(t)$ and $0.6 \times F(t)$ are shown as blue and green lines. Subevents found in this event are labeled by red triangles and their time windows are indicated with gray lines. Taken from [216].

Next, the spliTChan algorithm clusters hits that are close in time to form "time clusters". It starts from a time t_{rise}, where a 70 ns window has more than 9 hits. An offset is applied to shift t_{start} to 30 ns earlier ($t_{start} = t_{rise} - 30\,\text{ns}$) in order to catch early hits. Then, it expands the window to include late hits. The late edge of the time window is defined as $t_{end} = t_{fall} + t_{extend}$, where t_{fall} is found when the 70 ns window has no more than 9 hits and the duration between t_{fall} and t_{start} is $\geq$ 70 ns, and $t_{extend} = \max(0, -\frac{320}{800} \times nHits + 320)$. $nHits$ is the total number of hits in the cluster between t_{start} and t_{fall}. Any two adjacent clusters are merged if t_{end} of the earlier cluster is within 30 ns of the later one. This accounts for the fact that Cherenkov light can arrive over extended periods, especially when reflections or low light levels are involved.

Finally, subevent–cluster association is performed. Each subevent found in the

Peak Finder is matched to one of the spliTChan time clusters based on timing consistency. Subevents without a matching cluster are discarded, and clusters without subevents are ignored. When multiple subevents fall within a single cluster, they are treated as "in-gate" subevents and are fitted using shared hit data.

Single-ring fitting

After the vertex pre-fitting and the hit clustering, the single-ring fitter is performed on each subevent found in the previous step. The likelihood function Eq. 11.1 is maximized to obtain the best-fit values of the track parameters. Before running the fitter, the initial values of the track parameters have to be determined properly to avoid local maxima. The initial vertex position is set to the pre-fit vertex position, and the initial time is set to the peak time. The initial direction is found by scanning a grid of 400 points equally spaced on the unit sphere, with the momentum fixed. After that, all track parameters except the momentum are fixed to estimate the momentum seed value. When the initial values of the track parameters are set, single-ring fits are performed for all of the hypotheses: electron, muon, and charged-pion, *etc.*

The particle types are identified by comparing the best-fit likelihood values between different particle hypotheses. The process is called particle identification (PID). For example, to identify whether a particle is more likely a muon or an electron, the log likelihood ratio between the best-fit likelihood values of muon and electron hypotheses $\ln(L_e/L_\mu)$ is used.

Multi-ring fitting

In fiTQun, the multi-ring fitter is only applied to the first subevent. It runs up to 6-ring fits assuming every combination of all particle hypotheses. The multi-ring hypothesis is constructed by adding a new ring on top of the previous fit result iteratively, using the likelihood in Eq. 11.1. The kinetics parameters are varied in order to maximize the likelihood. To decide to whether add a new ring, the improvement in the best-fit likelihood gained by adding a new ring must be sufficient to indicate the presence of an additional particle. In other words, the log likelihood ratio between the previous fit and the new fit must exceed a certain threshold, because the increased degree-of-freedom inevitably results in an improved likelihood. For e-like events, the threshold for separating single-ring events and 2-ring events is 9.35. For μ-like events or charged-pion-like events, the threshold is 11.83. For multi-ring fits above 2-rings, the threshold is 8.37 regardless of e-like or μ-like or charged-pion-like events. The above process is repeated, until a new ring hypothesis is rejected or the number of rings reaches six.

The fitted rings are examined to remove fake rings. When a particle scatters off a

nucleus in the detector, its direction relative to the original track is usually less than 20°. Therefore, two rings with angular separation less than 20° will be merged into a new single ring, which will be refitted for all particle hypotheses. The other rings are fixed during this process. This is done for all ring candidates in descending order of their momenta.

The π^0 fit is a special multi-ring fit in fiTQun. A π^0 decays into two photons, which produce two e-like tracks via pair productions after traveling a distance. This distance is referred to as photon conversion length. The π^0 fit in fiTQun consists of two e-like rings, whose tracks point back to the same vertex position and time. The photon conversion length for each photon is taken into account, fitted for on an event-by-event basis. FiTQun uses the results of the single-ring fit for the e-like hypothesis to identify the first photon track. The second ring is seeded by a rough scan. Then, the direction, momenta, and photon conversion length of both rings, and their common vertex position and time are varied to find the best-fit values.

11.3 Optimizing the SK I PMT Response Model

As fiTQun presents excellent performance in the previous study for SK IV [211], it is natural to apply fiTQun to all SK data. In order to apply fiTQun to the SK I data, a performance check was performed. However, a data-MC discrepancy is observed in the PID likelihood distributions, where the e-like ($\ln(L_e/L_\mu) > 0$) MC distribution shifts to higher likelihood values than the data distribution, as shown in Figure 11.3. The PID likelihood distribution is for sub-GeV ($30\,\mathrm{MeV} < E_{vis} < 1330\,\mathrm{MeV}$) 1-ring samples in the SK I phase, where E_{vis} is the visible energy of the ring. In the left panel, a deficit of the MC events for $0 < \ln(L_e/L_\mu) < 400$, and an excess of the MC events for $1000 < \ln(L_e/L_\mu) < 2000$ are observed, suggesting an overall shift of the MC distribution to higher PID likelihood values. The right panel shows the ratio of the data over the MC, where the shift is seen more obviously. Such data-MC discrepancy is not observed in the APFit PID likelihood distribution as shown in Figure 11.4, and not observed in the fiTQun PID likelihood distribution for the SK IV period (Figure 11.5).

The difference in ring patterns between the e-like particles and the μ-like particles is that, Cherenkov rings produced by electrons tend to have fuzzy edges due to electromagnetic showers, while those produced by muons or charged pions have clear edges. As discussed in section 11.1 and 11.2 APFit and fiTQun are two distinct reconstruction tools. The fiTQun likelihood considers all PMTs, including those without registering hits. On the other hand, the APFit likelihood is computed using the corrected charge only from PMTs within an opening angle of 1.5 times the Cherenkov angle, θ_C, with respect to the particle's direction. In other words, fiTQun is more

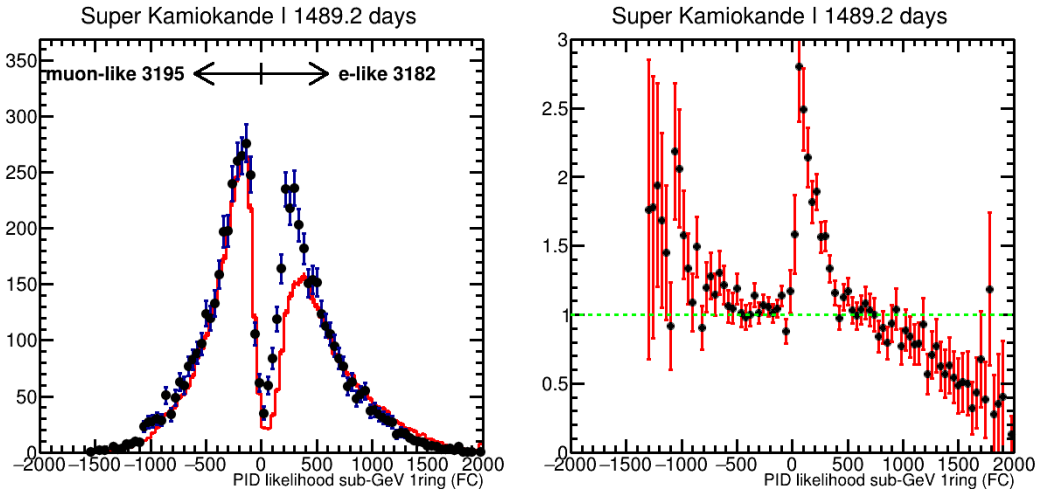

Figure 11.3: FiTQun PID likelihood ($\ln(L_e/L_\mu)$) distribution for sub-GeV single-ring events in the FC atmospheric neutrino samples. The data distribution (black dots) is compared with the MC distribution (red histogram) in the left panel. The ratio of data over MC is shown in the right panel. Events with likelihood < 0 is classified as μ-like, and those with likelihood>0 is classified as e-like. The MC is weighted by oscillation probability assuming normal mass ordering. The oscillation parameters are set to $\sin^2\theta_{12} = 0.307$, $\sin^2\theta_{13} = 0.022$, $\sin^2\theta_{23} = 0.546$, $\Delta m^2_{12} = 7.53 \times 10^{-5}\,\mathrm{eV}^2$, $\Delta m^2_{23} = 2.453 \times 10^{-3}\,\mathrm{eV}^2$, $\delta_{CP} = 0$. The same oscillation parameters are applied below.

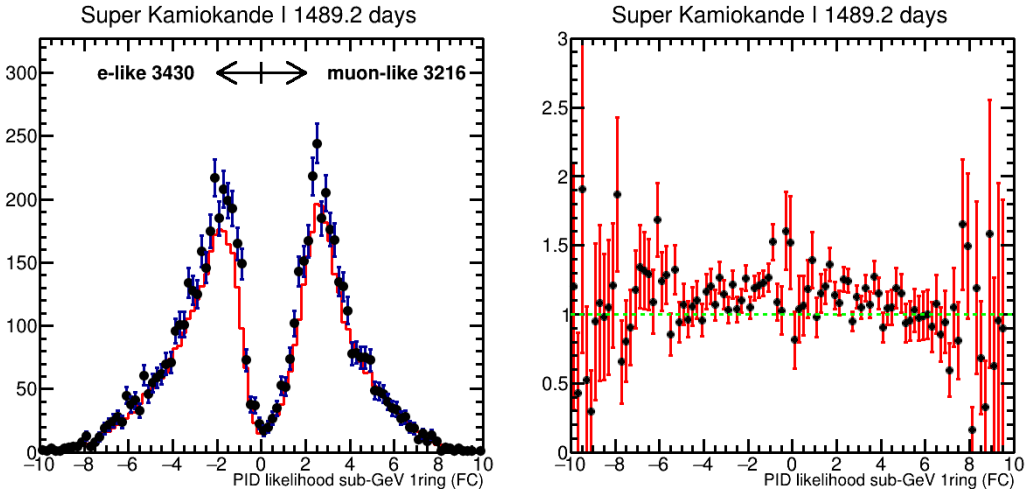

Figure 11.4: APFit PID likelihood ($\ln(L_e/L_\mu)$) distribution for sub-GeV single-ring events in the FC atmospheric neutrino samples. The representations are the same as those in Figure 11.3.

sensitive to the hit pattern compared to APFit.

To investigate the PMT hit pattern of true electron tracks, sample of decay electrons from cosmic-ray muons (Michel electrons) is used. Figure 11.6 shows the hit profile and charge profile of the Michel electrons in SK I. Hits within a TOF-subtracted residual time between -10 ns and +10 ns are selected, such that the hits are mostly due

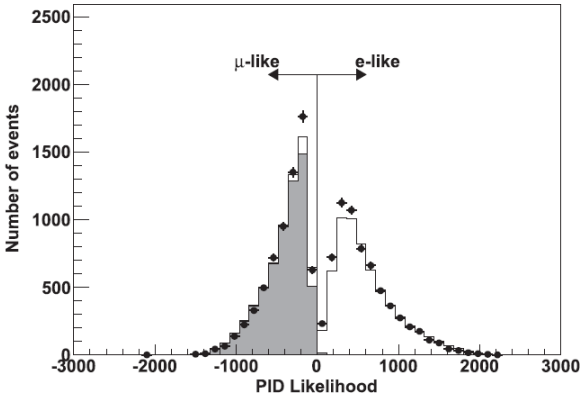

Figure 11.5: FiTQun PID likelihood distribution for FC sub-GeV 1-ring samples in the SK IV period. The dots denote FC atmospheric neutrino data and the line denotes MC. The shaded histogram shows the true ν_μ CC MC events. Taken from [211].

to direct Cherenkov lights. The horizontal axes θ are the angle between the direction of the particle and the connecting line between the vertex position and the hit PMT. The top left plot shows the event-by-event number of hits (nhits) as a function of θ, and the top right plot shows the hit-by-hit charge as a function of θ. The ratio of the data over the MCs are plotted in the bottom panels. The MC distributions are normalized by the number of events of the data. Both distributions peak at 42°, which is the opening angle of the Cherenkov cone of a relativistic particle in water. The plots show that there are more hits per event in the MC than in the data, while the charge per hit is lower in the MC. This suggests that the PMT response model for SK I in the detector simulator is inappropriate. It also provides a plausible explanation to the question why data-MC discrepancies are observed in fiTQun but not in APFit: fiTQun takes into account the probability that a PMT does not register a hit and therefore the extra hits with small charge can cause a large discrepancy on fiTQun while they have limited effects on APFit.

It is worth mentioning that different PMT response models are used in SK I, SK II, SK III, and SK IV and later periods. Moreover, in SK I the PMT response model for high-energy (e.g. atmospheric neutrino) analyses are different from that for low-energy analyses due to limited computational power. The single-PE distribution models and the threshold functions in SK I through SK IV are shown in Figure 11.7 and Figure 11.8. Therefore, the effect of the inappropriate PMT response model did not affect the low-energy analyses or the SK IV atmospheric neutrino analysis.

11.3.1 Optimization approach

To improve the PMT response model for high-energy analysis in SK I, a novel method using decay electrons from cosmic-ray muons (Michel electrons) is developed. The ideal method is to re-calibrate the single-PE distribution with the Nickel source data,

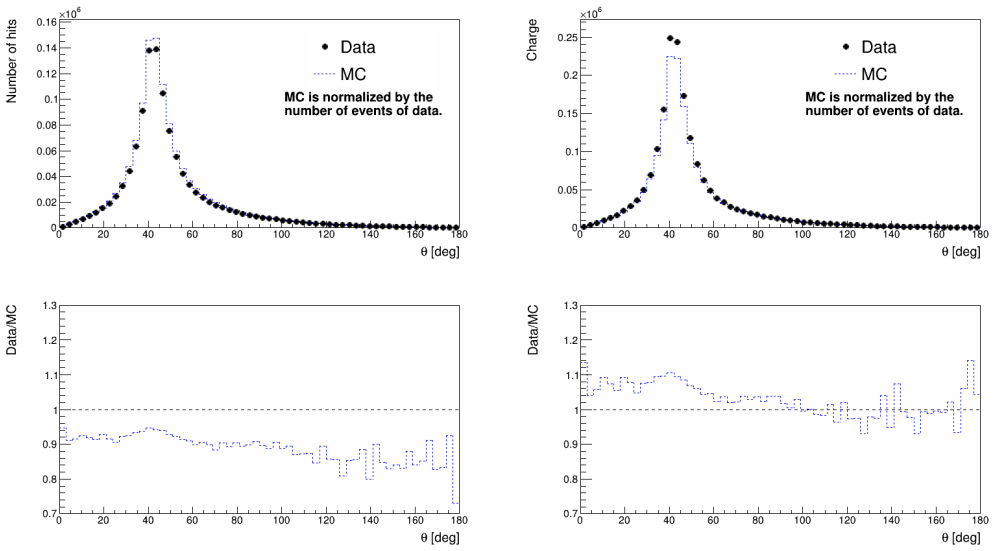

Figure 11.6: Hit (left) and charge (right) distributions of the SK I Michel electron sample as a function of θ, where θ is the angle between the direction of the particle and the connecting line between the vertex position and the hit PMT. **Top left:** The event-by-event number of hits (nhits) a function of θ. Dots denote the data, and blue dashed line denotes the MC normalized by the number of events of the data. **Bottom left:** The data/MC ratio of the nhits distribution. **Top right:** The hit-by-hit charge as a function of θ. **Bottom right:** The data/MC ratio of the charge distribution.

as discussed in Section 3.4.1. However, these data were lost over the years as they were taken nearly 30 years ago. Instead, the Michel electron data are used in this approach.

The Michel electron sample used in this approach is the same as that used in the energy scale uncertainty estimation, which will be discussed in Section B. Since a Michel electron has relatively low energy, a sizable fraction of the observed hits is due to single-PE. Choosing Michel electrons that are far from the ID walls along its own direction can make the Cherenkov light more sparse. Therefore, a cut requiring the vertex position of the electron at least 25 m away from the ID walls along its direction (Towall $>$ 25 m) is applied to further increase the purity of the single-PE hits, as illustrated in Figure 11.9. The purity of single-PE hits in Michel electron sample is improved to $\sim$ 90% after this cut. A residual time cut ($-10\,\text{ns} < T_{res} < 10\,\text{ns}$) is applied to select hits due to direct light.

After the selection cuts, the MC is used as a template to fit the data by varying the normalization and shifting and stretching the MC distribution, as illustrated in Figure 11.10. Assuming the proportion of single-PE hits in the MC is correct, this fraction is applied to the data to extract the single-PE distribution, as shown in Figure 11.11. The single-PE distribution of the data is then deconvolved with the threshold function to build the single-PE distribution model.

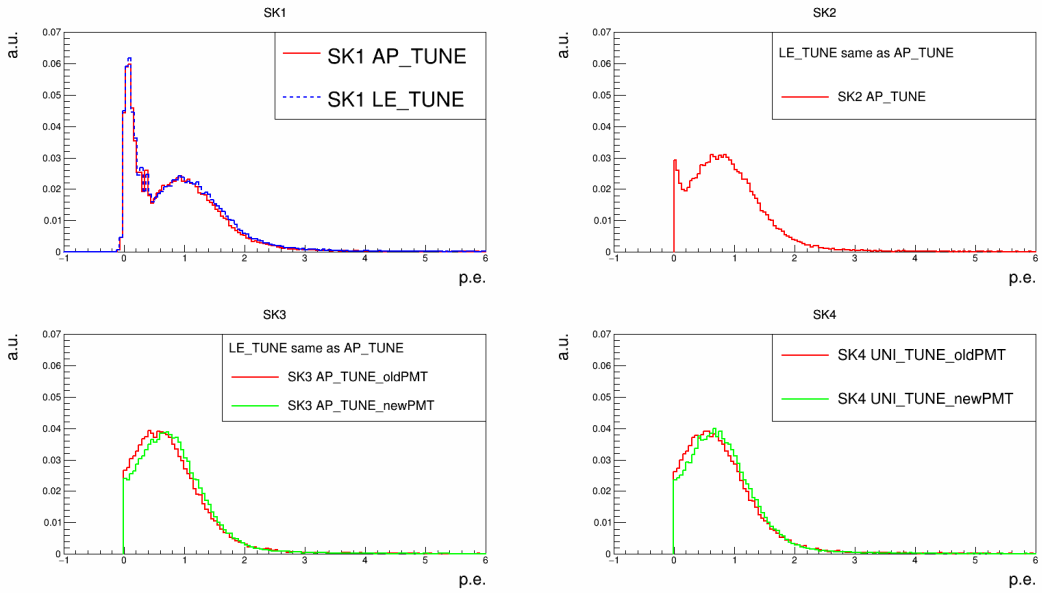

Figure 11.7: Single-PE distribution models in the SK simulator. **Top left:** Single-PE distribution models for SK I. The model for high-energy analyses is plotted as red line, and that for low-energy analyses is plotted as blue line. **Top right:** Single-PE distribution for SK II, common for high-energy and low-energy analyses. **Bottom left:** Single-PE distribution models for SK III. The red line denotes the model for old PMTs which survived the implosion, and the green line denotes the model for new PMTs installed after the implosion. The models are common for high-energy and low-energy analysis. **Bottom right:** Single-PE distribution models for SK IV. The red line is for old PMTs and the green line is for new PMTs. The models are common for high-energy and low-energy analysis.

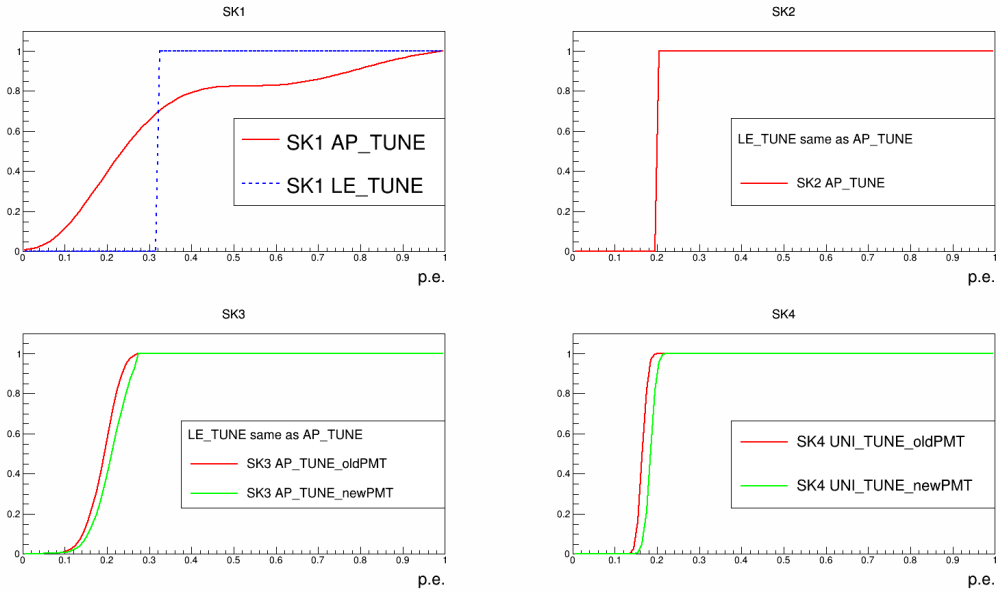

Figure 11.8: PMT threshold functions in the SK simulator. **Top left:** Threshold functions for SK I. **Top right:** Threshold function for SK II. **Bottom left:** Threshold functions for SK III. **Bottom right:** Threshold functions for SK IV. The representations are the same as those in Figure 11.7.

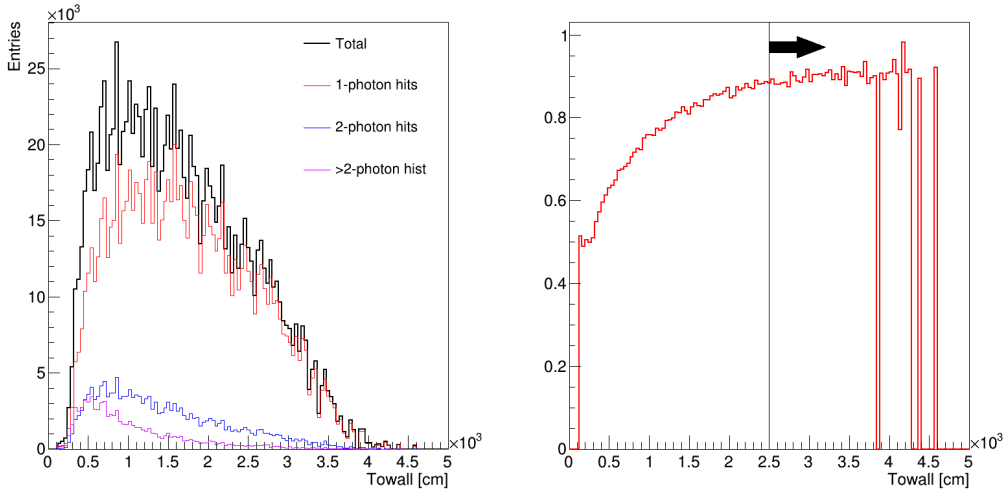

Figure 11.9: **Left:** Towall distribution of the Michel electron sample brokendown to number of photons in each hit. The black line denotes the total MC distribution. The red, blue and violet lines are the distribution of hits with 1 photons, 2 photons and more than 2 photons. **Right:** The proportion of hits with only 1 photon.

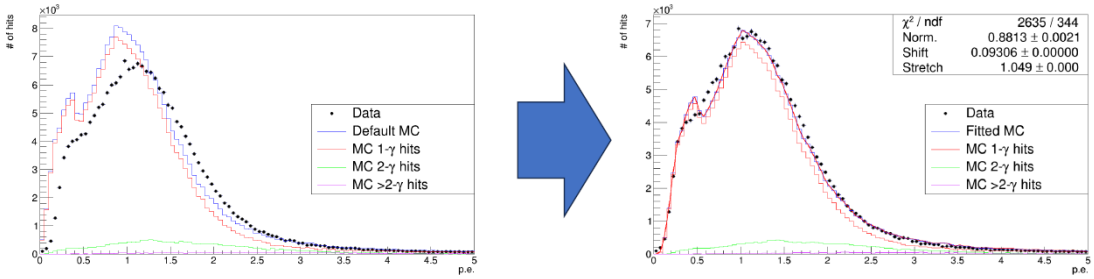

Figure 11.10: An illustration of the shifting and stretching approach. The data is fitted using the MC as a template. The data is plotted as dots, and the MC is plotted as blue lines. The MC is broken down to the hits with 1 photons, 2 photons and more than 2 photons, plotted as red, green, and violet lines, respectively. All of the components vary covariantly.

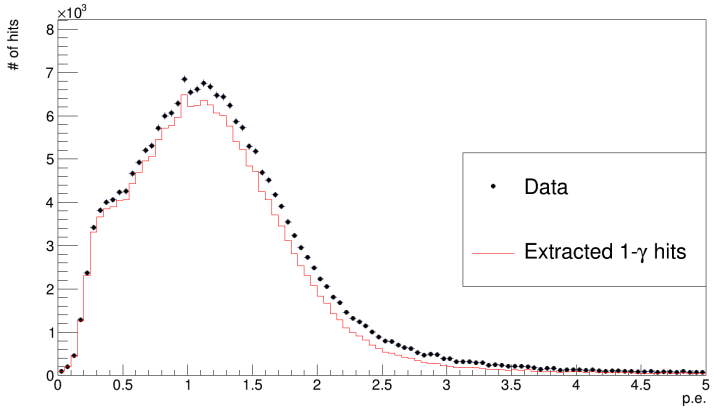

Figure 11.11: Single-PE distribution extracted from the Michel electron data. The Michel electron data after selection cuts are plotted as dots, and the extracted single-PE distribution is plotted as red line.

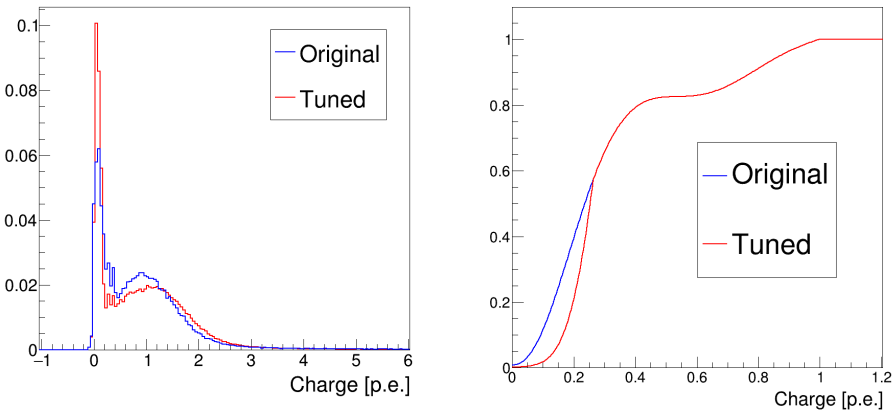

Figure 11.12: The improved single-PE distribution model (left) and threshold function (right) plotted as red lines. The original models are also plotted as blue lines for comparison.

The improved single-PE model and threshold function are shown in Figure 11.12. As discussed in Section 3.4.1, in the original model, the part where Q<0.3 pC is linear extrapolation of the measured distribution. In this tuning, this part is artificially increased such that the mean value of the model after tune is unchanged compared to the original model, given that the original MC's total charge agreed well with the data. The PMT threshold function is also modified accordingly to match with the Michel electron data. Figure 11.13 shows the hit profile and charge profile after tune. The data-MC agreement is improved compared to the original ones. The nhits distribution and the charge distribution are also shown in Figure 11.14. The PMT response model in fiTQun is also updated based on the simulation after tune.

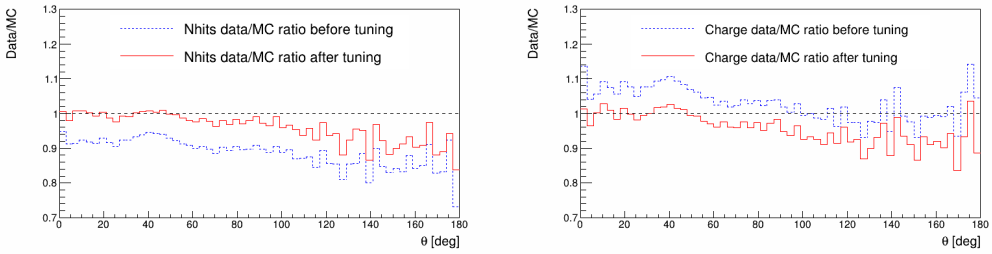

Figure 11.13: Data/MC ratio of hit (left) and charge (right) distributions of the SK I Michel electron sample as a function of θ, where θ is the angle between the direction of the particle and the connecting line between the vertex position and the hit PMT. The red lines denote the ratios after tune, and the blue dashed lines are the original ratios same as Figure 11.6.

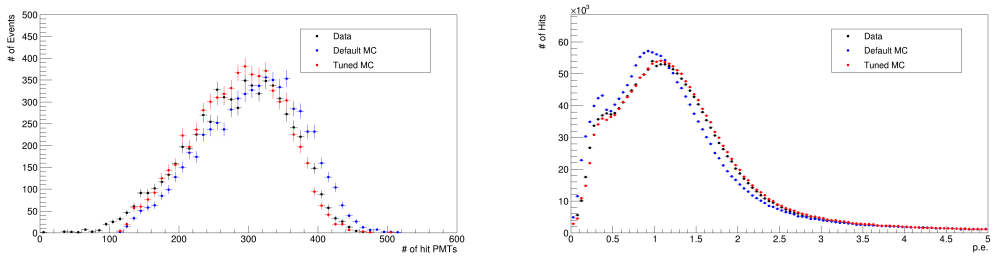

Figure 11.14: The event-by-event nhit distribution (left) and the hit-by-hit charge distribution. The black dots are the data, the blue dots are the original MC, and the red dots are the MC after tune.

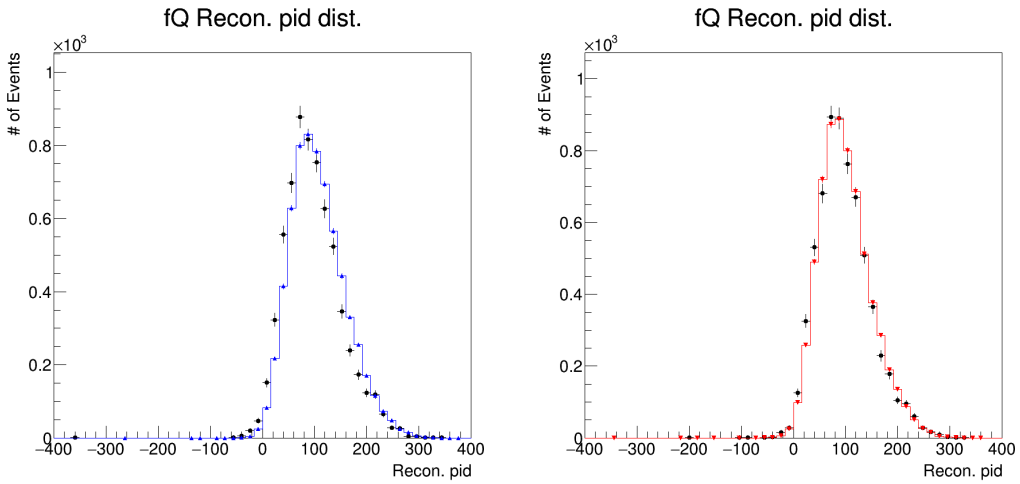

Figure 11.15: FiTQun PID likelihood distributions of the Michel electron sample before (left) and after (right) optimization. The data are plotted as black dots, and the MC before (after) optimization is plotted as blue (red) histogram.

11.3.2 Validation of the optimization

The improved PMT response model is validated using the control samples that are used in the estimation of energy scale uncertainty and the FC atmospheric neutrino samples. The fiTQun PID likelihood distributions of the Michel electron sample before and after tuning the PMT response model are shown in Figure 11.15. A good data-MC agreement for electron events is achieved after tune. The difference between the mean of the MC and the mean of the data ($\text{Mean}_{\text{MC}}/\text{Mean}_{\text{data}} - 1$) improved from 10.15% to 2.70%. Figure 11.16 shows the fiTQun PID distributions of the downward-going cosmic-ray muons (stopping muons) which stopped in the detector. No significant change is observed for muon events as expected.

Figure 11.17 shows the fiTQun PID likelihood distribution with improved PMT response model. The original distribution is on the left panel and the improved distribution is on the right panel. The two ratio plots share the same vertical range. The peak in the ratio where $\ln L_e/L_\mu > 0$ becomes lower, suggesting that the shift on the MC is mitigated. This tuning fixes the inappropriate PMT response for high-energy analyses in the SK I period, and partly resolves the PID likelihood issue of fiTQun.

We note that the PID likelihood discrepancy issue is not completely solved yet. The remainder suggests that fiTQun may be undertune in some aspect for SK I. Future efforts to further inspect the root cause of the PID likelihood issue is required. In particular, it is suggested to examine the hit-clustering algorithm of fiTQun. It is a known issue that the old electronics in SK I-III could not properly handle delay hits, which may require adjustment on the hit-clustering algorithm. However, the fiTQun

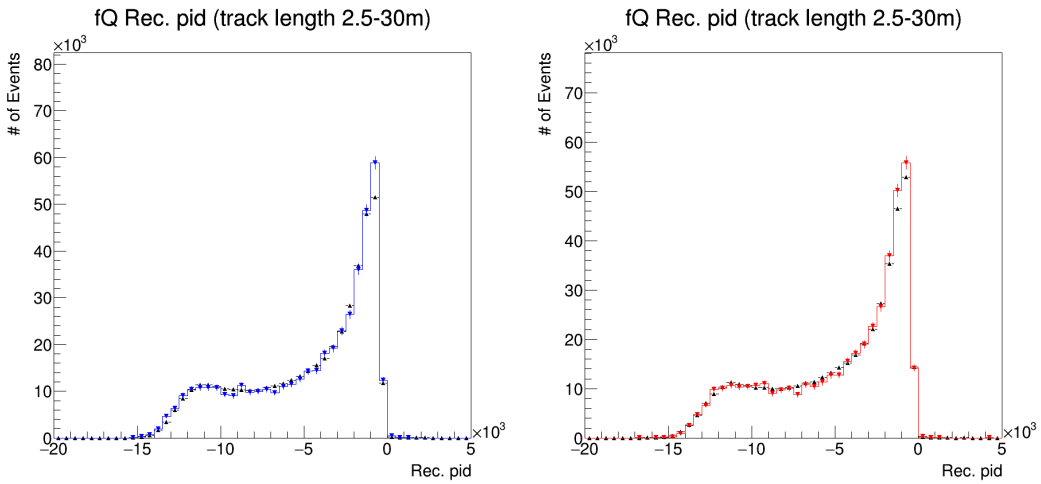

Figure 11.16: FiTQun PID likelihood distributions of the stopping muon sample before (left) and after (right) optimization. The data are plotted as black dots, and the MC before (after) optimization is plotted as blue (red) histogram.

hit-clustering algorithm is tuned according to the SK IV electronics and is used for SK I. This may result in an improper time window width, which can lead to a bias in the number of hits of an event and thus cause the ID likelihood discrepancy. One is also suggested to check if the PID likelihood discrepancy is related to the fiducial volume. The possible relation can be examined by dividing the FC neutrino samples into several subsamples with different distances to the detector walls, and checking if the shifts in the MC PID likelihood distributions become different. Furthermore, we noticed that the PID likelihood distributions of the two e-like rings in FC π^0 events show good data-MC agreements, as shown in Figure 12.10. It worth investigating why these gamma-induced e-like rings show different results than the electron-induced e-like rings in the neutrino samples. It is suggested to examine the possible relations between the PID likelihood distributions and the momenta of these rings.

11.4 Performance of fiTQun on the SK I Atmospheric Neutrino Sample

The performance of fiTQun on the SK I atmospheric neutrino MC is presented below. The vertex position resolution, direction resolution, and momentum resolution are first presented using MC samples that satisfy the following criteria:

- MC events pass FC selection.
- Reconstructed vertex position within the fiducial volume $D_{\text{wall}} > 200\,\text{cm}$.
- MC events are $\nu_e(\bar{\nu}_e)$ CCQE or $\nu_\mu(\bar{\nu}_\mu)$ CCQE events.

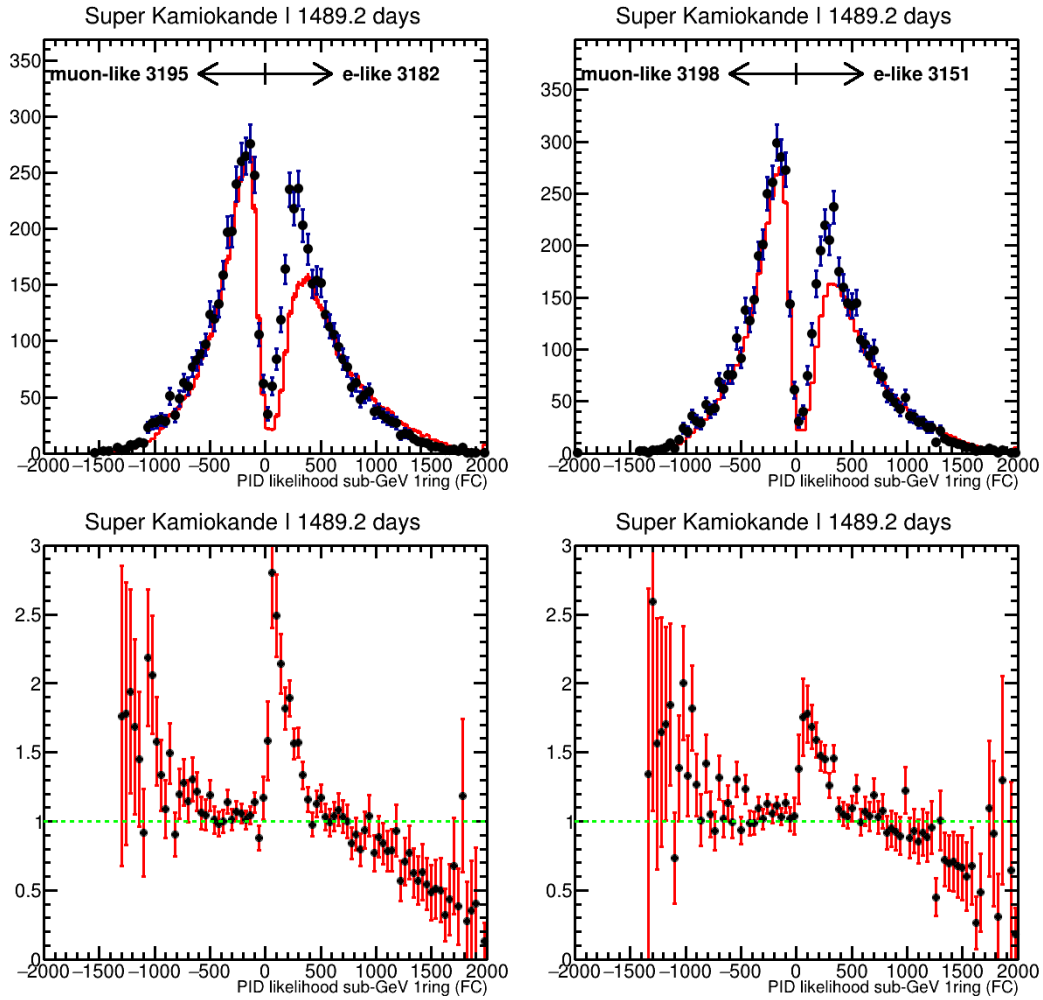

Figure 11.17: Side-by-side comparison of the fiTQun PID likelihood distribution for sub-GeV single-ring events in the FC atmospheric neutrino samples before (top left) and after tune (top right). The data distribution (black dots) is compared with the MC distribution (red histogram) in the left panel. The ratios of data over MC are shown in the bottom panels. The vertical axes of the ratio plots share the same range.

- Visible energy between 30 MeV and 1330 MeV.

Note that the definition of visible energy in fiTQun is slightly different from that in APFit. In APFit, visible energy is defined as the energy of an electromagnetic shower producing the same amount of Cherenkov light as observed in the event. In fiTQun, visible energy is defined as the part of the energy above the Cherenkov threshold, as written below:

$$E_{vis}^{fq} = \sqrt{(p_{rec}^2 + m_0^2)} - \sqrt{p_C^2 + m_0^2}, \tag{11.6}$$

where p_{rec} is the reconstructed momentum, m_0 is the mass at rest, and p_C is the Cherenkov threshold momentum defined as Eq. 3.2. Although the definitions are different, E_{vis} in fiTQun and APFit are comparable.

11.4.1 Vertex Resolution

Figure 11.18 shows the vertex displacement distributions for the CCQE electron and muon events in the SK I FC atmospheric neutrino samples, both by APFit and fiTQun. In addition to the above selection cuts, the true vertex positions are required to be within the fiducial volume. The vertex placement is defined as the distance from the reconstructed vertex position to the true vertex position. The vertex resolution is found by computing the 68.3 percentile, which are indicated by the vertical lines in the plots. Figure 11.19 presents the vertex resolutions of APFit and fiTQun as a function of E_{vis}. As a result, the vertex resolution of fiTQun for ν_e CCQE events is stable around 21 cm for 30 MeV $< E_{vis} <$ 1330 MeV, while the vertex resolution of APFit varies from 33.8 cm to 26.2 cm. For ν_μ CCQE events, fiTQun and APFit show similar trends as E_{vis} increases. The resolution of fiTQun for ν_μ CCQE events varies from 33.4 cm to 16.1 cm, while that of APFit varies from 33.7 cm to 18.9 cm. In both cases, fiTQun's performance on vertex reconstruction is better than APFit's performance.

11.4.2 Direction Resolution

The angular displacement distributions for the CCQE electron and muon events in the SK I FC atmospheric neutrino samples are shown in Figure 11.20. The angular displacement is defined as the angle between the reconstructed direction and the true direction. The definition of direction resolution is analogous to that of the vertex resolution. Figure 11.21 shows the direction resolutions as a function of E_{vis}. FiTQun has a similar performance as that of APFit for direction reconstruction. For ν_e CCQE samples, the direction resolution of fiTQun improves from 6.2° to 1.4° for 30 MeV $<$ $E_{vis} <$ 1330 MeV, while the direction resolution of APFit improves from 5.9° to 1.6° in the same energy range. For ν_μ CCQE events, it is 2.2° to 0.9° for fiTQun, and 2.2° to 1.1° for APFit.

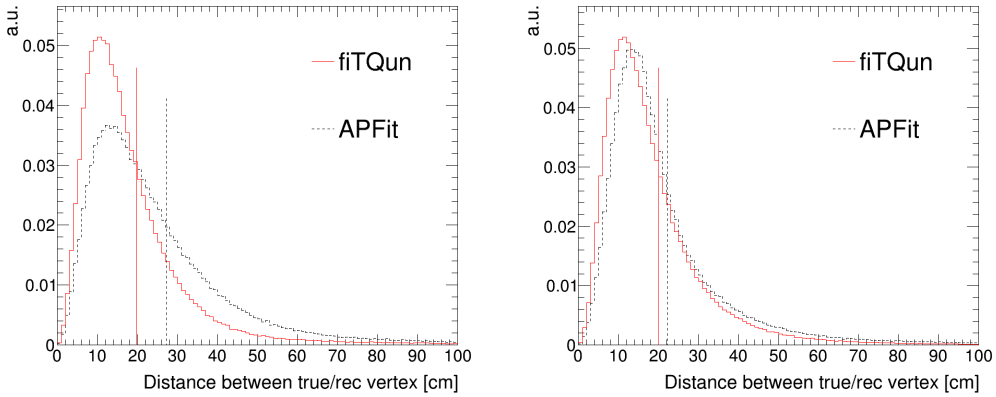

Figure 11.18: Vertex displacement distributions for single-ring electron (left) and muon (right) events in FC atmospheric neutrino CCQE samples. The red solid line is by fiTQun, and the black dashed line is by APFit. The vertical lines indicate the 68.3 percentile of the distributions. The true vertex positions are required to lie in the fiducial volume ($D_{\mathrm{wall}} > 200\,\mathrm{cm}$).

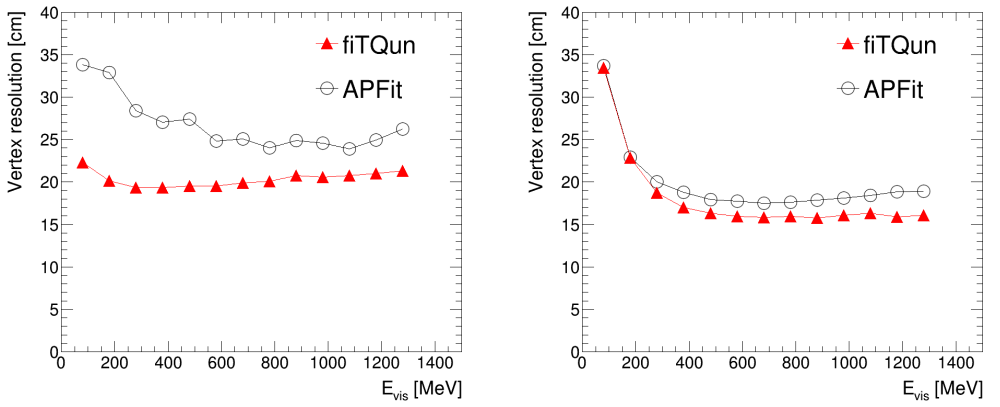

Figure 11.19: Vertex resolutions as a function of visible energy for single-ring electron (left) and muon (right) events in FC atmospheric neutrino CCQE samples. The red line with full triangles denotes the vertex resolution of fiTQun, and the black line with open circles denotes that of APFit.

11.4.3 Momentum Resolution

Figure 11.22 shows the ratio of the reconstructed momentum p_{rec} over the true momentum p_{true} for the same samples. The p_{rec}/p_{true} distribution is fitted by a Gaussian function at each E_{vis} bin, and the (1-μ) and the σ are reported as the bias and the resolution. μ is the mean and σ is the standard deviation. The derived momentum resolution and bias are shown in Figure 11.23. For ν_e CCQE events, the momentum resolution improves as E_{vis} increases. The momentum resolution of fiTQun is 6.6% in the first E_{vis} bin ($30\,\mathrm{MeV} < E_{vis} < 130\,\mathrm{MeV}$), and decreases to 2.9% in the last E_{vis} bin ($1230\,\mathrm{MeV} < E_{vis} < 1330\,\mathrm{MeV}$). As for APFit, the momentum

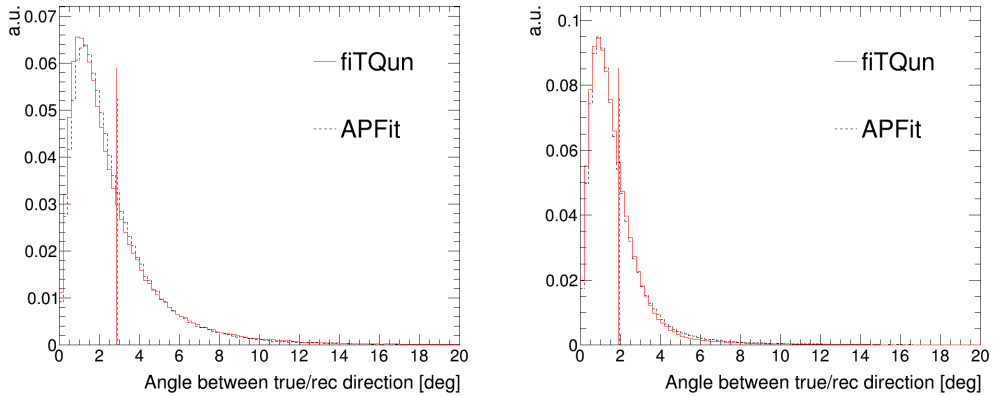

Figure 11.20: Angular displacement distributions for single-ring electron (left) and muon (right) events in FC atmospheric neutrino CCQE samples. The red solid line is by fiTQun, and the black dashed line is by APFit. The vertical lines indicate the 68.3 percentile of the distributions.

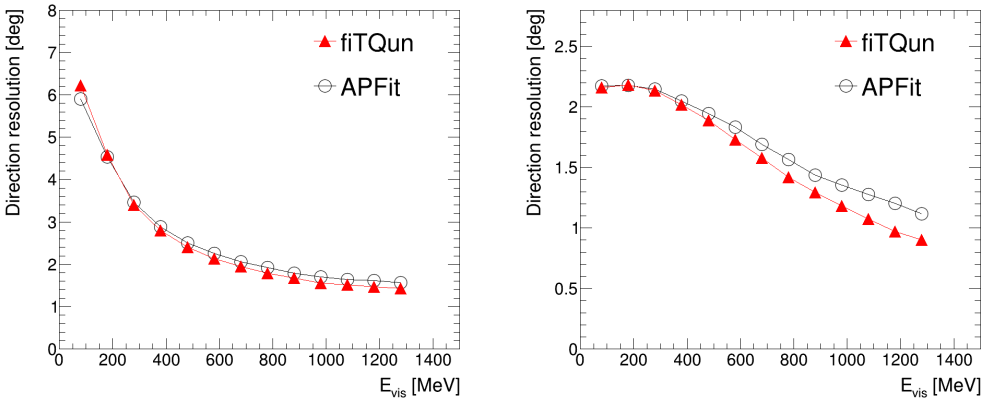

Figure 11.21: Direction resolutions on the lepton direction as a function of visible energy for single-ring electron (left) and muon (right) events in FC atmospheric neutrino CCQE samples. The red line with full triangles denotes the vertex resolution of fiTQun, and the black line with open circles denotes that of APFit.

resolution are 7.7% in the first bin and 3.1% in the last bin. For ν_μ CCQE events, the momentum resolution of both APFit and fiTQun are stable around 2.3%. The reconstruction momentum bias of both APFit and fiTQun are mostly within 1% for $30\,\mathrm{MeV} < E_{vis} < 1330\,\mathrm{MeV}$.

11.4.4 Ring Counting

The ring counting likelihood distributions of the SK I FC atmospheric neutrino samples are shown in Figure 11.24 for sub-GeV ($30\,\mathrm{MeV} < E_{vis} < 1330\,\mathrm{MeV}$) events. The performance of ring counting in fiTQun using the SK I FC sub-GeV MC events is listed in Table 11.1.

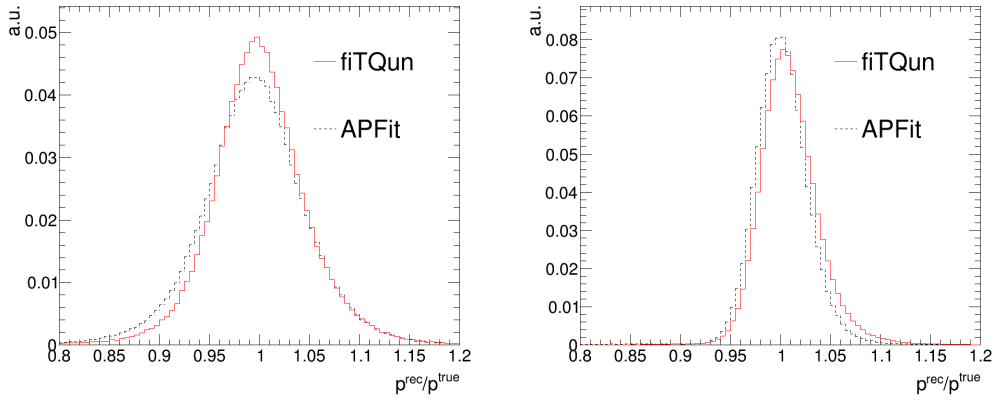

Figure 11.22: Ratio of reconstructed momentum over true momentum for single-ring electron (left) and muon (right) events in FC atmospheric neutrino CCQE samples. The red solid line is by fiTQun, and the black dashed line is by APFit.

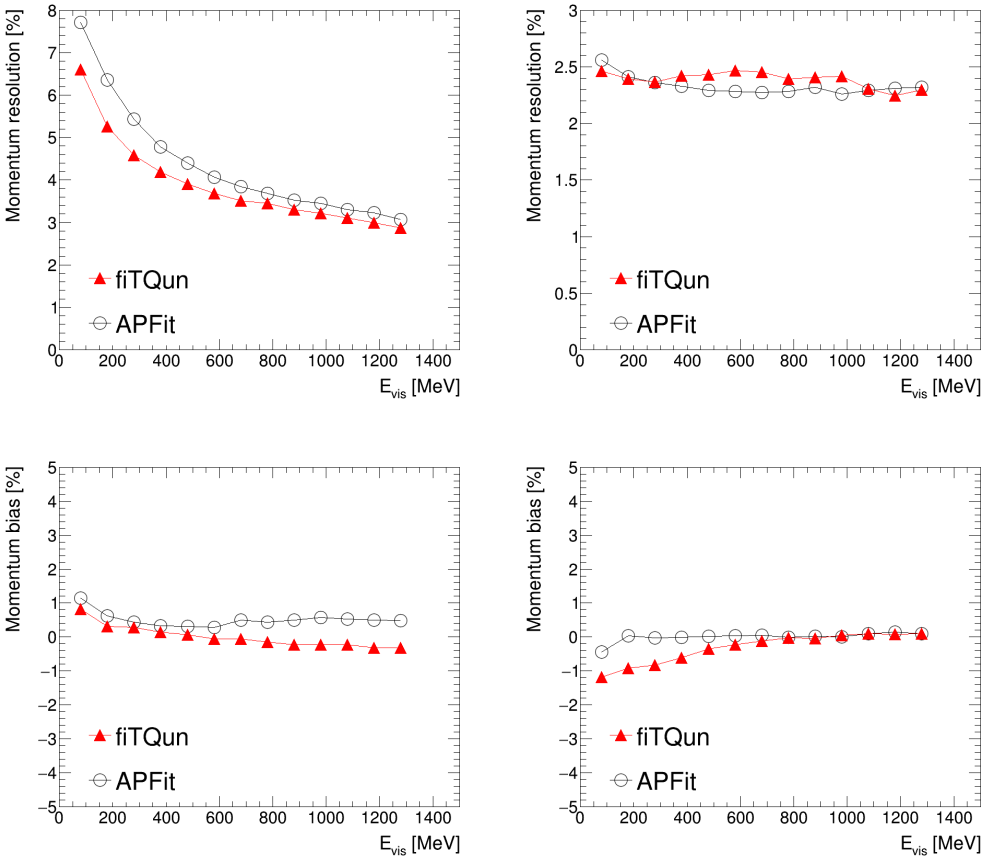

Figure 11.23: Momentum resolutions (upper) and bias (lower) as a function of visible energy for single-ring electron (left) and muon (right) events in FC atmospheric neutrino CCQE samples. The red line with full triangles denotes the vertex resolution of fiTQun, and the black line with open circles denotes that of APFit.

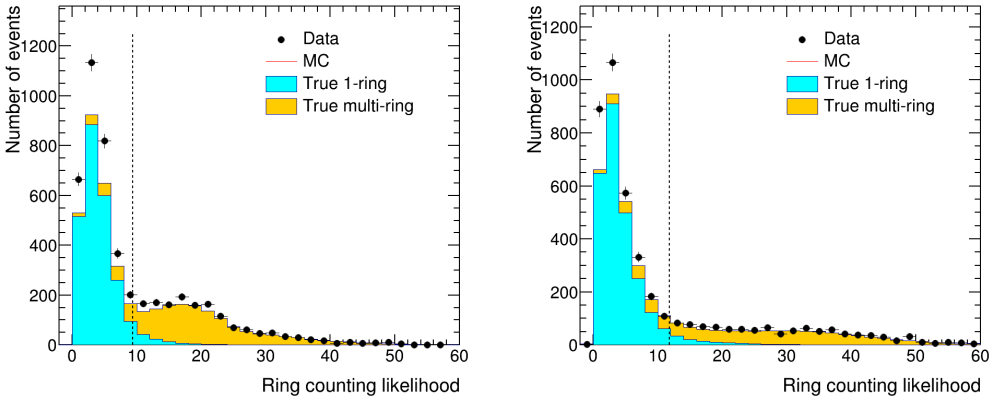

Figure 11.24: FiTQun ring counting likelihood distribution for sub-GeV e-like (left) and μ-like (right) events in the FC atmospheric neutrino samples. Dots denote the SK I FC atmospheric neutrino data. The histogram shows the FC atmospheric neutrino MC weighted by oscillation probability assuming normal mass ordering. The cyan shaded histogram denotes the true single-ring events in the MCs, and the orange shaded histogram denotes the true multi-ring events. The vertical dashed line indicates the cut to separate single-ring-like events from multi-ring-like events, with the events to the left classified as single-ring-like and those to the right classified as multi-ring-like.

Table 11.1: FiTQun ring counting efficiency on the SK I sub-GeV FC atmospheric neutrino MC.

	Rec. 1 ring	Rec. 2 rings	Rec. 3+ rings
True 1 ring	$96.06 \pm 0.16\%$	$3.39 \pm 0.02\%$	$0.55 \pm 0.01\%$
True 2 rings	$30.83 \pm 0.14\%$	$60.93 \pm 0.22\%$	$8.24 \pm 0.07\%$
True 3+ rings	$3.41 \pm 0.05\%$	$25.24 \pm 0.14\%$	$71.35 \pm 0.27\%$

11.4.5 Particle Identification

Figure 11.25 shows the PID likelihood distributions of single-ring events in the SK I FC atmospheric neutrino sample, using the improved PMT response model. A dip around $\ln(L_e/L_\mu) = 0$ indicates a clear separation between e-like and μ-like events for both sub-GeV and multi-GeV samples. The energy range of sub-GeV is defined as $30\,\text{MeV} < E_{vis} < 1330\,\text{MeV}$, and of multi-GeV it is $E_{vis} \geq 1330\,\text{MeV}$. The PID likelihood distributions of multi-ring events are shown in Figure 11.26. For multi-ring events, the particle type of the most energetic ring is identified and reported as the PID of the event. The separation between e-like and μ-like events is worse than that for single-ring events due to the overlap of Cherenkov rings. Moreover, the hadronic scattering of a muon may produce a fuzzy Cherenkov cone, which could be misidentified as an e-like ring. This is why a sizable fraction of the multi-ring ν_μ CC events are misidentified, as observed in Figure 11.26.

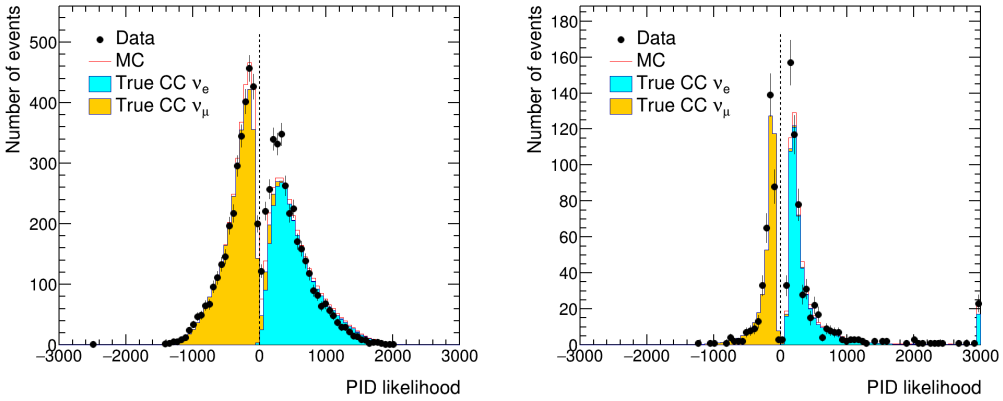

Figure 11.25: FiTQun PID likelihood distribution for single-ring events in the FC atmospheric neutrino samples for sub-GeV (left) and multi-GeV (right). Dots denote the SK I FC atmospheric neutrino data. The histogram shows the FC atmospheric neutrino MC weighted by oscillation probability assuming normal mass ordering. The cyan shaded histogram denotes the true ν_e CC events in the MCs, and the orange shaded histogram denotes the true ν_μ CC events. The two bins at the edges are overflow bins. The vertical dashed line indicates the cut to separate e-like events from μ-like events, with the events to the left classified as e-like and those to the right classified as μ-like.

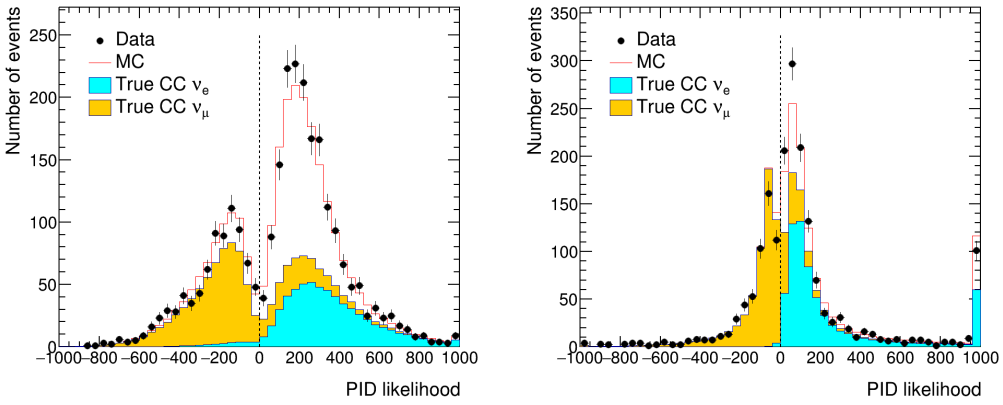

Figure 11.26: FiTQun PID likelihood distribution for multi-ring events in the FC atmospheric neutrino samples for sub-GeV (left) and multi-GeV (right). The representation is the same as that for Figure 11.25.

The mis-PID rate denotes the fraction of the misidentified particle in the MCs. Table 11.2 lists the mis-PID rates for electrons and muons, for single-ring and both sub-GeV and multi-GeV events. The small mis-PID rates demonstrate an excellent PID performance of fiTQun.

Table 11.2: Mis-PID rates for FC atmospheric neutrino MC in SK I.

Mis-PID rate	muon	electron
Sub-GeV	$0.75 \pm 0.01\%$	$0.13 \pm 0.01\%$
Multi-GeV	$2.13 \pm 0.05\%$	$0.02 \pm 0.00\%$

11.4.6 Summary

In summary, fiTQun provides excellent reconstruction performance on the SK I atmospheric neutrino samples. The vertex resolution is consistently better than that of APFit, while the direction and momentum resolutions are comparable between the two algorithms. Both reconstructions achieve $\mathcal{O}(0.1^\circ)$ angular precision at high visible energies and momentum resolutions at the level of a few percent. The momentum bias is small, remaining within 1% across the studied energy range. The vertex, direction, and momentum resolution and the momentum bias of fiTQun and APFit are summarized in Table 11.3. In addition, fiTQun demonstrates excellent ring counting performance, identifying single-ring events with over 96% efficiency, and provides reasonable separation for multi-ring events. The particle identification performance is also strong, with mis-PID rates below 1% for sub-GeV samples and at the level of a few percent for multi-GeV samples.

Table 11.3: Summary of fiTQun performance on SK I FC atmospheric neutrino CCQE MC events. The vertex, direction, and momentum resolution are tested on the MC CCQE events with a momentum between 100 MeV and 1330 MeV. The numbers listed here basically summarize the change in the resolution from low-energy to high-energy.

	fiTQun	APFit
Vertex resolution		
ν_e CCQE	stable at ∼21 cm	33.8 → 26.2 cm
ν_μ CCQE	33.4 → 16.1 cm	33.7 → 18.9 cm
Direction resolution		
ν_e CCQE	$6.2^\circ \rightarrow 1.4^\circ$	$5.9^\circ \rightarrow 1.6^\circ$
ν_μ CCQE	$2.2^\circ \rightarrow 0.9^\circ$	$2.2^\circ \rightarrow 1.1^\circ$
Momentum resolution		
ν_e CCQE	6.6% → 2.9%	7.7% → 3.1%
ν_μ CCQE	stable at ∼2.3%	stable at ∼2.3%
Momentum bias		
	<1%	<1%

Chapter 12

Scalar-NSI Analysis

This chapter describes the analysis procedure and results of the scalar-NSI search with the SK atmospheric neutrino data. In general, the analysis is performed by comparing data with MC. FC data in SK I, after the selection procedure described in Section 10.1, are used. The livetime is 1489.19 days. Five hundred years of MC neutrino events are generated. FC data and MC are both reconstructed by fiTQun and separated into subsamples by reconstruction information. Then, events are binned by the reconstructed zenith angle and momentum of the lepton. The MC events are weighted by neutrino oscillation probability including scalar-NSI. By varying the oscillation parameters and scalar-NSI parameters, different predictions for the data are generated. Systematic uncertainties related to the atmospheric neutrino flux, cross section models, and detector response also vary the MC predictions. The data-MC agreement is evaluated for each combination of parameters and is used for statistical tests.

12.1 FC Neutrino Sample Selection

As described in Section 10.1.6, the FC data events observed in SK I that passed the FC reduction are further selected by the following criteria:

1. NHITAC < 10 (16 for SK II and later periods),

   where NHITAC is the number of OD hits in the most energetic OD cluster.

2. Reconstructed visible energy $E_{vis} > 30\,\mathrm{MeV}$.

   where E_{vis} is defined as the sum of the reconstructed kinetic energy above the Cherenkov threshold for all rings,

3. $dwall > 200\,\mathrm{cm}$,

where *dwall* is the minimum distance from the reconstructed primary event vertex to the ID wall.

The same cuts apply to the MC events. These cuts remove the remaining cosmic-ray muon background events and low-energy background events.

FC data and MC events are then classified into 13 subsamples primarily based on the reconstructed visible energy, number of Cherenkov rings, lepton flavor, and number of decay electrons. The MC sample presented in this section are weighted by oscillation probabilities, which are computed based on the parameters listed in Table 12.1. Since the classification procedure is the same for data and MC, FC data and MC events are called "FC events" in the following discussion for simplicity. Figure 12.1 illustrates the subsample selection procedure. FC events are first classified by E_{vis}. Those with $E_{vis} \leq 1330\,\text{GeV}$ are categorized as sub-GeV events, otherwise they are termed multi-GeV events. The sub-GeV and multi-GeV events are further divided into single-ring samples and multi-ring samples, depending on the number of reconstructed rings. The PID information is used to separate the FC events into electron-like (e-like) and muon-like (ν-like) samples.

Table 12.1: Parameters used to calculate oscillation probabilities for nominal MC events.

	Value	
Parameter	Normal Ordering	Inverted Ordering
$\sin^2\theta_{12}$	0.307	0.307
$\sin^2\theta_{13}$	0.022	0.022
$\sin^2\theta_{23}$	0.546	0.539
Δm^2_{21} [eV^2]	7.53×10^{-5}	7.53×10^{-5}
Δm^2_{32} [eV^2]	2.453×10^{-3}	-2.536×10^{-3}
δ_{CP} [rad]	0	0

The number of decay electrons can help to further identify the neutrino flavor, the interaction mode, and whether it is neutrino or anti-neutrino. In $\nu_\mu(\bar{\nu}_\mu)$ CCQE interactions, a muon (anti-muon) is generated, which can decay into an electron (positron):

$$\begin{aligned} \nu_\mu(\bar{\nu}_\mu) + n \rightarrow \mu^\mp + p \\ \searrow \\ e^\mp + \nu_\mu(\bar{\nu}_\mu) + \bar{\nu}_e(\nu_e). \end{aligned} \tag{12.1}$$

On the other hand, decay electrons are not produced in a $\nu_e(\bar{\nu}_e)$ CCQE interaction, because the primary lepton is an electron or a positron. In CC1π interactions, a pion is generated in addition to a lepton. A decay electron can be produced in the pion

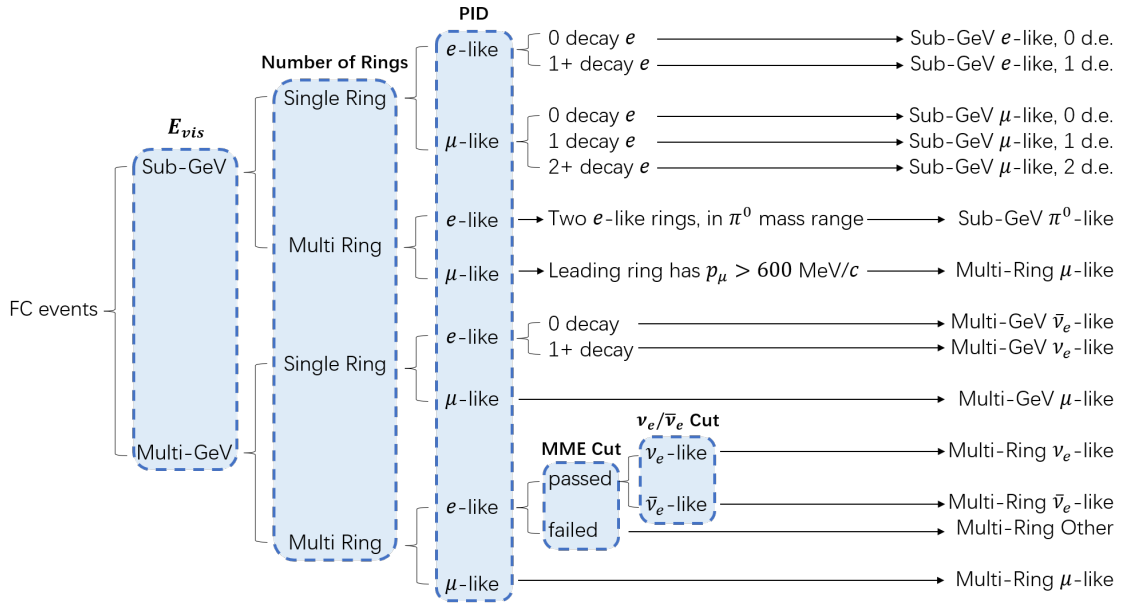

Figure 12.1: Schematic of FC event selection. Note that the Multi-Ring μ-like sample contains both sub-GeV and multi-GeV events. Reproduced from [216].

decay chain.

$$\begin{aligned} \pi^{\pm} \rightarrow \mu^{\pm} + \nu_{\mu}(\bar{\nu}_{\mu}) \\ \searrow \\ e^{\pm} + \bar{\nu}_{\mu}(\nu_{\mu}) + \nu_{e}(\bar{\nu}_{e}). \end{aligned} \tag{12.2}$$

However, not all of the pions and muons produce decay electrons in water. Almost all π^- and 18.4% of μ^- undergo nuclear capture in water [217, 218]. Table 12.2 lists the expected number of decay electrons for each neutrino flavor and interaction mode. The difference in the expected number of decay electrons can be used to statistically separate these interactions.

Table 12.2: Expected number of decay electrons produced in CCQE and CC1π events without FSI and SI. The observed number may change due to FSI, SI, detection inefficiency and misreconstruction. Taken from [219].

	ν_e	$\bar{\nu}_e$	ν_μ	$\bar{\nu}_\mu$
CCQE	0	0	0 or 1	1
CC1π	0 or 1	0	0, 1, or 2	1

12.1.1 Sub-GeV Single-Ring Samples

Sub-GeV single-ring events are separated into e-like and μ-like subsamples by the PID information. Low-energy events are rejected, because they are usually poorly reconstructed and may downgrade the physics sensitivity. For e-like events, those

with a reconstructed momentum below 100 MeV/c are vetoed. For μ-like events, the threshold momentum is 200 MeV/c.

The reconstructed number of decay electrons are used to identify the interaction mode, as discussed above. Sub-GeV single-ring e-like events are divided into two subsamples, *sub-GeV e-like 0 d.e.* and *sub-GeV e-like 1 d.e.*, based on whether there are decay electrons or not. The latter contains e-like events with one or more decay electrons, and is a ν_e-CC1π-enriched sample. The μ-like events are divided into three subsamples, *sub-GeV μ-like 0 d.e.*, *sub-GeV μ-like 1 d.e.*, and *sub-GeV μ-like 2 d.e.*, with 0, 1, and > 1 decay electrons. The *sub-GeV μ-like 0 d.e.* sample is enriched with ν_μ, and the *sub-GeV μ-like 2 d.e.* sample is enhanced with ν_μ CC1π events.

12.1.2 Sub-GeV Multi-Ring Samples

Sub-GeV multi-ring events are divided into two subsamples, *sub-GeV 2-ring π^0-like* and *multi-ring μ-like*. The former is a sample enriched with NCπ^0 events. A π^0 decays into two γs, leaving two e-like rings and not produce decay electrons. When exactly two e-like rings are found without decay electrons, and the reconstructed π^0 mass $m_{\pi^0}^{\rm rec}$ is between 85 MeV/c^2 and 215 MeV/c^2, the event is classified as *sub-GeV 2-ring π^0-like*. The reconstructed π^0 mass $m_{\pi^0}^{\rm rec}$ is given by

$$m_{\pi^0}^{\rm rec} = \sqrt{2P_{\gamma 1}P_{\gamma 2}(1 - cos\phi)}, \tag{12.3}$$

where $P_{\gamma 1}$ and $P_{\gamma 2}$ are the momenta of the two γ, and ϕ is the angle between their directions.

The *multi-ring μ-like* sample contains not only sub-GeV events but also multi-GeV events. For a multi-ring event, if its most energetic ring is μ-like with momentum greater than 600 MeV/c, then it is categorized as *multi-ring μ-like*. Other sub-GeV multi-ring events are not used because their neutrino flavors are hard to identify.

12.1.3 Multi-GeV Single-Ring Samples

Events with $E_{vis} > 1330$ MeV and only one ring are separated into three subsamples. If the event is a μ-like event, it is categorized as *multi-GeV μ-like*. Decay-electron-based selection is not performed for the *multi-GeV μ-like* sample. For e-like events, a separation similar to the sub-GeV single-ring e-like samples is applied. As discussed in Section 2.4.3, the upward-going ν_e and $\bar{\nu}_e$ events with $2 < E_\nu < 9$ GeV are important for identifying the correct neutrino mass ordering. An e-like event without decay electron is categorized as *multi-GeV $\bar{\nu}_e$-like*, otherwise it will be *multi-GeV ν_e-like*. This separation is based on the fact that only ν_e CC1π interactions are expected to produce a decay electron in the π^+ decay, as shown in Table 12.2. In contrast, no

decay electron is expected in a $\bar{\nu}_e$ CC1π process because the positron does not decay and the π^- will be captured by a nucleus in water before decaying.

12.1.4 Multi-GeV Multi-Ring Samples

Multi-GeV multi-ring events are first separated into e-like and μ-like subsamples by checking the PID of their most energetic rings. As described in Section 12.1.2, the multi-ring μ-like events in the multi-GeV region are categorized as *multi-ring μ-like*, if its most energetic ring has a momentum greater than 600 MeV/c. On the other hand, the e-like events undergoes a more sophisticated selection procedure.

The multi-GeV multi-ring e-like sample contains a large fraction of NC and $\nu_\mu(\bar{\nu}_\mu)$ CC events because high energy muons and charged mesons can experience hadronic scatterings in water and their Cherenkov rings can become blurred, mimicing e-like rings. This analysis adopts a two-stage likelihood-based method to statistically separate the ν_e CC and $\bar{\nu}_e$ CC events from NC and $\nu_\mu(\bar{\nu}_\mu)$ CC events [211]. The first stage is called multi-GeV multi-ring e-like (MME) selection, which extracts ν_e and $\bar{\nu}_e$ CC events. The second stage, ν_e-$\bar{\nu}_e$ separation, separates ν_e CC events and $\bar{\nu}_e$ CC events that are sensitive to neutrino mass ordering.

MME selection

The MME selection uses a likelihood function built from four reconstructed variables: the momentum fraction of the most energetic ring (MER), the momentum fraction of the most energetic π^+-like ring, the number of decay electrons, and the distance from the primary vertex to the most distant decay electron. The momentum fraction of the MER can effectively separate $\nu_e(\bar{\nu}_e)$ CC events from $\nu_\mu(\bar{\nu}_\mu)$ CC events and NC events. For $\nu_\mu(\bar{\nu}_\mu)$ CC events and NC events, the MER typically comes from a meson or muon and tends to carry a smaller fraction of energy being mis-reconstructed as e-like. In contrast, the momentum fraction of the MER of $\nu_e(\bar{\nu}_e)$ CC events tends to be higher. The momentum fraction of the most energetic π^+-like ring is used to identify $\nu_\mu(\bar{\nu}_\mu)$ CC events, since the primary muons are usually mis-reconstructed as π^+ rings which show higher momentum fractions than true π^+ rings produced in $\nu_e(\bar{\nu}_e)$ CC events or NC events. This variable is set to zero when there is no π^+-like ring found. True $\nu_e(\bar{\nu}_e)$ CC events tend to have a small number of decay electrons, as discussed earlier in this section. The distance to the furthest decay electron is expected to be larger in a $\nu_\mu(\bar{\nu}_\mu)$ CC event due to the energetic primary muon. On the other hand, muons produced in charged pion decays in $\nu_e(\bar{\nu}_e)$ CC events carry relatively lower energies, and travel shorter distances before decaying. In summary, $\nu_e(\bar{\nu}_e)$ CC events tend to have a large momentum fraction of the most energetic ring, a small momentum fraction of the most energetic π^+-like ring, a small number of decay electrons, and a short distance from the primary vertex to the most distant decay electron. The

distributions of these four variables are shown in Figure 12.2.

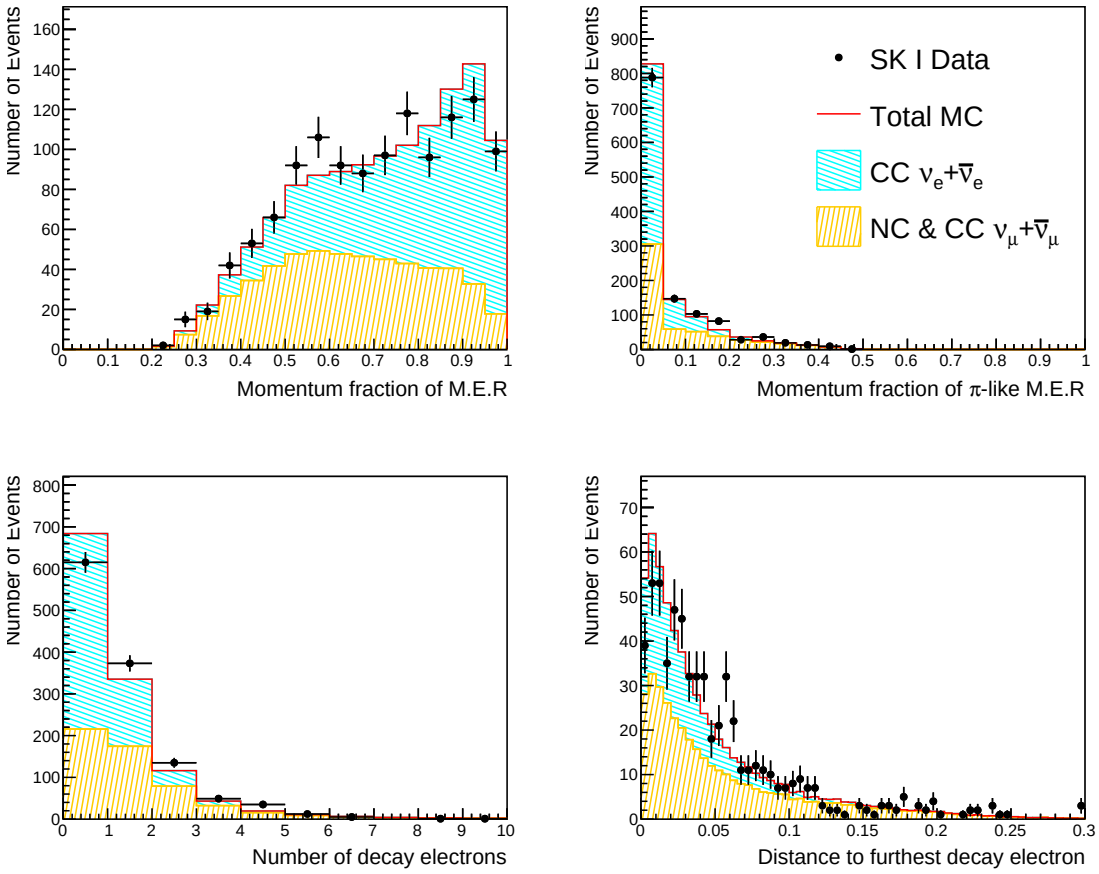

Figure 12.2: Distributions of the input variables of the MME selection likelihood for multi-GeV multi-ring e-like events. **Top-left:** Momentum fraction of the MER. **Top-right:** Momentum fraction of the most energetic π^+ ring. **Bottom-left:** Number of decay electrons. **Bottom-right:** Distance between the event vertex and the most distant decay electron. The dots denote the data and the red lines denote the oscillated MC normalized by livetime. The blue hatches are $\nu_e(\bar{\nu}_e)$ CC events. NC events and $\nu_\mu(\bar{\nu}_\mu)$ CC events are shown as yellow hatches. Oscillations are calculated using parameters listed in Table 12.1 assuming normal ordering.

The MME selection likelihood function based on these four variables is defined as,

$$\mathcal{L}_{\text{MME}} = \sum_{i=1}^{4} \log \Gamma_i^S(x_i) - \log \Gamma_i^B(x_i), \tag{12.4}$$

where Γ_i represents the probability distribution function (PDF) for the i^{th} variable and x_i is the measured value of the variable. The superscripts S and B label the signal and background PDFs, respectively. The signal is composed of $\nu_e(\bar{\nu}_e)$ CC events, and the background consists of NC, $\nu_\tau(\bar{\nu}_\tau)$ CC, and $\nu_\mu(\bar{\nu}_\mu)$ CC events. Figure 12.3 shows the MME selection likelihood distribution for the FC multi-GeV multi-ring events identified as e-like. Events with likelihood values above -0.25 pass the MME selection

cut and are further separated into ν_e-like and $\bar{\nu}_e$-like samples in the next stage. Those that fail this selection cut are categorized as *multi-ring other*. The selection efficiencies and sample purities are shown in Table 12.3.

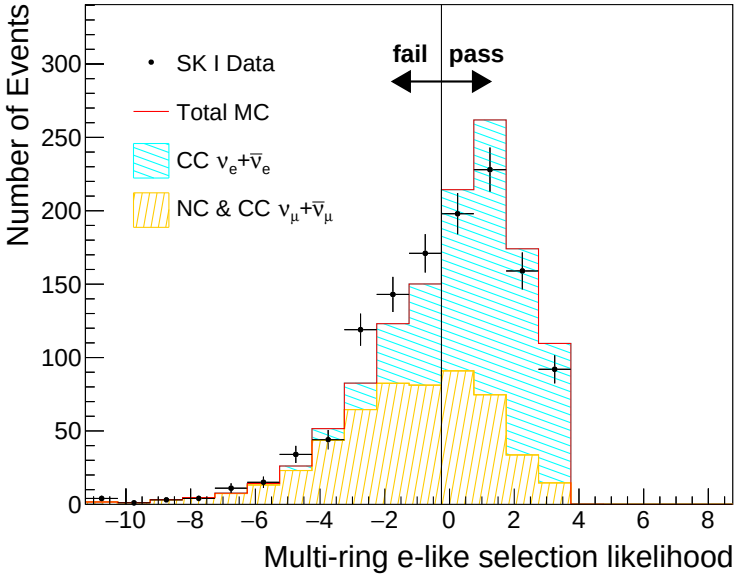

Figure 12.3: The MME selection likelihood distribution for multi-GeV multi-ring e-like events. The representations are the same as those in Figure 12.2. Events with likelihood values above the cut are further separated into ν_e-like and $\bar{\nu}_e$-like samples in the next stage. Otherwise the events are categorized as *multi-ring other*. Oscillations are calculated using parameters listed in Table 12.1 assuming normal ordering.

ν_e-$\bar{\nu}_e$ separation

The ν_e-$\bar{\nu}_e$ separation likelihood function is constructed based on three variables: the number of reconstructed rings, number of decay electrons, and transverse momentum of the event. The transverse momentum of the event is defined relative to the direction of the most energetic ring,

$$p_{\text{tran}} \equiv \frac{\sum_i p_i^{\text{rec}} \sin\theta_i}{\sum_i p_i^{\text{rec}}}, \tag{12.5}$$

where i goes over each ring, and θ_i is the angle between the ring and the MER, and p_i^{rec} is the reconstructed momentum of the ring. In general, neutrino CC processes have higher multiplicities of charged pions than anti-neutrino CC processes since they produce π^+. In addition, since most π^- will be captured by the nuclei in water without producing a decay electron, a $\bar{\nu}_e$ CC interaction tends to produce fewer Cherenkov rings and less decay electrons than a ν_e CC interaction. Due to the V-A structure of the weak interaction, the angular distribution of the primary leptons from $\bar{\nu}_e$ CC processes are more forward peaked than those from ν_e CC processes. Therefore, ν_e CC events tend to have more rings, more decay electrons, and larger transverse momenta.

Figure 12.4 shows the distributions of the variables.

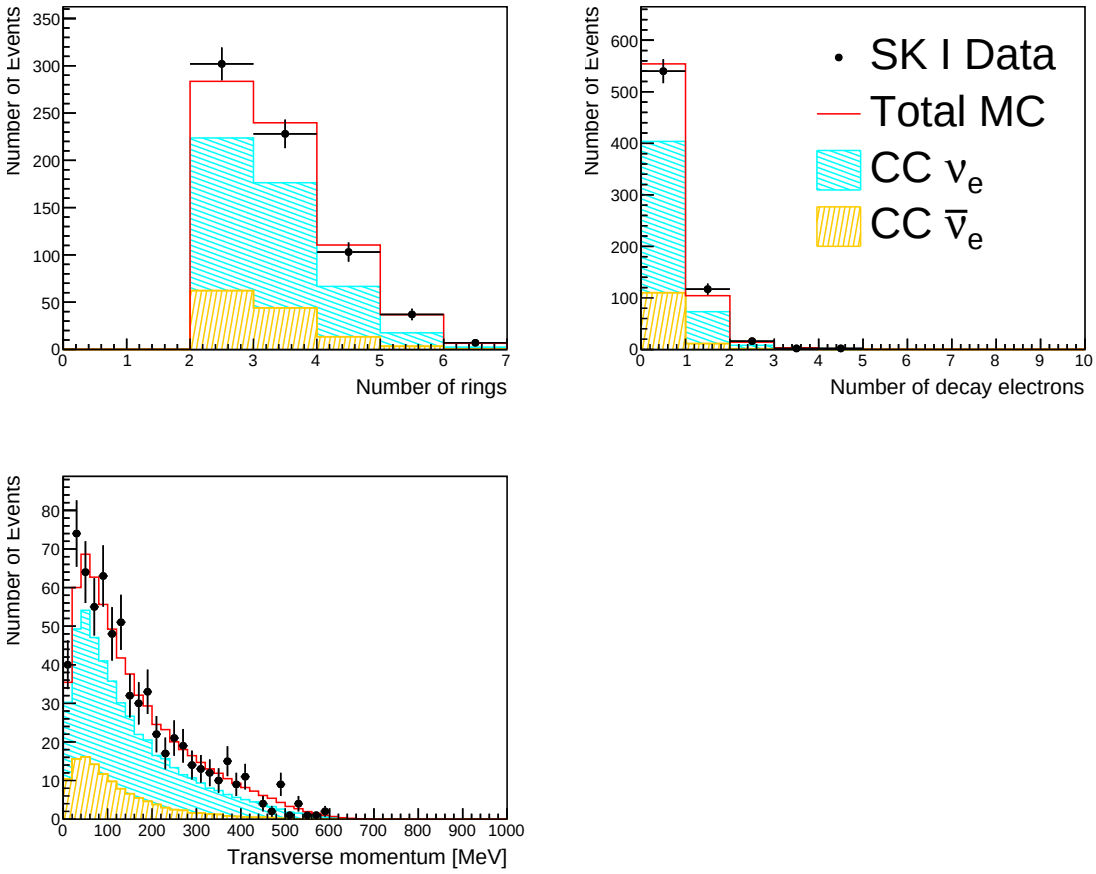

Figure 12.4: Distributions of the input variables of the ν_e-$\bar{\nu}_e$ separation likelihood for events that have passed the MME selection cut. **Top-left:** Number of reconstructed Cherenkov rings. **Top-right:** Number of decay electrons. **Bottom-left:** Transverse momentum of the event. The dots denote data and the red lines denote oscillated MC normalized by livetime. The blue hatches are ν_e CC events, and the yellow hatches are $\bar{\nu}_e$ CC events. Oscillations are calculated using parameters listed in Table 12.1 assuming normal ordering.

Similar to Eq. 12.4, the ν_e-$\bar{\nu}_e$ separation likelihood function is given by,

$$\mathcal{L}_{\nu_e-\bar{\nu}_e} = \sum_{i=1}^{3} \log \Gamma_i^{\nu_e}(x_i) - \log \Gamma_i^{\bar{\nu}_e}(x_i), \tag{12.6}$$

where $\Gamma_i^{\nu_e}$ and $\Gamma_i^{\bar{\nu}_e}$ are the PDFs for the i^{th} variable assuming ν_e CC and $\bar{\nu}_e$ CC, and x_i is the measured value of the variable. The likelihood distributions for the events that have passed the MME selection cut are shown in Figure 12.5. Events with positive likelihood values are designated *multi-ring ν_e-like*, otherwise they are categorized as *multi-ring $\bar{\nu}_e$-like*. Table 12.3 lists the selection efficiencies and sample purities of this separation.

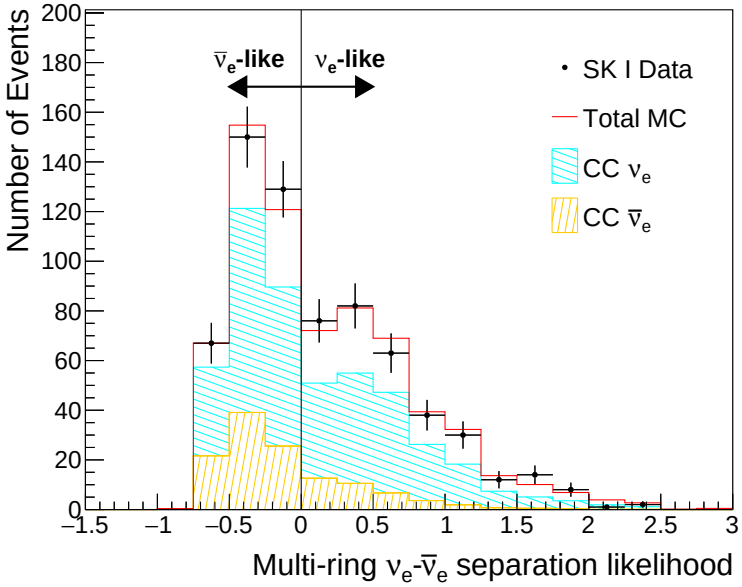

Figure 12.5: The ν_e-$\bar{\nu}_e$ separation likelihood distribution for multi-GeV multi-ring e-like events. The representations are the same as those in Figure 12.4. The cut value is set to 0 and is indicated by the vertical line. Events with negative (positive) likelihood values are categorized as $\bar{\nu}_e$-like ($\nu_)e$-like). Oscillations are calculated using parameters listed in Table 12.1 assuming normal ordering.

12.1.5 Summary

Table 12.4 lists for each subsample the number of data and MC events, as well as the fraction of each true neutrino flavor of MC events. The fractions are also presented in Figure 12.6. Each sample is sensitive to different oscillation effects or constrains systematic uncertainties. For example, the *sub-GeV 2-ring* π^0*-like* sample is mainly composed of NCπ^0 events and is not sensitive to neutrino flavor transition. It is used to constrain the atmospheric neutrino flux and cross section. The phenomena of neutrino oscillations in these samples in the presence of the scalar-NSI will be discussed in Section 12.4.

The neutrino energy E and the travel distance L determines the neutrino oscillation probability for an event. In this analysis, the baseline L is replaced by the cosine zenith angle $\cos\theta_z$ as discussed in Section 2.4.3. The FC events in each sample are binned into the neutrino energy and the zenith angle. In SK I, the neutrino energy is approximated by the sum of the magnitudes of the reconstructed momenta. The zenith angle is approximated as the angle between the vertical upward direction and the vector sum of the reconstructed momenta. The number of momentum bins and bin edges are summarized in Table 12.5. The zenith angle binning is common for most of the samples. The range [-1,1] is divided into 10 bins. The bin edges are symmetric with the horizontal direction, and are chosen to be ±1, ±0.839, ±0.644,

Table 12.3: Performance of the two-stage multi-GeV multi-ring e-like sample selection derived from oscillated MC events. The efficiency is defined as the fraction of selected events relative to all true events of interest. The purity is defined as the fraction of selected events of interest with respect to all selected events.

First stage	
Multi-GeV multi-ring e-like	
Efficiency	79.56%
Purity	71.89%
Second stage	
Multi-ring ν_e-like	
Efficiency	49.84%
Purity	54.23%
Multi-ring $\bar{\nu}_e$-like	
Efficiency	70.04%
Purity	25.18%

Table 12.4: FC data and nominal MC events in each subsample for this analysis. The number of the data and MC events are listed in column 2 and 3. The fractions of true neutrino flavor in the MC are shown in column 4 to 9. The MC events are weighted by oscillation probabilities and re-scaled by livetime. Oscillations are computed using parameters as listed in Table 12.1 assuming normal ordering.

FC samples	Events		MC Purity (%)					
	Data	MC	ν_e	$\bar{\nu}_e$	ν_μ	$\bar{\nu}_\mu$	$\nu_\tau(\bar{\nu}_\tau)$	NC
Sub-GeV single-ring								
e-like 0 d.e.	2923	2489.97	70.87	25.13	0.26	0.07	0.04	3.62
e-like 1 d.e.	228	207.66	87.84	1.85	3.73	0.85	0.10	5.64
μ-like 0 d.e.	921	856.47	0.29	0.14	72.46	16.92	0.08	10.10
μ-like 1 d.e.	1877	1714.21	0.01	0.00	67.23	30.38	0.05	2.33
μ-like 2 d.e.	127	122.61	0.00	0.00	94.50	3.47	0.03	2.01
Sub-GeV 2-ring								
π^0-like	642	565.41	5.02	1.42	1.86	0.15	0.02	91.53
Multi-GeV single-ring								
ν_e-like	85	78.36	65.03	7.86	6.06	1.17	3.55	16.34
$\bar{\nu}_e$-like	508	532.15	56.39	35.58	0.53	0.09	1.07	6.33
μ-like	381	419.00	0.02	0.01	59.93	39.68	0.31	0.05
Multi-GeV multi-ring								
ν_e-like	329	361.65	54.23	11.07	6.70	0.45	3.67	23.90
$\bar{\nu}_e$-like	348	371.53	53.12	25.18	3.82	0.42	2.35	15.11
μ-like	876	895.14	1.01	0.08	72.61	23.17	0.43	2.71
Other	549	449.31	27.46	2.67	31.04	2.62	4.84	31.37

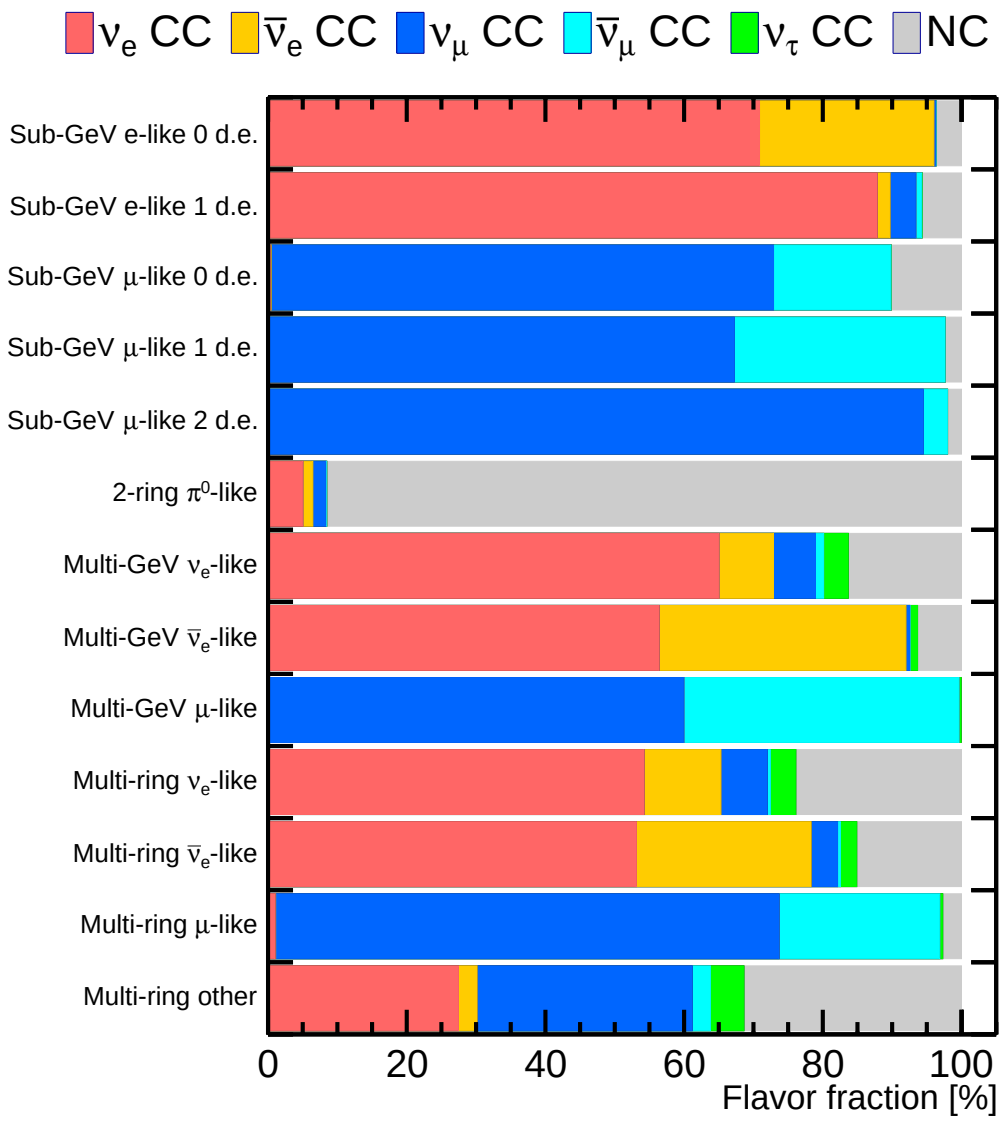

Figure 12.6: Fractions of neutrino flavors in the 13 subsamples in the SK I FC MC used for this analysis. The legend ν_τ CC denotes ν_τ and $\bar{\nu}_\tau$ CC events. The MC sample is oscillated using parameters listed in Table 12.1 assuming normal ordering.

± 0.448, ± 0.224, and 0, such that they align with the boundaries of the Earth's internal composition. Three samples, *sub-GeV e-like 1 d.e.*, *sub-GeV μ-like 2 d.e.*, and *sub-GeV 2-ring π^0-like*, are not binned into zenith angle. In total, 405 bins are used for the 13 FC samples in this analysis.

12.2 Systematic Uncertainties

This section provides an overview of the systematic uncertainties considered in this analysis. Systematic uncertainties in the atmospheric neutrino flux, cross section, detector response, and oscillation are taken into account. In total, 62 systematic

Table 12.5: Definition of the energy and zenith angle binning for each sample. The edge labeled 3.12 is exactly $\log_{10}(1330\text{MeV}/c)$.

FC samples	Number of bins	Edges of bins, $\log_{10}[p(\text{MeV}/c)]$
Sub-GeV single-ring		
e-like 0 d.e.		
e-like 1 d.e.		
μ-like 0 d.e.	5	2.0, 2.4, 2.6, 2.8, 3.0, 3.2
μ-like 1 d.e.		
μ-like 2 d.e.		
Sub-GeV 2-ring		
π^0*-like*	5	2.0, 2.2, 2.4, 2.6, 2.8, 3.2
Multi-GeV single-ring		
ν_e*-like*	4	3.0, 3.4, 3.7, 4.0, 5.0
$\bar{\nu}_e$*-like*	4	3.0, 3.4, 3.7, 4.0, 5.0
μ-like	2	3.0, 3.4, 5.0
Multi-GeV multi-ring		
ν_e*-like*	3	3.0, 3.4, 3.7, 5.0
$\bar{\nu}_e$*-like*	3	3.0, 3.4, 3.7, 5.0
μ-like	4	2.0, 3.12, 3.4, 3.7, 5.0
Other	4	3.0, 3.4, 3.7, 4.0, 5.0

uncertainties are included in this analysis. Of these, 18 are related to atmospheric neutrino flux, 24 are related to the cross section, 16 are related to the detector response, and 4 are related to the oscillation. The detector-related uncertainties are treated as independent among the SK phases.

The systematic uncertainties are treated using Gaussian error parameters that alter the prediction We define F_{ij} as the fractional change in the i^{th} analysis bin for a 1σ change in the j^{th} systematic uncertainty source. The F_{ij}s are then used to modify the expected number of events in each analysis bin, as will be discussed in Section 12.3.3.

The systematic uncertainties considered in this analysis are mostly based on those in the previous analysis [219]. Although the NEUT event generator, version 5.6.4, has been used for SK IV through SK VI in [219], it has not been applied to SK I. In this analysis, NEUT 5.6.4 is adopted to generate 500 years of MC events. Accordingly, the cross-section-related uncertainties for SK I are updated. The uncertainties related to reconstruction and energy scale are newly evaluated, because fiTQun is applied to the SK I data for the first time. Notably, the fiducial volume expansion is not applied in this analysis, and the systematic uncertainties are only considered for the conventional fiducial volume ($dwall > 200\,\text{cm}$).

12.2.1 Atmospheric Neutrino Flux Uncertainties

The atmospheric neutrino flux uncertainties are introduced below. These uncertainties are identical to those in the previous analysis [219].

Absolute flux normalization: The absolute flux normalization uncertainty is estimated from the combined uncertainties in the hadron production models, air density, and hadron interaction models [179]. It alters overall neutrino flux, and thus the event rate as a function of neutrino energy. Two independent uncertainties are assigned to events with neutrino energies below and above 1 GeV. The fractional change in event rate due to a 1σ fluctuation in the flux normalization is shown in Figure 12.7.

Relative flux normalization: The relative flux normalization uncertainty addresses the differences in the absolute flux normalization between three atmospheric neutrino flux models [179, 220, 221]. These three flux models are also used to evaluate the other flux uncertainties. The differences mainly appear at neutrino energy above 10 GeV, and affect the multi-GeV FC samples. Therefore, a 5% uncertainty is assigned to the relative normalization of the multi-GeV FC samples.

Flavor ratio: The flavor ratio uncertainty on $(\nu_\mu + \bar{\nu}_\mu)/(\nu_e + \bar{\nu}_e)$ is estimated from the difference in flavor ratio between the three flux models, averaged over all directions. This uncertainty is divided into three independent terms for neutrino energy below 1 GeV, between 1 and 10 GeV, and above 10 GeV. The fractional change in event rate as a function of neutrino energy for the flavor ratio uncertainty is shown in Figure 12.7.

Neutrino/anti-neutrino ratio: Two sets of uncertainties on the neutrino/anti-neutrino ratios, $\nu_e/\bar{\nu}_e$, and $\nu_\mu/\bar{\nu}_\mu$, are considered. They come from the differences between the ratios of π^+/π^- and K^+/K^- in the three flux models, averaged over all directions. Each of these has three independent terms for energy ranges identical to those in flavor ratio uncertainty. The fractional change in event rate for the flux uncertainties is shown in Figure 12.7.

K/π ratio: Atmospheric neutrino production through kaon decays takes a non-negligible fraction at neutrino energy above 10 GeV. The uncertainty in the K/π ratio is estimated by assuming an alternative K/π ratio in the Honda flux model [179] and taking the difference between this calculation and the nominal Honda model. The fractional change in event rate due to a 1σ fluctuation in the K/π ratio increases with increasing neutrino energy, and is $\sim 2.5\%$ at the highest energy bin.

Neutrino path length: The neutrino path length is determined by the neutrino production height, which can be varied by the atmospheric density profile. The uncertainty on the neutrino path length is negligible for upward-going neutrinos, but has a sizable effect to those coming from above the horizon. The systematic uncertainty is

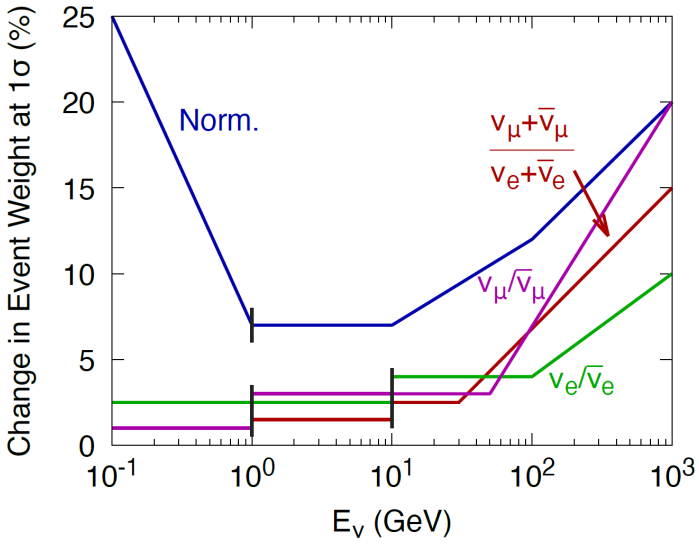

Figure 12.7: Fraction change in event rate as a function of neutrino energy due to a 1σ fluctuation in the absolute flux normalization, flavor ratio, and neutrino/anti-neutrino ratios systematic uncertainties. Taken from [60].

estimated from the difference between two calculations assuming two different atmospheric density models [222, 223]. Its 1σ effect on the event rate is less than 2% for all analysis bins.

Up/down ratio: As discussed in Section 9.1, the atmospheric neutrino flux is asymmetric with respect to the horizontal direction at low energies below 1 GeV. The uncertainty on this effect is estimated from the comparison of the zenith angle distributions calculated using the three flux models. The fractional change in event rate for a 1σ up/down ratio variation is at most 3%, and the most affected sample is *sub-GeV μ-like 0 d.e.* sample.

Horizontal/vertical ratio: The atmospheric neutrino flux peaks in horizontal directions because pions and muons have longer decay paths. The systematic uncertainty on the horizontal/vertical flux ratio primarily comes from the difference in the 3-dimensional flux calculation method in the three flux models. The uncertainty is estimated from the difference between the three models, and the corresponding 1σ fractional change in event rate is less than 3%.

Solar activity: The atmospheric neutrino flux is time dependent on the solar activity, as discussed in Section 9.1. A weight is applied to the predicted flux to account for this dependence in each SK phase. The systematic uncertainty on the weight is estimated by shifting the period of solar activity measurement by ± 1 year to calculate two different weights and comparing the two calculations with the nominal weight. For SK I, its 1σ effect on the event rate is $< 1.5\%$, and low-energy samples are most affected.

12.2.2 Neutrino Interaction Uncertainties

The cross section uncertainties are briefly described here. Several uncertainties in SK I related to quasi-elastic processes are updated for NEUT 5.6.4. The updated uncertainties are in the normalizations, shape, flavor ratio, and $\bar{\nu}/\nu$ ratios of CCQE, and are identical to those used for SK IV-VI in the previous analysis [219].

Quasi-elastic uncertainties

Quasi-elastic axial mass, M_A: The axial mass M_A that modifies the axial form factor is known to have a large experimental uncertainty, as discussed in Section 9.2.1. It can change the CCQE cross section, and thus the event rate. This uncertainty is evaluated from the comparison between two cross sections computed using the default value of $M_A = 1.21\,\mathrm{GeV}/c^2$ and an alternative value of $M_A = 1.05\,\mathrm{GeV}/c^2$. The fractional change in event rate is less than 10% for all analysis bins.

CCQE normalizations: The uncertainties in the CCQE normalizations are evaluated by comparing different nuclear models, as discussed in Section 9.2.1. The default nuclear model, the LFG model [199], and an alternative model, the SF model [200] are used to compute the uncertainties. Two independent terms are assigned to events with neutrino energies below and above 1 GeV, and the error sizes are around 10% and 3%, respectively.

CCQE shape: The CCQE shape uncertainty is also evaluated by comparing the LFG model and the SF model. The difference in the normalized cross section as a function of neutrino energy is taken as the systematic uncertainty on the CCQE shape. It mainly affects the sub-GeV samples, and the error size is less than 4%.

CCQE flavor ratio: The CCQE flavor ratio uncertainty on $(\nu_\mu + \bar{\nu}_\mu)/(\nu_e + \bar{\nu}_e)$ is also computed by comparing the LFG model and the SF model. The difference in the $(\nu_\mu + \bar{\nu}_\mu)/(\nu_e + \bar{\nu}_e)$ between the two models is taken as the uncertainty. The low-energy events in the *sub-GeV e-like 0 d.e.* sample are most affected, with a fraction change in event rate of $\sim 4\%$.

CCQE $\bar{\nu}/\nu$ ratio: Similar to the flavor ratio uncertainty, the CCQE neutrino/anti-neutrino ratio on $(\bar{\nu}_e + \bar{\nu}_\mu)/(\nu_e + \nu_\mu)$ is taken from the difference between the two models. Low-energy events are most affected, with a fractional change in event rate less than 4%.

2p2h: The uncertainty in the 2p2h cross section is set to 100% due to the less understood nature of the 2p2h process. A 1σ variation can change the event rate of the 1-ring samples by around 11%.

Single pion production uncertainties

$M_A^{\mathrm{Res}}, C_A^5(0), I_{\frac{1}{2}}$*:* Three input parameters, $M_A^{\mathrm{Res}}, C_A^5(0)$, and $I_{\frac{1}{2}}$, modifies the resonant pion production cross section, as discussed in Section 9.2.2. Their uncertainties are taken from the bubble chamber measurements of single pion production [224]. The 1σ ranges are $M_A^{\mathrm{Res}} = 0.95 \pm 0.15\,\mathrm{GeV}/c^2$, $C_A^5(0) = 1.01 \pm 0.12\,\mathrm{GeV}/c^2$, and $I_{\frac{1}{2}} = 1.30 \pm 0.20$. Variations in the resonant pion production cross section due to 1σ fluctuations of these parameters are considered systematic uncertainties.

CC1π neutrino/anti-neutrino ratio: This uncertainty is evaluated by comparing the cross section ratios of $\nu/\bar{\nu}$ computed with the default Rein-Sehgal model and an alternative model, the Hernández model [225]. The energy dependent difference between the two models is considered as the systematic uncertainties.

$\pi^0/\pi^\pm$ *ratio:* The resonant π^0 production cross section has a relatively large uncertainty. The uncertainty in the π^0 production relative to the $\pi^\pm$ production is evaluated by comparing the Rein-Sehgal model and the Hernández model. A 1σ variation increases the resonant π^0 production rate by 20% and decreases the resonant $\pi^\pm$ production rate by 20%.

Coherent pion production normalization: The systematic uncertainty in the coherent pion production normalization is estimated by comparing the Rein-Sehgal model with the experimental results. The 1σ effect changes the normalization of the CC ν_μ interaction by 100%, and the normalization of the NC and CC ν_e interactions by 50%.

DIS uncertainties

DIS normalization: The uncertainty in the DIS cross section normalization for neutrino energies from 30 GeV to 200 GeV is estimated to be 3.5% for neutrinos and 6.5% for anti-neutrinos, according to the agreement between measurements [226] and the prediction by NEUT.

PDF model difference: This uncertainty accounts for the difference in the DIS cross section between two different calculations with the nominal parton distribution function (PDF) from GRV98 [203] and the PDF from the CKMT model [227]. The uncertainty is computed separately for neutrinos and anti-neutrinos, as a function of energy. For neutrinos, it ranges from 5% to 30%, and decreases with increasing energy. The uncertainty for anti-neutrinos decreases from 50% to 10% with increasing energy.

DIS q^2 dependence: Four independent uncertainties are implemented to account for variations in the Bodek–Yang corrections [204] applied to the NEUT DIS cross sec-

tion models. For events with hadronic invariant mass W above $2\,\mathrm{GeV}/c^2$, a single uncertainty is defined as the difference in the DIS cross section with and without the Bodek–Yang corrections, expressed as a function of q^2, and treated as a 1σ variation. For events with invariant mass below $2\,\mathrm{GeV}/c^2$, three independent uncertainties are introduced to vary the vector component, the axial component, and the overall normalization of the Bodek–Yang correction. The vector uncertainty accounts for the effect of including next-to-leading-order QCD contributions to the F_2 and F_3 structure functions from Eq. 9.6. The axial uncertainty accounts for the possibility that the axial form factors deviate from the vector ones, which are assumed to be identical in the nominal Bodek–Yang correction. In both cases, the 1σ variation is implemented by reweighting events according to the ratio of cross sections with and without the additional features described in [228]. The normalization uncertainty corresponds to a uniform $\pm 3\%$ scaling of the correction.

Hadron multiplicity: This uncertainty is evaluated by comparing two hadron multiplicity models: the default model in NEUT and the AGKY model [229] implemented in GENIE. The resulting difference in the DIS cross section between the two models is assigned as the uncertainty, expressed as a function of the neutrino energy.

Other interaction uncertainties

FSI and SI: As introduced in Section 9.2.4, six parameters are included in NEUT to account for the normalizations of the probabilities of different FSI (SI) processes. The six input parameters are fitted to charged pion scattering data. The uncertainties in these parameters are estimated by varying their values within their correlated uncertainties to generate possible sets of values. The sets yielding the largest increase and decrease in the total event rate define the 1σ uncertainty.

NC/CC ratio: The 1σ variation of this systematic uncertainty in the NC/CC ratio is estimated to be 20%, due to the less-understood NC interactions.

CC ν_τ cross section: A 25% uncertainty on the CC ν_τ cross section is assumed which covers variations in different cross section models.

12.2.3 Detector Response Uncertainties

Detector-related systematic uncertainties are treated separately for each SK phase. For SK I, the reconstruction uncertainties are newly estimated for the samples reconstructed by fiTQun. Many of the detector-related uncertainties concern atmospheric neutrino event classifications, and are determined using a "scale-and-shift" method that fits MC to atmospheric neutrino data. Atmospheric neutrinos are used for this purpose because no other control sample spans the same energy range and event

topologies.

Scale-and-shift method

The scale-and-shift method is introduced here with a walk-through example of estimating the ring separation uncertainty for sub-GeV e-like samples with momentum p_e below 400 MeV/c. In the scale-and-shift method, the MC distribution of a reconstruction variable x, used to separate signal and background in the event classification, is fitted to data. The MC events are first labeled as true signal or background, and their respective x distributions are fitted to data independently by applying a linear transformation,

$$x' = \beta^1 x + \beta^0. \tag{12.7}$$

In total four parameters are fitted, including two scale parameters β^1_S and β^1_B, and two shift parameters β^0_S and β^0_B, where the subscripts S and B denote signal and background, respectively.

In the case of ring separation, the ring counting likelihood distributions are fitted. The signal is composed of true single-ring events[1], and the background is true multi-ring events. Figure 12.8 shows the best-fit likelihood distributions, where the best-fit MC is shown as red histogram, and the true single-ring and multi-ring components are shown as blue and violet histograms respectively.

After obtaining the best-fit values, the parameters are randomly varied with Gaussian fluctuations defined by their fit uncertainties. These variations shift events across the threshold used for selection, producing a distribution of signal and background counts. Probability density functions (PDFs) of the event counts are constructed based on the fit $\Delta\chi^2$ distributions following Wilks' theorem. The distributions of signal and background counts are then weighted by the PDFs. For the sub-GeV e-like ring separation ($p_e < 400$ MeV/c), the probability-weighted distributions of signal and background counts are shown in Figure 12.9. These distributions are fitted by Gaussian functions to obtain standard variations σ. The final ring separation uncertainty ϵ is given by,

$$\epsilon = \frac{|N_{\text{nominal}} - \bar{N}| + \sigma}{N_{\text{nominal}}}, \tag{12.8}$$

where N_{nominal} is the nominal event count and $\bar{N}$ is the best-fit event count. Two uncertainties, for sub-GeV single-ring e-like and sub-GeV multi-ring e-like, can be extracted.

[1] A true ring is defined as a ring produced by a particle that is 30 MeV more energetic than its Cherenkov threshold in water. Gamma rays with an energy above 30 MeV are also taken into account.

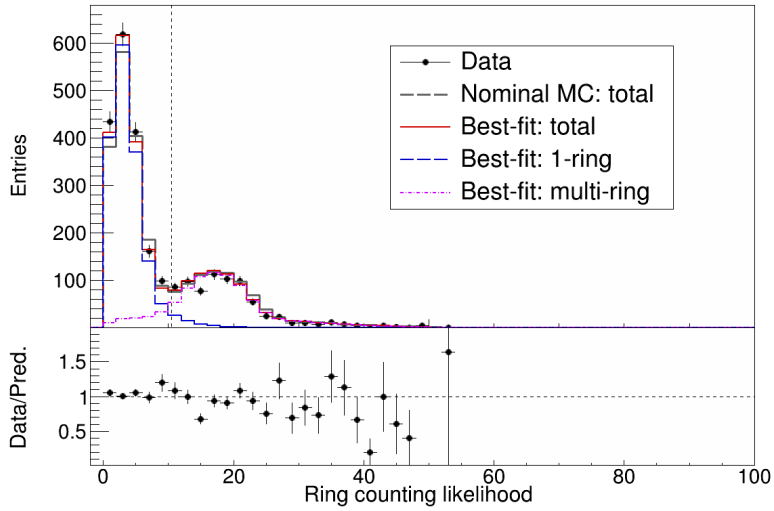

Figure 12.8: Ring counting likelihood distribution for sub-GeV e-like samples with momentum below 400 MeV/c. The dots denote the data and the gray dashed histogram denotes the nominal MC. The best-fit MC is shown as red histogram. Its two components, the true single-ring samples and the true multi-ring samples, are shown as blue dashed histogram and violet dotted-dashed histogram, respectively. The threshold is 10.5, indicated by the vertical dashed line. An event with ring counting likelihood below (above) the threshold is classified as a single-ring (multi-ring) event. The ratio of the data over the best-fit MC is plotted beneath the likelihood distributions.

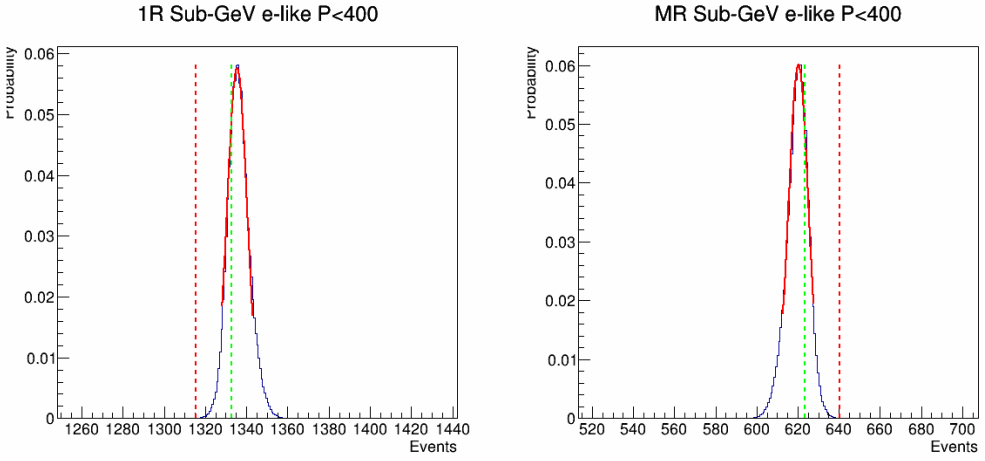

Figure 12.9: Distributions of signal and background counts obtained by independently fluctuating the scale and shift parameters around their best-fit values. The distributions, shown as black histograms, are after weighted by the probability density functions of the event counts. The nominal signal and background counts are indicated by vertical red lines, and the best-fit signal and background counts are indicated by vertical green lines. The distributions are further fitted by Gaussian functions, shown as red curves.

Reduction uncertainties

FC reduction: The FC reduction uncertainty is estimated by studying the cuts described in Section 10.1 using the scale-and-shift method. The flasher removal pro-

cedure in FC4 contributes a dominant part to the uncertainty. For SK I, the FC reduction uncertainty is estimated to be 0.2%.

FC/PC separation: An FC *multi-GeV μ-like* event can be mis-identified as a PC event, depending on NHITAC, the OD hits in the largest OD cluster. The scale-and-shift method is applied to the NHITAC to analyze the performance of FC/PC separation. The FC/PC separation uncertainty is estimated to be 0.6% for SK I.

Reconstruction uncertainties

Ring separation: The uncertainty on the separation between single-ring and multi-ring events is estimated with the scale-and-shift method. The MC distributions of ring counting likelihood, as partly shown in Figure 11.24, are fitted to the data distributions. Ten uncertainties are estimated for sub-GeV and multi-GeV samples, both e-like and μ-like. For sub-GeV single-ring samples, the uncertainties are treated separately for momentum below and above 400 MeV/c. The estimated ring separation uncertainties are listed in Table 12.6. Errors from a particular uncertainty are assumed to be fully correlated or anti-correlated among all of the analysis samples. A negative sign of a number in the table indicates anti-correlation. The systematic uncertainties from different sources are assumed to be independent from each other.

PID: Similar to the ring separation uncertainty, the scale-and-shift method is applied to the PID likelihoods partly shown in Figure 11.25 and Figure 11.26 to extract uncertainties on the separations between e-like and μ-like events. Eight uncertainties are estimated, for sub-GeV and multi-GeV, single-ring and multi-ring, and e-like and μ-like. Table 12.6 lists these uncertainties.

MME selection: The uncertainty on the selection of multi-GeV multi-ring e-like sample is also estimated with the scale-and-shift method. The MC distributions of MME likelihood, as shown in Figure 12.3, are fitted to the data distribution. Two uncertainties on the multi-GeV multi-ring e-like sample and the *multi-ring other* sample are extracted. Table 12.6 lists these uncertainties.

$\nu_e - \bar{\nu}_e$ separation: Similarly, two uncertainties on the selection of the *multi-ring ν_e-like* sample and the *multi-ring $\bar{\nu}_e$-like* sample are estimated with the scale-and-shift method, using the distributions of $\nu_e - \bar{\nu}_e$ separation likelihood as shown in Figure 12.5. Table 12.6 lists these uncertainties.

Two-ring π^0: The uncertainty on the selection of *2-ring π^0-like* sample is estimated by considering the ring separation and PID uncertainties for both rings. To select samples for this estimation, a primary selection of sub-GeV events without decay electron is performed. These events are further selected to form four sets of likelihood distributions. The likelihood and corresponding selection criteria are listed in Table 12.7.

Table 12.6: Systematic uncertainties on the ring separation, PID, MME selection, and $\nu_e - \bar{\nu}_e$ separation. Errors from a particular uncertainty are assumed to be fully correlated or anti-correlated among all of the analysis samples. A negative sign of a number in the table indicates anti-correlation. The systematic uncertainties from different sources are assumed to be independent from each other.

Uncertainty	1σ value [%]
Ring separation	
Sub-GeV single-ring	
e-like, $p < 400\,\mathrm{MeV}/c$	1.91
e-like, $p > 400\,\mathrm{MeV}/c$	−0.82
μ-like, $p < 400\,\mathrm{MeV}/c$	−1.22
μ-like, $p > 400\,\mathrm{MeV}/c$	0.90
Sub-GeV multi-ring	
e-like	−2.53
μ-like	−2.11
Multi-GeV single-ring	
e-like	−8.88
μ-like	6.59
Multi-GeV multi-ring	
e-like	5.00
μ-like	−4.68
PID	
Sub-GeV single-ring	
e-like	−0.20
μ-like	0.20
Sub-GeV multi-ring	
e-like	−1.22
μ-like	0.96
Multi-GeV single-ring	
e-like	0.15
μ-like	−0.11
Multi-GeV multi-ring	
e-like	−3.00
μ-like	1.48
MME selection	
Multi-ring ν_e&$\bar{\nu}_e$-like	−10.3
Muiti-ring other	16.8
$\nu_e - \bar{\nu}_e$ **separation**	
Multi-ring ν_e-like	0.12
Multi-ring $\bar{\nu}_e$-like	−0.26

For all distributions, the signal components are NCπ^0 events, and the background components are the other events. The scale-and-shift method is applied to each set of distribution, and the best-fit distributions are shown in Figure 12.10. Four uncertainties are extracted and summarized in Table 12.8. The sum in quadrature of these four uncertainties is considered as the final two-ring π^0 uncertainty, and is 3.47%.

Table 12.7: Selection criteria and likelihood for ring counting and PID of the first and second rings. The superscripts RC denotes ring counting, and 1 and 2 denote the first and second rings. The subscripts list the PID of each ring. For example, $\mathcal{L}_{ee}$ is the log-likelihood by assuming two e-like ring.

Criteria	Likelihood
None	$\Delta\mathcal{L}^{\mathrm{RC1}} = \mathcal{L}_e - \mathcal{L}_{ex}$
2+ e-like rings	$\Delta\mathcal{L}^{\mathrm{RC2}} = \mathcal{L}_{ee} - \mathcal{L}_{eex}$
2 rings	$\Delta\mathcal{L}^{\mathrm{PID1}} = \mathcal{L}_\mu - \mathcal{L}_e$
2 rings	$\Delta\mathcal{L}^{\mathrm{PID2}} = \mathcal{L}_{x\mu} - \mathcal{L}_{xe}$

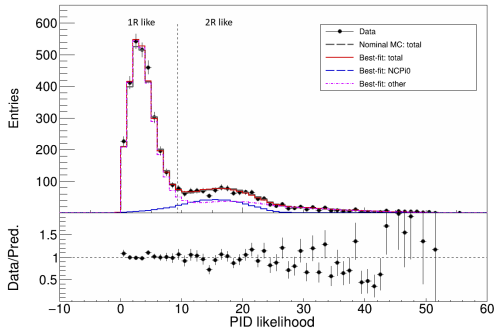

(a) Ring counting likelihood for 1st ring

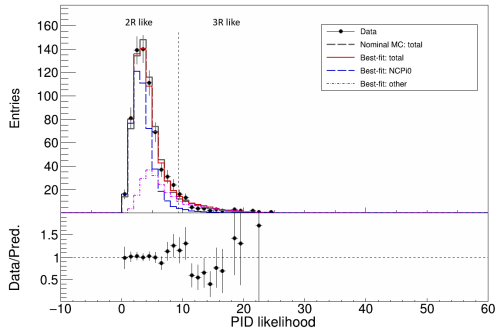

(b) Ring counting likelihood for 2nd ring

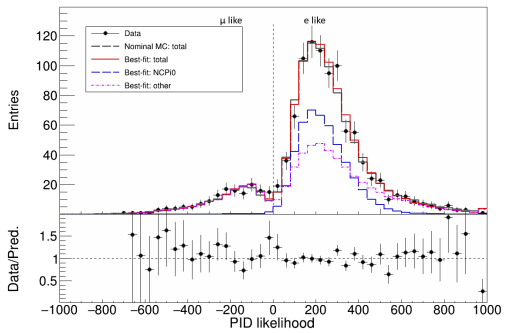

(c) PID likelihood for 1st ring

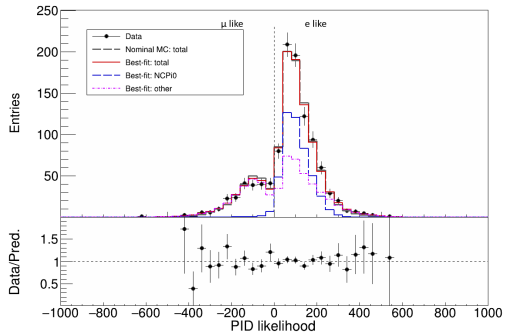

(d) PID likelihood for 2nd ring

Figure 12.10: Ring counting and PID likelihood distributions for both first ring and second ring of two-ring π^0 samples. The dots denote the data and the gray dashed histograms denote the nominal MCs. The best-fit MCs are shown as red histograms. The true NCπ^0 samples are shown as blue dashed histograms. The vertical dashed lines indicate the threshold values.

Absolute energy calibration: SK uses several control samples to estimate the energy reconstruction performance at different energy regions. Below 100 MeV, the Michel electron momentum spectrum from cosmic-ray stopping muons is used. Around 100 MeV,

Table 12.8: Results of the scale-and-shift analyses for *2-ring* π^0*-like* sample selection.

	First ring	Second ring
Ring counting	2.91%	1.67%
PID	0.70%	0.49%

the reconstructed mass of π^0 in the FC atmospheric neutrino sample is used. The differences in these spectra between the data and MC are taken as systematic uncertainties. Cosmic-ray stopping muons are also used to estimate the energy reconstruction performance at higher energies. Of them, the sub-GeV stopping muons account for energies from 280 MeV to 440 MeV. The data-MC disagreement in the sub-GeV stopping muons' reconstructed momentum spectra is considered as systematic uncertainty. Multi-GeV stopping muons are used to measure the energy calibration uncertainty at several GeV by comparing the ratios of the momentum over track length between data and MC. The fractional differences in these samples are shown in Figure 12.11. The largest difference is found to be 2.3%, and is considered as the systematic uncertainty. The time variation of energy reconstruction performance is also taken into account. The time variation of the fractional differences for Michel electron and multi-GeV stopping muon are evaluated. The larger value of them is found to be 0.73%, and is considered as the uncertainty from time variation. The final energy calibration uncertainty is the quadrature sum of the two values, computed to be 2.4%. The estimation procedure is detailed in Appendix B.

Up-down energy calibration: The uncertainty from the up/down asymmetry of the detector is estimated using Michel electrons. The difference in momentum distribution between data and MC is evaluated for in different zenith angle bins. The standard deviation over all zenith angle bins is assigned as the up/down energy calibration uncertainty for SK I. It is estimated to be 0.8%. Details may be found in Appendix B.

Other uncertainties

Decay electron tagging: A positive variation of the decay electron efficiency increases the event rates in the samples with decay electrons and decreases those without decay electrons. This uncertainty is evaluated to be 1.5% for SK I, using cosmic-ray stopping muons.

Fiducial volume: Due to imperfect vertex reconstruction, FC events within the fiducial volume (200 cm from the ID wall) can be mis-identified as outside the fiducial volume. To account for this effect, a 2% uncertainty on the normalization of FC events is assumed at 1σ. Note that this number is based on the vertex resolution of APFit. In stead of APFit, fiTQun is used in this analysis. The 2% uncertainty is conservative given fiTQun has better vertex resolution than APFit, as discussed in Section 11.4.1.

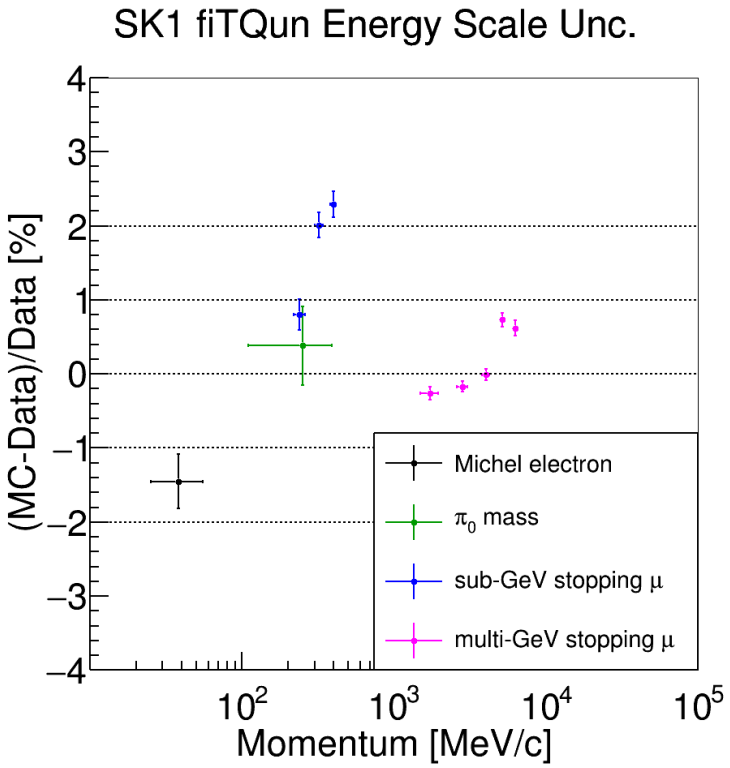

Figure 12.11: Absolute energy scale differences between data and MC for Michel electron, FC π^0, sub-GeV stopping muon, and multi-GeV stopping muon. The largest difference is considered as the systematic uncertainty.

Non-ν contamination: Non-neutrino background rates are treated as uncertainties, and are estimated by manual inspection into the final sample, as mentioned in Section 10.1.6. The uncertainties for e-like and μ-like samples are assumed independent, since their dominant backgrounds differ: flashers for e-like and cosmic-ray muons for μ-like. The average background rate in the FC samples is about 0.3%.

Non-ν_e contamination in e-like samples: This uncertainty accounts for the normalization of ν_μ contamination in the multi-GeV e-like samples. It is estimated using the scale-and-shift method applied to the ring-counting likelihood, by treating true ν_μ CC events as signal and other events as background. The uncertainty is defined as the ratio of the best-fit to the nominal fraction of ν_μ events misidentified as e-like.

NC contamination in single-ring μ-like samples: An NC event can be incorrectly classified as a single-ring μ-like event when it produces a charged pion which is difficult to be distinguished from a muon. A 10% uncertainty at 1σ is placed on the normalization of NC events in single-ring μ-like samples.

12.2.4 Oscillation Uncertainties

$\theta_{12}, \Delta m^2_{12}, \theta_{13}$*:* Atmospheric neutrinos have very limited sensitivity to θ_{12} and Δm^2_{12}. As for θ_{13}, the short baseline reactor neutrino experiments provide a better constraint. Therefore, these parameters are treated as systematic errors with starting values at the central values of the global best fit. Table 2.2 lists the global best-fit points with 1σ uncertainties, for both normal ordering and inverted ordering. In this analysis, when one neutrino mass ordering is assumed, these parameters are fixed to the corresponding best-fit point. The fraction change in event rates due to a 1σ fluctuation in each of these parameters is taken as a systematic uncertainty.

Matter effect: The electron number density in the Earth is assumed to have a 6.8% uncertainty, considering the difference between the electron-to-proton ratio of a pure iron core and a core with lighter elements. The effect on the event rates is less than 2%, and appears only in the upward-going samples.

12.3 Analysis Procedure

A χ^2 test is performed to test the agreement between the data and the prediction in the presence of the scalar-NSI. Free parameters include the scalar-NSI parameters and the neutrino oscillation parameters, except for Δm^2_{21}, θ_{12}, and θ_{13}. A series of predictions are generated by applying oscillation weights with different combinations of free parameters to the MC events. These oscillated predictions are fit to the data by minimizing the χ^2 over systematic uncertainties. A map of best-fit χ^2 values are then obtained for different combinations of free parameters. The global best-fit point and the allowed regions are determined from this map.

12.3.1 Oscillation Probability Calculation

The neutrino oscillation probability calculation is discussed in Section 2.3.2 and Section 8.2. The calculation of standard three flavor neutrino oscillation probability requires 6 parameter: θ_{12}, θ_{13}, θ_{23}, Δm^2_{21}, Δm^2_{32}, and δ_{CP}. In the presence of the scalar-NSI, 7 more parameters are required, in addition to the standard oscillation parameters. Recalling the discussion in Section 8.2, a 3×3 matrix δM encodes the effects of the scalar-NSI, and is parameterized as

$$\delta M = S_m \begin{pmatrix} \eta_{ee} & \eta_{e\mu} & \eta_{e\tau} \\ \eta^*_{e\mu} & \eta_{\mu\mu} & \eta_{\mu\tau} \\ \eta^*_{e\tau} & \eta^*_{\mu\tau} & \eta_{\tau\tau} \end{pmatrix}, \tag{12.9}$$

where the diagonal elements $\eta_{\alpha\alpha}$ are real and off-diagonal elements $\eta_{\alpha\beta}$ $(\beta \neq \alpha)$ are complex. From Eq. 8.5, the absolute mass scale of neutrino is associated with

the scalar-NSI contribution as $U\mathbb{M}U^{\dagger} + \delta M$, where U is the PMNS matrix, and $\mathbb{M} \equiv \mathrm{diag}(m_1, m_2, m_3)$ is the neutrino mass matrix. In this analysis, we include the lightest neutrino mass m_l as a parameter, where $m_l \equiv m_1$ in normal ordering and $m_l \equiv m_3$ in inverted ordering. The other two neutrino mass values are computed from it using the mass squared differences. However, m_l is fixed to 0 in this analysis for simplicity. Its impact on neutrino oscillations may be studied in the future. The scale factor S_m is set to 0.05 eV.

To compute the oscillation probability for an MC event, its true zenith angle is first converted to its path length. If the neutrino comes from below the horizon, it may experience a changing matter density that complicates the oscillation probability calculation. To account for the non-constant matter density, a simplified Preliminary Reference Earth Model (PREM) [61] is used, where the Earth is modeled as a four-layer symmetric sphere. Each layer has a different constant matter density, as listed in Table 12.9. The atmosphere is assumed to have zero matter density. For each layer along a neutrino's path, a matrix of transition amplitude X given by Eq. 2.44 is computed. The matrices are multiplied to obtain the oscillation probability along the entire path, as written in Eq. 2.46.

Table 12.9: Matter densities of the neutrino propagation layers used in this analysis. The layers are defined by ranges of radius R from the center of the Earth.

Layer	Range of R [km]	Density [g cm^{-3}]
Atmosphere	$6371 < R$	0
Crust	$5701 < R < 6371$	3.3
Mantle	$3480 < R < 5701$	5.0
Outer core	$1220 < R < 3480$	11.3
Inner core	$0 < R < 1220$	13.0

12.3.2 Oscillation Weight Calculation

The calculation of oscillation weights on MC events is introduced below. Low-energy upward-going neutrinos can experience fast oscillations due to large L/E. These fast oscillation features are not observable in the data because of limited energy and angular resolution. However, they can appear in the MC samples when exact L and E are used, producing artifacts or even biases in oscillation fits. Generating larger MC samples could mitigate this, but it is computationally inefficient. Instead, the oscillation probabilities are averaged over both energy and path length. For each MC event, 20 "neighbor" events that have the nearest true neutrino energies, with the same flavor, in the same sub-sample, and in the same zenith angle bin, are found. The RMS value of the energies of the neibor events E_{RMS} is used to define five energy sampling points: $E \pm E_{\mathrm{RMS}}$, $E \pm E_{\mathrm{RMS}}/2$, and E. For each of the five energy, oscillation probabilities are computed for 20 neutrino production heights sampled from the data

in [179], and are averaged over to form the oscillation probability for this energy. Next, the oscillation probabilities for all five energies are further averaged over. The final average oscillation probability is adopted as the oscillation probability of the MC event. Details are documented in [230].

Since it is impossible to know the original flavor of a neutrino event before oscillation, all possible original flavors must be considered when computing oscillation weight on an MC event. The oscillation weight on a ν_α event is given by

$$w_\alpha = P_{\nu_\alpha \to \nu_\alpha} + \sum_{\beta \neq \alpha} \frac{\Phi_{\nu_\alpha}}{\Phi_{\nu_\beta}} P_{\nu_\beta \to \nu_\alpha}, \tag{12.10}$$

where Φ_{ν_x} denotes the atmospheric neutrino flux as a function of true neutrino energy and direction, and x can be e or μ. Tau neutrinos are not intrinsic to the atmospheric neutrino flux. Their oscillation weights are given by

$$w_\tau = P_{\nu_\mu \to \nu_\tau} + \frac{\Phi_{\nu_\mu}}{\Phi_{\nu_e}} P_{\nu_e \to \nu_\tau}. \tag{12.11}$$

12.3.3 χ^2 Calculation

The χ^2 statistic is constructed based on the assumption that the observed event counts follow Poisson distributions. The probability of observing $\mathcal{O}_i$ events in the i^{th} bin is given by

$$P_i = \frac{e^{-E_i} E_i^{\mathcal{O}_i}}{\mathcal{O}_i!}, \tag{12.12}$$

where E_i is the expected number of events in this bin. The likelihood for observing a set of event counts in n bins is the product of the probabilities for all bins, and is written as

$$\mathcal{L}(E|\mathcal{O}) = \prod_{i=1}^{n} \frac{e^{-E_i} E_i^{\mathcal{O}_i}}{\mathcal{O}_i!}, \tag{12.13}$$

where i runs over all n bins. The χ^2 statistic is constructed as the log-likelihood ratio

$$\chi^2 = -2\log\frac{\mathcal{L}(E|\mathcal{O})}{\mathcal{L}(\mathcal{O}|\mathcal{O})} = 2\sum_{i=1}^{n}\left(E_i - \mathcal{O}_i + \mathcal{O}_i \log\frac{\mathcal{O}_i}{E_i}\right), \tag{12.14}$$

where the likelihood for an observation of $\mathcal{O}$ with an expectation of E is divided by its own maximum likelihood value.

Systematic uncertainties are accounted for using F_{ij}s, where an F_{ij} is the fractional change in the i^{th} bin for a 1σ fluctuation in the j^{th} systematic uncertainty source. Assuming a fluctuation of ϵ_j (with units of σ) in the j^{th} systematic uncertainty source,

the expected event count in the i^{th} bin is modified as

$$E_i \to E_i \left(1 + \sum_j^{n_{\text{syst.}}} \epsilon_j F_{ij}\right). \tag{12.15}$$

The ϵ_js are added to the χ^2 formulation as penalty terms:

$$\chi^2 = 2\sum_{i=1}^{n}\left[E_i\left(1+\sum_j^{n_{\text{syst.}}}\epsilon_j F_{ij}\right) - \mathcal{O}_i + \mathcal{O}_i \log\frac{\mathcal{O}_i}{E_i\left(1+\sum_j^{n_{\text{syst.}}}\epsilon_j F_{ij}\right)}\right] + \sum_j^{n_{\text{syst.}}}\epsilon_j. \tag{12.16}$$

Eq. 12.16 is the final χ^2 formulation. For each combination of free parameters, Eq. 12.16 is minimized by varying ϵ_js. The minimization is done by numerically solving the system of equations $\partial\chi^2/\partial\epsilon_j = 0$ for all ϵ_js.

12.4 Phenomena of the Scalar-NSI

In this section we describe the expected phenomena on atmospheric neutrinos driven by the scalar-NSI. As expressed in Eq. 8.7, the effects of the scalar-NSI are matter dependent and energy independent. The effects of the scalar-NSI appear exclusively on the neutrinos coming from below the horizon, and thus are visible when $\cos\theta < 0$. Figure 12.12 shows the oscillation probabilities $P_{\nu_\mu\to\nu_\mu}$ and $P_{\nu_\mu\to\nu_e}$ in the presence of diagonal scalar-NSI parameters $\eta_{\alpha\alpha}$. The standard three flavor oscillation probabilities are shown in Figure 12.13 for reference. The appearance probabilities with non-zero off-diagonal scalar-NSI parameters $\eta_{\alpha\beta}$ are shown in Figure 12.14. The complex $\eta_{\alpha\beta}$s are expressed in the form $\eta_{\alpha\beta} = |\eta_{\alpha\beta}|e^{i\phi_{\alpha\beta}}$.

12.4.1 Analytical Discussions

In general, it is very complicated to analytically evaluate the impact of the scalar-NSI on neutrino oscillations because the neutrino masses are directly modified. The non-constant matter density of atmospheric neutrinos has worsened the situation. Nevertheless, we can try to understand the effects of the scalar-NSI on neutrino oscillations under a two neutrino mixing framework. We assume a mixing between ν_μ, ν_τ and ν_2, ν_3, since the $\nu_\mu - \nu_\tau$ oscillations are dominant in atmospheric neutrino oscillations. Although under this assumption we may not be able to cover all 6 scalar-NSI parameters in the discussion, the discussion itself will be easier to understand.

Under the above assumption, the neutrino mixing is described by the mixing angle θ_{23} and the neutrino masses $\mathbb{M} = \text{diag}(m_2, m_3)$. From Eq. 8.5, the two flavor effective

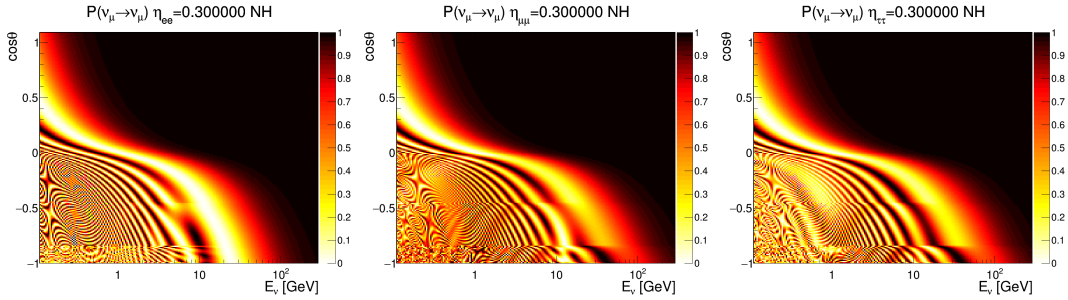

(a) $\eta_{ee} = 0.3$ (b) $\eta_{\mu\mu} = 0.3$ (c) $\eta_{\tau\tau} = 0.3$

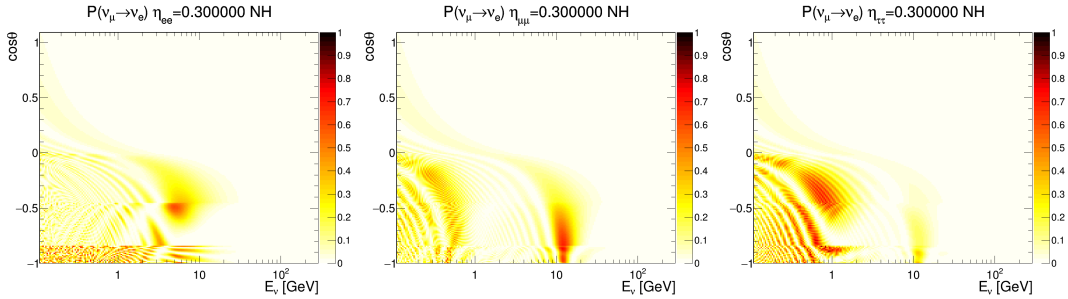

(d) $\eta_{ee} = 0.3$ (e) $\eta_{\mu\mu} = 0.3$ (f) $\eta_{\tau\tau} = 0.3$

Figure 12.12: Oscillation probabilities of $\nu_\mu \to \nu_\mu$ and $\nu_\mu \to \nu_e$ assuming non-zero diagonal scalar-NSI parameters. The survival probabilities are shown in the top row, and the appearance probabilities are shown in the bottom row. For each plot, all other scalar-NSI parameters are set to zero. The oscillation probabilities are shown as a function of neutrino energy and zenith angle. Standard oscillation parameters are taken from Table 12.1 assuming normal ordering. The lightest neutrino mass m_l is set to zero.

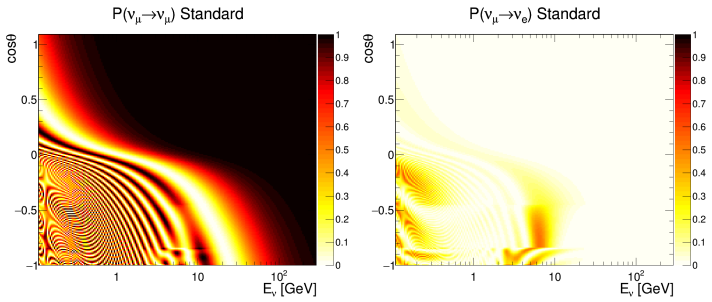

(a) Standard oscillation (b) Standard oscillation

Figure 12.13: Standard ν_μ disappearance and $\nu_\mu \to \nu_e$ appearance probabilities. Oscillation parameters are taken from Table 12.1 assuming normal ordering.

Hamiltonian with scalar-NSI $\mathcal{H}_F^{\text{scalar}-\text{NSI}}$ can be written as

$$\mathcal{H}_F^{\text{scalar}-\text{NSI}} = \frac{\left(U\mathbb{M}U^\dagger + \delta M\right)\left(U\mathbb{M}U^\dagger + \delta M\right)^\dagger}{2E}, \tag{12.17}$$

where the correction term δM due to the scalar-NSI is given by

$$\delta M = S_m \begin{pmatrix} \eta_{\mu\mu} & \eta_{\mu\tau} \\ \eta^*_{\mu\tau} & \eta_{\tau\tau} \end{pmatrix}. \tag{12.18}$$

For this analysis we set $S_m = 0.05\,\text{eV}$. In the next, we discuss one-by-one how the scalar-NSI parameters affect the effective mixing angle $\tilde{\theta}_{23}$ and the effective mass squared difference $\Delta\tilde{m}^2_{32}$.

First, we consider only $\eta_{\mu\mu}$ and set $\eta_{\tau\tau}$ and $\eta_{\mu\tau}$ to zero. For simplicity, we adopt $a_{\alpha\beta} = S_m\eta_{\alpha\beta}$. By diagonalizing the effective Hamiltonian from Eq. 12.17, the eigenvalues of which are given by

$$\lambda_\pm = \left(\frac{a_{\mu\mu} + m_2 + m_3}{2} \pm \frac{\sqrt{(m_3 - m_2)^2 - 2a_{\mu\mu}(m_3 - m_2) + a^2_{\mu\mu}}}{2} \right)^2. \tag{12.19}$$

Therefore, the absolute effective mass squared difference $|\Delta\tilde{m}^2_{32}|$ is given by

$$|\Delta\tilde{m}^2_{32}| = (a_{\mu\mu} + m_2 + m_3)\sqrt{(m_3 - m_2)^2 - 2a_{\mu\mu}(m_3 - m_2)\cos 2\theta_{23} + a^2_{\mu\mu}}. \tag{12.20}$$

The effective mass splitting takes the negative sign in the inverted ordering case ($m_3 < m_2$). By expanding the equation around $a_{\mu\mu} = 0$ and omitting the high-order terms, the relative correction due to the scalar-NSI is written as

$$\pm|\Delta\tilde{m}^2_{32}| - \Delta m^2_{32} = 2a_{\mu\mu}(m_3\cos^2\theta_{23} - m_2\sin^2\theta_{23}). \tag{12.21}$$

In the limit $\theta_{23} \to \pi/2$, the correction has the same sign as $\eta_{\mu\mu}$ in the normal ordering, and has the opposite sign relative to $\eta_{\mu\mu}$ in the inverted ordering. In both cases, a positive $\eta_{\mu\mu}$ enlarges the absolute effective mass splitting $|\Delta\tilde{m}^2_{32}|$, and a negative $\eta_{\mu\mu}$ makes $|\Delta\tilde{m}^2_{32}|$ smaller. Therefore, the atmospheric neutrino data may be fitted with a combination of a negative $\eta_{\mu\mu}$ and an enlarged $|\Delta m^2_{32}|$, and vice versa. Since there are several matter densities for atmospheric neutrino as discussed in Section 12.3.1, there may be several sets of $\eta_{\mu\mu}$ and $|\Delta m^2_{32}|$ that partially reproduce the data, causing quasi-degeneracies. The effective mixing angle $\tilde{\theta}_{23}$ in the presence of $\eta_{\mu\mu}$ is given by

$$\tan 2\tilde{\theta}_{23} = \frac{\tan 2\theta_{23}}{1 - \frac{a_{\mu\mu}}{(m_3 - m_2)\cos 2\theta_{23}}}. \tag{12.22}$$

The structure of the denominator indicates a correlation between $a_{\mu\mu}$ and $\cos 2\theta_{23}$, and thus an anti-correlation between $\eta_{\mu\mu}$ and $\sin^2\theta_{23}$. In the inverted ordering case, this becomes a correlation between $\eta_{\mu\mu}$ and $\sin^2\theta_{23}$.

In the presence of $\eta_{\tau\tau}$, the correction term has the same form as Eq. 12.21. There-

fore, the above discussions about the mass squared difference applies to $\eta_{\tau\tau}$. As for the effective mixing angle $\tilde{\theta}_{23}$ with non-zero $\eta_{\tau\tau}$, the correlation between $\eta_{\tau\tau}$ and $\sin^2\theta_{23}$ is in contrast to that between $\eta_{\mu\mu}$ and $\sin^2\theta_{23}$. That is, in the normal ordering case, $\eta_{\tau\tau}$ correlates with $\sin^2\theta_{23}$. In the inverted ordering case, $\eta_{\tau\tau}$ anti-correlates with $\sin^2\theta_{23}$.

Next, we derive the correction to the effective mass splitting and the effective mixing angle with a non-zero real $\eta_{\mu\tau}$. In the normal ordering case, the correction to the effective mass splitting is given by

$$|\Delta\tilde{m}^2_{32}| - \Delta m^2_{32} = -2a_{\mu\tau}(m_3 + m_2)\sin 2\theta_{23}. \tag{12.23}$$

The correction has an opposite sign relative to $\eta_{\mu\tau}$, suggesting that data may be fitted with a larger $|\Delta m^2_{32}|$ when $\eta_{\mu\tau} > 0$. In the inverted ordering case, the correction becomes

$$-|\Delta\tilde{m}^2_{32}| - \Delta m^2_{32} = 2a_{\mu\tau}(m_3 + m_2)\sin 2\theta_{23}. \tag{12.24}$$

If $\eta_{\mu\tau} < 0$, i.e. $\pi/2 < \phi_{\mu\tau} < 3\pi/2$, data may be fitted with a larger $|\Delta m^2_{32}|$. The effective mixing angle in the presence of $\eta_{\mu\tau}$ is given by

$$\tan 2\tilde{\theta}_{23} = \tan 2\theta_{23} + \frac{2a_{\mu\tau}}{(m_2 - m_3)\cos 2\theta_{23}}. \tag{12.25}$$

In the limit $\theta_{23} \to \pi/2$, the correction term $2a_{\mu\tau}/(m_2 - m_3)\cos 2\theta_{23} \ll \tan 2\theta_{23}$. Therefore, no correlation between $\eta_{\mu\tau}$ and θ_{23} is expected.

12.4.2 Oscillation Predictions

We now describe the analysis samples expected to be most sensitive to the scalar-NSI effects. Figure 12.12 shows that a non-zero η_{ee} has little impact on survival probabilities, whereas non-zero $\eta_{\mu\mu}$ or $\eta_{\tau\tau}$ shift the oscillation pattern in energy. The effects of $\eta_{\mu\mu}$ and $\eta_{\tau\tau}$ are similar in survival probabilities, but $\eta_{\tau\tau}$ also produces a clear modification in appearance probabilities. Consequently, μ-like samples provide constraints on both $\eta_{\mu\mu}$ and $\eta_{\tau\tau}$, while e-like samples are primarily sensitive to $\eta_{\tau\tau}$. In contrast, SK has limited sensitivity to η_{ee}. The samples showing the largest deviations from standard oscillations for $\eta_{\alpha\alpha} = 0.3$ are illustrated in Figure 12.15.

For the off-diagonal scalar-NSI parameters $\eta_{\alpha\beta}$, the oscillation probabilities $P_{\nu_\mu\to\nu_e}$ for $|\eta_{\alpha\beta}| = 0.3$ and phases $\phi_{\alpha\beta} = 0, \pi/2, \pi$ are shown in Figure 12.14. In the presence of $\eta_{e\mu}$, $P_{\nu_\mu\to\nu_e}$ generally increases for upward-going neutrinos, making the e-like samples sensitive to this parameter. A similar enhancement is observed for $\eta_{e\tau}$, although its effect is less pronounced than that of $\eta_{e\mu}$. The impact of $\eta_{\mu\tau}$ becomes significant when $\phi_{\mu\tau} = \pi$, in which case e-like samples are expected show sensitivity. The samples exhibiting the largest deviations from the standard oscillation prediction for

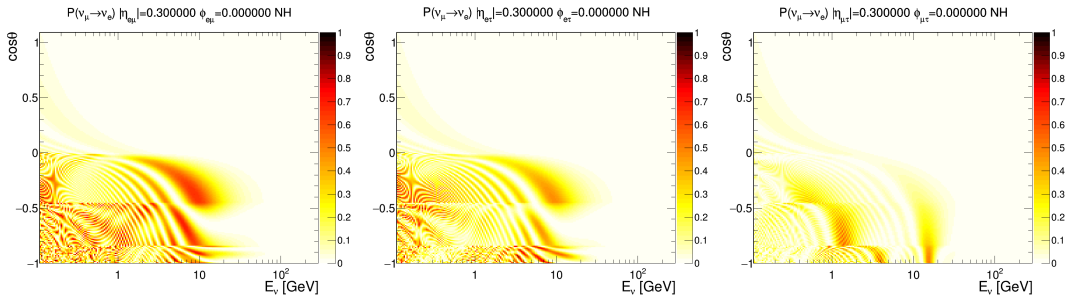

(a) $\eta_{e\mu} = 0.3$ (b) $\eta_{e\tau} = 0.3$ (c) $\eta_{\mu\tau} = 0.3$

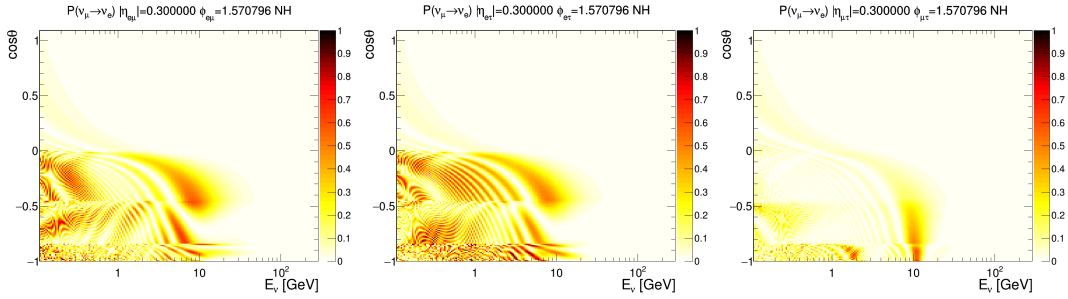

(d) $\eta_{e\mu} = 0.3e^{i\pi/2}$ (e) $\eta_{e\tau} = 0.3e^{i\pi/2}$ (f) $\eta_{\mu\tau} = 0.3e^{i\pi/2}$

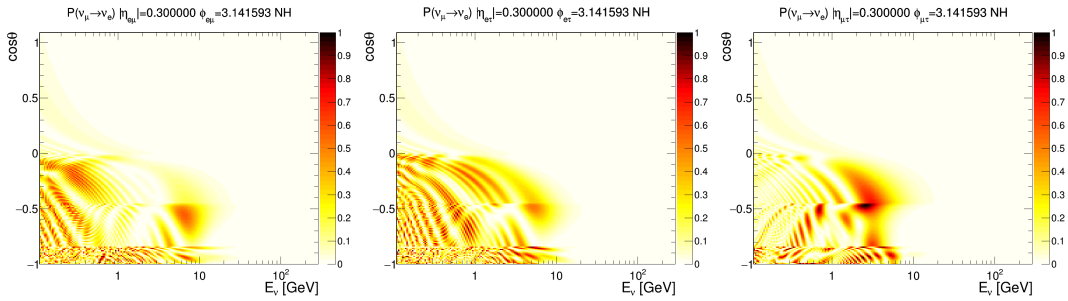

(g) $\eta_{e\mu} = 0.3e^{i\pi}$ (h) $\eta_{e\tau} = 0.3e^{i\pi}$ (i) $\eta_{\mu\tau} = 0.3e^{i\pi}$

Figure 12.14: Oscillation probabilities of $\nu_\mu \to \nu_e$ assuming non-zero off-diagonal scalar-NSI parameters. From left to right, the cases of non-zero $\eta_{e\mu}$, $\eta_{e\tau}$, and $\eta_{\mu\tau}$ are shown. The phases are $\phi_{\alpha\beta} = 0$ in the top row, $\phi_{\alpha\beta} = \pi/2$ in the middle row, and $\phi_{\alpha\beta} = \pi$ in the bottom row. The configurations of computation are identical to what is shown in Figure 12.12.

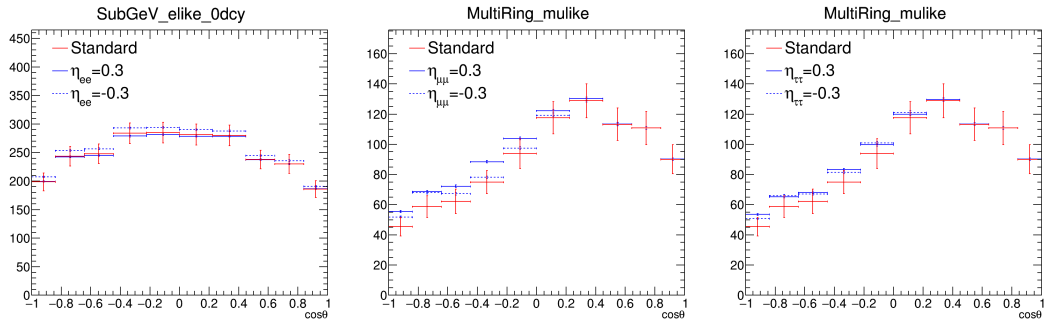

(a) $\eta_{ee} = \pm 0.3$ (b) $\eta_{\mu\mu} = \pm 0.3$ (c) $\eta_{\tau\tau} = \pm 0.3$

Figure 12.15: Zenith angle distributions of analysis samples that are sensitive to $\eta_{\alpha\alpha}$.

$\eta_{\alpha\beta} = 0.3e^{i\phi_{\alpha\beta}}$, $(\phi_{\alpha\beta} = 0, \pi/2, \pi)$ are presented in Figure 12.16. As can be seen, μ-like samples are also sensitive to $\eta_{\mu\tau}$ with $\phi_{\mu\tau} = \pi$.

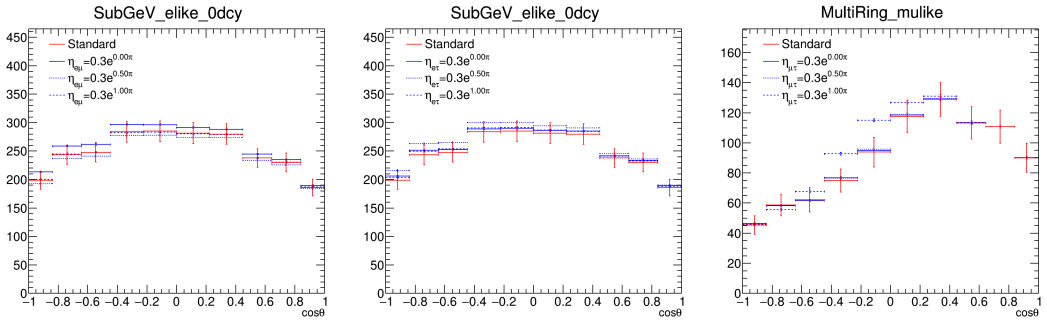

(a) $|\eta_{e\mu}| = \pm 0.3$ (b) $|\eta_{e\tau}| = \pm 0.3$ (c) $|\eta_{\mu\tau}| = \pm 0.3$

Figure 12.16: Zenith angle distributions of analysis samples that are sensitive to $\eta_{\alpha\beta}$.

12.4.3 Summary of the Expected Phenomena

We adopted a two neutrino mixing framework to discuss analytically the impact of the scalar-NSI parameters $\eta_{\mu\mu}$, $\eta_{\tau\tau}$ and $\eta_{\mu\tau}$ on the neutrino oscillations. Within this framework, both $\eta_{\mu\mu}$ and $\eta_{\tau\tau}$ have correlations with $|\Delta m^2_{32}|$, regardless of neutrino mass ordering. In the normal ordering case, $\eta_{\mu\mu}$ anti-correlates with θ_{23}, while $\eta_{\tau\tau}$ correlates with θ_{23}. In contrast, there is a correlation between $\eta_{\mu\mu}$ and θ_{23}, and an inverse correlation between $\eta_{\tau\tau}$ and θ_{23} in the inverted ordering. For $\eta_{\mu\tau}$, it is correlated with $|\Delta m^2_{32}|$ in the normal ordering, and is anti-correlated with $|\Delta m^2_{32}|$ in the inverted ordering. However, no correlation is found between this parameter and θ_{23}.

We show the oscillation predictions with the scalar-NSI effects using the explicit formulas as introduced in Section 8.2. The diagonal scalar-NSI parameters primarily affect μ-like samples through modifications to survival probabilities, with $\eta_{\tau\tau}$ also influencing e-like samples via appearance probabilities. However, sensitivity to η_{ee} remains limited. The off-diagonal parameters, by contrast, impact appearance channels more directly. The appearance probability $P_{\nu_\mu \to \nu_e}$ is enhanced by $\eta_{e\mu}$ and $\eta_{e\tau}$ to different degrees, making e-like samples sensitive to these parameters. When the phase of $\eta_{\mu\tau}$ is $\pi/2 < \phi_{\mu\tau} < 3\pi/2$, notable effects appear in both μ-like and e-like samples.

12.5 Result of Scalar-NSI Analysis

We present the values of the scalar-NSI parameters allowed by the FC atmospheric neutrino data in SK I. The results are derived by computing the χ^2 function from Eq. 12.16 on a grid of free parameters, listed in Table 12.10. To analyze a diagonal

scalar-NSI parameter $\eta_{\alpha\alpha}$, the grid is scanned with all other scalar-NSI parameters fixed to zero. As for an off-diagonal scalar-NSI parameter $\eta_{\alpha\beta}$, its magnitude $|\eta_{\alpha\beta}|$ and phase $\phi_{\alpha\beta}$ are allowed to vary while δ_{CP} is fixed to global best-fit value [22] ($\delta_{CP} = 1.19$) to save computational time, and all other scalar-NSI parameters are fixed to zero. It is safe to fix δ_{CP} in the analysis because SK has very limited sensitivity to δ_{CP}. For each scalar-NSI parameter, the grid is scanned twice for normal mass ordering and inverted mass ordering. The lightest neutrino mass is fixed to zero throughout this analysis. The fit values of scalar-NSI parameters will be presented at a density of $2.6\,\mathrm{g/cm^3}$.

Table 12.10: The grid of oscillation parameters and scalar-NSI parameters for this analysis. The mass squared difference is $|\Delta m^2_{32}|$ in normal ordering, and $|\Delta m^2_{31}|$ in inverted ordering. Parameters are scanned in equally spaced steps, including the minimum and maximum points.

Parameter	Min.	Max.	Steps
$\sin^2\theta_{23}$	0.2	0.78	30
$\|\Delta m^2_{32}\|$ or $\|\Delta m^2_{31}\|$ $[10^{-3}\,\mathrm{eV}^2]$	0.85	5.2	30
δ_{CP}	0.0	2π	11
$\eta_{\alpha\alpha}$	-1.0	1.0	101
$\|\eta_{\alpha\beta}\|$	0.0	0.64	33
$\phi_{\alpha\beta}$	0.0	2π	33

12.5.1 Diagonal Scalar-NSI Parameters

Figure 12.17 shows the 1D $\Delta\chi^2$ profiles of the scalar-NSI parameters $\eta_{\mu\mu}$ and $\eta_{\tau\tau}$. The fit results for non-zero η_{ee} are not shown because the SK atmospheric neutrino data have very limited sensitivities to η_{ee}. At each point, the value of χ^2 is minimized over all other parameters. The solid lines are the results of fit to the FC atmospheric neutrino data in SK I. The dashed lines are the sensitivities at the best-fit points. The horizontal dotted lines indicate the confidence level (CL) of 68%, 90%, and 99%. The results are shown for both normal mass ordering and inverted ordering. The best-fit values and 90% allowed intervals of $\eta_{\mu\mu}$ and $\eta_{\tau\tau}$ are summarized in Table 12.11. The zenith angle distributions of the best-fit predictions are shown in Appendix C.

Table 12.11: Best-fit values and 90% allowed intervals of $\eta_{\mu\mu}$ and $\eta_{\tau\tau}$. There are two allowed intervals for $\eta_{\tau\tau}$ in both normal and inverted ordering. The sign $\oplus$ denotes that there are two allowed intervals.

Mass Ordering	Parameter	Best-fit	90% allowed interval
Normal	$\eta_{\mu\mu}$	-0.38	[-0.430,0.102]
	$\eta_{\tau\tau}$	-0.36	[-0.798,-0.673]$\oplus$[-0.428,0.056]
Inverted	$\eta_{\mu\mu}$	-0.04	[-0.188,0.124]
	$\eta_{\tau\tau}$	-0.04	[-0.391,-0.236]$\oplus$[-0.211,0.124]

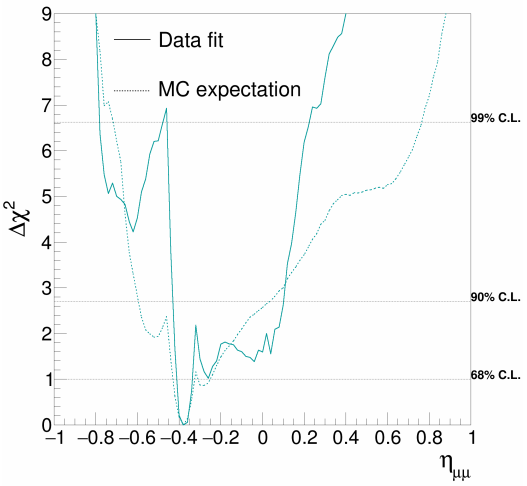

(a) $\eta_{\mu\mu}$, NO

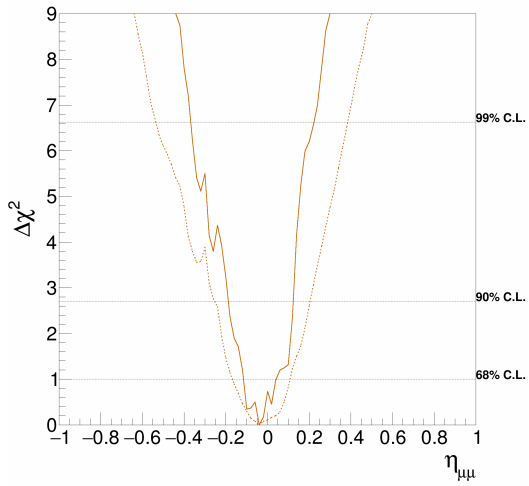

(b) $\eta_{\mu\mu}$, IO

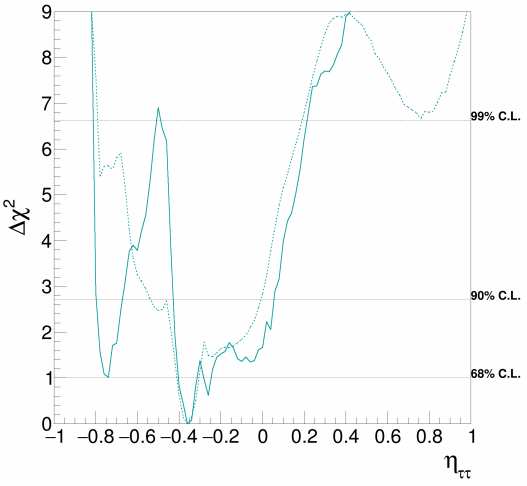

(c) $\eta_{\tau\tau}$, NO

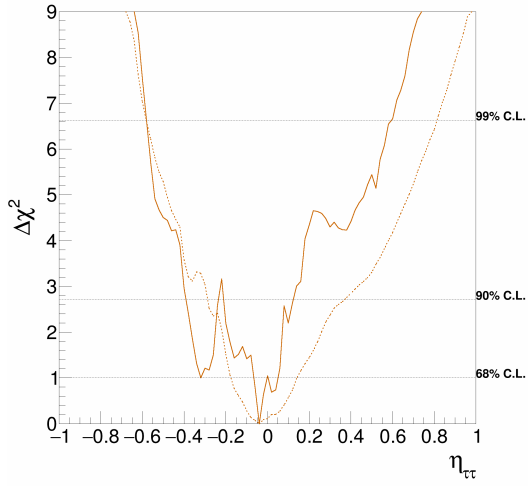

(d) $\eta_{\tau\tau}$, IO

Figure 12.17: 1D $\Delta\chi^2$ profiles of the fitted scalar-NSI parameters. The value of the scalar-NSI parameters are presented to be at a density of 2.6 g/cm^3. The $\Delta\chi^2$ values are taken with respect to the best-fit in the same parameter space ($\Delta\chi^2 \equiv \chi^2 - \chi^2_{\text{min}}$). Normal mass ordering is assumed for the left plots, and inverted mass ordering is assumed for the right plots. Solid lines show the result of data fit, and dashed lines show the fit to the MC assuming the best-fit scalar-NSI parameters. The horizontal dotted lines indicate 68%, 90%, and 99% confidence level (CL).

In the case of inverted mass ordering, the results are in agreement with standard neutrino oscillations where the best-fit values of $\eta_{\mu\mu}$ and $\eta_{\tau\tau}$ are around zero. However, in normal ordering, both $\eta_{\mu\mu}$ and $\eta_{\tau\tau}$ favor a negative value around -0.37. This result is explained by the $\eta_{\mu\mu}(\eta_{\tau\tau}) - |\Delta m^2_{32}|$ correlation discussed in Section 12.4.1, that is, a combination of a negative $\eta_{\mu\mu}(\eta_{\tau\tau})$ and a larger $|\Delta m^2_{32}|$ can fit the data. The impact on the measurements of the oscillation parameters will be discussed in Section 12.5.2.

To compare the results of this analysis with other data fit results, the allowed

values of $\eta_{\mu\mu}$ and $\eta_{\tau\tau}$ are converted to the fundamental quantity $\zeta_{\alpha\beta} \equiv y_q y_{\alpha\beta}/m_\phi^2$ under the assumption that the scalar mediator ϕ couples only to up and down quarks in matter with equal strength. For our results, the conversion factor is $1.49 \times 10^{-12}\,\mathrm{eV}^{-2}$. The allowed values are compared with the results from the solar neutrino data [1] in Table 12.12. Solar neutrinos set much more stringent constraints on the scalar-NSI thanks to the large matter density of the Sun. For each parameter, the allowed intervals derived in this analysis are wider than those given by solar neutrino data by two orders of magnitude. Given that the solar neutrino data fit is a phenomenological study, we can still regard the allowed intervals from this atmospheric neutrino study as valuable benchmark.

Table 12.12: The 90% allowed regions on scalar-NSI parameters from this analysis and from the latest Borexino and SNO data [1], converted to $\zeta_{\alpha\beta} \equiv y_q y_{\alpha\beta}/m_\phi^2$ with proper conversion factors. The values are in units of $10^{-15}\,\mathrm{eV}^2$. The sign $\oplus$ denotes that there are two allowed intervals.

Parameter	SK $[10^{-15}\,\mathrm{eV}^{-2}]$	Solar $[10^{-15}\,\mathrm{eV}^{-2}]$
$\zeta_{\mu\mu}$	[-640,152] (NO) [-280,185] (IO)	[-19.23,-16.75]$\oplus$[-6.77,1.00]
$\zeta_{\tau\tau}$	[-1188,-1002]$\oplus$[-637,83.4] (NO) [-582,-351]$\oplus$[-314,185] (IO)	[-17.22,-15.28]$\oplus$[-4.96,0.40]

We note that only less than 20% of the SK atmospheric neutrino data is used in this analysis, and the upward-going muon samples which are expected to be sensitive to scalar-NSI are not included yet. We show the expected sensitivities for the full SK FC neutrino data assuming a livetime of 9400 days in Figure 12.23, by fitting the MCs with scalar-NSI against an Asimov MC assuming standard neutrino oscillations. For each $\eta_{\alpha\alpha}$ parameter, the allowed interval at 90% becomes smaller and is 1/3 of that for the SK I FC neutrino data.

12.5.2 Impact of the Diagonal Scalar-NSI Parameters

Next, we discuss the impact of the scalar-NSI on the measurement of oscillation parameters. The 1D and 2D $\Delta\chi^2$ profiles of $\eta_{\mu\mu}(\eta_{\tau\tau})$ and other free oscillation parameters are shown in Figure 12.18, 12.19, 12.20, and 12.21. The best-fit values and 1σ errors of the free parameters are summarized in Table 12.13.

We demonstrate the $\eta_{\mu\mu}(\eta_{\tau\tau})-|\Delta m^2_{32}|$ correlation in Figure 12.18 and Figure 12.20. In Figure 12.18, an anti-correlation is observed in the $\eta_{\mu\mu} - |\Delta m^2_{32}|$ plane, with a best-fit point at (-0.38, $4.15 \times 10^{-3}\,\mathrm{eV}^2$). The same is observed in the $\eta_{\tau\tau} - |\Delta m^2_{32}|$ plane in Figure 12.20. The presence of $\eta_{\mu\mu}$ or $\eta_{\tau\tau}$ results in an ambiguity of the fit value of $|\Delta m^2_{32}|(|\Delta m^2_{31}|)$. However, given the correlation, external constraints on $|\Delta m^2_{32}|(|\Delta m^2_{31}|)$ from short-baseline experiments, where the effects of the scalar-NSI

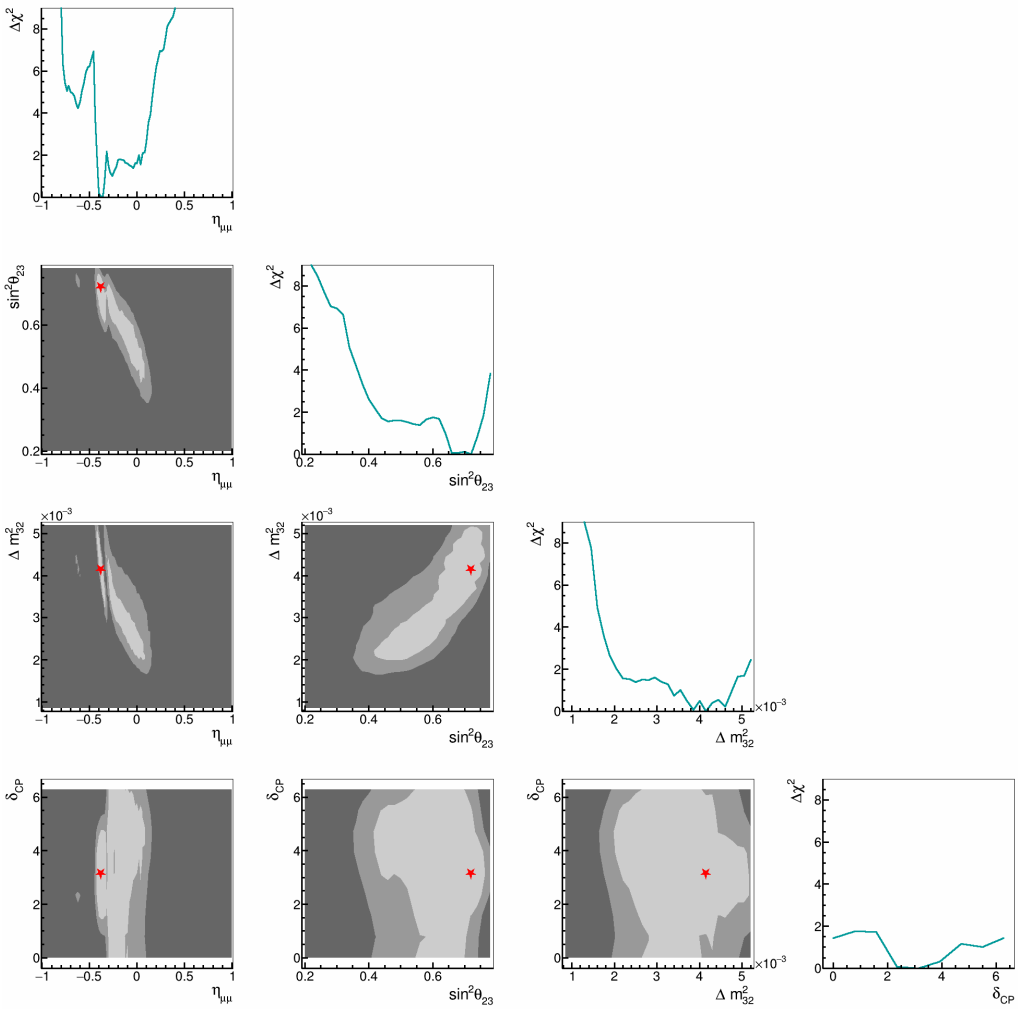

Figure 12.18: 1D and 2D $\Delta\chi^2$ profiles of all parameters in the $\eta_{\mu\mu}$ data fit assuming normal ordering. The values of $\Delta\chi^2$ are computed in the same manner as those in Figure 12.17. Red stars indicate the best-fit point. In the 2D contours, the light gray regions are favored at 68% CL, while it is 90% in the transition gray regions.

Table 12.13: Best-fit values and 1σ errors of $\eta_{\alpha\alpha}$, $\sin^2\theta_{23}$, $|\Delta m^2_{32}|$ ($|\Delta m^2_{31}|$ in inverted ordering), and δ_{CP}. NO denotes normal ordering, and IO denotes inverted ordering.

	$\eta_{\alpha\alpha}$	$\sin^2\theta_{23}$	$\lvert\Delta m^2_{32}\rvert(\lvert\Delta m^2_{31}\rvert)$ $[10^{-3}\,\mathrm{eV}^2]$	δ_{CP} [rad]
$\eta_{\mu\mu}$ NO	$-0.38^{+0.04}_{-0.03}$	$0.72^{+0.02}_{-0.08}$	$4.15^{+0.04}_{-0.82}$	$3.14^{+1.42}_{-1.22}$
$\eta_{\mu\mu}$ IO	$-0.04^{+0.08}_{-0.08}$	$0.48^{+0.08}_{-0.07}$	$2.50^{+0.52}_{-0.53}$	$3.14^{+3.22}_{-2.02}$
$\eta_{\tau\tau}$ NO	$-0.36^{+0.06}_{-0.04}$	$0.34^{+0.08}_{-0.05}$	$3.85^{+0.86}_{-0.65}$	$4.71^{+3.64}_{-1.25}$
$\eta_{\tau\tau}$ IO	$-0.04^{+0.04}_{-0.03}$	$0.54^{+0.05}_{-0.10}$	$2.50^{+0.20}_{-0.53}$	$3.93^{+2.25}_{-3.14}$

are suppressed by low matter density, may help improve the sensitivity to place limits on $\eta_{\mu\mu}(\eta_{\tau\tau})$.

In Figure 12.18, an inverse correlation is found in the $\eta_{\mu\mu} - \sin^2\theta_{23}$ plane. This anti-correlation becomes a correlation when replacing $\eta_{\mu\mu}$ with $\eta_{\tau\tau}$, as expected. A

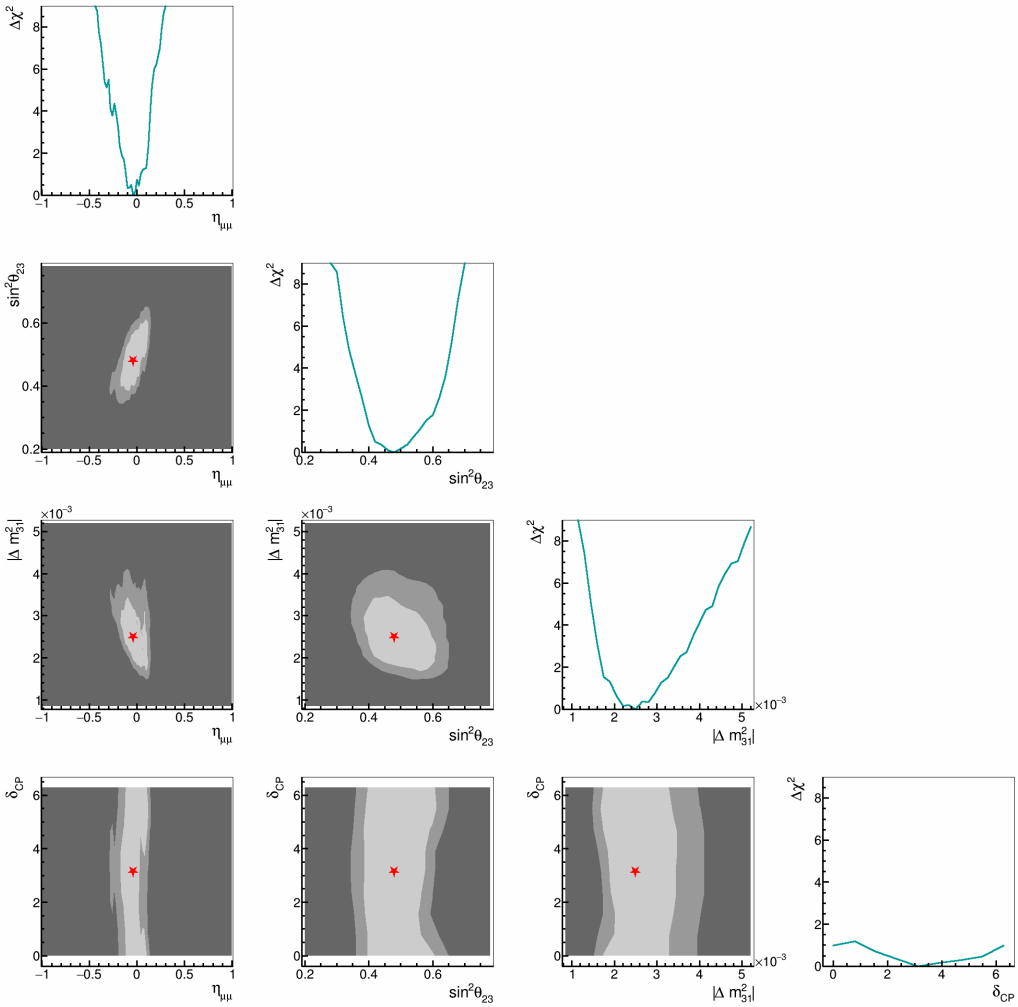

Figure 12.19: 1D and 2D $\Delta\chi^2$ profiles of all parameters in the $\eta_{\mu\mu}$ data fit assuming inverted ordering. The representations are the same as those in Figure 12.18.

flip of the correlation between $\eta_{\mu\mu}(\eta_{\tau\tau})$ and θ_{23} is observed when the neutrino mass ordering is inverted, as shown in Figure 12.19 and Figure 12.21. A non-zero $\eta_{\mu\mu}$ or $\eta_{\tau\tau}$ induces a significant ambiguity in the determination of θ_{23}. In all of these cases, the constraints on δ_{CP} are very limited, and there is no correlation between δ_{CP} and $\eta_{\alpha\alpha}$.

Finally, we note that the wiggles in the 1D $\Delta\chi^2$ profiles are due to the existence of multiple quasi-degeneracies. Because atmospheric neutrinos pass through multiple layers of matter each has a different matter density, there can be multiple sets of $\eta_{\mu\mu}$ and $|\Delta m^2_{32}|$ that partially reproduce the data, causing small wiggles. Concerning that the wiggles might be caused by rapid oscillations given that the scalar-NSI corrections modify the neutrino masses directly, we tested different energy averaging schemes in the calculation of oscillation probabilities. We increased the number of sampling points and extended the range of energy sampling, and tested the new energy averaging scheme using fit to toy MCs. As a result, the new energy averag-

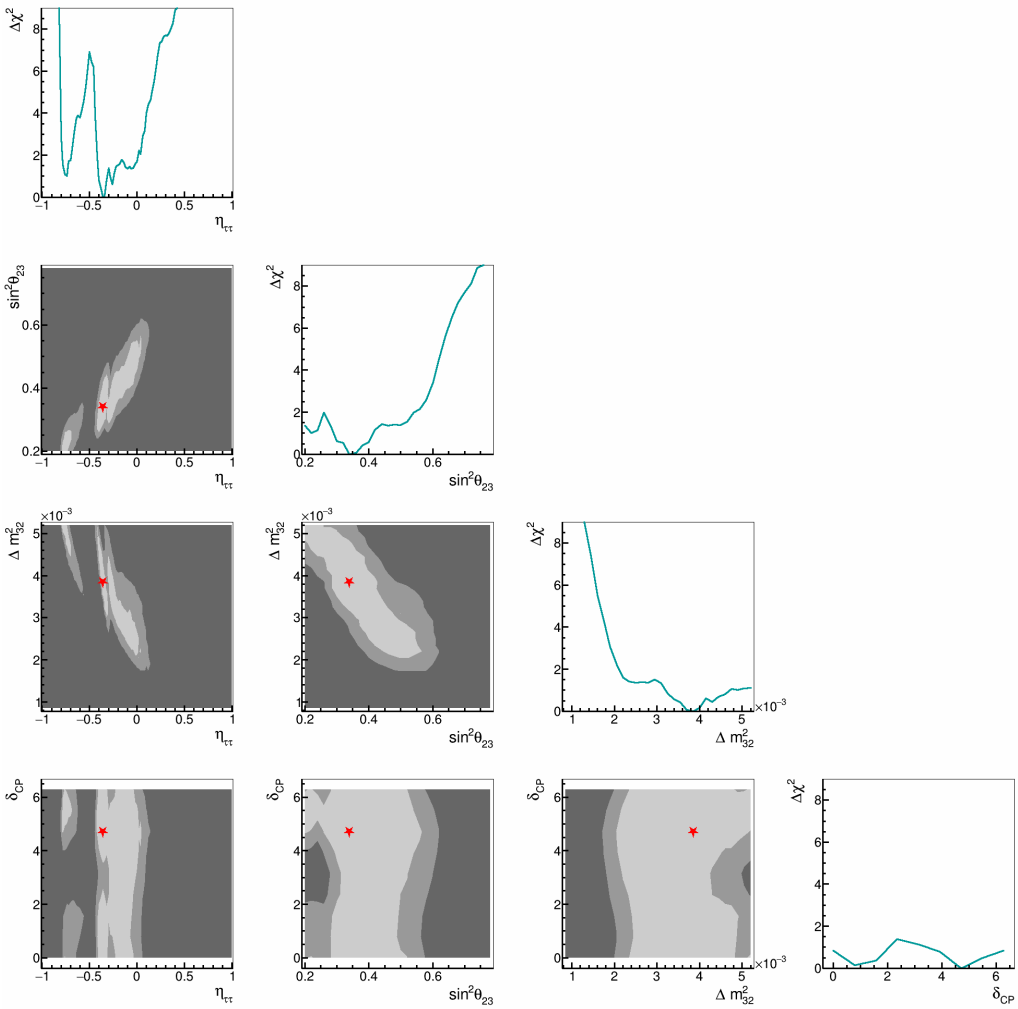

Figure 12.20: 1D and 2D $\Delta\chi^2$ profiles of all parameters in the $\eta_{\tau\tau}$ data fit assuming normal ordering. The representations are the same as those in Figure 12.18.

ing scheme shows no significant change relative to the conventional energy averaging method. Therefore, we continue to use the conventional energy averaging method introduced in Section 12.3.2 in this analysis.

12.5.3 Off-diagonal Scalar-NSI Parameters

We present in Figure 12.22 the allowed regions of the off-diagonal scalar-NSI parameters given by the FC atmospheric neutrino data in SK I. The results are shown on the $|\eta_{\alpha\beta}| - \phi_{\alpha\beta}$ plane. $|\Delta m^2_{32}|$ and $\sin^2\theta_{23}$ are minimized over, and δ_{CP} is fixed to 1.19. The red stars indicate the best-fit points derived from this analysis. For $\eta_{e\mu}$ and $\eta_{e\tau}$, non-zero values are slightly preferred, while the pure neutrino oscillation is still within 90% CL. For $\eta_{\mu\tau}$, non-zero values are favored, with a phase $\phi_{\mu\tau} \sim \pi$ in the case of normal mass ordering, and $\phi_{\mu\tau} \sim 0$ in inverted ordering. The values of $|\Delta m^2_{32}|(|\Delta m^2_{31}|)$ at the best-fit points are $3.85 \times 10^{-3}\,\mathrm{eV}^2$ and $4 \times 10^{-3}\,\mathrm{eV}^2$ for normal and inverted ordering respectively. This is again as expected along the discussions in

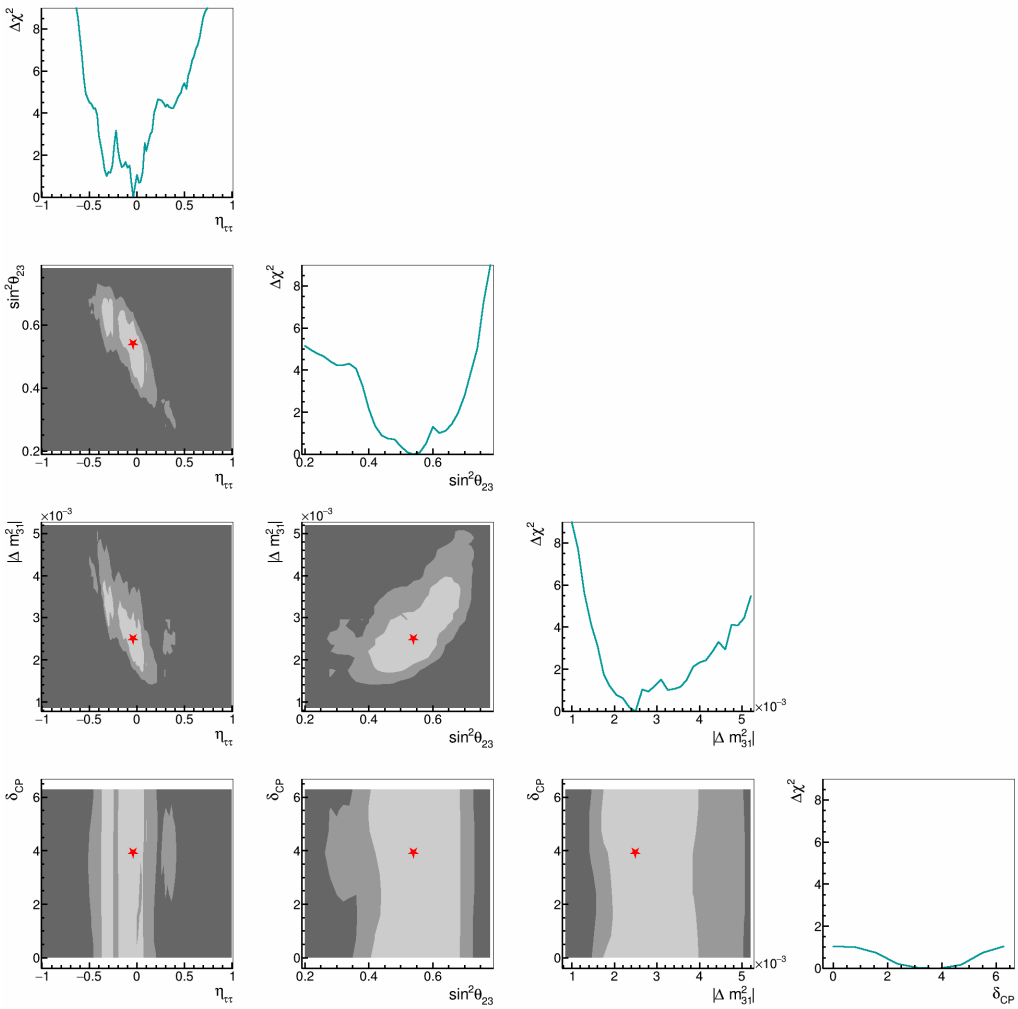

Figure 12.21: 1D and 2D $\Delta\chi^2$ profiles of all parameters in the $\eta_{\tau\tau}$ data fit assuming normal ordering. The representations are the same as those in Figure 12.18.

Section 12.4.1, where $\eta_{\mu\tau}$ is expected to correlate with $|\Delta m^2_{32}|$ in normal ordering, and inversely correlate with $|\Delta m^2_{31}|$ in inverted ordering. For the analyses of $\eta_{e\mu}$ and $\eta_{e\tau}$, the best-fit values of $|\Delta m^2_{32}|(|\Delta m^2_{31}|)$ agree with the global best-fit values for standard oscillations. The zenith angle distributions of the best-fit predictions in the presence of $\eta_{\mu\tau}$ are shown in Appendix C.

We also show in Figure 12.22 the best-fit results given by NOvA and T2K data from [7]. These best-fit values were reported at a density of $3\,\mathrm{g/cm^3}$, and are rescaled to what they would be for a density of $2.6\,\mathrm{g/cm^3}$. We find that the best-fit points in [7] fall within the 90% allowed regions obtained in our analysis. This coincidence may suggest a connection between these results and is worth clarifying in future work.

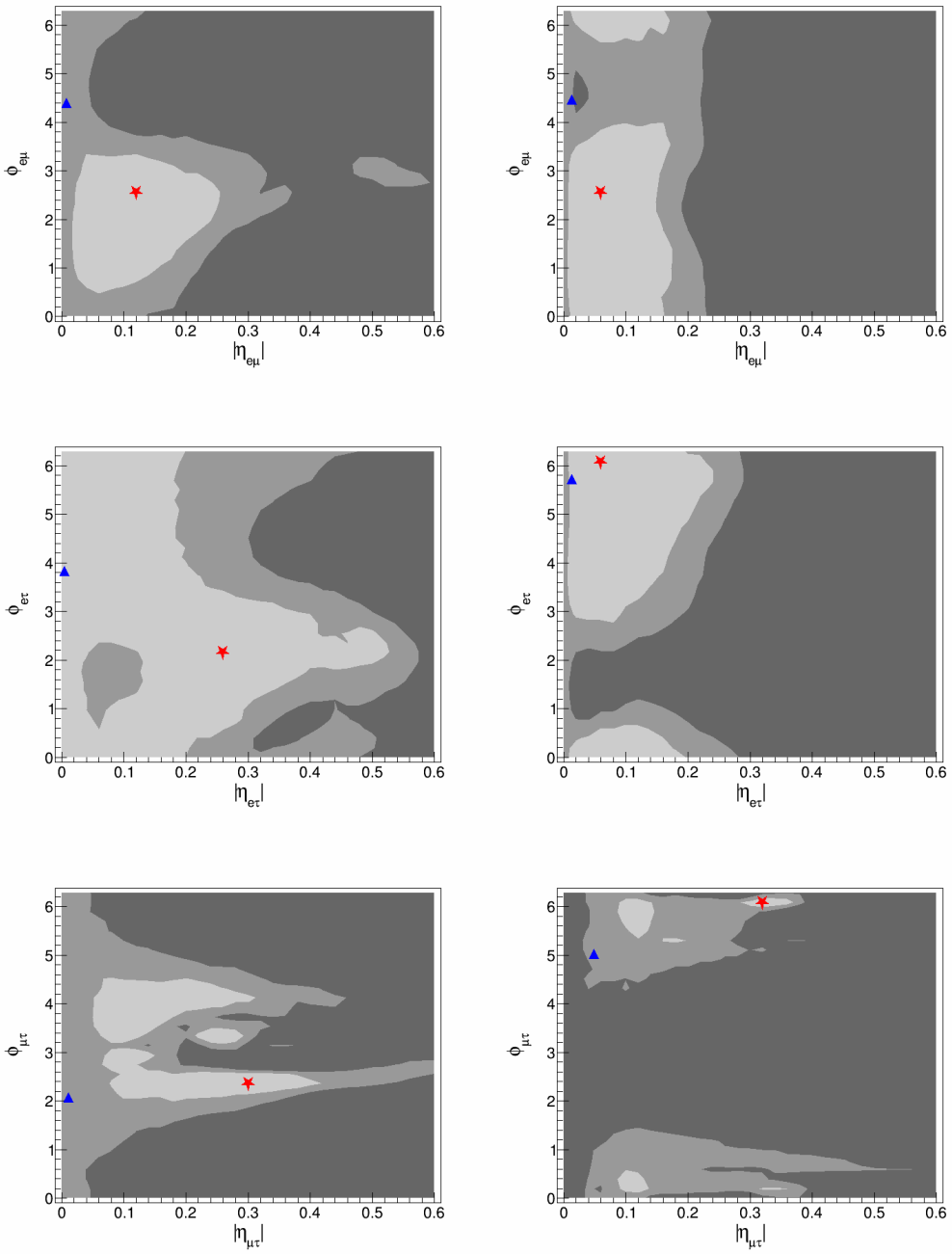

Figure 12.22: 2D $\Delta\chi^2$ profiles of the off-diagonal scalar-NSI parameters $\eta_{\alpha\beta}$ in the $|\eta_{\alpha\beta}| - \phi_{\alpha\beta}$ plane. The value of the scalar-NSI parameters are presented to be at a density of 2.6 g/cm^3. The $\Delta\chi^2$ values are taken with respect to the best-fit in the same parameter space ($\Delta\chi^2 \equiv \chi^2 - \chi^2_{\text{min}}$). Normal mass ordering is assumed for the left plots, and inverted mass ordering is assumed for the right plots. In all contours, the light gray regions are favored at 68% CL, while it is 90% in the transition gray regions. The red stars indicate the best-fit points from this analysis, and the blue triangles denote the best-fit points given by NOvA and T2K data, taken from [7] and rescaled properly to be at a matter density of 2.6 g/cm^3.

12.6 Conclusion and Outlook

The scalar-NSI is a new physics scenario that assumes neutrinos coupling with a hypothetical scalar field. It appears in the neutrino Hamiltonian as corrections to the neutrino masses. The size of effects of the scalar-NSI depends only on the matter density that neutrinos encounter. If such interactions exist, they could modify the neutrino masses when neutrinos pass through matter. Therefore, the presence of the scalar-NSI has the potential to modify the interpretation of neutrino oscillation data, leading to shifts in the measured values of oscillation parameters such as the mass splittings, mixing angles, and the CP-violating phase. Therefore, it is crucial to probe their existence using data and to establish experimental constraints on their magnitude.

We performed the first fit to the scalar-NSI parameters using the fully-contained atmospheric neutrino data in the SK I phase. These data are processed by a precision reconstruction tool, fiTQun. The analysis probed both the diagonal and off-diagonal scalar-NSI parameters, with the fit performed for both normal and inverted mass orderings. The lightest neutrino mass is fixed to zero throughout the analysis, and the results are presented as they would be at a matter density of $2.6\,\mathrm{g/cm^3}$. Results of this analysis are consistent with the standard neutrino oscillation within 90% C.L. No significant sign of the scalar-NSI is found.

For the diagonal parameters, the inverted ordering results are consistent with standard oscillations, whereas the normal ordering favors negative values of $\eta_{\mu\mu}$ and $\eta_{\tau\tau}$ are found to be $-0.38^{+0.04}_{-0.03}$ and $-0.36^{+0.06}_{-0.04}$, respectively. Meanwhile, the values of $|\Delta m^2_{32}|$ in the normal ordering results are $4.15^{+0.04}_{-0.82} \times 10^{-3}\,\mathrm{eV}^2$ and $3.85^{+0.86}_{-0.65}$ for a non-zero $\eta_{\mu\mu}$ and $\eta_{\tau\tau}$, larger than the global best-fit value for the standard neutrino oscillations. These results reflect the strong correlation between $\eta_{\mu\mu}(\eta_{\tau\tau})$ and $|\Delta m^2_{32}|$, whereby a non-zero $\eta_{\mu\mu}(\eta_{\tau\tau})$ can be compensated by shifts in the fit mass squared difference. The analysis also shows that the scalar-NSI has broaden the allowed regions of the oscillation parameters, especially in the determination of θ_{23}, while leaving δ_{CP} essentially unconstrained. When converted to the fundamental parameters $\zeta_{\alpha\beta} \equiv y_q y_{\alpha\beta}/m^2_\phi$, where m^2_ϕ is the mass of the scalar mediator and y_q and $y_{\alpha\beta}$ are coupling constants to quarks and neutrinos, the bounds obtained from SK I are weaker by two orders of magnitude compared to those from solar neutrinos. That said, this result is still an important benchmark as it is from the first experimental study of the scalar-NSI.

For the off-diagonal sector, the analysis finds a preference for $|\eta_{\mu\tau}| = 0.3$, with phases $\phi_{\mu\tau} \sim \pi$ (normal ordering) and $\phi_{\mu\tau} \sim 0$ (inverted ordering). The values of $|\Delta m^2_{32}|(|\Delta m^2_{31}|)$ are $3.85 \times 10^{-3}\,\mathrm{eV}^2$ and $4 \times 10^{-3}\,\mathrm{eV}^2$, again larger than the global best-fit value for the standard neutrino oscillations. This result also demonstrates

the fact that the atmospheric neutrino data can be accommodated by the interplay between $\eta_{\mu\tau}$ and a larger $|\Delta m^2_{32}|$. The best-fit values are found to be compatible with those obtained from fit to NOvA and T2K data within the 90% allowed region, indicating that the results are not in tension and may point to a connection worth further investigation.

While placing limits on the scalar-NSI, these results demonstrate that the presence of a non-zero scalar-NSI can affect the measurement of oscillation parameters significantly. The ambiguities presented in the measurement of $|\Delta m^2_{32}|(|\Delta m^2_{31}|)$ in the presence of the scalar-NSI suggest the need for external data, where the effects of the scalar-NSI are suppressed, to further improve the constraints on the scalar-NSI.

Although the present analysis is based on only a subset of the SK atmospheric neutrino data, we demonstrate that atmospheric neutrinos can provide constraints on the scalar-NSI. With the inclusion of the full SK data set, the sensitivity is expected to improve significantly. We present the expected sensitivities to the scalar-NSI parameters for the full SK FC neutrino data assuming a livetime of 9400 days in Figure 12.23 and 12.24. With the full SK data, we expect to narrow the allowed interval at 68% CL on each diagonal scalar-NSI parameter to 1/3 of that derived using SK I data. The 68% limits of the off-diagonal parameters $\eta_{\alpha\beta}$ are expected to be improved to < 0.1, equivalent to $|\zeta_{\alpha\beta}| = 1.49 \times 10^{-13}\text{eV}^{-2}$.

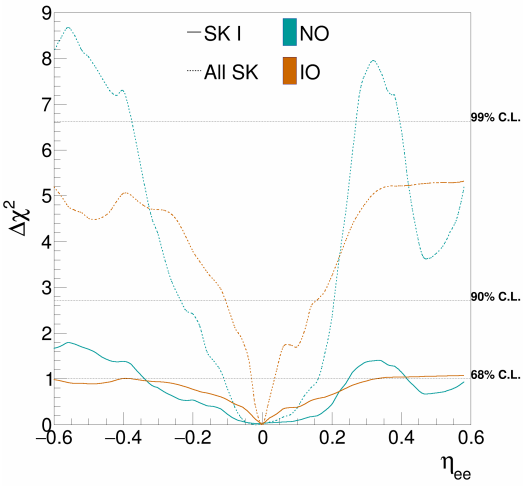

(a) η_{ee}

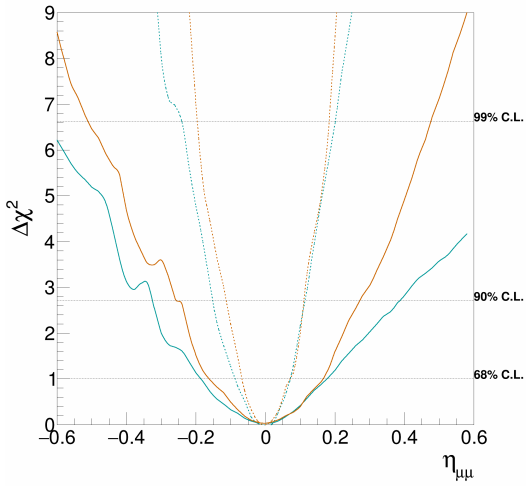

(b) $\eta_{\mu\mu}$

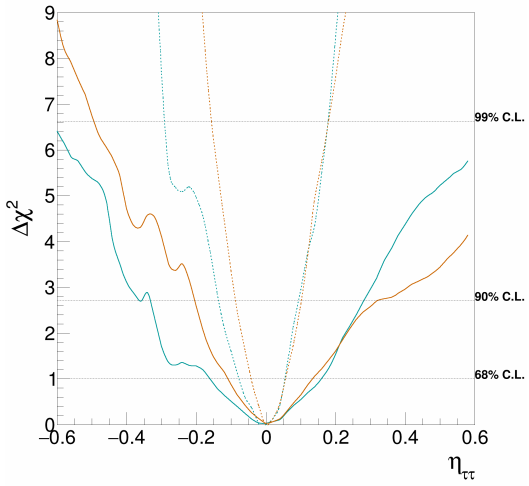

(c) $\eta_{\tau\tau}$

Figure 12.23: Sensitivity to measure the diagonal scalar-NSI parameters using SK I FC atmospheric neutrino data (solid lines) and the expected sensitivity for full SK data set (dotted lines) till the beginning of HK's operation, assuming a livetime of 9400 days.

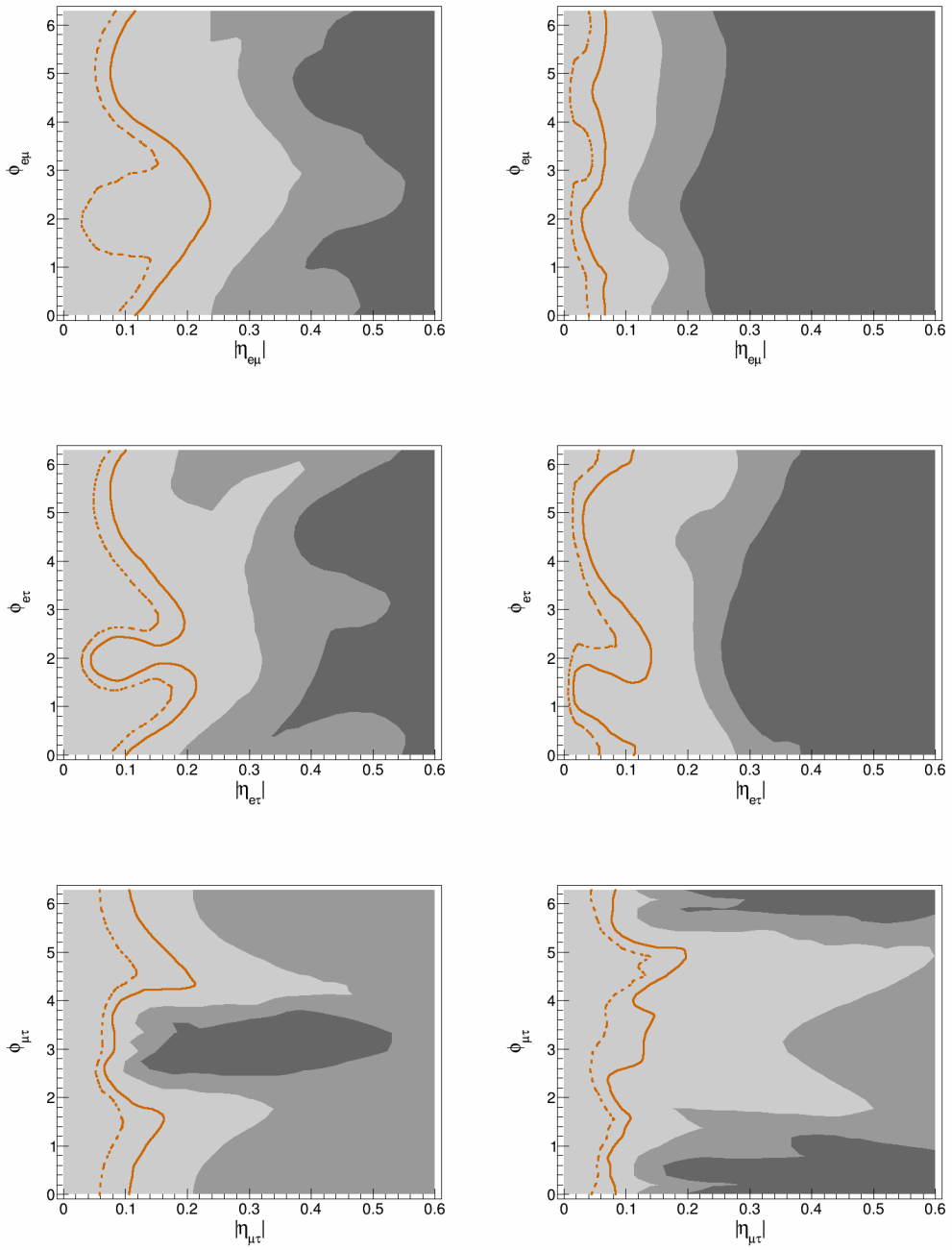

Figure 12.24: Sensitivity to measure the off-diagonal scalar-NSI parameters using SK I FC atmospheric neutrino data (filled contours) and the expected sensitivity for full SK data set (orange lines) till the beginning of HK's operation, assuming a livetime of 9400 days. In each plot, the light gray region is favored at 68% CL, while it is 90% in the transition gray regions for the SK I FC data. The expected limits from the full SK data at 68% and 90% are indicated by the orange dotted line and solid line, respectively.

Part 3

Summary

Chapter 13

Conclusions and Outlook

This thesis covers two major topics focusing on neutrinos. The first topic is the combined pre-supernova alert system with the KamLAND experiment and the Super-Kamiokande experiment. We present updates on the sensitivity of pre-supernova (pre-SN) neutrinos from a Betelgeuse-like star using the individual alert systems of KamLAND and Super-Kamiokande (SK), and introduce a combined pre-SN alert system integrating both detectors. For the sensitivity studies, pre-SN neutrino fluxes are calculated based on the models of [101] and [103], including neutrino oscillation effects. Reactor neutrinos from Japanese nuclear power plants represent a significant background due to their similar energy range, and this study considers varying reactor activity levels. Assuming nearby reactors operate at 100% load, background rates are estimated at 0.19 events/day in KamLAND and 12.4 events/day in SK.

The optimal warning times differ between detectors depending on flux assumptions. For the Odrzywolek model with normal mass ordering, KamLAND can provide a 6.5-hour warning, detecting pre-SN neutrinos up to 280 pc. SK achieves an optimistic warning of 10.9 hours and a distance coverage of 500 pc for the Patton model.

The combined alert system, operational since May 2023, performs a joint statistical test using data from both detectors. By leveraging their complementary properties, the combined system improves sensitivity, providing an optimistic warning of 12.4 hours for the Patton model with normal ordering—longer than either detector individually. Its coverage extends to 510 pc for 15 $M_\odot$ progenitors. Even under increased reactor backgrounds, the system remains sensitive, with warning times exceeding 2.2 hours, sufficient to accommodate data-processing latency, allowing for preparation time for supernova burst neutrino and gravitational wave observations. Additionally, it reduces dead time, enabling continuous monitoring if one detector is offline.

Currently, directional information cannot be obtained, as both KamLAND and SK rely on inverse beta decay, which smears the correlation between positron and neutrino directions. Studies on electron scattering detection in SK and the use of time-dependent flux "shape analysis" are ongoing and may further enhance early warning capabilities. Future plans include incorporating additional pre-SN neutrino detectors, such as JUNO, Hyper-Kamiokande, and DUNE. Different levels of participation will be considered, from full data sharing to alert-only contributions, ensuring the combined system remains feasible and expandable.

The second topic in this thesis is the first experimental search of non-standard neutrino interactions mediated by a scalar particle with 1489.2 days of atmospheric neutrino data from the SK I phase using the precision reconstruction algorithm, fiTQun. The PMT response model for the simulation in the SK I phase is refined to resolve the data-MC discrepancy observed in the particle type discrimination distributions. Using Michel electron from cosmic-ray muons as a calibration source, the single-photoelectron distribution and the PMT threshold function are optimized. New MC predictions are produced using the updated PMT response model, and are processed by fiTQun together with the data.

Using the data and MC, we performed fits assuming the existence of the scalar-NSI. Both the diagonal and off-diagonal scalar-NSI parameters are probed for normal and inverted mass orderings, assuming a vanishing lightest neutrino mass. Results are presented at a matter density of $2.6\,\mathrm{g/cm^3}$. We did not find significant signal of the scalar-NSI in this analysis.

For diagonal couplings, $\eta_{\mu\mu}$ is determined to be $-0.38^{+0.04}_{-0.03}$ in the normal ordering and $-0.04^{+0.08}_{-0.08}$ in the inverted ordering. The value of $|\Delta m^2_{32}|$ in the normal ordering result is $4.15^{+0.04}_{-0.82}\times10^{-3}\,\mathrm{eV}^2$, larger than global best-fit value for the standard neutrino oscillations, suggesting a degeneracy in the presence of $\eta_{\mu\mu}$. The values of $\eta_{\tau\tau}$ in the normal and inverted ordering are $-0.36^{+0.06}_{-0.04}$ and $-0.04^{+0.04}_{-0.03}$. Similar to the $\eta_{\mu\mu}$ analysis, the normal ordering fit value of $|\Delta m^2_{32}|$ in the presence of $\eta_{\tau\tau}$ is $3.85^{+0.86}_{-0.65}$, larger than the standard neutrino oscillation global best-fit value. The existence of these parameters broaden the allowed ranges of θ_{23} and $|\Delta m^2_{32}|$ ($|\Delta m^2_{31}|$ in the inverted ordering) and show correlations with θ_{23} and $|\Delta m^2_{32}|(|\Delta m^2_{31}|)$, while leaving δ_{CP} unconstrained. Converted to the fundamental parameters $\zeta_{\alpha\beta} = y_q y_{\alpha\beta}/m^2_\phi$, the SK bounds are weaker by two orders of magnitude than those from a phenomenological study of solar neutrinos [7]. The allowed intervals for $\zeta_{\mu\mu}$ is $[-640, 152]$ in normal ordering and $[-280, 185]$ in inverted ordering at 90% C.L., in units of $10^{-15}\mathrm{eV}^{-2}$. For $\zeta_{\tau\tau}$, the 90% allowed intervals are $[-1188, -1002] \oplus [-637, 83.4]$ in normal ordering and $[-582, -351] \oplus [-314, 185]$ in inverted ordering, in units of $10^{-15}\mathrm{eV}^{-2}$. Despite weaker constraints, we regard the results important benchmark for global experiments

as this is the first experimental result. Due to limited sensitivity, the results of η_{ee} are disregarded.

For off-diagonal couplings, SK indicates a preference for $|\eta_{\mu\tau}| \simeq 0.3$ with $\phi_{\mu\tau} \sim \pi$ (normal ordering) and $\phi_{\mu\tau} \sim 0$ (inverted ordering), while places less stringent limits to $\eta_{e\mu}$ and $\eta_{e\tau}$. The values of $|\Delta m^2_{32}|(|\Delta m^2_{31}|)$ in the $\eta_{\mu\tau}$ analyses are $3.85 \times 10^{-3}\,\mathrm{eV}^2$ and $4.00 \times 10^{-3}\,\mathrm{eV}^2$, again larger than the standard neutrino oscillation global best-fit value. We note that the results [7] from NOvA and T2K data fall within the 90% allowed region of $\eta_{\mu\tau}$, warranting further study for clarification. The fit values of $\eta_{e\mu}$ and $\eta_{e\tau}$ are in agreement with the standard neutrino oscillations.

Although this analysis uses only a subset of the SK atmospheric neutrino data, it demonstrates that atmospheric neutrinos can provide constraints on the scalar-NSI. Including the full SK data set is expected to significantly improve the sensitivity. Based on projections for a livetime of 9400 days, which is approximately the livetime till the end of SK, the allowed 68% confidence intervals for the diagonal scalar-NSI parameters are expected to shrink to roughly one-third of the ranges obtained with SK I data. For the off-diagonal parameters $\eta_{\alpha\beta}$, the 68% limits are expected to improve to below 0.1, roughly corresponds to $|\zeta_{\alpha\beta}| = 1.49 \times 10^{-13}\mathrm{eV}^{-2}$. In summary, the presence of scalar-NSI introduces degeneracies in the determination of $|\Delta m^2_{32}|(|\Delta m^2_{31}|)$, highlighting the importance of combining atmospheric neutrino data with external measurements to achieve more robust constraints.

Part 4

Appendices

Appendix A

PMT Model with Internal Structure

This document describes a new PMT model with internal structure developed for SK. This model is motivated by the data-MC discrepancy observed in the PMT reflectivity calibration. Figure A.1 shows the PMT reflectivity calibration data in SK V. The red histogram is the best-fit MC, which has a deficit in the reflection region compared to the data. This deficit has been a long-standing issue in SK, and the development of the new PMT model aims to resolve the issue. The same is also observed in the backward lights in the cosmic-ray through-going muon measurements.

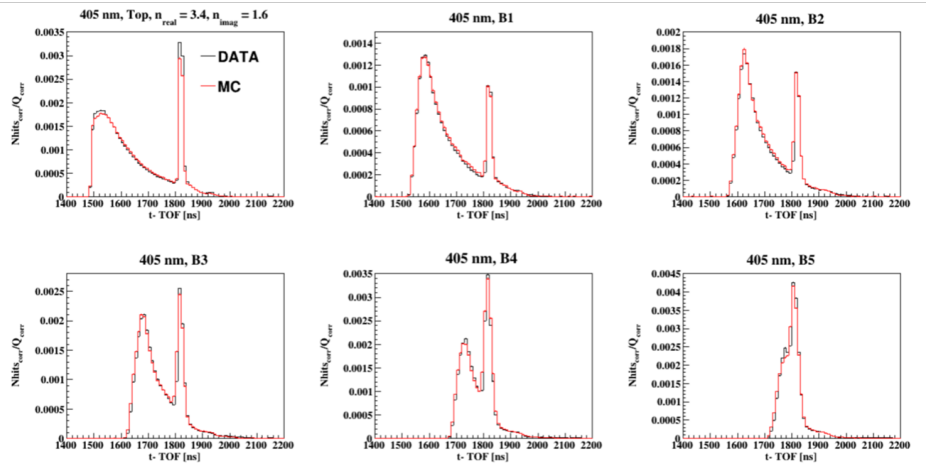

Figure A.1: Time-of-flight corrected timing distribution for the laser data (black) and the best-fit MC (red) for SK V. From top-left to bottom-right, the distributions are from the top, and B1-B5 regions respectively. The data were taken using a 405 nm laser calibration source. In each plot, the spike on the right corresponds to the lights reflected on PMTs. The plots are taken from [231].

Currently, the PMT internal structure is not modeled in SK's detector simulator,

and optical processes inside a PMT are omitted. The lack of PMT internal structure model may have resulted in the missing part of light reflection. Although effective refractive indices are adopted and are set to values larger than realistic values to compensate for the missing light reflection, the resultant angular distribution of reflected light may not match the true angular distribution.

An appropriate PMT model benefits all physics analyses using backward lights, for example, the study of proton decay into $\bar{\nu}$ and K^+. One of the search methods is to search for K^+ decay at rest into π^0 and π^+ with a branching ratio of 21%. The two mesons are in opposite directions. The π^0 decays into two photons, producing a characteristic signal. However, the π^+ is barely visible in the SK detector, leaving only several hits in the opposite direction of the π^0. An appropriate PMT model helps distinguish between true π^+ activities and reflected lights.

To develop a new PMT model with internal structure, we begin with the geometry. Since the exact dimensions of the SK PMT is confidential information, we measure the dimensions from the profile plot of the SK PMT in Figure A.2. The measured dimensions are shown in Figure A.3. As can be seen from the plots, only the "crown" is modeled. The cylinder part below the dynode is not modeled for simplicity, because photons are unlikely reflected back from this part. The PMT model consists of 5 components: top glass, upper side glass, lower side glass, stainless steel support structure, and dynode. We continued to use the PMT glass model in SKDETSIM and extend it to cover the lower side glass. The glass is modeled by a combination of a semi-sphere and a partial torus. We define the origin as the center of the torus as indicated in the plots. The top glass of the PMT model is a semi-sphere centered at (0,0,-12.7 cm) with a radius of 31.5 cm. The upper and lower side glass is modeled by a part of a self-intersecting spindle torus with $R = 10.4$ cm and $r = 15$ cm. The stainless steel support structure is modeled by a combination of open cylinders and rings, and is located 6 cm below the origin. The dynode is a venetian blind structure in a real SK PMT. It is symplified as a circle plate with a radius of 3.8 cm in this model.

Optical properties are assigned to the components according their materials. For the top glass and upper side glass, we followed the model in SKDETSIM, which consists of a glass layer with a thickness of 4 mm and a inner bialkali photocathod layer with a thickness of 11.5 nm. An effective complex refractive index determines the optical processes on the top glass and upper side glass. Photons can be reflected, absorbed, or transmitted on these two components. For photons that hit the PMT from the outside, a look-up table containing the absorbance, transmittance, and reflectance as a function of incident angle is used to determine the processes. When photons hit the top glass and upper side glass from the inside, the same table is used with the

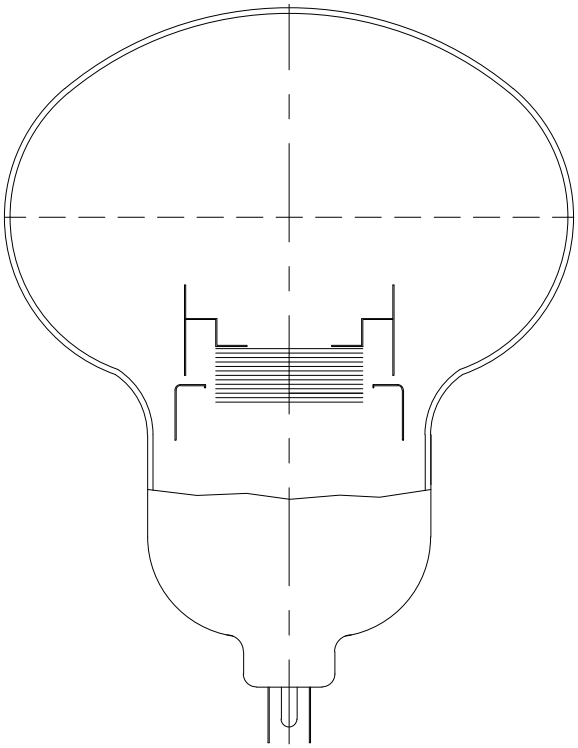

Figure A.2: Side view of an SK R3600 PMT.

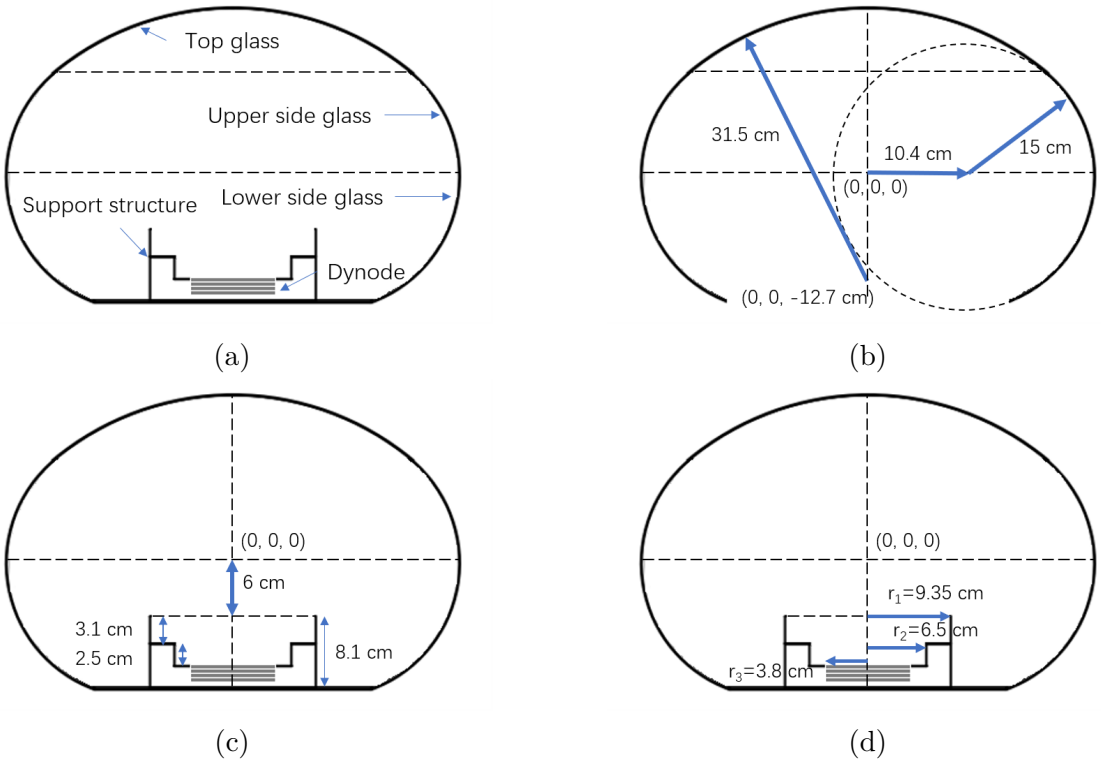

Figure A.3: Components and dimensions of the new PMT model.

incident angle in vacuum converted to that in water by the following transformation,

$$n_{\text{water}} \sin\theta_{\text{water}} = n_{\text{vacuum}} \sin\theta_{\text{vacuum}}, \tag{A.1}$$

where n_{water} and n_{vacuum} are refractive incides of water and vacuum, respectively. We note that this approach is not precise and may be improved using the transfer-matrix method [232]. The lower side glass is coated by aluminum, and a 92% specular reflection and a 8% of absorption on the lower side glass is assumed. For the stainless steel, we assumed a 40% change of specular reflection and the rest is absorption. For the dynode, 100% absorption is assumed.

The model is locally implemented in SKDETSIM for tests. Once a photon is transmitted on the surface of PMT in SKDETSIM, a separate routine is called to track the photon in the PMT model. Photons undergo different processes when interacting with the model based on the properties of the materials. When a photon exits the PMT model through the glass, a new photon is generated and passed to SKDETSIM, with proper position, direction and time. If a photon is absorbed by the photocathod and produces a photoelectron, corresponding routines to handle photoelectrons in SKDETSIM are called. Figure A.4 demonstrates example photon tracks.

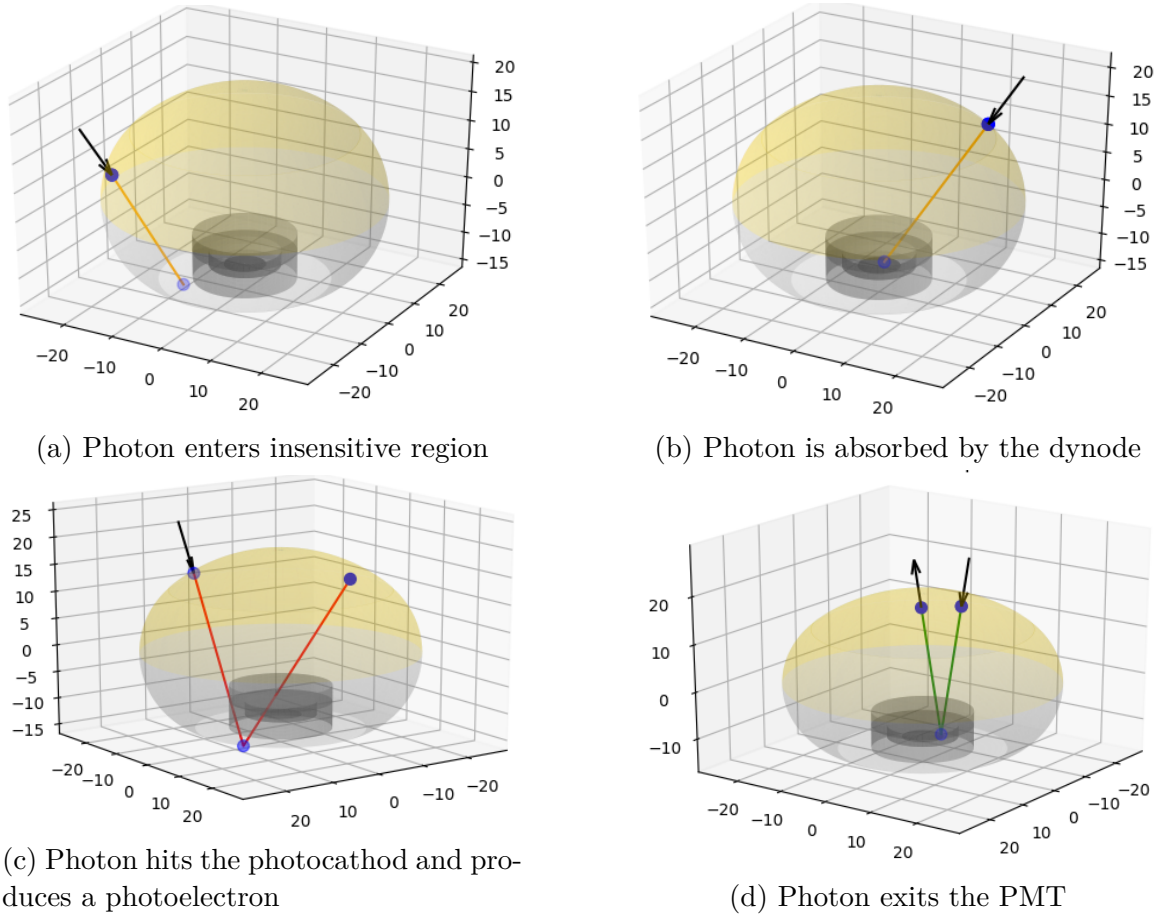

(a) Photon enters insensitive region

(b) Photon is absorbed by the dynode

(c) Photon hits the photocathod and produces a photoelectron

(d) Photon exits the PMT

Figure A.4: Examples of photon tracks in the new PMT model. Colors of tracks represent the fates of the photons. Yellow denotes elimination, red denotes photoelectron production, and green denotes transmision.

The performance of the new PMT model is tested by fits to the laser calibration data. The fits take the same approach as the PMT reflectivity calibration, and the

Wavelength [nm]	n_{imag}
337	1.4
375	1.5
405	1.6
445	1.7

Table A.1: Imaginary part of refractive index of bialkali taken from ellipsoidal PMT data [233].

data of 337 nm, 375 nm, 405 nm and 445 nm laser are fitted. The free parameters are the effective complex refractive index of the PMT glass and photocathod, and the reflectance of the stainless steel. These parameters are scanned in a grid. The real part of the refractive index vary from 1.5 to 4.0 with a step size of 0.1. The imaginary part for each wavelength is fixed to ellipsometry value [233], as listed in Table A.1. The reflectance of the stainless steel vary from 40% to 49% with a step size of 1%. The best-fit MCs with the new PMT model and the default PMT model are shown in Figure A.5. Best-fit values of parameters are listed in Table A.2. An improved data-MC agreement is achieved for the reflection peaks using the new PMT model. Meanwhile, the enlarged refractive indices of the PMT glass and photocathod become smaller. However, enhancement is seen in both scattering regions and reflection peaks, indicating a possible need for tuning the PMT model together with the optical properties of water.

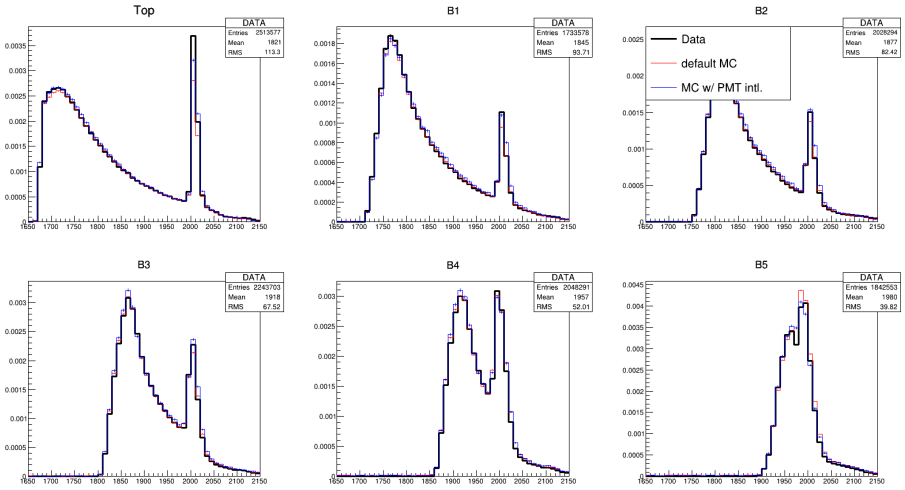

Figure A.5: Time-of-flight corrected timing distribution of laser calibration data in SK V. Data points are indicated by black histogram. Blue and red histograms are best-fit MC with the new PMT model and with the default PMT model. From top-left to bottom-right, the distributions are from the top, and B1-B5 regions respectively. The data were taken using a 375 nm laser calibration source. In each plot, the spike on the right corresponds to the lights reflected on PMTs.

To summarize, a new PMT model that enables photon tracking inside a PMT

Wavelength [nm]	New PMT model		Default PMT model
	n_{real}	Steel reflectance	n_{real}
337	2.0	46%	2.6
375	2.7	49%	3.0
405	3.0	45%	3.3
445	3.3	49%	3.6

Table A.2: Best-fit values of parameters. For both models, n_{imag} are fixed to ellipsometry values as listed in Table A.1.

is developed. The model is ready for use in SKDETSIM. Via fitting the SK V laser calibration data, better data-MC agreement is achieved for the reflection peaks using the new PMT model. In the future, this model can be improved by updating the computation of optical properties of the PMT glass for outward photons, using the transfer-matrix method. Tunable parameters may include the reflectance of the stainless steel support structure, the lower side glass, and the dynode. However, to reduce the complexity of fitting, one may first investigate their correlations with the effective refractive index and decide whether or not to fit these parameters. Last but not least, since the PMT model affects the light collection efficiency, a simultanous calibration of PMT reflectivity and the optical properties of water may be needed.

Appendix B

Energy scale calibration

The estimation of energy scale uncertainty for SK I based on fiTQun is described here as a supplymentary note to Section 12.2.3. The evaluation processes of three uncertainties are documented, including the absolute energy scale uncertainty, the time variation uncertainty of energy scale, and up-down energy calibration uncertainty. The former two uncertainties are merged to form the *absolute energy calibration* uncertainty. These uncertainties are used in the analysis of scalar-NSI. The energy scale uncertainties based on APFit are also updated for future analyses.

B.1 Absolute Energy Scale Uncertainty

SK uses the following control samples to evaluate the absolute energy scale uncertainty:

- Michel electrons from cosmic-ray muon decays.
- Sub-GeV stopping cosmic-ray muons.
- Multi-GeV stopping cosmic-ray muons.
- π^0 in fully-contained atmospheric neutrino samples.

For each sample, MC events are generated by SKDETSIM, and are reconstructed using both APFit and fiTQun. Selection cuts are applied to both data and MC events to purify the sample. After that, the difference between data and MC in a certain reconstruction quantity is measured and taken as an energy scale uncertainty.

B.1.1 Michel electron

The energy scale uncertainty in Michel electron is evaluated using the reconstructed momentum spectrum. Instead of Michel electron data taken in normal runs, the so-called "special decay electron" data are used, because the electronics in SK I-III phases could not properly handle delayed hits. The special decay electron data are taken with a special trigger that is not triggered by the primary cosmic-ray muon but the Michel electron. The MC is generated using particle gun based on the theoretical momentum spectrum of Michel electron. The MC events are uniformly distributed in the detector.

A common selected Michel electron sample is used, with the selection performed based on APFit reconstructed quantities. The selection criteria for Michel electrons are as follows:

1. Only one decay electron is found.
2. The Michel electron satisfies the sub-event type (See Appendix D.5 in [210] for definitions of decay electron event types).
3. The goodness of vertex fit is greater than 0.5.
4. The time difference between the primary cosmic-ray muon event and the Michel electron event is between 2 and 8 μs.
5. Number of PMT hits within a 50 ns sliding time window is larger than 60.
6. Vertex position of the decay electron is reconstructed within the fiducial volume, 200 cm from the detector walls.

Note that Criterion 1 and 4 do not apply to the MC events because they do not contain cosmic-ray muons. For the fiTQun analysis, there is an additional cut to require the fiTQun reconstructed vertex be within the fiducial volume.

The Michel electron reconstructed momentum spectra of the data and MC for APFit and fiTQun are shown in Figure B.1. The differences in the mean values between the data and MC are taken as the energy scale uncertainties, summarized in Table B.1.

B.1.2 Sub-GeV Stopping Cosmic-ray Muon

To evaluate the energy scale uncertainty in this sample, the ratio of reconstructed momentum P_{pe} and the momentum calculated using reconstructed Cherenkov angle

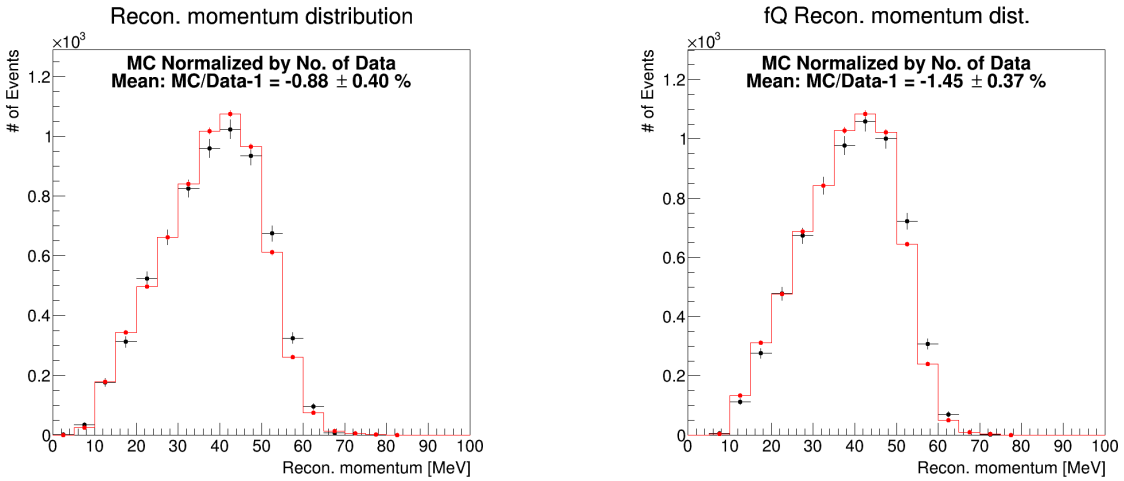

(a) APFit (b) fiTQun

Figure B.1: Michel electron momentum distributions reconstructed by **(a)** APFit and **(b)** fiTQun in SK I. The data are shown as black dots with statistical error bars, and the MCs are shown as red histograms. In each plot, the number of events in the MC is normalized to that of the data.

P_θ is used. The latter is given by

$$P_\theta = m\sqrt{\frac{1}{n^2\cos^2\theta_C} - 1}, \tag{B.1}$$

where m is muon mass, n is refractive index of water, and θ_C is reconstructed Cherenkov angle. The difference between the data and MC in the ratio P_{pe}/P_θ is considered as energy scale uncertainty. The above approach applies to the data reconstructed by APFit. For fiTQun, all quantities are simutanously fitted and there is not a separate fit for Cherenkov angle. Therefore, the ratio between P_{pe} reconstructed by fiTQun and P_θ by APFit is used.

Similar to Michel electron, a common sub-GeV stopping muon sample selected based on APFit reconstructed quantities is used in the subsequent APFit and fiTQun analyses. The sub-GeV stopping muon selection criteria are as follows:

1. The reconstructed muon vertex $z > 1720\,\text{cm}$.
2. The reconstructed muon direction $\cos\theta_z > 0.87$.
3. The momentum calculated from the reconstructed Cherenkov angle is between 200 and 440 MeV/c.
4. The goodness of muon fit is no less than 0.6.
5. The total observed charge in the ID is between 500 p.e. and 5000 p.e.

6. Only one decay electron is found.

7. The time difference between the muon event and its decay electron event is longer than 1.2 μs.

The selected events are divided into 3 subsamples based on P_θ: $200 < P_\theta < 280$, $280 < P_\theta < 360$, and $360 < P_\theta < 440\,\mathrm{MeV}/c$. The P_{pe}/P_θ distributions in each subsample in SK I for APFit and fiTQun are shown in Figure B.2. The differences in the mean values between the data and MC are taken as the energy scale uncertainties, and are listed in Table B.1.

B.1.3 Multi-GeV Stopping Cosmic-ray Muon

The energy scale uncertainty in multi-GeV stopping muon is evaluated using the ratio between reconstructed momentum and track length. Similar to the above two samples, this analysis uses a common multi-GeV stopping muon sample for APFit and fiTQun. The sample is selected based on APFit reconstructed quantities, and the selection criteria are:

1. The reconstructed muon vertex $z = 1810\,\mathrm{cm}$.

2. The reconstructed muon direction $\cos\theta_z > 0.94$.

3. The goodness of muon fit is greater than 0.

4. Only one decay electron is found.

The selected events are divided into 5 subsamples based on track length L: $7 < L < 10$, $10 < L < 15$, $15 < L < 20$, $20 < L < 25$, and $25 < L < 30\,\mathrm{m}$. The distributions of the ratio of reconstructed muon momentum relative to track length are shown in Figure B.3 and Figure B.4. Mean values are obtained from Gaussian fits to the distributions. The differences in the fitted mean values between data and MC are taken as the energy scale uncertainties, summarized in Table B.1.

B.1.4 FC π^0

The energy scale uncertainty in FC π^0 is evaluated from comparison of reconstructed π^0 invariant mass between the data and MC. The FC π^0 events are taken from the final sample as defined in Section 10.1. Unlike the above samples, two FC π^0 samples are selected based on the APFit and fiTQun reconstructed quantities respectively. The selection criteria are as follows:

1. Two e-like rings are found.

2. No decay electron is detected.

Figure B.5 shows the data and MC distributions of π^0 invariant mass by APFit and fiTQun. The energy scale uncertainties are calculated by comparing the Gaussian mean values of the data and MC, and are listed in Table B.1.

B.1.5 Summary of absolute energy scale uncertainty

Figure B.6 shows the energy scale uncertainties in each control sample. The same uncertainties are listed in Table B.1. Of them, the one with the largest absolute value is considered as the absolute energy scale uncertainty. For both APFit and fiTQun, the sub-GeV stopping muon samples are the most discrepant control samples, and the absolute energy scale uncertainties are taken from them. The absolute energy scale uncertainty is 2.45% for APFit, and is 2.30% for fiTQun.

Control sample	APFit	fiTQun
Michel electron	$-0.88 \pm 0.40\%$	$-1.45 \pm 0.37\%$
Sub-GeV stopping muon		
$200 < P_\theta < 280\,\mathrm{MeV}/c$	$0.56 \pm 0.20\%$	$0.80 \pm 0.21\%$
$280 < P_\theta < 360\,\mathrm{MeV}/c$	$1.97 \pm 0.17\%$	$2.01 \pm 0.17\%$
$360 < P_\theta < 440\,\mathrm{MeV}/c$	$2.44 \pm 0.19\%$	$2.29 \pm 0.18\%$
Multi-GeV stopping muon		
$7 < L < 10\,\mathrm{m}$	$0.35 \pm 0.13\%$	$-0.26 \pm 0.09\%$
$10 < L < 15\,\mathrm{m}$	$0.60 \pm 0.10\%$	$-0.17 \pm 0.07\%$
$15 < L < 20\,\mathrm{m}$	$0.85 \pm 0.11\%$	$-0.01 \pm 0.08\%$
$20 < L < 25\,\mathrm{m}$	$1.47 \pm 0.12\%$	$0.73 \pm 0.09\%$
$25 < L < 30\,\mathrm{m}$	$1.53 \pm 0.12\%$	$0.62 \pm 0.10\%$
FC π^0	$-0.55 \pm 0.62\%$	$0.38 \pm 0.53\%$

Table B.1: Summary of the energy scale uncertainties from each control sample.

B.2 Time Variation of Energy Scale

The uncertainty from time variation of energy scale is estimated using the time evolution of the energy scale uncertainties in Michel electron and multi-GeV stopping muon. The approach is the same as that for absolute energy scale uncertainty, but the samples are binned by time. For Michel electron, the data and MC are grouped into equal-width time bins with a bin width of 3 months. As for multi-GeV stopping muon, a binning of 1 month wide is used. The time evolution of the energy scale uncertainties in Michel electron and multi-GeV stopping muon are shown in Figure B.7 and Figure B.8. The time variation error is defined as the ratio of the RMS relative to the mean value of the energy scale uncertainties. The largest error from the two samples is taken as the final time variation error. For APFit, the largest value comes from the multi-GeV stopping muon sample, and is 0.91%. For fiTQun, the time variation error is 0.73%, taken from the Michel electron sample. The final energy calibration

uncertainty is the sum in quadrature of the absolute energy scale uncertainty and the time variation uncertainty. For APFit, the value is 2.60%. As for fiTQun, the final energy calibration uncertainty is 2.40%.

B.3 Up-down Energy Calibration

The up-down energy calibration uncertainty, also called the uncertainty of detector uniformity in some other SK literatures, is evaluated using the selected Michel electron sample as described above. In SK IV and later, the directions of Michel electrons are required to be perpendicular to those of the primary muons to remove muon polarization effect. However, since the muon information are not captured in the special decay electron samples used in SK I-III, this requirement does not apply to SK I-III. Data and MC are equally binned by cosine of zenith angle with a bin width of 0.4. For each bin, the mean values of reconstructed momentum of the data and MC are computed, and their ratio form a zenith angle distribution as shown in Figure B.9. The uncertainty from up-down energy calibration is defined as the standard deviation of the ratios. For APFit, the up-down energy calibration uncertainty is 0.52%. For fiTQun, this uncertainty is 0.78%.

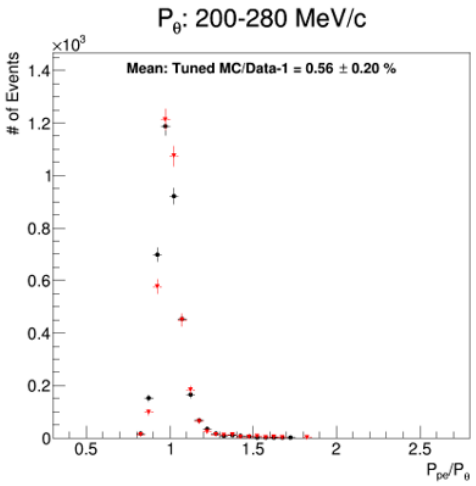

(a) APFit: $200 < P_\theta < 280\,\mathrm{MeV}/c$

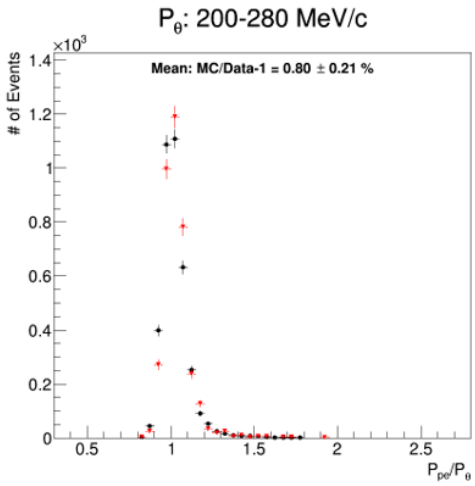

(b) fiTQun: $200 < P_\theta < 280\,\mathrm{MeV}/c$

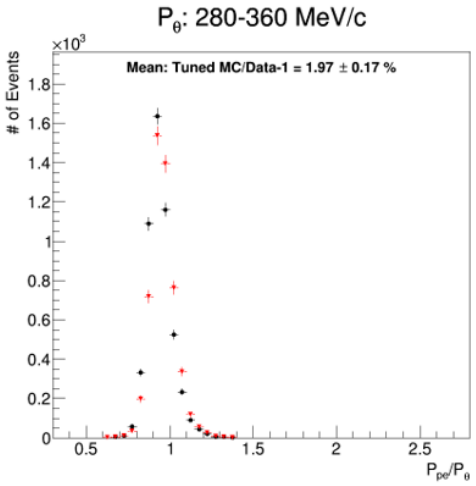

(c) APFit: $280 < P_\theta < 360\,\mathrm{MeV}/c$

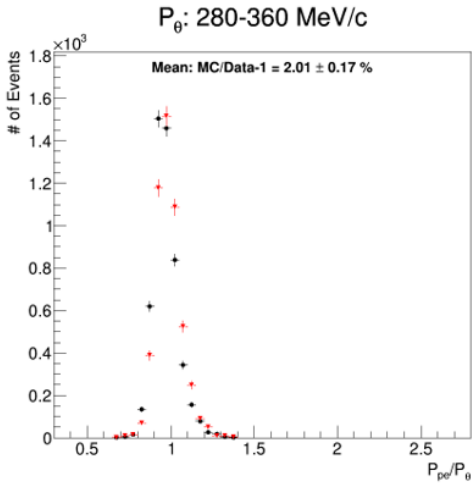

(d) fiTQun: $280 < P_\theta < 360\,\mathrm{MeV}/c$

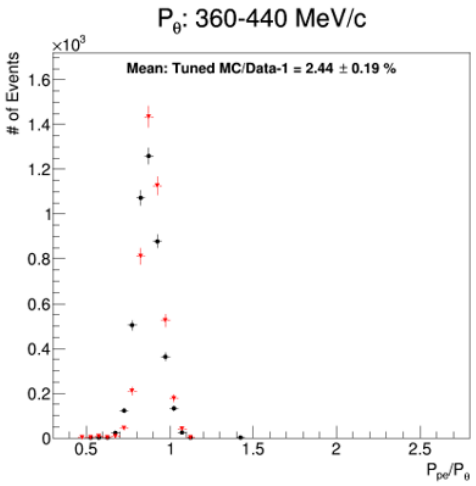

(e) APFit: $360 < P_\theta < 440\,\mathrm{MeV}/c$

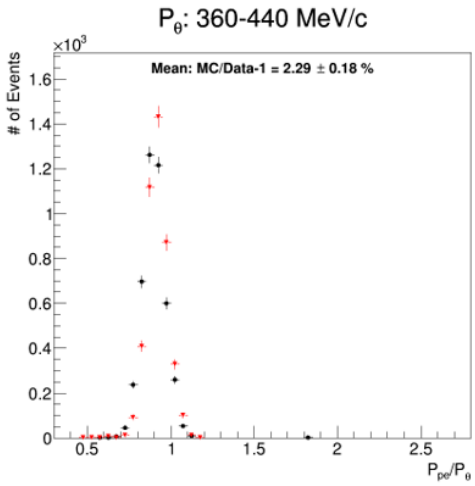

(f) fiTQun: $360 < P_\theta < 440\,\mathrm{MeV}/c$

Figure B.2: Distributions of the ratio P_{pe}/P_θ by APFit and fiTQun for SK I. The distributions by APFit are in the left column, and those by fiTQun are in the right column. From top to bottom, P_θs increase. The black dots with statistical error bars denote the data, and the red histograms denote the MCs. In each plot, the number of events in the MC is normalized to that of the data.

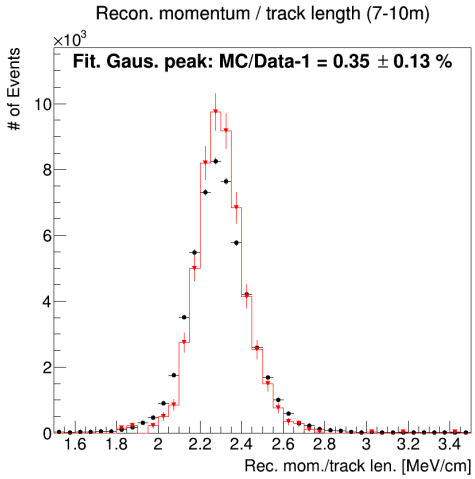

(a) APFit: $7 < L < 10\,\mathrm{m}$

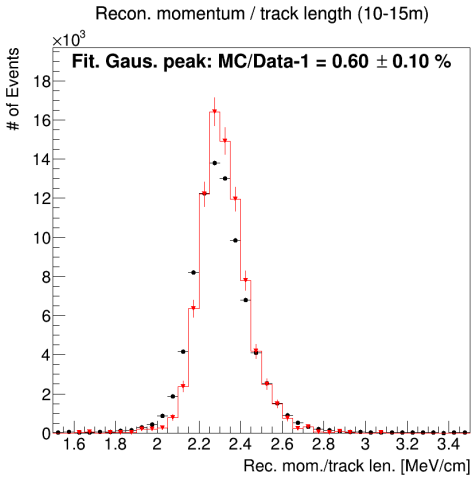

(b) APFit: $10 < L < 15\,\mathrm{m}$

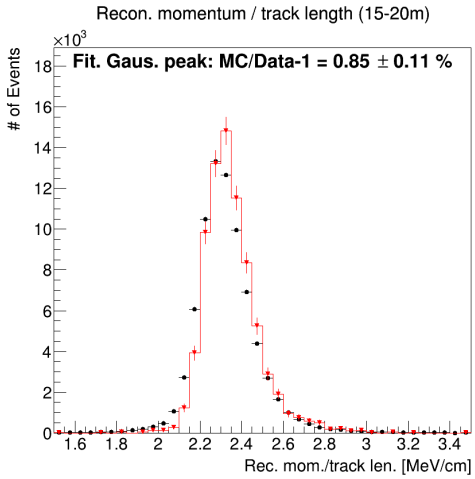

(c) APFit: $15 < L < 20\,\mathrm{m}$

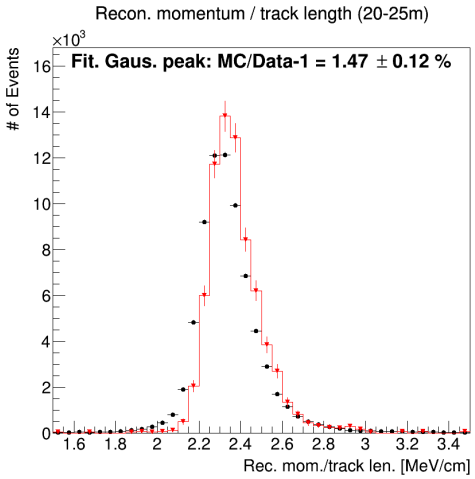

(d) APFit: $20 < L < 25\,\mathrm{m}$

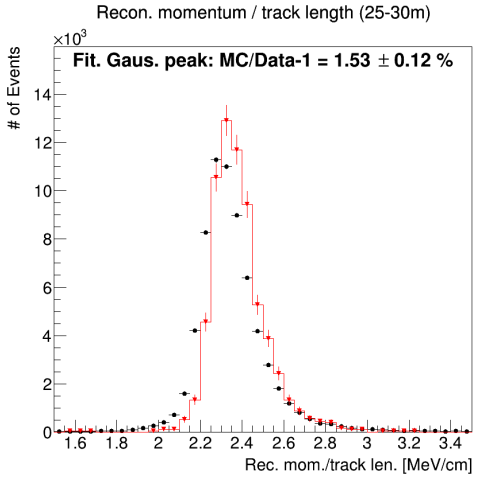

(e) APFit: $25 < L < 30\,\mathrm{m}$

Figure B.3: Distributions of the ratio of reconstructed muon momentum over track length by APFit for SK I. The black dots with statistical error bars denote the data, and the red histograms denote the MCs. In each plot, the number of events in the MC is normalized to that of the data.

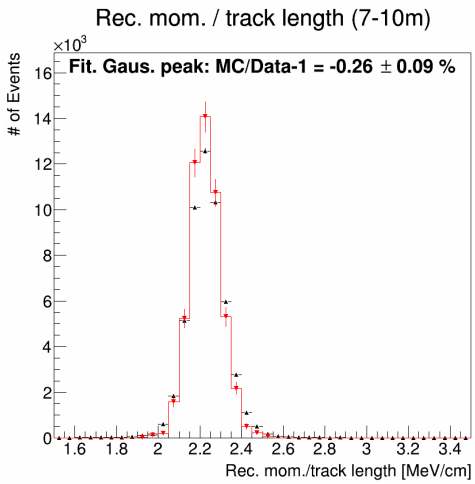

(a) fiTQun: $7 < L < 10\,\mathrm{m}$

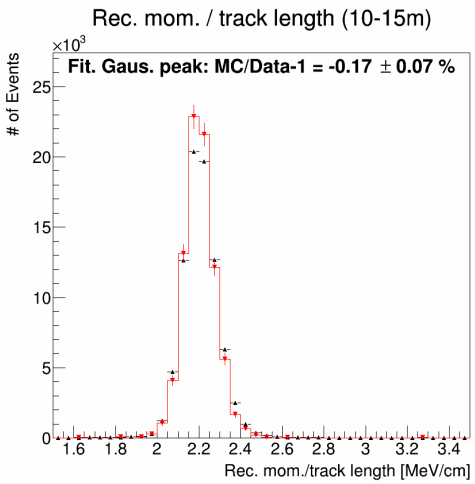

(b) fiTQun: $10 < L < 15\,\mathrm{m}$

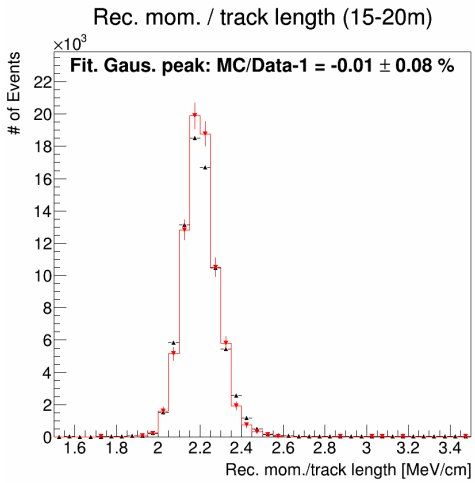

(c) fiTQun: $15 < L < 20\,\mathrm{m}$

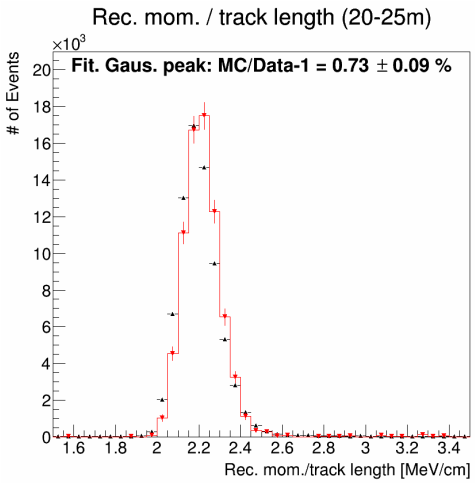

(d) fiTQun: $20 < L < 25\,\mathrm{m}$

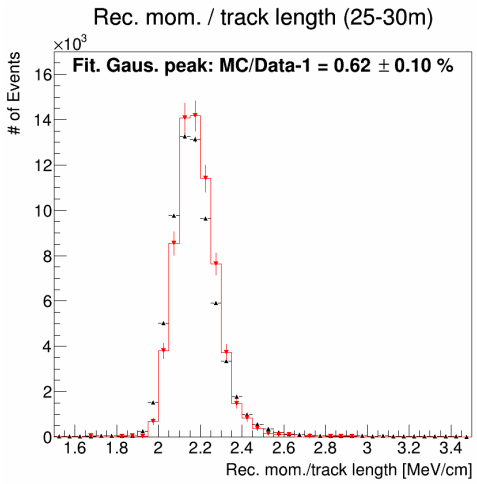

(e) fiTQun: $25 < L < 30\,\mathrm{m}$

Figure B.4: Distributions of the ratio of reconstructed muon momentum over track length by fiTQun for SK I. The black dots with statistical error bars denote the data, and the red histograms denote the MCs. In each plot, the number of events in the MC is normalized to that of the data.

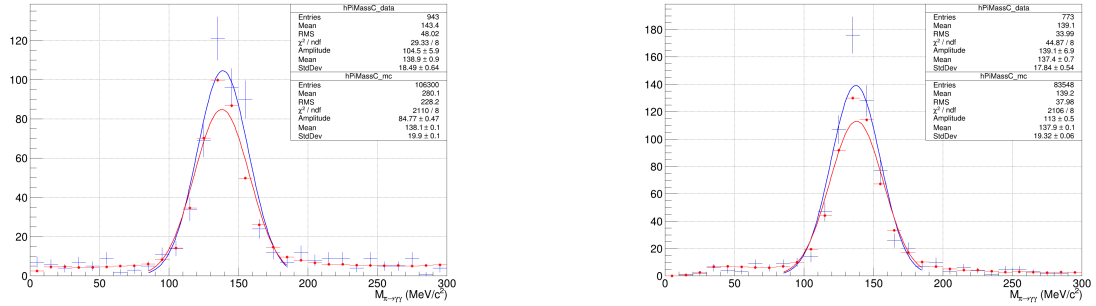

(a) APFit (b) fiTQun

Figure B.5: Neutral pion mass distributions by **(a)** APFit and **(b)** fiTQun in SK I. The data are shown as blue dots with statistical error bars, and the MCs are shown as red histograms. The Gaussian fit curves are also shown. In each plot, the number of events in the MC is normalized to that of the data.

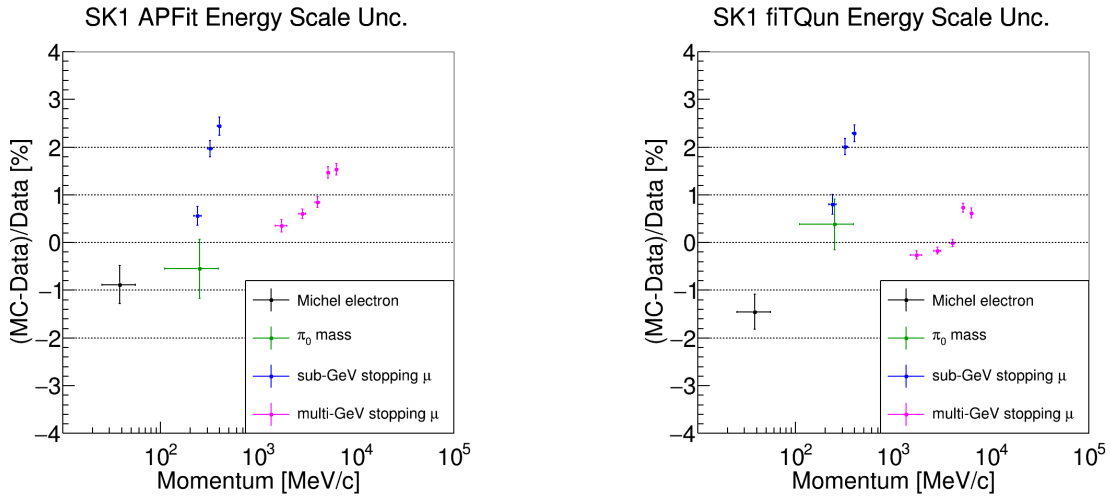

(a) APFit (b) fiTQun

Figure B.6: Absolute energy scale uncertainties from four control samples by **(a)** APFit and **(b)** fiTQun in SK I. The vertical error bars denote the statistical uncertainty, and the horizontal bars indicate the momentum range for each control sample.

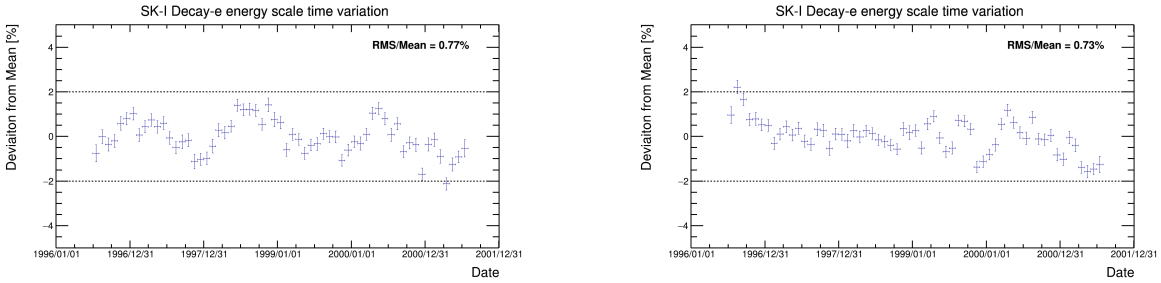

(a) APFit (b) fiTQun

Figure B.7: Time evolution of the energy scale uncertainties in the Michel electron samples by **(a)** APFit and **(b)** fiTQun in SK I. The vertical error bars denote the statistical uncertainty. Each data point corresponds to a 1-month-average.

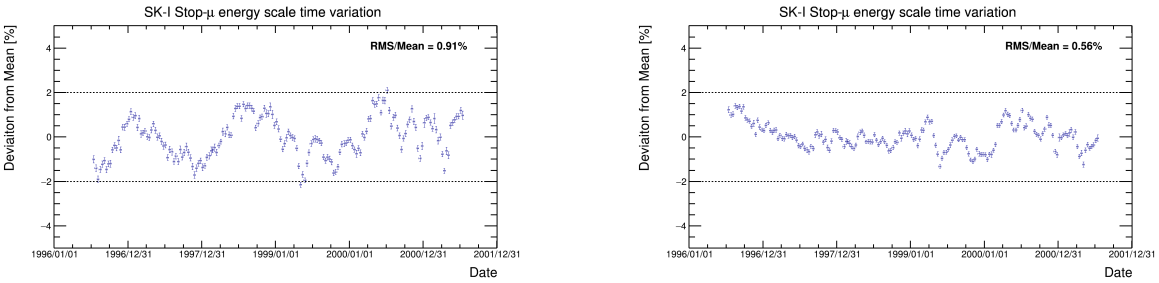

(a) APFit (b) fiTQun

Figure B.8: Time evolution of the energy scale uncertainties in the multi-GeV stopping muon samples by **(a)** APFit and **(b)** fiTQun in SK I. The vertical error bars denote the statistical uncertainty. Each data point corresponds to a 3-month-average.

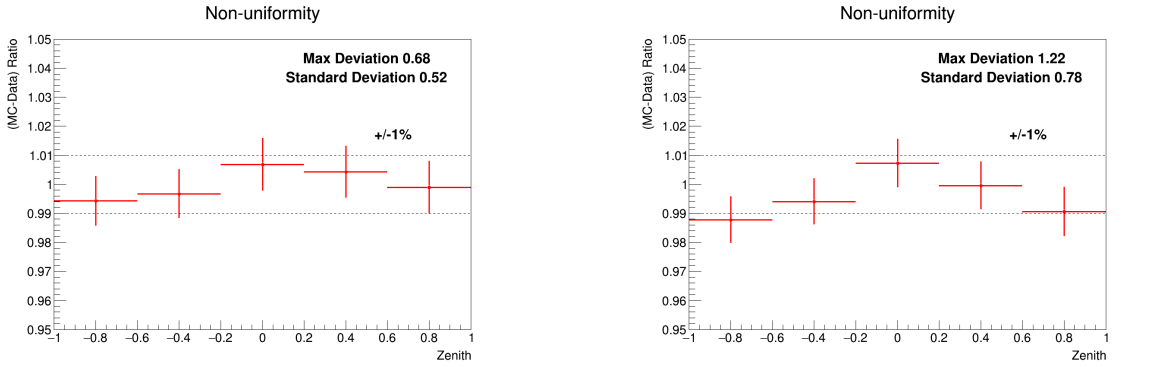

(a) APFit (b) fiTQun

Figure B.9: Zenith angle distributions of the ratios of the average momentum between the data and MC by **(a)** APFit and **(b)** fiTQun in SK I. The vertical error bars denote the statistical uncertainty.

Appendix C

Best-fit Zenith Angle and Momentum Distributions

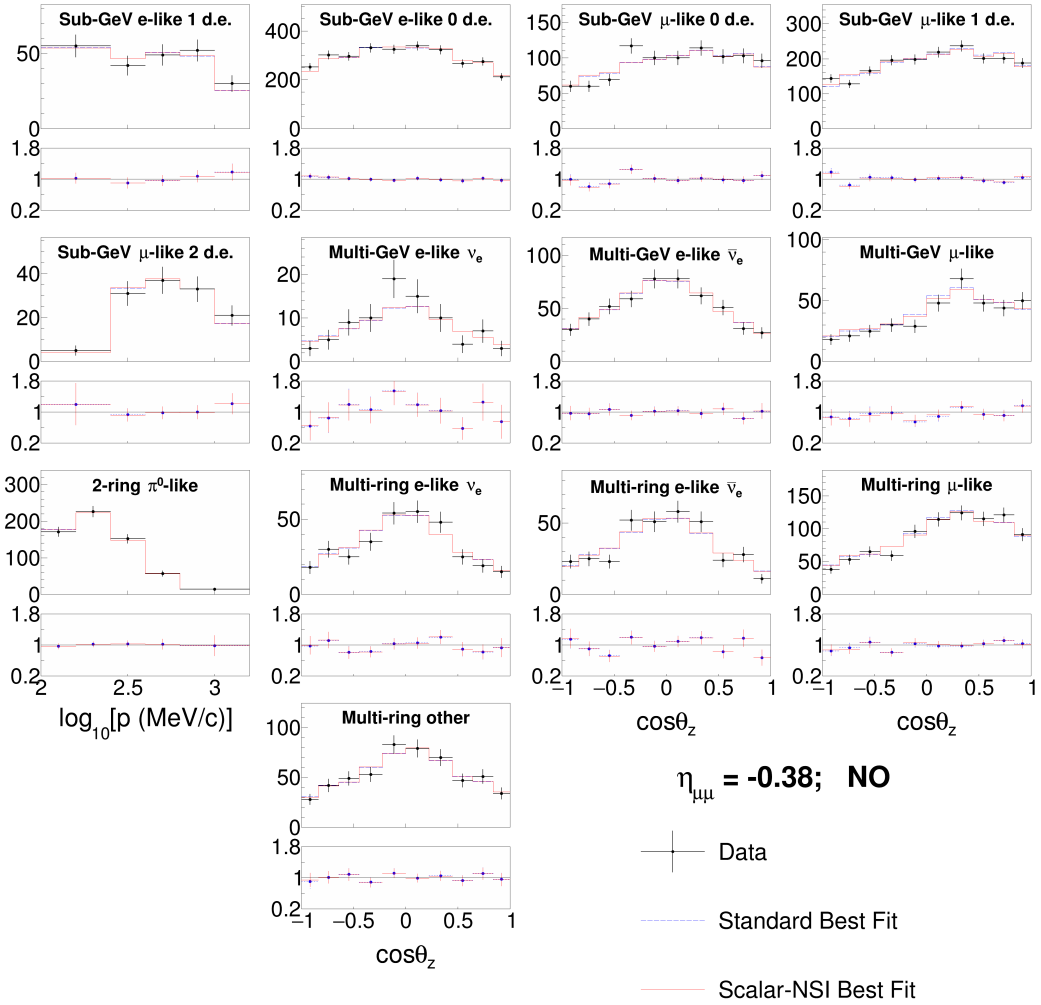

Figure C.1: Zenith angle and momentum distributions of best-fit predictions in the presence of $\eta_{\mu\mu}$, assuming normal ordering.

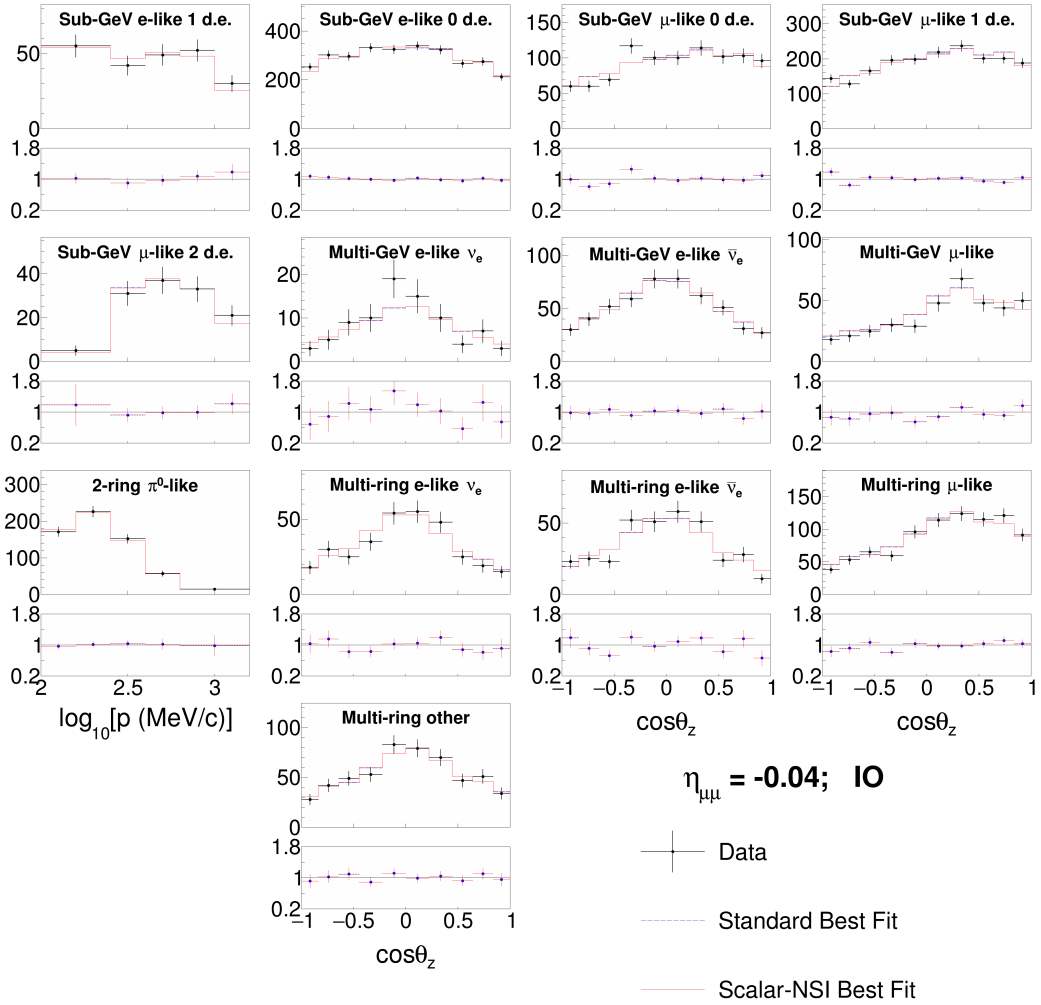

Figure C.2: Zenith angle and momentum distributions of best-fit predictions in the presence of $\eta_{\mu\mu}$, assuming inverted ordering.

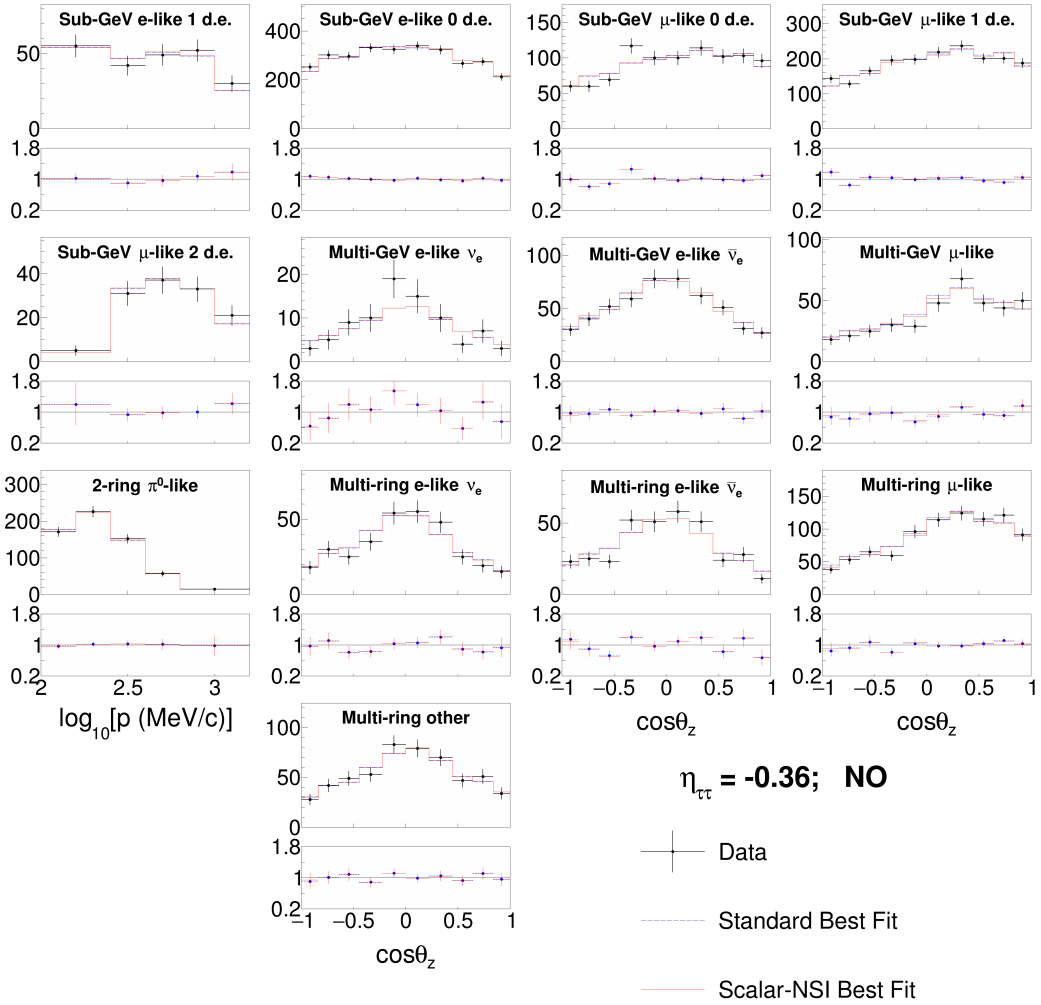

Figure C.3: Zenith angle and momentum distributions of best-fit predictions in the presence of $\eta_{\tau\tau}$, assuming normal ordering.

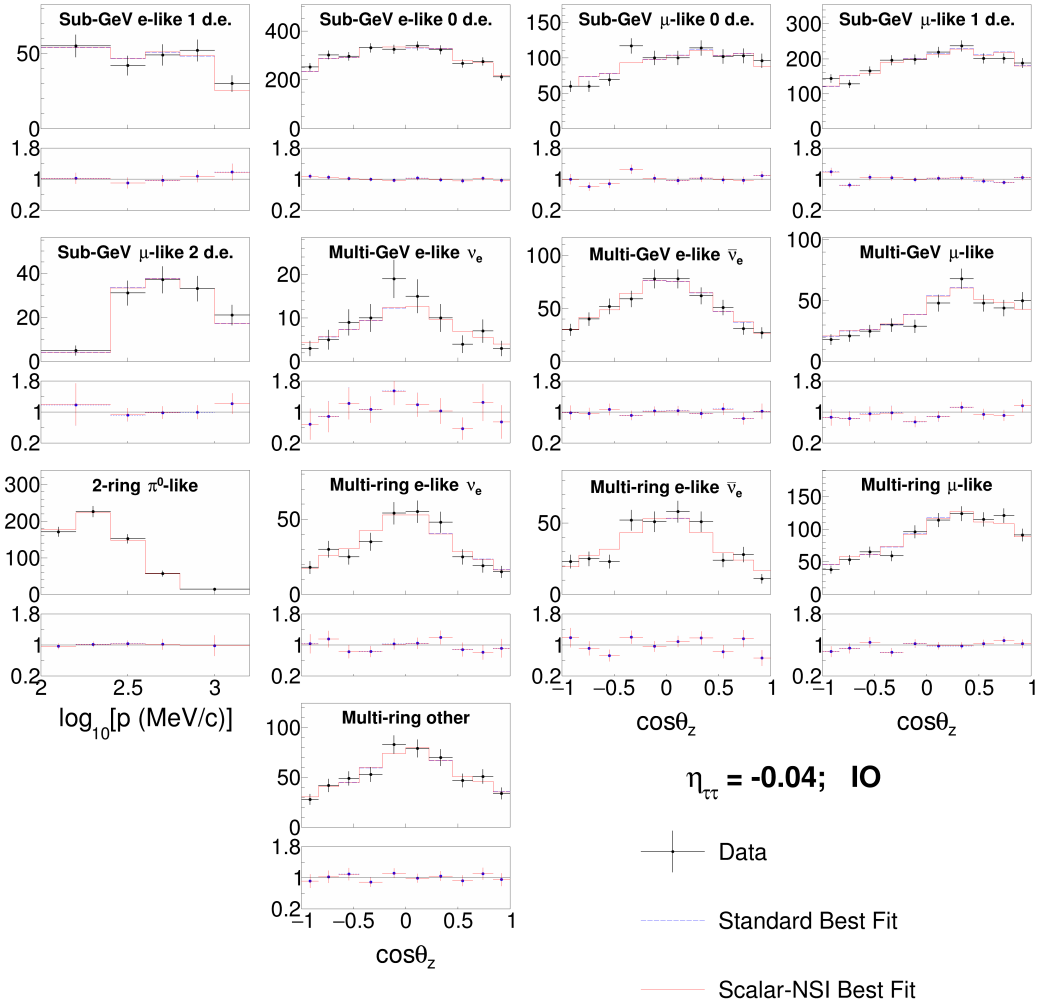

Figure C.4: Zenith angle and momentum distributions of best-fit predictions in the presence of $\eta_{\tau\tau}$, assuming inverted ordering.

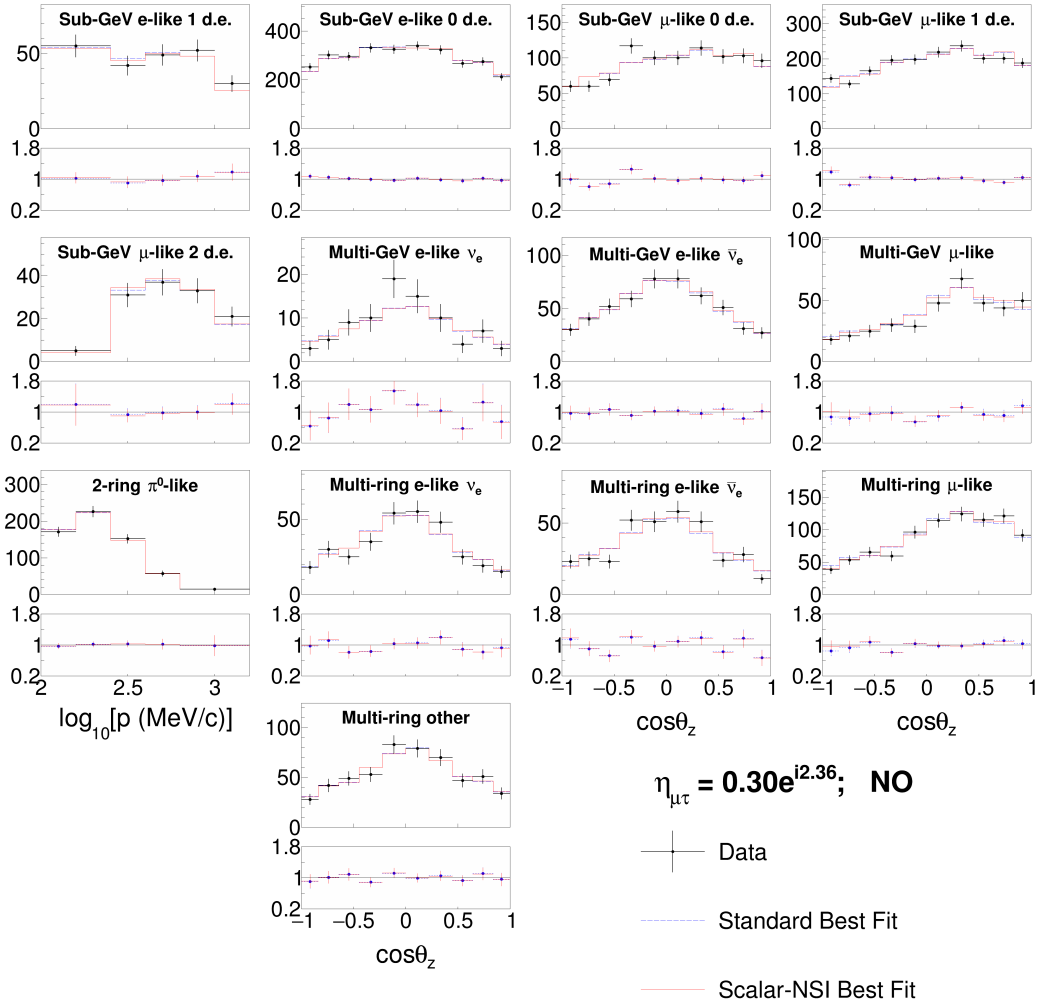

Figure C.5: Zenith angle and momentum distributions of best-fit predictions in the presence of $\eta_{\mu\tau}$, assuming normal ordering.

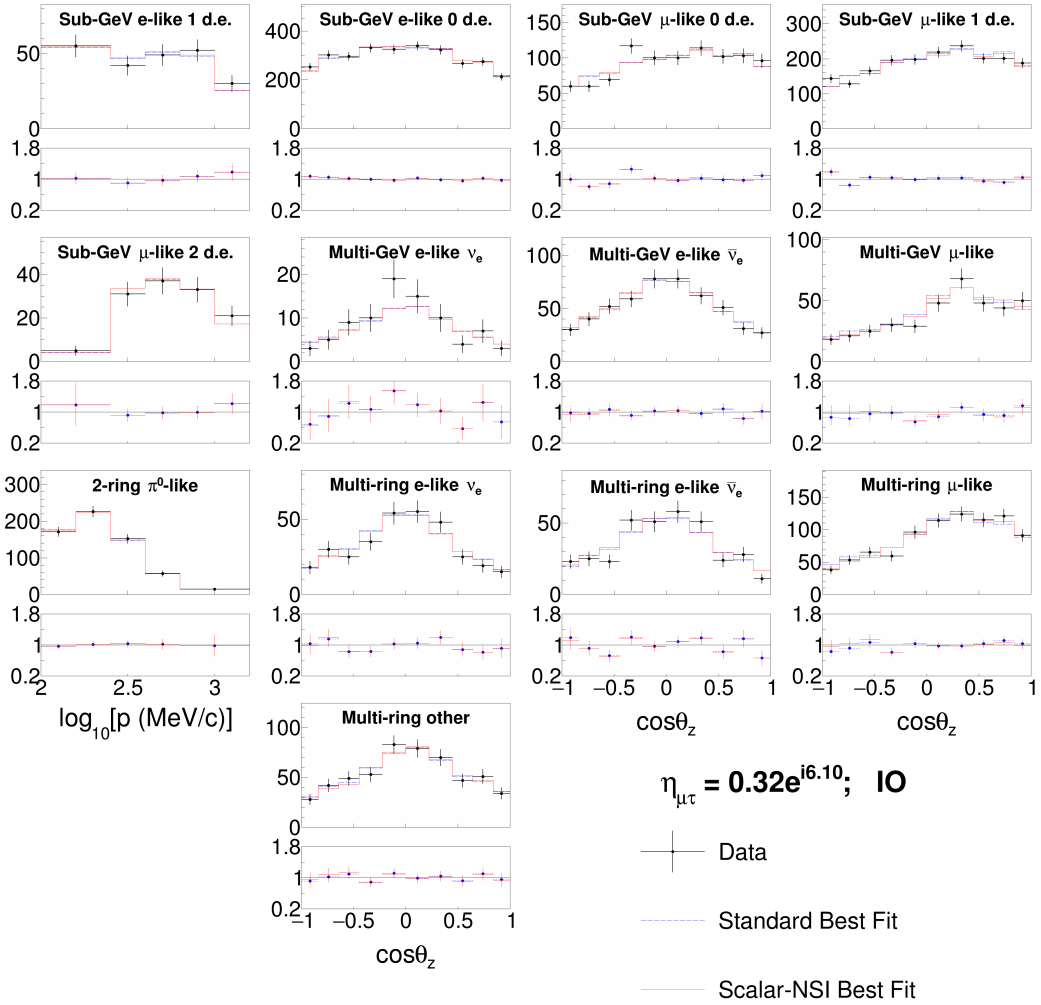

Figure C.6: Zenith angle and momentum distributions of best-fit predictions in the presence of $\eta_{\mu\tau}$, assuming inverted ordering.

Bibliography

[1] Peter B. Denton, Alessio Giarnetti, and Davide Meloni. "Solar neutrinos and the strongest oscillation constraints on scalar NSI". In: *JHEP* 01 (2025), p. 097. DOI: 10.1007/JHEP01(2025)097. arXiv: 2409.15411 [hep-ph].

[2] K. Hirata et al. "Observation of a Neutrino Burst from the Supernova SN 1987a". In: *Phys. Rev. Lett.* 58 (1987). Ed. by K. C. Wali, pp. 1490–1493. DOI: 10.1103/PhysRevLett.58.1490.

[3] R. M. Bionta et al. "Observation of a Neutrino Burst in Coincidence with Supernova SN 1987a in the Large Magellanic Cloud". In: *Phys. Rev. Lett.* 58 (1987), p. 1494. DOI: 10.1103/PhysRevLett.58.1494.

[4] E. N. Alekseev et al. "Possible Detection of a Neutrino Signal on 23 February 1987 at the Baksan Underground Scintillation Telescope of the Institute of Nuclear Research". In: *JETP Lett.* 45 (1987). Ed. by J. Tran Thanh Van, pp. 589–592.

[5] Scott M. Adams et al. "Observing the Next Galactic Supernova". In: *Astrophys. J.* 778 (2013), p. 164. DOI: 10.1088/0004-637X/778/2/164. arXiv: 1306.0559 [astro-ph.HE].

[6] Shao-Feng Ge and Stephen J. Parke. "Scalar Nonstandard Interactions in Neutrino Oscillation". In: *Phys. Rev. Lett.* 122.21 (2019), p. 211801. DOI: 10.1103/PhysRevLett.122.211801. arXiv: 1812.08376 [hep-ph].

[7] Peter B. Denton, Alessio Giarnetti, and Davide Meloni. "How to identify different new neutrino oscillation physics scenarios at DUNE". In: *JHEP* 02 (2023), p. 210. DOI: 10.1007/JHEP02(2023)210. arXiv: 2210.00109 [hep-ph].

[8] Abinash Medhi, Debajyoti Dutta, and Moon Moon Devi. "Exploring the effects of scalar non standard interactions on the CP violation sensitivity at DUNE". In: *JHEP* 06 (2022), p. 129. DOI: 10.1007/JHEP06(2022)129. arXiv: 2111.12943 [hep-ph].

[9] Abinash Medhi, Moon Moon Devi, and Debajyoti Dutta. "Imprints of scalar NSI on the CP-violation sensitivity using synergy among DUNE, T2HK and

T2HKK". In: *JHEP* 01 (2023), p. 079. DOI: 10.1007/JHEP01(2023)079. arXiv: 2209.05287 [hep-ph].

[10] Bhaskar Dutta et al. "Non-standard neutrino interactions mediated by a light scalar at DUNE". In: *JHEP* 07 (2024), p. 213. DOI: 10.1007/JHEP07(2024)213. arXiv: 2401.02107 [hep-ph].

[11] W. Pauli. "Dear radioactive ladies and gentlemen". In: *Phys. Today* 31N9 (1978), p. 27.

[12] Laurie M. Brown. "The idea of the neutrino". In: *Phys. Today* 31N9 (1978), pp. 23–28. DOI: 10.1063/1.2995181.

[13] E. Fermi. "An attempt of a theory of beta radiation. 1." In: *Z. Phys.* 88 (1934), pp. 161–177. DOI: 10.1007/BF01351864.

[14] Fred L. Wilson. "Fermi's Theory of Beta Decay". In: *Am. J. Phys.* 36.12 (1968), pp. 1150–1160. DOI: 10.1119/1.1974382.

[15] C. L. Cowan et al. "Detection of the free neutrino: A Confirmation". In: *Science* 124 (1956), pp. 103–104. DOI: 10.1126/science.124.3212.103.

[16] F. Reines and C. L. Cowan. "The neutrino". In: *Nature* 178 (1956), pp. 446–449. DOI: 10.1038/178446a0.

[17] G. Danby et al. "Observation of High-Energy Neutrino Reactions and the Existence of Two Kinds of Neutrinos". In: *Phys. Rev. Lett.* 9 (1962), pp. 36–44. DOI: 10.1103/PhysRevLett.9.36.

[18] K. Kodama et al. "Observation of tau neutrino interactions". In: *Phys. Lett. B* 504 (2001), pp. 218–224. DOI: 10.1016/S0370-2693(01)00307-0. arXiv: hep-ex/0012035.

[19] M. Acciarri et al. "Determination of the number of light neutrino species from single photon production at LEP". In: *Phys. Lett. B* 431 (1998), pp. 199–208. DOI: 10.1016/S0370-2693(98)00519-X.

[20] R. Akers et al. "Measurement of single photon production in e+ e- collisions near the Z0 resonance". In: *Z. Phys. C* 65 (1995), pp. 47–66. DOI: 10.1007/BF01571303.

[21] D. Buskulic et al. "A Direct measurement of the invisible width of the Z from single photon counting". In: *Phys. Lett. B* 313 (1993), pp. 520–534. DOI: 10.1016/0370-2693(93)90027-F.

[22] S. Navas et al. "Review of particle physics". In: *Phys. Rev. D* 110.3 (2024), p. 030001. DOI: 10.1103/PhysRevD.110.030001.

[23] Y. Fukuda et al. "Evidence for oscillation of atmospheric neutrinos". In: *Phys. Rev. Lett.* 81 (1998), pp. 1562–1567. DOI: 10.1103/PhysRevLett.81.1562. arXiv: hep-ex/9807003.

[24] Q. R. Ahmad et al. “Measurement of the rate of $\nu_e + d \rightarrow p + p + e^-$ interactions produced by ^{8}B solar neutrinos at the Sudbury Neutrino Observatory”. In: *Phys. Rev. Lett.* 87 (2001), p. 071301. DOI: 10.1103/PhysRevLett.87.071301. arXiv: nucl-ex/0106015.

[25] Max Aker et al. “Direct neutrino-mass measurement based on 259 days of KATRIN data”. In: *Science* 388.6743 (2025), adq9592. DOI: 10.1126/science.adq9592. arXiv: 2406.13516 [nucl-ex].

[26] A. G. Adame et al. “DESI 2024 VI: cosmological constraints from the measurements of baryon acoustic oscillations”. In: *JCAP* 02 (2025), p. 021. DOI: 10.1088/1475-7516/2025/02/021. arXiv: 2404.03002 [astro-ph.CO].

[27] B. Pontecorvo. “Neutrino Experiments and the Problem of Conservation of Leptonic Charge”. In: *Zh. Eksp. Teor. Fiz.* 53 (1967), pp. 1717–1725.

[28] Ziro Maki, Masami Nakagawa, and Shoichi Sakata. “Remarks on the unified model of elementary particles”. In: *Prog. Theor. Phys.* 28 (1962), pp. 870–880. DOI: 10.1143/PTP.28.870.

[29] B. T. Cleveland et al. “Measurement of the solar electron neutrino flux with the Homestake chlorine detector”. In: *Astrophys. J.* 496 (1998), pp. 505–526. DOI: 10.1086/305343.

[30] J. N. Abdurashitov et al. “Measurement of the solar neutrino capture rate with gallium metal. III: Results for the 2002–2007 data-taking period”. In: *Phys. Rev. C* 80 (2009), p. 015807. DOI: 10.1103/PhysRevC.80.015807. arXiv: 0901.2200 [nucl-ex].

[31] G. Bellini et al. “Precision measurement of the 7Be solar neutrino interaction rate in Borexino”. In: *Phys. Rev. Lett.* 107 (2011), p. 141302. DOI: 10.1103/PhysRevLett.107.141302. arXiv: 1104.1816 [hep-ex].

[32] J. Hosaka et al. “Solar neutrino measurements in super-Kamiokande-I”. In: *Phys. Rev. D* 73 (2006), p. 112001. DOI: 10.1103/PhysRevD.73.112001. arXiv: hep-ex/0508053.

[33] B. Aharmim et al. “Combined Analysis of all Three Phases of Solar Neutrino Data from the Sudbury Neutrino Observatory”. In: *Phys. Rev. C* 88 (2013), p. 025501. DOI: 10.1103/PhysRevC.88.025501. arXiv: 1109.0763 [nucl-ex].

[34] L. Wolfenstein. “Neutrino Oscillations in Matter”. In: *Phys. Rev. D* 17 (1978), pp. 2369–2374. DOI: 10.1103/PhysRevD.17.2369.

[35] S. P. Mikheev and A. Yu. Smirnov. “Resonance Amplification of Oscillations in Matter and Spectroscopy of Solar Neutrinos”. In: *Sov. J. Nucl. Phys.* 42 (1985), pp. 913–917.

[36] S. P. Mikheev and A. Yu. Smirnov. "Resonant amplification of neutrino oscillations in matter and solar neutrino spectroscopy". In: *Nuovo Cim. C* 9 (1986), pp. 17–26. DOI: 10.1007/BF02508049.

[37] T. Wester et al. "Atmospheric neutrino oscillation analysis with neutron tagging and an expanded fiducial volume in Super-Kamiokande I-V". In: *Phys. Rev. D* 109.7 (2024), p. 072014. DOI: 10.1103/PhysRevD.109.072014. arXiv: 2311.05105 [hep-ex].

[38] Vernon D. Barger et al. "Matter Effects on Three-Neutrino Oscillations". In: *Phys. Rev. D* 22 (1980), p. 2718. DOI: 10.1103/PhysRevD.22.2718.

[39] John N. Bahcall, M. H. Pinsonneault, and Sarbani Basu. "Solar models: Current epoch and time dependences, neutrinos, and helioseismological properties". In: *Astrophys. J.* 555 (2001), pp. 990–1012. DOI: 10.1086/321493. arXiv: astro-ph/0010346.

[40] John N. Bahcall and M. H. Pinsonneault. "What do we (not) know theoretically about solar neutrino fluxes?" In: *Phys. Rev. Lett.* 92 (2004), p. 121301. DOI: 10.1103/PhysRevLett.92.121301. arXiv: astro-ph/0402114.

[41] Núria Vinyoles et al. "A new Generation of Standard Solar Models". In: *Astrophys. J.* 835.2 (2017), p. 202. DOI: 10.3847/1538-4357/835/2/202. arXiv: 1611.09867 [astro-ph.SR].

[42] Xun-Jie Xu, Zhe Wang, and Shaomin Chen. "Solar neutrino physics". In: *Prog. Part. Nucl. Phys.* 131 (2023), p. 104043. DOI: 10.1016/j.ppnp.2023.104043. arXiv: 2209.14832 [hep-ph].

[43] W. Hampel et al. "Final results of the GALLEX solar neutrino experiment". In: *Phys. Lett. B* 447 (1999), pp. 127–133. DOI: 10.1016/S0370-2693(99)00092-3.

[44] Q. R. Ahmad et al. "Direct evidence for neutrino flavor transformation from neutral-current interactions in the Sudbury Neutrino Observatory". In: *Phys. Rev. Lett.* 89 (2002), p. 011301. DOI: 10.1103/PhysRevLett.89.011301.

[45] B. Aharmim et al. "Electron energy spectra, fluxes, and day-night asymmetries of B-8 solar neutrinos from measurements with NaCl dissolved in the heavy-water detector at the Sudbury Neutrino Observatory". In: *Phys. Rev. C* 72 (2005), p. 055502. DOI: 10.1103/PhysRevC.72.055502. arXiv: nucl-ex/0502021.

[46] S. Fukuda et al. "Determination of solar neutrino oscillation parameters using 1496 days of Super-Kamiokande I data". In: *Phys. Lett. B* 539 (2002), pp. 179–187. DOI: 10.1016/S0370-2693(02)02090-7. arXiv: hep-ex/0205075.

[47] M. Agostini et al. "Comprehensive measurement of pp-chain solar neutrinos". In: *Nature* 562 (2018), pp. 505–510. DOI: 10.1038/s41586-018-0624-y.

[48] S. Abe et al. “Precision Measurement of Neutrino Oscillation Parameters with KamLAND”. In: *Phys. Rev. Lett.* 100 (2008), p. 221803. DOI: 10.1103/PhysRevLett.100.221803.

[49] K. Eguchi et al. “First results from KamLAND: Evidence for reactor anti-neutrino disappearance”. In: *Phys. Rev. Lett.* 90 (2003), p. 021802. DOI: 10.1103/PhysRevLett.90.021802. arXiv: hep-ex/0212021.

[50] F. P. An et al. “Observation of electron-antineutrino disappearance at Daya Bay”. In: *Phys. Rev. Lett.* 108 (2012), p. 171803. DOI: 10.1103/PhysRevLett.108.171803.

[51] J. K. Ahn et al. “Observation of Reactor Electron Antineutrino Disappearance in the RENO Experiment”. In: *Phys. Rev. Lett.* 108 (2012), p. 191802. DOI: 10.1103/PhysRevLett.108.191802.

[52] Y. Abe et al. “Indication of Reactor $\bar{\nu}_e$ Disappearance in the Double Chooz Experiment”. In: *Phys. Rev. Lett.* 108 (2012), p. 131801. DOI: 10.1103/PhysRevLett.108.131801.

[53] F. P. An et al. “Precision Measurement of Reactor Antineutrino Oscillation at Kilometer-Scale Baselines by Daya Bay”. In: *Phys. Rev. Lett.* 130.16 (2023), p. 161802. DOI: 10.1103/PhysRevLett.130.161802. arXiv: 2211.14988 [hep-ex].

[54] G. Mention et al. “The Reactor Antineutrino Anomaly”. In: *Phys. Rev. D* 83 (2011), p. 073006. DOI: 10.1103/PhysRevD.83.073006.

[55] F. P. An et al. “Measurement of the Reactor Antineutrino Flux and Spectrum at Daya Bay”. In: *Phys. Rev. Lett.* 116 (2016), p. 061801. DOI: 10.1103/PhysRevLett.116.061801.

[56] M. Andriamirado et al. “Improved short-baseline neutrino oscillation search and energy spectrum measurement with the PROSPECT experiment at HFIR”. In: *Phys. Rev. D* 103.3 (2021), p. 032001. DOI: 10.1103/PhysRevD.103.032001.

[57] H. Almazan et al. “Improved Sterile Neutrino Constraints from the STEREO Experiment with 179 Days of Reactor-On Data”. In: *Phys. Rev. D* 102.5 (2020), p. 052002. DOI: 10.1103/PhysRevD.102.052002.

[58] Angel Abusleme et al. “Prediction of Energy Resolution in the JUNO Experiment”. In: *Chin. Phys. C* 49.1 (2025), p. 013003. DOI: 10.1088/1674-1137/ad83aa. arXiv: 2405.17860 [hep-ex].

[59] Angel Abusleme et al. “Sub-percent precision measurement of neutrino oscillation parameters with JUNO”. In: *Chin. Phys. C* 46.12 (2022), p. 123001. DOI: 10.1088/1674-1137/ac8bc9. arXiv: 2204.13249 [hep-ex].

[60] Thomas Wester. "Discerning the Neutrino Mass Ordering using Atmospheric Neutrinos in Super-Kamiokande I-V". PhD thesis. Boston University, Boston U., 2023.

[61] C. V. Achar et al. "Detection of muons produced by cosmic ray neutrinos deep underground". In: *Phys. Lett.* 18 (1965), pp. 196–199. DOI: 10.1016/0031-9163(65)90712-2.

[62] F. Reines et al. "Evidence for high-energy cosmic ray neutrino interactions". In: *Phys. Rev. Lett.* 15 (1965), pp. 429–433. DOI: 10.1103/PhysRevLett.15.429.

[63] K. S. Hirata et al. "Observation of a small atmospheric muon-neutrino / electron-neutrino ratio in Kamiokande". In: *Phys. Lett. B* 280 (1992), pp. 146–152. DOI: 10.1016/0370-2693(92)90788-6.

[64] D. Casper et al. "Measurement of atmospheric neutrino composition with IMB-3". In: *Phys. Rev. Lett.* 66 (1991), pp. 2561–2564. DOI: 10.1103/PhysRevLett.66.2561.

[65] M. Ambrosio et al. "Measurement of the atmospheric neutrino induced upgoing muon flux using MACRO". In: *Phys. Lett. B* 517 (2001), pp. 59–66. DOI: 10.1016/S0370-2693(01)01078-5.

[66] M. Sanchez et al. "Observation of atmospheric neutrino oscillations in Soudan 2". In: *Phys. Rev. D* 68 (2003), p. 113004. DOI: 10.1103/PhysRevD.68.113004.

[67] R. Abbasi et al. "Measurement of Atmospheric Neutrino Oscillation Parameters Using Convolutional Neural Networks with 9.3 Years of Data in IceCube DeepCore". In: *Phys. Rev. Lett.* 134.9 (2025), p. 091801. DOI: 10.1103/PhysRevLett.134.091801. arXiv: 2405.02163 [hep-ex].

[68] S. Aiello et al. "Letter of intent for KM3NeT 2.0". In: *J. Phys. G* 48 (2021), p. 070501. DOI: 10.1088/1361-6471/abf3c3.

[69] M. G. Aartsen et al. "PINGU: A Vision for Neutrino and Particle Physics at the South Pole". In: *J. Phys. G* 44.5 (2017), p. 054006. DOI: 10.1088/1361-6471/44/5/054006. arXiv: 1607.02671 [hep-ex].

[70] K. Abe et al. "Hyper-Kamiokande Design Report". In: (May 2018). arXiv: 1805.04163 [physics.ins-det].

[71] A. Kumar et al. "Physics Potential of the ICAL detector at the India-based Neutrino Observatory (INO)". In: *Pramana* 88 (2017), p. 79. DOI: 10.1007/s12043-017-1373-4.

[72] M. H. Ahn et al. "Measurement of Neutrino Oscillation by the K2K Experiment". In: *Phys. Rev. D* 74 (2006), p. 072003. DOI: 10.1103/PhysRevD.74.072003.

[73] M. H. Ahn et al. “Indications of neutrino oscillation in a 250 km long baseline experiment”. In: *Phys. Rev. Lett.* 90 (2003), p. 041801. DOI: 10.1103/PhysRevLett.90.041801. arXiv: hep-ex/0212007.

[74] P. Adamson et al. “Measurement of Neutrino and Antineutrino Oscillations Using Beam and Atmospheric Data in MINOS”. In: *Phys. Rev. Lett.* 110 (2013), p. 251801. DOI: 10.1103/PhysRevLett.110.251801.

[75] K. Abe et al. “The T2K Experiment”. In: *Nucl. Instrum. Meth. A* 659 (2011), pp. 106–135. DOI: 10.1016/j.nima.2011.06.067. arXiv: 1106.1238 [physics.ins-det].

[76] K. Abe et al. “Indication of Electron Neutrino Appearance from an Accelerator-produced Off-axis Muon Neutrino Beam”. In: *Phys. Rev. Lett.* 107 (2011), p. 041801. DOI: 10.1103/PhysRevLett.107.041801. arXiv: 1106.2822 [hep-ex].

[77] D. S. Ayres et al. “The NOvA Technical Design Report”. In: (Oct. 2007). DOI: 10.2172/935497.

[78] K. Abe et al. “Updated T2K measurements of muon neutrino and antineutrino disappearance using 3.6×1021 protons on target”. In: *Phys. Rev. D* 108.7 (2023), p. 072011. DOI: 10.1103/PhysRevD.108.072011. arXiv: 2305.09916 [hep-ex].

[79] M. A. Acero et al. “An Improved Measurement of Neutrino Oscillation Parameters by the NOvA Experiment”. In: *Phys. Rev. D* 106.3 (2022), p. 032004. DOI: 10.1103/PhysRevD.106.032004.

[80] B. Abi et al. “Deep Underground Neutrino Experiment (DUNE), Far Detector Technical Design Report, Volume II: DUNE Physics”. In: *arXiv:2002.03005* (2020). URL: https://arxiv.org/abs/2002.03005.

[81] H. A. Bethe and J. R. Wilson. “Revival of a stalled supernova shock by neutrino heating”. In: *Astrophys. J.* 295 (1985), pp. 14–23.

[82] A. Burrows and J. M. Lattimer. “The birth of neutron stars”. In: *Astrophys. J.* 307 (1986), pp. 178–196.

[83] G. Pietrzyński et al. “A distance to the Large Magellanic Cloud that is precise to one per cent”. In: *Nature* 567.7747 (2019), pp. 200–203. DOI: 10.1038/s41586-019-0999-4.

[84] G. G. Raffelt. *Stars as Laboratories for Fundamental Physics*. University of Chicago Press, 1996.

[85] Masayuki Nakahata. “SN1987A heralds the start of neutrino astronomy”. In: *CERN Courier* 47.1 (2007), pp. 23–24.

[86] G. Alimonti et al. “The Borexino detector at the Laboratori Nazionali del Gran Sasso”. In: *Nucl. Instrum. Meth. A* 600 (2009), pp. 568–593. DOI: 10.1016/j.nima.2008.11.076. arXiv: 0806.2400 [physics.ins-det].

[87] Lutz Köpke. “Improved Detection of Supernovae with the IceCube Observatory”. In: *J. Phys. Conf. Ser.* 1029.1 (2018), p. 012001. DOI: 10.1088/1742-6596/1029/1/012001. arXiv: 1704.03823 [astro-ph.HE].

[88] S. Abe et al. “Search for supernova neutrinos and constraint on the galactic star formation rate with the KamLAND data”. In: (Apr. 2022). DOI: 10.3847/1538-4357/ac7a3f. arXiv: 2204.12065 [astro-ph.HE].

[89] N. Y. Agafonova et al. “Implication for the Core-collapse Supernova Rate From 21 Years of Data of the Large Volume Detector”. In: *Astrophys. J.* 802.1 (2015), p. 47. DOI: 10.1088/0004-637X/802/1/47. arXiv: 1411.1709 [astro-ph.HE].

[90] M. A. Acero et al. “Supernova neutrino detection in NOvA”. In: *JCAP* 10 (2020), p. 014. DOI: 10.1088/1475-7516/2020/10/014. arXiv: 2005.07155 [physics.ins-det].

[91] S. Andringa et al. “Current Status and Future Prospects of the SNO+ Experiment”. In: *Adv. High Energy Phys.* 2016 (2016), p. 6194250. DOI: 10.1155/2016/6194250. arXiv: 1508.05759 [physics.ins-det].

[92] K. Abe et al. “Real-Time Supernova Neutrino Burst Monitor at Super-Kamiokande”. In: *Astropart. Phys.* 81 (2016), pp. 39–48. DOI: 10.1016/j.astropartphys.2016.04.003. arXiv: 1601.04778 [astro-ph.HE].

[93] P. Antonioli *et al.* “SNEWS: The Supernova Early Warning System”. In: *New J. Phys.* 6 (2004), p. 114.

[94] K. Scholberg *et al.* “The SuperNova Early Warning System”. In: *Astropart. Phys.* 123 (2020), p. 102491.

[95] B. Abi et al. “Supernova neutrino burst detection with the Deep Underground Neutrino Experiment”. In: *Eur. Phys. J. C* 81.5 (2021), p. 423. DOI: 10.1140/epjc/s10052-021-09166-w. arXiv: 2008.06647 [hep-ex].

[96] Angel Abusleme et al. “Real-time Monitoring for the Next Core-Collapse Supernova in JUNO”. In: (Sept. 2023). arXiv: 2309.07109 [hep-ex].

[97] S. Aiello et al. “The KM3NeT potential for the next core-collapse supernova observation with neutrinos”. In: *Eur. Phys. J. C* 81.5 (2021), p. 445. DOI: 10.1140/epjc/s10052-021-09187-5. arXiv: 2102.05977 [astro-ph.HE].

[98] J. F. Beacom. “The Diffuse Supernova Neutrino Background”. In: *Ann. Rev. Nucl. Part. Sci.* 60 (2010), pp. 439–462.

[99] K. Abe et al. “Diffuse supernova neutrino background search at Super-Kamiokande”. In: *Phys. Rev. D* 104.12 (2021), p. 122002. DOI: 10.1103/PhysRevD.104.122002. arXiv: 2109.11174 [astro-ph.HE].

[100] M. Harada et al. “Search for Astrophysical Electron Antineutrinos in Super-Kamiokande with 0.01% Gadolinium-loaded Water”. In: *Astrophys. J. Lett.* 951.2 (2023), p. L27. DOI: 10.3847/2041-8213/acdc9e. arXiv: 2305.05135 [astro-ph.HE].

[101] Andrzej Odrzywolek and Alexander Heger. “Neutrino signatures of dying massive stars: From main sequence to the neutron star”. In: *Acta Phys. Polon. B* 41 (2010). Ed. by Agnieszka Zalewska, pp. 1611–1628.

[102] Andrzej Odrzywolek, M. Misiaszek, and M. Kutschera. “Neutrinos from presupernova star”. In: *Acta Phys. Polon. B* 35 (2004). Ed. by Marek Jezabek and Henryk Wilczynski, p. 1981. arXiv: astro-ph/0405006.

[103] Kelly M. Patton et al. “Neutrinos from beta processes in a presupernova: probing the isotopic evolution of a massive star”. In: *Astrophys. J.* 851.1 (2017), p. 6. DOI: 10.3847/1538-4357/aa95c4. arXiv: 1709.01877 [astro-ph.HE].

[104] Chinami Kato et al. “Neutrino emissions in all flavors up to the pre-bounce of massive stars and the possibility of their detections”. In: *Astrophys. J.* 848.1 (2017), p. 48. DOI: 10.3847/1538-4357/aa8b72. arXiv: 1704.05480 [astro-ph.HE].

[105] K. Asakura et al. “KamLAND Sensitivity to Neutrinos from Pre-Supernova Stars”. In: *Astrophys. J.* 818.1 (2016), p. 91. DOI: 10.3847/0004-637X/818/1/91. arXiv: 1506.01175 [astro-ph.HE].

[106] L. N. Machado et al. “Pre-supernova Alert System for Super-Kamiokande”. In: *Astrophys. J.* 935.1 (2022), p. 40. DOI: 10.3847/1538-4357/ac7f9c. arXiv: 2205.09881 [hep-ex].

[107] Y. Fukuda et al. “The Super-Kamiokande detector”. In: *Nucl. Instrum. Meth. A* 501 (2003). Ed. by V. A. Ilyin, V. V. Korenkov, and D. Perret-Gallix, pp. 418–462. DOI: 10.1016/S0168-9002(03)00425-X.

[108] Shunichi Mine. “The Super-Kamiokande and Other Detectors: A Case Study of Large Volume Cherenkov Neutrino Detectors”. In: *Instrumentation and Techniques in High Energy Physics*. Chap. Chapter 8, pp. 251–290. DOI: 10.1142/9789819801107_0008. eprint: https://worldscientific.com/doi/pdf/10.1142/9789819801107_0008. URL: https://worldscientific.com/doi/abs/10.1142/9789819801107_0008.

[109] K. Abe et al. “First gadolinium loading to Super-Kamiokande”. In: *Nucl. Instrum. Meth. A* 1027 (2022), p. 166248. DOI: 10.1016/j.nima.2021.166248. arXiv: 2109.00360 [physics.ins-det].

[110] John F. Beacom and Mark R. Vagins. "GADZOOKS! Antineutrino Spectroscopy with Large Water Cherenkov Detectors". In: *Phys. Rev. Lett.* 93 (2004), p. 171101. DOI: 10.1103/PhysRevLett.93.171101. arXiv: hep-ph/0309300.

[111] Arpad Horvath. *The geometry of the Cherenkov radiation*. URL: https://commons.wikimedia.org/wiki/File:Cherenkov.svg. (accessed: 02.19.2025).

[112] A. Suzuki et al. "Improvement of 20-inch diameter photomultiplier tubes". In: *Nucl. Instrum. Meth. A* 329 (1993), pp. 299–313. DOI: 10.1016/0168-9002(93)90949-I.

[113] Hirokazu Ikeda et al. "Front end hybrid circuit for Super-Kamiokande". In: *Nucl. Instrum. Meth. A* 320 (1992), pp. 310–316. DOI: 10.1016/0168-9002(92)90791-2.

[114] H. Nishino et al. "High-speed charge-to-time converter ASIC for the Super-Kamiokande detector". In: *Nucl. Instrum. Meth. A* 610 (2009), pp. 710–717. DOI: 10.1016/j.nima.2009.09.026. arXiv: 0911.0986 [physics.ins-det].

[115] S. Yamada et al. "Commissioning of the new electronics and online system for the Super-Kamiokande experiment". In: *IEEE Trans. Nucl. Sci.* 57 (2010). Ed. by Sascha Marc Schmeling, pp. 428–432. DOI: 10.1109/TNS.2009.2034854.

[116] K. Abe et al. "Calibration of the Super-Kamiokande Detector". In: *Nucl. Instrum. Meth. A* 737 (2014), pp. 253–272. DOI: 10.1016/j.nima.2013.11.081. arXiv: 1307.0162 [physics.ins-det].

[117] Seisho Abe et al. "Combined Pre-supernova Alert System with KamLAND and Super-Kamiokande". In: *Astrophys. J.* 973.2 (2024), p. 140. DOI: 10.3847/1538-4357/ad5fee. arXiv: 2404.09920 [hep-ex].

[118] W. Hillebrandt and J. C. Niemeyer. "Type Ia supernova explosion models". In: *Ann. Rev. Astron. Astrophys.* 38 (2000), pp. 191–230.

[119] S. J. Smartt. "Progenitors of Core-Collapse Supernovae". In: *Ann. Rev. Astron. Astrophys.* 47 (2009), pp. 63–106.

[120] Carlo Giunti and Chung W. Kim. *Fundamentals of Neutrino Physics and Astrophysics*. 2007. ISBN: 978-0-19-850871-7.

[121] M. M. Phillips. "The absolute magnitudes of Type Ia supernovae". In: *Astrophys. J. Lett.* 413 (1993), pp. L105–L108.

[122] Jan J Eldridge and Elizabeth R Stanway. "New insights into the evolution of massive stars and their effects on our understanding of early galaxies". In: *Annual Review of Astronomy and Astrophysics* 60 (2022), pp. 455–494.

[123] S. E. Woosley, A. Heger, and T. A. Weaver. "The evolution and explosion of massive stars". In: *Rev. Mod. Phys.* 74 (2002), pp. 1015–1071. DOI: 10.1103/RevModPhys.74.1015.

[124] Luca Boccioli and Lorenzo Roberti. "The Physics of Core-Collapse Supernovae: Explosion Mechanism and Explosive Nucleosynthesis". In: *Universe* 10.3 (2024), p. 148. DOI: 10.3390/universe10030148. arXiv: 2403.12942 [astro-ph.SR].

[125] Toshitaka Kajino, Grant J. Mathews, and Takehito Hayakawa. "Neutrinos in core-collapse supernovae and nucleosynthesis". In: *J. Phys. G* 41 (2014), p. 044007. DOI: 10.1088/0954-3899/41/4/044007.

[126] Rémi. Kazeroni et al. "The non-linear onset of neutrino-driven convection in two and three-dimensional core-collapse supernovae". In: *Mon. Not. Roy. Astron. Soc.* 480.1 (2018), pp. 261–280. DOI: 10.1093/mnras/sty1742. arXiv: 1802.08125 [astro-ph.SR].

[127] Tomoya Takiwaki, Kei Kotake, and Katsuhiko Sato. "Special Relativistic Simulations of Magnetically-dominated Jets in Collapsing Massive Stars". In: *Astrophys. J.* 691 (2009), pp. 1360–1379. DOI: 10.1088/0004-637X/691/2/1360. arXiv: 0712.1949 [astro-ph].

[128] K. Kotake. "Multiple physical elements to determine the gravitational wave signatures of core-collapse supernovae". In: *Comptes Rendus Physique* 14 (2013), pp. 318–351.

[129] B. P. Abbott *et al.* (LIGO Scientific Collaboration and Virgo Collaboration). "Prospects for observing and localizing gravitational-wave transients with Advanced LIGO, Advanced Virgo, and KAGRA". In: *Living Rev. Relativ.* 23 (2020), p. 3.

[130] David Arnett. *Supernovae and Nucleosynthesis: An Investigation of the History of Matter, from the Big Bang to the Present*. Princeton University Press, Mar. 1996. ISBN: 978-0-691-01147-9.

[131] Virginia Trimble. "1987A: The greatest supernova since Kepler". In: *Rev. Mod. Phys.* 60 (1988), pp. 859–871. DOI: 10.1103/RevModPhys.60.859.

[132] A. Odrzywolek, Marcin Misiaszek, and M. Kutschera. "Detection possibility of the pair - annihilation neutrinos from the neutrino - cooled pre-supernova star". In: *Astropart. Phys.* 21 (2004), pp. 303–313. DOI: 10.1016/j.astropartphys.2004.02.002. arXiv: astro-ph/0311012.

[133] Takashi Yoshida et al. "Presupernova neutrino events relating to the final evolution of massive stars". In: *Phys. Rev. D* 93.12 (2016), p. 123012. DOI: 10.1103/PhysRevD.93.123012. arXiv: 1606.04915 [astro-ph.HE].

[134] Kelly M. Patton, Cecilia Lunardini, and Robert J. Farmer. "Presupernova neutrinos: realistic emissivities from stellar evolution". In: *Astrophys. J.* 840.1 (2017), p. 2. DOI: 10.3847/1538-4357/aa6ba8. arXiv: 1511.02820 [astro-ph.SR].

[135] Chinami Kato, Ryosuke Hirai, and Hiroki Nagakura. "The sensitivity of pre-supernova neutrinos to stellar evolution models". In: *Mon. Not. Roy. Astron. Soc.* 496.3 (2020), pp. 3961–3972. DOI: 10.1093/mnras/staa1738. arXiv: 2005.03124 [astro-ph.HE].

[136] C. Kato, K. Ishidoshiro, and T. Yoshida. "Theoretical Prediction of Presupernova Neutrinos and Their Detection". In: *Annual Review of Nuclear and Particle Science* 70.1 (2020), pp. 121–145. DOI: 10.1146/annurev-nucl-040620-021320. eprint: https://doi.org/10.1146/annurev-nucl-040620-021320. URL: https://doi.org/10.1146/annurev-nucl-040620-021320.

[137] Giada Carminati. "The new Wide-band Solar Neutrino Trigger for Super-Kamiokande". In: *Physics Procedia* 61 (2015). 13th International Conference on Topics in Astroparticle and Underground Physics, TAUP 2013, pp. 666–672. ISSN: 1875-3892. DOI: https://doi.org/10.1016/j.phpro.2014.12.068. URL: https://www.sciencedirect.com/science/article/pii/S1875389214006816.

[138] Charles Henry Simpson. "Pre-supernova neutrinos at Super-Kamiokande with gadolinium". PhD thesis. University of Oxford, Oxford U., 2019.

[139] K. Abe et al. "Solar neutrino results in Super-Kamiokande-III". In: *Phys. Rev. D* 83 (2011), p. 052010. DOI: 10.1103/PhysRevD.83.052010. arXiv: 1010.0118 [hep-ex].

[140] Michael Smy. "Low Energy Event Reconstruction and Selection in Super-Kamiokande-III". In: *30th International Cosmic Ray Conference*. Vol. 5. July 2007, pp. 1279–1282.

[141] Zbiri Karim. *Additional Gadolinium Support for GLG4sim*. https://web.archive.org/web/20060907034310/neutrino.phys.ksu.edu/~GLG4sim/Gd.html. Archived from original on 07 Sep 2006. Sept. 2006. URL: https://web.archive.org/web/20060907034310/neutrino.phys.ksu.edu/~GLG4sim/Gd.html.

[142] Iwa Ou et al. "Measurement of the Energy, Multiplicity and Angular Correlation of γ-rays from the Thermal Neutron Capture Reaction Gd(n, γ)". In: *JPS Conf. Proc.* 1 (2014), p. 013053. DOI: 10.7566/JPSCP.1.013053.

[143] Steve Dye and Andrew Barna. "Global Antineutrino Modeling for a Web Application". In: (Oct. 2015). arXiv: 1510.05633 [physics.ins-det].

[144] Lucas Machado. "Pre-Supernova Alert System for Super-Kamiokande with Gadolinium". PhD thesis. Naples U., 2021.

[145] B. P. Roe *et al.* "Boosted decision trees as an alternative to artificial neural networks for particle identification". In: *Nucl. Instrum. Meth. A* 543 (2005), pp. 577–584.

[146] Y. Freund and R. E. Schapire. "A Decision-Theoretic Generalization of On-Line Learning and an Application to Boosting". In: *Proc. 2nd European Conf. on Computational Learning Theory*. 1997, pp. 23–37.

[147] A. Hoecker *et al.* "TMVA: Toolkit for Multivariate Data Analysis". In: *PoS* ACAT (2007), p. 040.

[148] A. Gando et al. "Measurement of the double-β decay half-life of ^{136}Xe with the KamLAND-Zen experiment". In: *Phys. Rev. C* 85 (2012), p. 045504. DOI: 10.1103/PhysRevC.85.045504. arXiv: 1201.4664 [hep-ex].

[149] S. Abe et al. "Limits on Astrophysical Antineutrinos with the KamLAND Experiment". In: *Astrophys. J.* 925.1 (2022), p. 14. DOI: 10.3847/1538-4357/ac32c1. arXiv: 2108.08527 [astro-ph.HE].

[150] Atsuto Suzuki. "Antineutrino Science in KamLAND". In: *Eur. Phys. J. C* 74.10 (2014), p. 3094. DOI: 10.1140/epjc/s10052-014-3094-x. arXiv: 1409.4515 [hep-ex].

[151] S. Abe et al. "Search for the Majorana Nature of Neutrinos in the Inverted Mass Ordering Region with KamLAND-Zen". In: *Phys. Rev. Lett.* 130.5 (2023), p. 051801. DOI: 10.1103/PhysRevLett.130.051801. arXiv: 2203.02139 [hep-ex].

[152] B. E. Berger et al. "The KamLAND Full-Volume Calibration System". In: *JINST* 4 (2009), P04017. DOI: 10.1088/1748-0221/4/04/P04017. arXiv: 0903.0441 [physics.ins-det].

[153] T. I. Banks et al. "A compact ultra-clean system for deploying radioactive sources inside the KamLAND detector". In: *Nucl. Instrum. Meth. A* 769 (2015), pp. 88–96. DOI: 10.1016/j.nima.2014.09.068. arXiv: 1407.0413 [physics.ins-det].

[154] J. B. Birks. "Scintillations from Organic Crystals: Specific Fluorescence and Relative Response to Different Radiations". In: *Proc. Phys. Soc. A* 64 (1951), pp. 874–877. DOI: 10.1088/0370-1298/64/10/303.

[155] A. Gando et al. "A study of extraterrestrial antineutrino sources with the KamLAND detector". In: *Astrophys. J.* 745 (2012), p. 193. DOI: 10.1088/0004-637X/745/2/193. arXiv: 1105.3516 [astro-ph.HE].

[156] A. Gando et al. "Reactor On-Off Antineutrino Measurement with KamLAND". In: *Phys. Rev. D* 88.3 (2013), p. 033001. DOI: 10.1103/PhysRevD.88.033001. arXiv: 1303.4667 [hep-ex].

[157] S. Abe et al. "A Search for Charged Excitation of Dark Matter with the KamLAND-Zen Detector". In: (Jan. 2021). arXiv: 2101.06049 [hep-ex].

[158] S. Abe et al. “Precision Measurement of Neutrino Oscillation Parameters with KamLAND”. In: *Phys. Rev. Lett.* 100 (2008), p. 221803. DOI: 10.1103/PhysRevLett.100.221803. arXiv: 0801.4589 [hep-ex].

[159] Patrick Huber. “Determination of antineutrino spectra from nuclear reactors”. In: *Phys. Rev. C* 84 (2011), p. 024617. DOI: 10.1103/PhysRevC.84.024617.

[160] Th. A. Mueller et al. “Improved predictions of reactor antineutrino spectra”. In: *Phys. Rev. C* 83 (2011), p. 054615. DOI: 10.1103/PhysRevC.83.054615.

[161] P. Vogel et al. “Reactor antineutrino spectra and their application to antineutrino-induced reactions. II”. In: *Phys. Rev. C* 24 (1981), pp. 1543–1553. DOI: 10.1103/PhysRevC.24.1543.

[162] S. Enomoto et al. “Neutrino geophysics with KamLAND and future prospects”. In: *Earth and Planetary Science Letters* 258 (2007), pp. 147–159. DOI: https://doi.org/10.1016/j.epsl.2007.03.038.

[163] Glen Cowan et al. “Asymptotic formulae for likelihood-based tests of new physics”. In: *Eur. Phys. J. C* 71 (2011). [Erratum: Eur.Phys.J.C 73, 2501 (2013)], p. 1554. DOI: 10.1140/epjc/s10052-011-1554-0. arXiv: 1007.1727 [physics.data-an].

[164] Louis Lyons. “Open statistical issues in Particle Physics”. In: *Ann. Appl. Stat.* 2 (2008), pp. 887–915. DOI: 10.1214/08-AOAS163.

[165] C. Simpson et al. “Sensitivity of Super-Kamiokande with Gadolinium to Low Energy Anti-neutrinos from Pre-supernova Emission”. In: *Astrophys. J.* 885 (2019), p. 133. DOI: 10.3847/1538-4357/ab4883. arXiv: 1908.07551 [astro-ph.HE].

[166] Bill Paxton et al. “Modules for Experiments in Stellar Astrophysics (MESA)”. In: *Astrophys. J. Suppl.* 192 (2011), p. 3. DOI: 10.1088/0067-0049/192/1/3. arXiv: 1009.1622 [astro-ph.SR].

[167] A. Yu. Smirnov. “The MSW effect and solar neutrinos”. In: *10th International Workshop on Neutrino Telescopes*. May 2003, pp. 23–43. arXiv: hep-ph/0305106.

[168] Meridith Joyce et al. “Standing on the Shoulders of Giants: New Mass and Distance Estimates for Betelgeuse through Combined Evolutionary, Asteroseismic, and Hydrodynamic Simulations with MESA”. In: *The Astrophysical Journal* 902.1 (Oct. 2020), p. 63. DOI: 10.3847/1538-4357/abb8db. URL: https://dx.doi.org/10.3847/1538-4357/abb8db.

[169] M. A. Acero et al. “White paper on light sterile neutrino searches and related phenomenology”. In: *J. Phys. G* 51.12 (2024), p. 120501. DOI: 10.1088/1361-6471/ad307f. arXiv: 2203.07323 [hep-ex].

[170] V. Alan Kostelecky and Stuart Samuel. "Spontaneous Breaking of Lorentz Symmetry in String Theory". In: *Phys. Rev. D* 39 (1989), p. 683. DOI: 10.1103/PhysRevD.39.683.

[171] Aman Gupta, Debasish Majumdar, and Suprabh Prakash. "Neutrino oscillation measurements with KamLAND and JUNO in the presence of scalar NSI". In: *Phys. Dark Univ.* 49 (2025), p. 102011. DOI: 10.1016/j.dark.2025.102011. arXiv: 2306.07343 [hep-ph].

[172] J. Aguilar et al. "Study of nonstandard interactions mediated by a scalar field at the ESSnuSB experiment". In: *Phys. Rev. D* 109.11 (2024), p. 115010. DOI: 10.1103/PhysRevD.109.115010. arXiv: 2310.10749 [hep-ex].

[173] Jose F. Nieves and Palash B. Pal. "Generalized Fierz identities". In: *Am. J. Phys.* 72 (2004), pp. 1100–1108. DOI: 10.1119/1.1757445. arXiv: hep-ph/0306087.

[174] C. C. Nishi. "Simple derivation of general Fierz-like identities". In: *Am. J. Phys.* 73 (2005), pp. 1160–1163. DOI: 10.1119/1.2074087. arXiv: hep-ph/0412245.

[175] Mariia Redchuk. "Comprehensive measurement of pp-chain solar neutrinos with Borexino". In: *PoS* EPS-HEP2019 (2020), p. 400. DOI: 10.22323/1.364.0400.

[176] Alex Himmel. *New Oscillation Results from the NOvA Experiment*. July 2020. DOI: 10.5281/zenodo.3959581. URL: https://doi.org/10.5281/zenodo.3959581.

[177] Patrick Dunne. *Latest Neutrino Oscillation Results from T2K*. July 2020. DOI: 10.5281/zenodo.3959558. URL: https://doi.org/10.5281/zenodo.3959558.

[178] K. S. Babu, Garv Chauhan, and P. S. Bhupal Dev. "Neutrino nonstandard interactions via light scalars in the Earth, Sun, supernovae, and the early Universe". In: *Phys. Rev. D* 101.9 (2020), p. 095029. DOI: 10.1103/PhysRevD.101.095029. arXiv: 1912.13488 [hep-ph].

[179] Morihiro Honda et al. "Improvement of low energy atmospheric neutrino flux calculation using the JAM nuclear interaction model". In: *Physical Review D—Particles, Fields, Gravitation, and Cosmology* 83.12 (2011), p. 123001.

[180] Yoshinari Hayato and Luke Pickering. "The NEUT neutrino interaction simulation program library". In: *The European Physical Journal Special Topics* 230.24 (2021), pp. 4469–4481.

[181] René Brun et al. *GEANT 3: user's guide Geant 3.10, Geant 3.11*. Tech. rep. CERN, 1987.

[182] Th K Gaisser and M Honda. "Flux of atmospheric neutrinos". In: *Annual Review of Nuclear and Particle Science* 52.1 (2002), pp. 153–199.

[183] T Sanuki et al. “Precise Measurement of Cosmic-Ray Proton and HeliumSpectra with the BESS Spectrometer”. In: *The Astrophysical Journal* 545.2 (2000), p. 1135.

[184] Koh Abe et al. “Measurements of proton, helium and muon spectra at small atmospheric depths with the BESS spectrometer”. In: *Physics Letters B* 564.1-2 (2003), pp. 8–20.

[185] Sadakazu Haino et al. “Measurements of primary and atmospheric cosmic-ray spectra with the BESS-TeV spectrometer”. In: *Physics Letters B* 594.1-2 (2004), pp. 35–46.

[186] J Alcaraz et al. “Cosmic protons”. In: *Physics Letters B* 490.1-2 (2000), pp. 27–35.

[187] J Alcaraz et al. “Protons in near earth orbit”. In: *Physics Letters B* 472.1-2 (2000), pp. 215–226.

[188] J Alcaraz et al. “Helium in near Earth orbit”. In: *Physics Letters B* 494.3-4 (2000), pp. 193–202.

[189] Koji Niita et al. “PHITS—a particle and heavy ion transport code system”. In: *Radiation measurements* 41.9-10 (2006), pp. 1080–1090.

[190] Stefan Roesler, Ralph Engel, and Johannes Ranft. “The monte carlo event generator dpmjet-iii”. In: *Advanced Monte Carlo for Radiation Physics, Particle Transport Simulation and Applications: Proceedings of the Monte Carlo 2000 Conference, Lisbon, 23–26 October 2000*. Springer. 2001, pp. 1033–1038.

[191] Maria Gabriella Catanesi et al. “Measurement of the production cross-sections of $\pi\pm$in p–C and $\pi\pm$–C interactions at 12 GeV/c”. In: *Astroparticle Physics* 29.4 (2008), pp. 257–281.

[192] Maria Gabriella Catanesi et al. “Forward $\pi\pm$production in p–O2 and p–N2 interactions at 12 GeV/c”. In: *Astroparticle Physics* 30.3 (2008), pp. 124–132.

[193] JA Simpson Jr. “The latitude dependence of neutron densities in the atmosphere as a function of altitude”. In: *Physical Review* 73.11 (1948), p. 1389.

[194] CH Llewellyn Smith. “Neutrino reactions at accelerator energies”. In: *Physics Reports* 3.5 (1972), pp. 261–379.

[195] N. J. Baker et al. “Quasielastic Neutrino Scattering: A Measurement of the Weak Nucleon Axial Vector Form-Factor”. In: *Phys. Rev. D* 23 (1981), pp. 2499–2505. DOI: 10.1103/PhysRevD.23.2499.

[196] M. Martini et al. “A Unified approach for nucleon knock-out, coherent and incoherent pion production in neutrino interactions with nuclei”. In: *Phys. Rev. C* 80 (2009), p. 065501. DOI: 10.1103/PhysRevC.80.065501. arXiv: 0910.2622 [nucl-th].

[197] R. Gran et al. “Measurement of the quasi-elastic axial vector mass in neutrino-oxygen interactions”. In: *Phys. Rev. D* 74 (2006), p. 052002. DOI: 10.1103/PhysRevD.74.052002. arXiv: hep-ex/0603034.

[198] A. A. Aguilar-Arevalo et al. “Measurement of Muon Neutrino Quasi-Elastic Scattering on Carbon”. In: *Phys. Rev. Lett.* 100 (2008), p. 032301. DOI: 10.1103/PhysRevLett.100.032301. arXiv: 0706.0926 [hep-ex].

[199] R Gran et al. “Neutrino-nucleus quasi-elastic and 2p2h interactions up to 10 GeV”. In: *Phys. Rev. D* 88.arXiv: 1307.8105 (2013).

[200] Omar Benhar et al. “Spectral function of finite nuclei and scattering of GeV electrons”. In: *Nuclear Physics A* 579.3-4 (1994), pp. 493–517.

[201] Dieter Rein and Lalit M Sehgal. “Neutrino-excitation of baryon resonances and single pion production”. In: *Annals of Physics* 133.1 (1981), pp. 79–153.

[202] Ch Berger and LM Sehgal. “Lepton mass effects in single pion production by neutrinos”. In: *Physical Review D—Particles, Fields, Gravitation, and Cosmology* 76.11 (2007), p. 113004.

[203] M Glück, E Reya, and A Vogt. “Dynamical parton distributions revisited”. In: *The European Physical Journal C-Particles and Fields* 5.3 (1998), pp. 461–470.

[204] Arie Bodek and Un-ki Yang. “A Unified Model for inelastic e- N and v- N cross sections at all Q 2”. In: *AIP Conference Proceedings*. Vol. 792. 1. American Institute of Physics. 2005, pp. 257–260.

[205] Torbjörn Sjöstrand. “High-energy-physics event generation with PYTHIA 5.7 and JETSET 7.4”. In: *Computer Physics Communications* 82.1 (1994), pp. 74–89.

[206] Roger D Woods and David S Saxon. “Diffuse surface optical model for nucleon-nuclei scattering”. In: *Physical Review* 95.2 (1954), p. 577.

[207] LL Salcedo et al. “Computer simulation of inclusive pion nuclear reactions”. In: *Nuclear Physics A* 484.3-4 (1988), pp. 557–592.

[208] C Zeitnitz and TA Gabriel. “The GEANT-Calor Interface”. In: *Proceedings of International Conference on Calorimetry in High Energy Physics*. World Scientific. 1993, p. 376.

[209] Lee Ka Pik. “Study of the neutrino mass hierarchy with the atmospheric neutrino data observed in Super-Kamiokande”. PhD thesis. Tokyo U., 2012.

[210] Gaku Mitsuka. “Study of Non-Standard Neutrino Interactions with Atmospheric Neutr ino Data in Super-Kamiokande”. PhD thesis. Tokyo U., 2009.

[211] M. Jiang et al. “Atmospheric Neutrino Oscillation Analysis with Improved Event Reconstruction in Super-Kamiokande IV”. In: *PTEP* 2019.5 (2019), 053F01. DOI: 10.1093/ptep/ptz015. arXiv: 1901.03230 [hep-ex].

[212] M. Shiozawa. "Reconstruction algorithms in the Super-Kamiokande large water Cherenkov detector". In: *Nucl. Instrum. Meth. A* 433 (1999). Ed. by A. Breskin, R. Chechik, and T. Ypsilantis, pp. 240–246. DOI: 10.1016/S0168-9002(99)00359-9.

[213] RB Patterson et al. "The extended-track event reconstruction for MiniBooNE". In: *Nuclear Instruments and Methods in Physics Research Section A: Accelerators, Spectrometers, Detectors and Associated Equipment* 608.1 (2009), pp. 206–224.

[214] K. Abe et al. "First Joint Oscillation Analysis of Super-Kamiokande Atmospheric and T2K Accelerator Neutrino Data". In: *Phys. Rev. Lett.* 134.1 (2025), p. 011801. DOI: 10.1103/PhysRevLett.134.011801. arXiv: 2405.12488 [hep-ex].

[215] F. James. "MINUIT Function Minimization and Error Analysis: Reference Manual Version 94.1". In: (1994).

[216] Miao Jiang. "Study of the neutrino mass hierarchy with the atmospheric neutrino data collected in Super-Kamiokande IV". PhD thesis. Kyoto U., Mar. 2019. DOI: 10.14989/doctor.k21948.

[217] T. Suzuki, David F. Measday, and J. P. Roalsvig. "Total Nuclear Capture Rates for Negative Muons". In: *Phys. Rev. C* 35 (1987), p. 2212. DOI: 10.1103/PhysRevC.35.2212.

[218] Pierre A. M. Guichon et al. "MU- PARTIAL CAPTURE RATES IN O-16". In: *Phys. Rev. C* 19 (1979), pp. 987–997. DOI: 10.1103/PhysRevC.19.987.

[219] Shintaro Miki. "Neutrino mass ordering determination using atmospheric neutrinos with neutron detection in Super-Kamiokande". PhD thesis. The University of Tokyo, U. Tokyo (main), 2025.

[220] G. Battistoni et al. "The FLUKA atmospheric neutrino flux calculation". In: *Astropart. Phys.* 19 (2003). [Erratum: Astropart.Phys. 19, 291–294 (2003)], pp. 269–290. DOI: 10.1016/S0927-6505(02)00246-3. arXiv: hep-ph/0207035.

[221] G. D. Barr et al. "A Three - dimensional calculation of atmospheric neutrinos". In: *Phys. Rev. D* 70 (2004), p. 023006. DOI: 10.1103/PhysRevD.70.023006. arXiv: astro-ph/0403630.

[222] United States Committee on Extension to the Standard Atmosphere. *US standard atmosphere, 1976*. National Oceanic and Amospheric [sic] Administration, 1976.

[223] Alan E Hedin. "MSIS-86 thermospheric model". In: *Journal of Geophysical Research: Space Physics* 92.A5 (1987), pp. 4649–4662.

[224] Callum Wilkinson et al. “Reanalysis of bubble chamber measurements of muon-neutrino induced single pion production”. In: *Phys. Rev. D* 90.11 (2014), p. 112017. DOI: 10.1103/PhysRevD.90.112017. arXiv: 1411.4482 [hep-ex].

[225] E. Hernandez, J. Nieves, and M. Valverde. “Neutrino induced weak pion production off the nucleon”. In: *Mod. Phys. Lett. A* 23 (2008). Ed. by Atsushi Hosaka et al., pp. 2317–2320. DOI: 10.1142/S0217732308029289. arXiv: 0802.1627 [hep-ph].

[226] R. L. Workman et al. “Review of Particle Physics”. In: *PTEP* 2022 (2022), p. 083C01. DOI: 10.1093/ptep/ptac097.

[227] A. Capella et al. “Structure functions and low x physics”. In: *Phys. Lett. B* 337 (1994), pp. 358–366. DOI: 10.1016/0370-2693(94)90988-1. arXiv: hep-ph/9405338.

[228] Arie Bodek and Un-ki Yang. “Axial and Vector Structure Functions for Electron- and Neutrino- Nucleon Scattering Cross Sections at all Q^2 using Effective Leading order Parton Distribution Functions”. In: (Nov. 2010). arXiv: 1011.6592 [hep-ph].

[229] T. Yang et al. “A Hadronization Model for Few-GeV Neutrino Interactions”. In: *Eur. Phys. J. C* 63 (2009), pp. 1–10. DOI: 10.1140/epjc/s10052-009-1094-z. arXiv: 0904.4043 [hep-ph].

[230] Roger Alexandre Wendell. “Three Flavor Oscillation Analysis of Atmospheric Neutrinos in Super-Kamiokande”. PhD thesis. North Carolina U., 2008.

[231] Lakshmi S. Mohan et al. *Laser reflectivity tuning for SK5 with dark noise subtraction and its impact on e/π^0 separation in T2K ν_e analysis*. Super-Kamiokande Collaboration Meeting. Internal report. May 2022.

[232] Tom G Mackay and Akhlesh Lakhtakia. *The transfer-matrix method in electromagnetics and optics*. Springer Nature, 2022.

[233] Dario Motta and Stefan Schonert. “Optical properties of Bialkali photocathodes”. In: *Nucl. Instrum. Meth. A* 539 (2005), pp. 217–235. DOI: 10.1016/j.nima.2004.10.009. arXiv: physics/0408075.